UNIVERSITY OF SOUTHAMPTON

SYNTHESIS, STRUCTURE AND MAGNETIC PROPERTIES OF SOME LOW DIMENSIONAL METAL COMPOUNDS

Thesis for the Degree of Doctor of Philosophy

By

Rina Patel

SCHOOL OF CHEMISTRY
FACULTY OF SCIENCE

February 2008

UNIVERSITY OF SOUTHAMPTON

ABSTRACT

SCHOOL OF CHEMISTRY
FACULTY OF SCIENCE

Doctor of Philosophy

SYNTHESIS, STRUCTURE AND MAGNETIC PROPERTIES OF SOME LOW DIMENSIONAL METAL COMPOUNDS

By Rina Patel

A selection of low dimensional metal compounds have been synthesised; the structures and magnetic properties of these materials have been characterised using Rietveld analysis of powder X-ray and powder neutron data and magnetic susceptibility measurements.

Refinements on the $LnSrScO_4$ (Ln = La – Sm) were performed in several space groups accommodating octahedral tilts. Based on the statistics the A*bma* description was used to model the data and the orthorhombic distortion results from tilting of the ScO_6 octahedra within the perovskite layer. Graphs of the *b/a* ratio against temperature show that the level of distortion increases between 25 – 300 °C and decreases between 300 – 1200 °C; for $LaSrScO_4$ and $PrSrScO_4$ the compounds revert to the ideal K_2NiF_4-type structure at approximately 900 and 1100 °C respectively. A similar analysis was undertaken for $LnSrInO_4$ (Ln = La and Pr), these compounds adopt the P*bca* space group at room temperature. A comprehensive study has been carried out to investigate the factors that lead to the choice of structure and drive distortions of the K_2NiF_4-type structure away from an I*4/mmm* description.

An investigation into the $LnSrCoO_4$ (Ln = La - Gd) series has been performed. As the smaller lanthanides are incorporated into the structure (La→Er), the K_2NiF_4 structure is maintained until Tb. At which point the mismatch between the perovskite Co-O layer and the rocksalt (Sr/ Ln)-O layers become too great, resulting in the formation of $SrLn_2O_4$. Graphs of Co-O axial bond distances against temperature were plotted in order to determine whether a thermally induced spin transition occurs, anomalous behaviour for all compounds was observed. A comparison of the thermal expansion of the axial B-O distances in the compounds; $LaSrCoO_4$, $LaSrFeO_4$, $La_{1.8}Sr_{0.2}CuO_4$ and $LaBaCoO_4$ enabled us to identify that the Co^{3+} compounds expand much faster in the apical direction. If low spin Co^{3+}, (t_{2g}^6, e_g^0) $dxy^2dzy^2dxz^2$ can be thermally excited to an intermediate-spin, ($t_{2g}^5e_g^1$), the electron density would transfer to the dz^2 orbital. This would expand the axial distance faster than a normal thermal effect. Based on this there is strong evidence that a spin transition occurs in these compounds.

Novel analogues of $La_2Ba_6Co_4O_{15}$ have been synthesised by replacing La^{3+} with Nd^{3+} and Sm^{3+}. The structure of these phases and the previously reported $La_2Ba_6Co_4O_{15}$ have been determined from analysis of neutron diffraction data and adopt the P*63mc* space group. The compound consists of one CoO_6 octahedron and three CoO_4 tetrahedra linked by corner sharing oxygen ions, forming a Co_4O_{15} cluster. The clusters form a triangular based lattice that resembles a honeycomb. Magnetic data reveal an antiferromagnetic transition due to the long range ordering of clusters at 4, 8.5 and 17.5 K for $Ln_2Ba_6Co_4O_{15}$ (Ln = La, Nd and Sm) respectively. The ZFC and FC susceptibilities have been discussed in detail.

Three complex transition metal triazole compounds have been synthesised and investigated by single crystal X-ray diffraction. 1) $[Co_2Cl(3\text{-amino-}1,2,4\text{-triazole})_3]$ is an intriguing magnetically coupled coordination network. The implications of the observed ferrimagnetic ordering are discussed in the context of the topological structural disorder. The compound was obtained from a hydrothermal synthesis, crystallising in a primitive hexagonal cell a good structural model for $[Co_2Cl(3\text{-amino-}1,2,4\text{-triazole})_3]$ was obtained in the non-polar space group *P6₃/mmc*, revealing a 3-D coordination network. 2) $[CuCl(3\text{-amino-}1,2,4\text{-triazole})_2.Cl]$ crystallises in the orthorhombic space group P*bcm* and displays a zig-zag polymeric structure. 3) $[Cu_5Cl_2(3,5\text{-diamino-triazolate})_3].H_2O$ consists of unusual chains of trinuclear units with a 3,5-diamino-triazole linking the trimeric units. These trimeric entities are bridged by Cu coordinated to Cl forming a chain, which are in turn linked by Cu-Cl in a zig-zag formation to form layers.

TABLE OF CONTENTS

***Chapter One:* Introduction**

1.1 Introduction 2

1.2 First Row Transition Metals 2

1.3 Structural Chemistry of Scandium(III) 4

1.4 Structural Chemistry of Cobalt 5

1.4.1 Structural Chemistry of Cobalt(II) 5

1.4.2 Structural Chemistry of Cobalt(III) 6

1.4.3 Structural Chemistry of Cobalt(IV) 6

1.4.4 Mixed Valence Cobalt Systems 7

1.5 Structural Chemistry of Copper 7

1.5.1 Structural Chemistry of Copper(I) 8

1.5.2 Structural Chemistry of Copper(II) 8

1.5.2.1 The Jahn-Teller Effect 8

1.5.2.2 Four, Five and Six-Coordinate Copper(II) Compounds 10

1.6 Structural Chemistry of Indium(III) 11

1.7 The Lanthanide Series 12

1.8 The Structures of Oxide Materials 13

1.8.1 The Perovskite Structure 13

1.8.2 Double Perovskites 16

1.8.3 Random Structure Perovskites 17

1.8.4 Rock Salt Perovskites 18

1.8.5 Layered Structure Perovskites 18

1.8.6 The K_2NiF_4 Structure 19

1.8.7 The Ruddlesden-Popper Phases 20

1.8.8 Oxygen Deficiency in Perovskites 21

1.9 Spin-Crossover 23

1.9.1 Applications of Spin-Crossover Systems 26

1.9.2 Spin-Crossover in 1,2,4-Triazole Complexes 27

1.10 Scope of this Work 29

1.11 References 31

Chapter Two: **Experimental Techniques**

2.1 Introduction 36

2.2 Synthetic Methods 36

2.2.1 Direct Solid State Route 36

2.2.2 The Sol-Gel Method 37

2.2.3 Hydrothermal Synthesis 38

2.3 Powder X-ray Diffraction 39

2.3.1 X-ray Radiation 40

2.3.2 Powder X-ray Diffraction Theory 42

2.3.3 Instrumentation 46

2.3.4 Variable Temperature PXD 49

2.3.5 Analysis of PXD Data 50

2.4 Powder Neutron Diffraction 52

2.4.1 Constant Wavelength PND 53

2.4.2 Time of Flight (TOF) PND 54

2.4.3 TOF Instrument POLARIS 57

2.4.4 TOF Instrument HRPD 58

2.5 The Rietveld Method 59

2.5.1 Criteria of Fit 63

2.6 Single Crystal X-ray Diffraction 65

2.7 Magnetic Measurements 68

2.8 Thermal Analysis 73

2.9 Infra-Red Spectroscopy 74

2.10 References 75

Chapter Three: **Synthesis and Structural Characterisation of the $LnSrScO_4$ and $LnSrInO_4$ phases and Discussion of the A_2BO_4 oxides**

3.1 Introduction 78

3.2 The $LnSrScO_4$ (Ln = La, Ce, Pr, Nd and Sm) Phases 81

3.2.1 Synthesis 81

3.2.2 Structural Characterisation 82

3.2.2.1 Variable Temperature PXD Structure Refinement of $LnSrScO_4$ 82

3.2.2.2 Variable Temperature PND Structure Refinement of $LnSrScO_4$ (Ln = La, Pr and Nd) 92

3.2.3 Discussion 97

3.3 The $LnSrInO_4$ (Ln = La and Pr) Phases 103

3.3.1 Synthesis 103

3.3.2 Structural Characterisation 103

3.3.2.1 Variable Temperature PXD Structure Refinement of $LnSrInO_4$ 103

3.3.2.2 PND Structure Refinement of $LaSrInO_4$ 112

3.3.3 Discussion 114

3.4 Structural Distortions in the K_2NiF_4-type Structures 118

3.5 Conclusion 123

3.6 References 124

***Chapter Four:* Synthesis, Structural and Magnetic Characterisation of the $LnSrCoO_4$ series**

4.1 Introduction 127

4.2 Synthesis 129

4.3 Room Temperature PXD Studies of the $LnSrCoO_4$ (Ln = La, Pr, Nd, Eu, Sm and Gd Systems) 131

4.3.1 PXD Structure Refinement 131

4.3.2 Discussion 133

4.4 Magnetic Characterisation 137

4.5 Variable Temperature PXD and PND Studies of the $LnSrCoO_4$ (Ln = La – Gd) Systems 139

4.5.1 Variable Temperature PXD Structure Refinement 139

4.5.2 Variable Temperature PND Structure Refinement of $LnSrCoO_4$ (Ln = La, Nd, ^{154}Sm and ^{160}Gd) 143

4.5.3 Discussion 148

4.6 Thermal Analysis 162

4.7 Comparison with other K_2NiF_4 oxides 163

4.8 Conclusion 166

4.9 References 168

Chapter Five: Synthesis, Structural and Magnetic Characterisation of $La_{1+x}Ba_{1-x}CoO_4$

5.1 Introduction 171

5.2 Synthesis 171

5.3 Structural Characterisation of $LaBaCoO_4$ 173

5.3.1 Variable Temperature PXD Structure Refinement of $LaBaCoO_4$ 173

5.3.2 Variable Temperature PND Structure Refinement of $La_{1+x}Ba_{1-x}CoO_4$ 176

5.4 Magnetic Characterisation 180

5.5 Discussion 182

5.6 Conclusion 187

5.7 References 188

Chapter Six: Synthesis, Structural and Magnetic Characterisation of $Ln_2Ba_6Co_4O_{15}$ (Ln = La, Pr, Nd and Sm)

6.1 Introduction 190

6.2 Synthesis 191

6.3 Structural Characterisation 192

6.3.1 PXD Structure Refinement of $Ln_2Ba_6Co_4O_{15}$ (Ln = La, Pr, Nd and Sm) 192

6.3.2 PND Structural Characterisation of $Ln_2Ba_6Co_4O_{15}$ (Ln = La and Nd) 194

6.3.3 Discussion 201

6.4 Magnetic Characterisation 204

6.5 A comparison of $La_2Ba_6Co_4O_{15}$ with $La_2Ba_6Fe_4O_{15}$ 209

6.6 Conclusion 211

6.7 References 213

Chapter Seven: Transition Metal Complexes of 1,2,4-triazoles

7.1 Introduction 215

7.1.1 Coordination Complexes of 1,2,4-triazoles 215

7.1.2 Objective 219

7.2 [Co_2Cl(3-amino-1,2,4-triazole)$_3$] 220

7.2.1 Synthesis 220

7.2.2 Results and Discussion 221

7.2.3 Magnetic Susceptibility Measurements of [Co_2Cl(3-amino-1,2,4-triazole)$_3$] 225

7.3 [CuCl(3-amino-1,2,4-triazole)$_2$.Cl] 230

7.3.1 Synthesis 230

7.3.2 Results and Discussion 230

7.4 [Cu_5Cl_2(3,5-diamino-triazolate)$_3$].H_2O 233

7.4.1 Synthesis 233

7.4.2 Results and Discussion 233

7.5 Conclusion 238

7.6 References 240

Appendix A 243

Appendix B 258

ACKNOWLEDGEMENTS

I am very grateful to my supervisor Professor Mark Weller for his guidance and support over the past four years. Thanks also go to Dr Daniel Price, Department of Chemistry, University of Glasgow who collected and analysed the magnetic data for those compounds described in chapter 7.

Professor Brian Rainford in the School of Physics and Charles Simon in the School of Chemistry, University of Southampton also deserve my thanks for the collection of SQUID and VSM data for selected samples. Thanks are also due to the Southampton crystallography department and especially Dr Mark Light for the use of the equipment and advice on solving crystal structures.

I owe particular thanks to Dr Bob Hughes and Peter Hickey; Bob for the considerable level of support he gave me on a daily basis throughout my PhD and Peter for his help in the collection of powder neutron diffraction data at the I.L.L and R.A.L

I would also like to extend my thanks to the Weller group past and present who have made the past three years enjoyable, including Jenny Armstrong, Stuart Henderson, Seth Wiggin, Mark Hogben, Florian Norindr, Rosa Galati, Kate Burden, Jess Rouse and Sergio Russo.

Finally and most importantly, I must thank my family; Simon, Mum, Dad, Sandhya, Sneha and Minesh, for their love and support without which this would not have been possible.

ABBREVIATIONS

Some commonly used abbreviations in this work:

PXD	Powder X-ray Diffraction
PND	Powder Neutron Diffraction
TOF	Time of Flight
TGA	Thermogravimetric Analysis
DTA	Differential Thermal Analysis
IR	Infra-red
JCPDS	Joint Committee on Powder Diffraction Standards
GSAS	General Structure Analysis System
esd	Estimated Standard Deviation
FWHM	Full Width at Half Maximum
RT	Room Temperature
HS	High Spin
IS	Intermediate Spin
LS	Low Spin
RAL	Rutherford Appleton Laboratories
ILL	Institute Laue Langevin

Chapter One

Introduction

1.1 Introduction

Complex metal oxides have a wide variety of industrial applications, which utilise the unique chemical, and physical properties of the materials.[1] As a result, both the structural chemistry and the physical properties of these materials have been the focus of many studies in the last 5 decades. Characteristics such as electrical and magnetic behaviour or variable oxygen stoichiometry may be exploited. Applications of complex metal oxides include solid state devices such as capacitors, heating elements and rechargeable batteries.

The majority of complex oxides consist of multi-dimensional units constructed from metal-oxygen polyhedra. Applications such as semiconductors,[2] superconductors,[3] ferroelectrics[4] and piezoelectrics[5] arise from the cooperative electronic effects facilitated by extended structures formed by linked MO_n polyhedra. A large amount of interest in the perovskite structure type was prompted by the discovery of ferroelectricity in $BaTiO_3$ by Von Hippel.[6] The three-dimensional (3D) perovskite or related (2D) layered structure represented by the general formula $(AO)_n(ABO_3)_n$ (A = lanthanide/ rare earth, B = transition metal/ post transition metal) are adopted by a number of phases exhibiting similar properties to $BaTiO_3$. Studies by Galasso revealed that the A and B sites can each accommodate two or more ions in varying oxidation states,[7] allowing researchers to tune the properties to create new thermistors,[8] IR windows,[9] semiconductors[2] and recently high temperature superconductors or spin crossover materials. [10,11]

1.2 First Row Transition Metals

The transition elements can be classified as metals with partially filled *d*-orbitals in either the neutral atom or its ions. Characteristically they have high melting points, alloy forming capabilities, and with very few exceptions display variable oxidation states. As a consequence, transition elements exhibit many different coordination geometries e.g. octahedral, square pyramidal and square planar.

The maximum attainable oxidation state is dependent upon the position of the element in the transition metal series; the highest oxidation state of the elements in the first row initially rises and then falls as the series is traversed. (Table 1).

Table 1 Known oxidation states of the first-row transition elements in oxides.

Element	Oxidation states
Sc	3
Ti	2 3 4
V	2 3 4 5
Cr	2 3 4 5 6
Mn	2 3 4 5 6 7
Fe	2 3 4 5 6
Co	2 3 4 5
Ni	2 3 4
Cu	1 2 3

This pattern is a result of the changing screening power of the extra nuclear electrons. Although in hydrogen the subshells of each shell are equally energetic, in the more complex atoms the *s*, *p*, *d* and *f* subshells split apart and drop to lower energies. This descent in energy occurs because the extent to which an electron in a particular orbital is shielded from the nuclear charge by other electrons decreases with atomic number. The effective nuclear charge therefore rises with atomic number, for a particular oxidation state within a subshell. However, the increase in the third ionisation potential after iron reflects a decrease in the screening power and consequently the higher oxidation states become more difficult to attain. This is demonstrated by the greater amount of compounds containing trivalent iron than trivalent nickel. The fall in the oxidation state after manganese is also indicative of the drop in screening power. The highest level of oxidation continues to decrease until copper where the prevalent valances are Cu(I) and Cu(II) and the maximum Cu(III). In the following section transition metals (TM) of importance in this work will be described in more detail.

1.3 Structural Chemistry of Scandium(III)

The most common oxidation state of scandium is Sc(III) with typically octahedral coordination geometry e.g ScO_6. Scandium chemically resembles yttrium and the rare earth metals more than it resembles aluminium or titanium. Thus scandium is sometimes seen as Sc_2O_3 and as $ScCl_3$. Scandium(III) oxide is a white amorphous powder used in high temperature systems (for its resistance to heat and chemical shock), electronic ceramics and glass composition. Unlike its higher homologues yttrium oxide and lanthanum oxide, scandium oxide will dissolve in alkali to form scandate salts.

Examples of scandate phases include the $LnScO_3$ (Ln = La – Ho) orthorhombic perovskites, adopting space group P*bnm*, containing distorted polyhedra of both Ln and Sc ions, together with strongly tilted ScO_6 octahedra (Figure 1).[12] Another example is the germanate compound $Cu_2Sc_2Ge_4O_{13}$,[13] synthesised by solid state ceramic sintering techniques between 1173 and 1423 K. The compound crystallises in the monoclinic space group P*21/m*. The structure consists of crank shaft like chains of edge sharing ScO_6 octahedra running parallel to the crystallographic *b*-axis. These chains are linked laterally by $[Cu_2O_6]^{8-}$ dimers forming a sheet of metal-oxygen-polyhedra within the *ab* plane. These sheets are separated along the *c* axis by $[Ge_4O_{13}]^{10-}$ units.

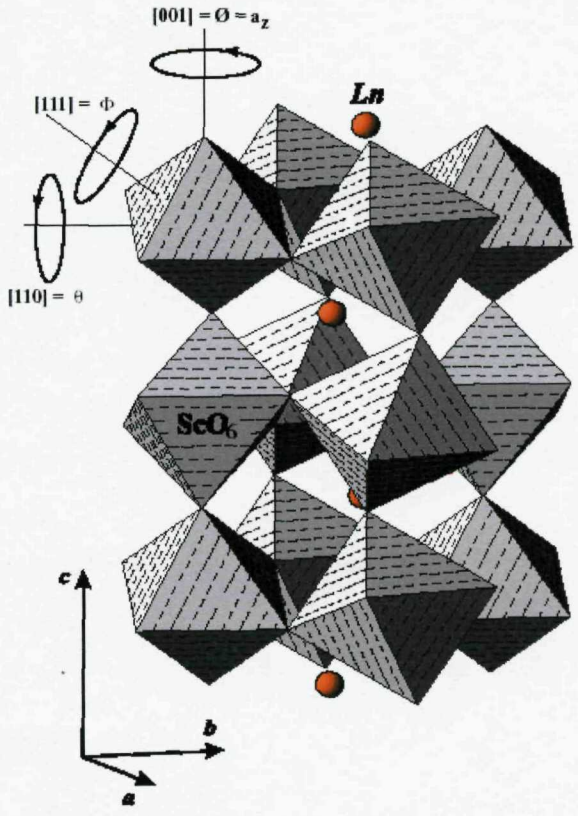

Figure 1 A polyhedral representation of $LnScO_3$[12]

1.4 Structural Chemistry of Cobalt

The most common oxidation states of cobalt are Co(II) and Co(III) with typically tetrahedral or octahedral coordination geometries. In the solid state cobalt primarily favours a trivalent oxidation state, exemplified by the oxidation of CoO to Co_3O_4 upon sintering in air. Despite these materials being sensitive to atmospheric moisture they are commonly used as a starting material for the synthesis of cobalt materials. Extreme conditions are required to attain Co(IV) in the solid state; e.g. the synthesis of $SrCoO_{3.0}$ occurs at 1000 °C using a diamond anvil device to provide a pressure of 65 Kbar.[14]

1.4.1 Structural Chemistry of Cobalt(II)

As a result of the d^7 electronic configuration of Co^{2+}, the complexes formed by cobalt(II) generally contain tetrahedral units, this is due to the d^7 electronic configuration favouring a tetrahedral over octahedral geometry. Cobalt(II) materials containg octahedral, five coordinate and square planar geometries have

also been reported. Tetrahedral complexes of the form $[CoX_4]^{2-}$ are generally formed with monodentate ligands such as the halides Cl, Br and I. Octahedral Co(II) favours a high spin configuration, the low spin octahedral complexes lose ligands to become five or four-coordinate. An example of a pure Co^{2+} material in the solid state is La_2CoO_4[15] which is prepared by the reaction of CoO and La_2O_3 at 2000 °C under carbon dioxide or argon. It adopts an orthorhombic structure based on a K_2NiF_4 tetragonal system. The CoO_6 octahedra consist of equatorial interactions (1.944 Å) and two axial bonds (2.034 Å). Other examples include $La_2Co_2O_5$,[16] which adopts the brownmillerite-type structure, where single layers of corner sharing CoO_6-octahedra are connected by layers with chains of corner sharing CoO_4 tetrahedra running along the [100] plane. $La_2Co_2O_5$ was prepared by the isothermal reduction of the single phase $LaCoO_3$.

1.4.2 Structural Chemistry of Cobalt(III)

The majority of trivalent compounds in the solid state are octahedrally coordinated; this is due to the increased stability of the octahedral low spin d^6 configuration. Compounds containing trivalent cobalt in the solid state are quite abundant; however pure cobalt(III) materials such as the brownmillerite, $Sr_2Co_2O_5$,[17] are quite rare. Other examples of cobalt(III) materials of recent interest include $LiCoO_2$[18] which has a potential application as a cathode material, containing layers of octahedral Co and Li and $LaSrCoO_4$,[19] a material adopting the K_2NiF_4 structure in which spin-crossover can be thermally induced. The thermally induced spin-state and subsequent nonmetal-metal interactions in the perovskite-type cobalt oxide $LaCoO_3$ has also been of considerable interest yet remains far from being completely understood.[20,21]

1.4.3 Structural Chemistry of Cobalt (IV)

There are few examples of materials containing cobalt displaying this oxidation state in the literature, however the solid state synthesis of several materials have been reported. These materials often contain an alkali or an alkali-earth metal ion such as sodium or strontium. A variety of complex structures are present,

although cobalt is usually found in six-coordination e.g. $K_6Co_2O_7$[22] or Li_8CoO_6.[23]

1.4.4 Mixed Valence Cobalt Systems

One oxide that has been previously mentioned which is a good example of a material containing cobalt in a mixed 2+/ 3+ valence state is $Co^{2+}Co^{3+}{}_2O_4$. The material adopts the spinel structure, with Co^{2+} in tetrahedral and Co^{3+} in octahedral sites within the oxide lattice. Recently the oxygen deficient Ruddlesden-Popper type phases $Sr_3Co_2O_{7-x}$ ($0.94 \leq x \leq 1.22$) have been reported.[24] The partial occupancy of oxide sites in this structure leads to cobalt adopting both octahedral and square pyramidal coordination geometries with a range of Co-O distances (~ 2.0 – 1.87 Å). $SrCoO_{3-x}$[25] and $La_{1-x}Sr_xCoO_3$[26] are examples of mixed 3+/ 4+ valence cobaltates, these materials exhibit a wide range of oxygen non-stoichiometry and a variety of perovskite related structures.

1.5 Structural Chemistry of Copper

Copper is known to exist in five different oxidation states (0, +1, +2, +3 and +4), the most common of which are Cu(I) and Cu(II) with typically tetrahedral, square planar or distorted octahedral coordination. In the solid state copper favours a divalent oxidation state displayed by the most common oxide CuO; a black solid which adopts a monoclinic structure due to the presence of highly distorted CuO_6 octahedra. Cu(III) is much less stable and requires extreme conditions for the preparation e.g. the synthesis of Cs_3CuF_6 is performed using high pressure fluorination of CsCl and $CuCl_2$. The least stable and most rare ion is Cu(IV) which is known to exist in the fluoride phases such as the brick red material Cs_2CuF_6. In this study we are primarily interested in the Cu(II) and Cu(I) oxidation states and the structural chemistry is described.[27]

1.5.1 Structural Chemistry of Copper(I)

Monovalent copper forms two collinear bonds or more commonly four tetrahedral bonds. The tetrahedral geometry of Cu(I) is normally observed in systems where copper is bonded to halides, cyanides and sulphides as opposed to oxygen atoms. Cu(I) oxide systems, such as those found in superconducting materials, prefer a linear geometry which is often referred to as the dumbbell configuration; examples include Cu_2O[28] and ternary oxides such as KCuO[29] and $FeCuO_2$.[30] In KCuO, $[CuO_4]$ square planes are formed from a combination of Cu-O linkages. A similar arrangement of Cu-O groups is also observed in $SrCu_2O_2$[31] where zig-zags of O-Cu-O groups run along the [100] and [010] planes.

1.5.2 Structural Chemistry of Copper(II)

Due to the structural flexibility of the most common and important oxidation state, Cu^{2+} exists in a wide range of coordination geometries in numerous compounds and exhibits extensive structural chemistry. The most common coordination numbers of Cu(II) are four, five and six fold. However regular geometries are rare because the d^9 configuration adopted by Cu^{2+} results in Jahn-Teller distortion if placed in an environment of cubic symmetry i.e. regular octahedral or tetrahedral coordination geometries. This has a significant effect on the stereochemistry of Cu(II).

1.5.2.1 The Jahn-Teller Effect

The Jahn-Teller theorem states that any non-linear molecular system in a degenerate electronic state will be unstable and will therefore undergo a distortion that will lower its symmetry and split the degenerate state. This is of particular relevance for transition metals adopting the degenerate d^9, d^7 (low spin) and d^4 (high spin) electronic configurations. For example, an octahedral d^9 complex ($Cu^{2+}(t_{2g}^6e_g^3)$) is degenerate because the odd electron can occupy either the $d_{x^2-y^2}$ or d_{z^2} orbital. A tetragonal distortion corresponding to extension along the z axis and compression along the x and y axes removes the degeneracy by

increasing the energy of the $d_{x^2-y^2}$ orbital and lowering that of the d_{z^2} orbital (Figure 2). The reduction in energy of the doubly occupied d_{z^2} orbital stabilises the distorted coordination. Further distortion towards square planar geometry may occur and the d_{z^2} orbital approaches the level of the d_{xy}/d_{xz} orbitals. Alternatively the electrons can pair in the $d_{x^2-y^2}$ orbital, with the d_{z^2} orbital singly occupied and a distortion arises whereby the axial ligands in the z direction are drawn in more than the four equatorial ligands in the xy-plane. The Jahn-Teller effect results in distorted geometries of Cu(II) complexes, which can be described as possessing four ligands forming a square planar arrangement with one or two weaker orthogonal interactions. The geometries are often referred to as '4', '4+1' and '4+2'.[32] The theorem only identifies an unstable geometry; it does not predict the preferred distortion and the effect is not equal for the same element in different environments. For example in CuF_2 the distortion is small (2F x 1.93 Å and 4F x 2.27 Å) and larger in $CuBr_2$ (2Br x 3.18 Å and 4Br x 2.30 Å).

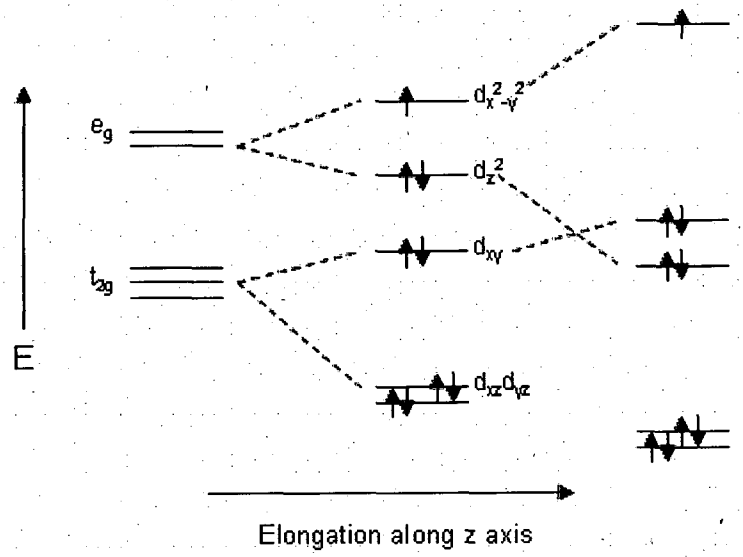

Figure 2 Energy level diagram showing tetragonal (middle) and ultimately square planar (right) distortion for d^9 Cu^{2+}.

1.5.2.2 Four, Five and Six-Coordinate Copper(II) Compounds

Due to the Jahn-Teller effect Cu^{2+} is rarely found in a regular tetrahedral coordination. For four-coordinate copper, square planar geometries are more commonly encountered. The few materials that do exhibit approximate tetrahedral geometry are mostly spinel-type materials where the copper can be observed in either the tetrahedral or octahedral sites is the spinel structure; e.g. Cr_2CuO_4[33] contains copper in a tetrahedral environment. In both octahedral and tetrahedral cases, the Cu^{2+} causes the crystal structure to distort from the regular cubic structure commonly observed in most spinel materials.

Divalent copper is often found to be five coordinate; typically displaying a distorted square based pyramidal geometry. The elongated square pyramidal coordination can be denoted as a '4+1' structure. Materials adopting this structure are often seen to have four relatively strong planar bond lengths, comparable to square planar '4' structures, and one weaker elongated axial bond. Despite the similarity of the four planar bonds in five coordinate systems to square planar structures, the bond lengths are slightly longer than the values of 1.95 Å seen in square planar oxides. The longer axial bond is generally found to be in the region 2.1 - 2.4 Å. As for purely square planar structures, linking of CuO_4 planes either by edge or corner sharing to form chains, is observed for '4+1' geometries. This is present in many superconducting phases, e.g. $YBa_2Cu_3O_{7-\delta}$[34] in which copper exists in two different coordination environments, both square planar and square pyramidal.

Additionally as a result of the Jahn-Teller effect the formation of a regular octahedron geometry CuX_6 where all Cu-X bonds are equal in length has not yet been observed. Instead the tetragonally distorted '4+2' arrangement is observed, where four relatively strong equatorial square planar bonds exist with two weaker orthogonal interactions. In some structures where a 3D copper-oxygen network is present, the axial bonds can be as long as 2.6 Å. However, in these cases, it is difficult to determine the significance of these interactions and whether they should be classified as '4' or '4+2' type geometries. As with CuO_4 and CuO_5 groups, Cu^{2+} in six coordinate geometries is observed in many

superconducting oxides, as two dimensional layers of corner-sharing or edge-sharing octahedra. In certain cases, lattice constraints prevent the existence of the tetragonally distorted '4+2' structure and a '4+1+1' type distortion is observed. As in the '4+2' structure, four relatively strong equatorial square planar bonds exist, however the two longer axial bonds have two significantly different bond lengths. This type of distortion is observed in $PbCu_2(SeO_3)_3$[35] where the equatorial bond lengths are ~1.9 – 2.0 Å and the two weaker orthogonal interactions are 2.32 and 2.59 Å.[36] The '4+2' distortion is the type most commonly encountered for Cu^{2+} in 6-coordinate geometry, however theoretical considerations do not exclude the possibility of '2+4' type distortions. In exceptional cases, this type of distortion is known to exist and has been reported for K_2CuF_4[37] where two relatively short interactions and four longer interactions of 1.95 and 2.05 Å respectively are observed.

1.6 Structural Chemistry of Indium(III)

Indium is a group 13 element, the valence configuration of these elements is ns^2p^1 and all the elements adopt the +3 oxidation state, which renders these ions strongly acidic. As a result they typically coordinate to electron rich, neutral or anionic donors. The heavier elements of the group also form compounds with the metal in the +1 oxidation state, the stability of which increases as you go down the group, therefore the most common oxidation state of thalium is Tl(I).

In^{3+} can be found in 4, 6 and 8 coordinate sites, Tl^{3+} also prefers these coordination geometries; in contrast Al^{3+} compounds are generally 4, 5 or 6 coordinate. The 6 coordinate In^{3+} metal centres adopt an octahedral geometry, the ionic radius of In^{3+} is in the range 0.62 – 0.92 Å depending upon the coordination environment adopted. In_2O_3 is an amphoteric oxide of indium, it forms bixbyte-type cubic crystals. Indium oxide is used in some types of batteries, thin film infrared reflectors transparent to visible light, some optical coatings and some antistatic coatings. Thin films of chromium-doped indium oxide ($In_{2-x}Cr_xO_3$) were recently reported to be magnetic semiconductors displaying high-temperature ferromagnetism, a single-phase crystal structure,

and semiconductor behavior with high concentrations of charge carriers. These have possible applications in spintronics as a material for spin injectors.

Other examples of indium phases include $LaInO_3$[38] and $La_{1+x}A_{1-x}InMnO_6$ (A = Sr and Ba).[39] $LaInO_3$ was synthesised *via* a conventional solid state route; La_2O_3 and In_2O_3 powders were mixed with ZrO_2 balls in ethanol for 24 h. The powder was dried, calcined at 1573 K for 4 h in air, pressed into a disc and then sintered at 1723 K for 4 h. $LaInO_3$ is an orthorhombic perovskite adopting the P*mna* space group. The structure is distorted by the in phase and antiphase tilting of oxygen octahedra in the $a^+b^-b^-$ system of the InO_6 polyhedra as proposed by Glazer.[40,41] In the P*mna* space group, the In atoms lie on an inversion centre and the La atom and one of the O atoms lie on a mirror plane. $La_{1+x}A_{1-x}InMnO_6$ (A = Sr and Ba) are a series of double perovskites, in all cases the B-site is occupied by a disordered arrangement of In^{3+} and $Mn^{3+/4+}$ cations. $La_{1+x}Ba_{1-x}InMnO_6$ exhibits two octahedral tilts and exists in a body-centred cell, space group I*mma*, however $La_{1+x}Sr_{1-x}InMnO_6$ adopts the three tilt $GdFeO_3$[42] structure and has a primitive orthorhombic structure, space group P*mna*. Magnetic susceptibility data show that all the compositions synthesised exhibit a spin glass freezing transition at ~ 8 K.

1.7 The Lanthanide Series

The lanthanide series comprises of 15 elements with atomic numbers 57 through to 71, from lanthanum through to lutecium. All lanthanides are *f*-block elements, corresponding to the filling of the 4*f* electron shell. The lanthanides are all very reactive and electropositive. The chemistry is dominated by the Ln(III) oxidation state, other oxidation states are only stable when an empty, half filled, or full *f* subshell is present. Thus Ce^{3+}, which is an f^1 ion, can be oxidised to the f^0 ion Ce^{4+}, a strong and useful oxidising agent. The next most common of the atypical oxidation states is Eu^{2+}, which is an f^7 ion that reduces water.

Despite the high charge, the large size of the Ln(III) ions result in low charge densities and their compounds are primarily ionic in character. The ionic radii decrease smoothly across the series (lanthanide contraction). The lanthanide contraction is caused by the increase in effective nuclear charge across the series due to the poor shielding ability of the 4*f* electrons. This is seen in every period as a shell is filled, however it is particularly important for lanthanides because of the length of the *f* series and the directional characteristics of the *f* orbitals. The *f* orbitals are 'angularly diffuse' and the electrons are able to occupy different volumes of space (different lobes) and so avoid each other. The Ln(III) ions are also hard in character so they tend to bond to O, N and F donors with F preferred to Cl > Br > I. They generally adopt high coordination numbers e.g. crystallised $Ln(H_2O)_9^{3+}$ have a coordination number of 9 and are tricapped trigonal prisms and LnF_3 (Ln = Sm-Lu) have a coordination number of 8 and are dicapped trigonal prisms. This is contrasted with the 3*d* metals where coordination numbers of 6 and 4 are common. The smooth decrease in the ionic radii results in a regular variation in chemical properties, the salts become (somewhat) less ionic across the series. This leads to small changes in their chemical properties e.g. $Ce(OH)_3$ is more basic than $Yb(OH)_3$ and $Lu(OH)_3$, $Ln^{3+}(aq)$ ions become increasingly acidic as the series is crossed and as the Ln(III) radius decreases, the hydration enthalpy and complexation energies increase.

1.8 The Structures of Oxide Materials

1.8.1 The Perovskite Structure

The most widespread ternary phase is represented by the perovskite structure, frequently adopted by materials of the stoichiometry ABO_3. Perovskites are named after the mineral $CaTiO_3$[43] which was identified by the Russian mineralogist L. A. Perovski and has retained its name even after the mineral has been found to be orthorhombic as opposed to the cubic symmetry normally associated with perovskite materials. In the notation ABO_3, A represents a large electropositive cation, e.g. Ba^{2+}, Sr^{2+} and B represents a small transition metal/ main group ion, e.g. Co^{3+}, Fe^{3+} or Cu^{2+}. The coordination geometry of the B

cation is octahedral while that of the A cation is 12-fold; thus the structure can be described as a framework of corner sharing BO_6 octahedra containing 12-coordination A cations.

In the ideal structure, where the atoms are touching one another, the B-O distance is equal to $a/2$ (a is the cubic unit cell parameter) while the A-O distance is $(a/\sqrt{2})$ and the following relationship between the ionic radii holds:

$$r_A + r_O = \sqrt{2}(r_B + r_O)$$

However it was found that the cubic structure was still retained in ABO_3 compounds, even though this equation is not exactly obeyed. As a measure of the deviation from the ideal situation, Goldschmidt[44] introduced a tolerance factor (t), defined by the equation:

$$t = (r_A + r_O)/\sqrt{2}(r_B + r_O)$$

This is applicable at room temperature to the empirical ionic radii. In the ideal case, t is unity ($t \approx 1.06$) and the perovskite structure crystallises with cubic symmetry in space group P*m-3m*. For t values below 1 ($t \approx 0.85$) super structures of the cubic variant often form. When a smaller A-cation than ideal is included in the close packed layers, the tolerance factor will be below 1. In these cases the A cation relaxes towards the O^{2-} anions and as a consequence the BO_6 octahedra will tilt in order to fill the space. Values above unity indicate formation of a hexagonal structure and are formed due to the insertion of an A ion larger than ideal, or a smaller B ion, leading to a contraction of the BO_6 octahedra. Face sharing among the octahedra leads to the formation of cavities where the larger A cations fit better. The structure of $BaNiO_3$[45] where $t = 1.10$, can be said to be of ideal hexagonal type with pure hexagonal stacking of the close packed layers.

Another factor that may lead to the lowering of symmetry from cubic involves Jahn-Teller effects. These include perovskite compounds where B is high-spin Mn^{3+}, Cr^{2+} and Fe^{4+}, low spin Ni^{3+} and also Cu^{2+}. In for example $LnMnO_3$

(Ln=La, Pr or Nd)[46,47] the Mn^{3+} ion is in the octahedral coordination field causing elongation of the MnO_6 polyhedron.

The large number of perovskites is due to both the cation sizes and the number of possible valences, which can be incorporated within the structure. In order to retain charge neutrality and fulfil the coordination requirements of the cations there are three possible combinations of A and B cations when considering integral compositions of oxide perovskites. These include A^+B^{5+} e.g. $KNbO_3$,[48] $A^{2+}B^{4+}$, e.g. $SrTiO_3$[49] and $BaSnO_3$[50] and $A^{3+}B^{3+}$ e.g. $LaCoO_3$.[51] A wide range of perovskites are also possible due to A-cation and oxide non-stoichiometries such as tungsten bronzes Na_xWO_3[52] and the cobaltates $SrCoO_{3-x}$.[53] Varying the ratio and oxidation states of the A and B cations e.g. $A^{2+}(B^{2+}_{0.33}B^{5+}_{0.67})$ $Ba(Sr_{0.33}Ta_{0.67})O_3$ and $Ba_{0.5}Sr_{0.5}SnO_3$[54] may further increase the number of possible stoichiometries.

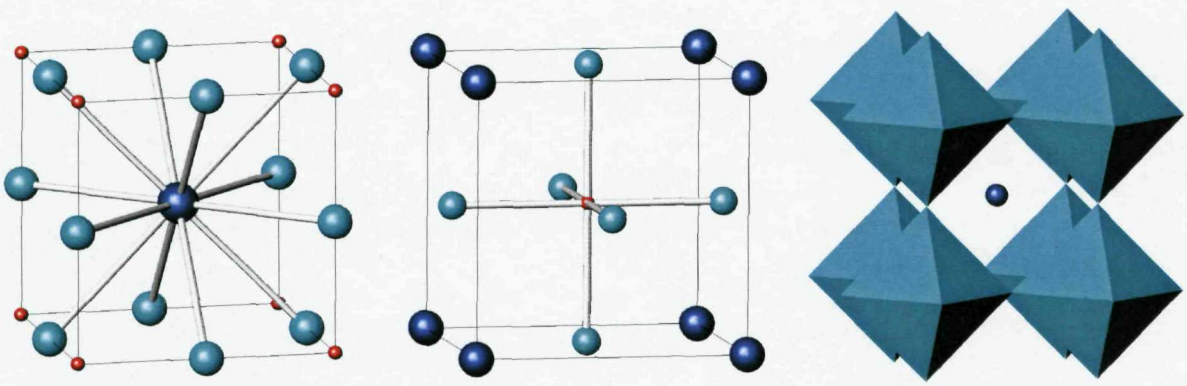

BaO_{12} coordination ***SnO_6 coordination*** ***3D network of octahedra***

Figure 3 The $BaSnO_3$ perovskite structure showing the AO_{12} (A=Ba) and BO_6 (B=Sn) coordination geometry. The 3D network of octahedron is also displayed.

Perovskites are an important class of materials because they can exhibit numerous properties attracting extensive research, including high T_c superconductivity, ferroelectricity, piezoelectricity, colossal magnetoresistance and metal insulator transitions. These properties are a result of cooperative effects arising from the 3D network of transition metal ions connected *via* an oxide lattice, which can be accurately controlled by doping at either the A or B

cation sites. Due to the strong overlap of unfilled and therefore magnetic, 3*d* electron orbitals with the oxygen 2*p* orbitals, these compounds display strong correlations between crystallographic, magnetic and transport properties.

1.8.2 Double Perovskites

The basic double perovskite structure is generated by introducing another ion (B') on half of the B positions yielding the basic double perovskite structure formula $A_2BB'O_6$. A large increase in double perovskite research was initiated in 1998 when the compound Sr_2FeMoO_6[55] was found to exhibit magnetoresistive effects at temperatures above 298 K. In particular, the half-metallicity of this and similar compounds below the magnetic ordering temperature is very interesting for future spintronics applications.

The properties of the double perovskite compounds are determined by the relative sizes, valences and ordering of the A and B site ions. Given the vast possibilities in variation of these parameters, interesting and useful physics is likely to appear from further studies of this class of materials. Double perovskite structures can adopt one of three distinct B-cation arrangements random, rock-salt and layered, depending on the charge, size and coordination geometry of the B cations and the A:B size ratio. As the difference in charge/size of the B cations increases, the systems are more likely to be ordered. The three B cation sub-lattice types, common cell sizes, cystal systems and space groups are shown in Table 2. When assignment of sublattice type is based upon Powder X-ray Diffraction (PXD) data, ambiguities may arise, and may be resolved using neutron diffraction or electron microscopy.

Table 2 A summary of crystallographic information for common double perovskites; a*p* = lattice parameter for cubic ABO_3 perovskites (~ 4 Å).

Sublattice Type	Cell Size	Crystal System	*Space Group*
Random	a*p* x a*p* x a*p*	Cubic	P*m3m*
	√2a*p* x √2a*p* x 2a*p*	Orthorhombic	P*bnm*
Rock Salt	2a*p* x 2a*p* x 2a*p*	Cubic	F*m3m*
	√2a*p* x √2a*p* x 2a*p*	Monoclinic	$P2_1/n$
Layered	*2a*p *x 2a*p *x 2a*p	*Monoclinic*	$P2_1/m$

1.8.3 Random Structure Perovskites

Compounds that adopt a random structure show no evidence of B-cation order and generally have a cubic 1*ap* unit cell e.g. $BaLaFeMoO_6$[56] or an orthorhombic $\sqrt{2}a_p$ x $\sqrt{2}a_p$ x $2a_p$ unit cell such as that adopted by $SrLaCuRuO_6$ (Figure 4).[57] The orthorhombic cell results from rotations of the BO_6 octahedra about the 011 and 100 planes, and results in the absence of *0kl* reflections (where $k = 2n + 1$). The octahedral tilt reduces internal bond strain within the structure.

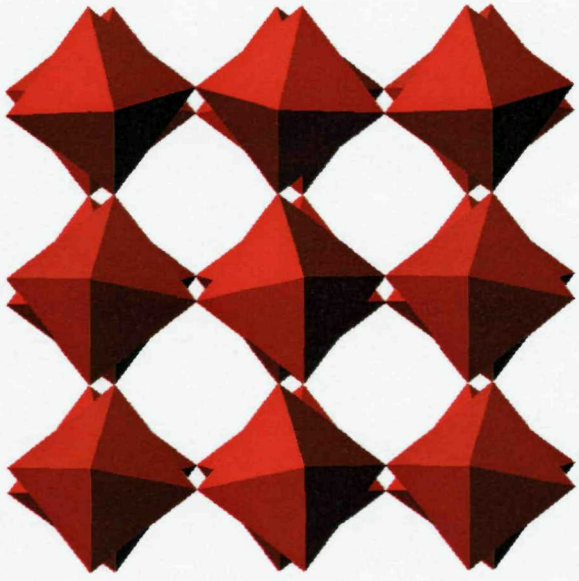

Figure 4 Polyhedral representation of $SrLaCuRuO_6$, Strontium and Lanthanum atoms have been removed for clarity.[57]

1.8.4 Rock Salt Structure Perovskites

The rock salt structure consists of a sub-lattice in which the B cations B' and B'' resemble the AX arrangement of the anions and cations in the rock salt structure. Generally they possess a cubic $2a_p$ (Sr_2FeMoO_6) (Figure 5)[55] or a monoclinic $\sqrt{2}a_p$ x $\sqrt{2}a_p$ x $2a_p$ unit cell (Sr_2LuRuO_6).[58] A monoclinic cell usually results from rotation of the BO_6 octahedra about the 011 and 100 planes. Compounds with a rocksalt sub-lattice show evidence of B-cation order; the indication of ordered cations for the cubic cell is the doubling of lattice parameters with respect to those for a random distribution of B-cations and the presence of the 111 reflection.

Figure 5 Polyhedral representation of Sr_2FeMoO_6[49] *(MoO_6 octahedra in red, SnO_6 octahedra in blue, strontium atoms have been removed for clarity).*

1.8.5 Layered Structure Perovskites

Compounds with a layered structure also show evidence of B-cation ordering, the layered arrangement is distinguished from the 'rocksalt' unit cell by the presence of the h0l reflections (where h + 1 = 2n + 1) and the absence of the 111

reflection. One material that exhibits a layered arrangement is La_2CuSnO_6 (Figure 6)[59] which has a monoclinic cell derived from a $2a_p$ x $2a_p$ x $2a_p$ unit cell. An example of an oxygen deficient double perovskite is $Ba_2InCuO_{4+\delta}$[60] which crystallises with tetragonal symmetry.

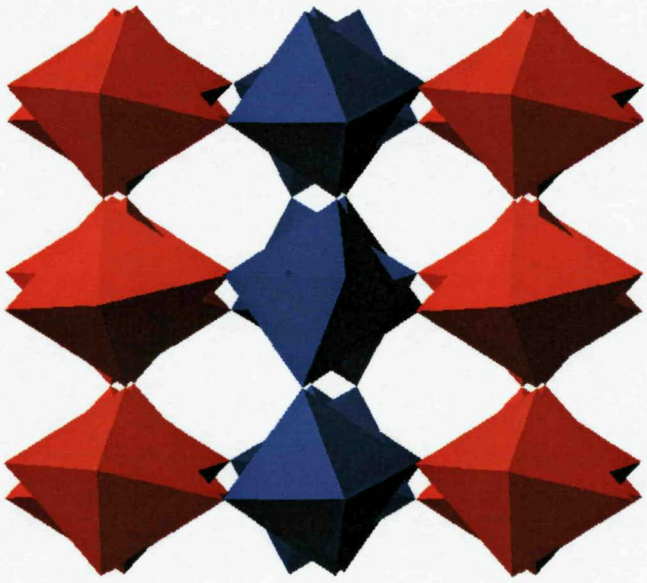

Figure 6 Polyhedral representation of La_2CuSnO_6. The CuO_6 octahedra are in red and the SnO_6 octahedra are in blue, lanthanum atoms have been removed for clarity.[57]

1.8.6 The K_2NiF_4 Structure

The K_2NiF_4 structure[61] is tetragonal and is closely related to the perovskite structure adopting a general formula $AO(ABO_3)_n$. When n = 1, a 'layered' perovskite structure is formed, which is the structure type of the first member of the Ruddlesden-Popper series. The K_2NiF_4 structure is shown in Figure 7 and consists of sheets of NiF_6 octahedra sharing four vertices. These layers are separated by K^+ ions in nine fold coordination to fluorine. The structure is widely adopted by ternary oxides of the stoichiometry A_2BO_4 where the A cation is surrounded by nine oxygen atoms and the B cation is in six-fold coordination. As with simple perovskites, the charge neutrality of these materials may be satisfied in a range of ways, i.e. $A^{2+}{}_2B^{4+}$ (e.g. Sr_2TiO_4), $A^{3+}A^{2+}B^{3+}$(e.g.$LaSrCoO_4$)[19] or $A^{3+}{}_2B^{2+}$ (e.g. La_2CoO_4).[15]

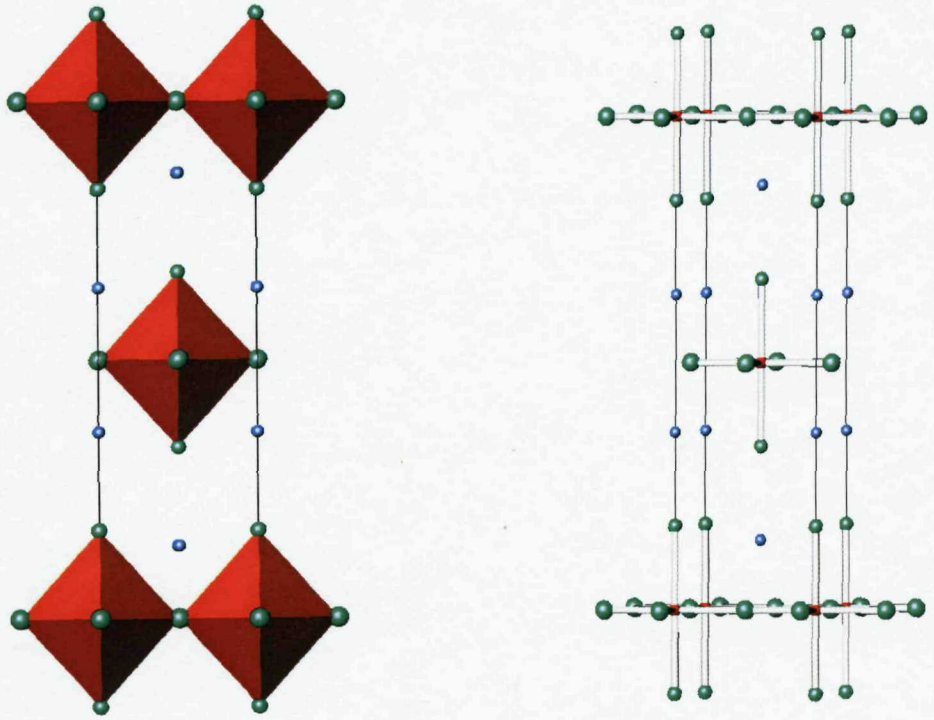

Figure 7 The structure of K_2NiF_4 showing the NiF_6 coordination and the infinite sheets of octahedra.

1.8.7 The Ruddlesden-Popper Phases

Ruddlesden-Popper[62] (RP) phases are layered Perovskites with the general formula $AO(ABO_3)_n$. Corner sharing BO_6 octahedra form layers, with *A* atoms occupying the 9 and 12 coordinate interstitial sites. The first characterised RP phases were the $SrO(SrTiO_3)_n$ series (Figure 8), fully characterised by Ruddlesden and Popper for n = 1, 2 and 3. $n = \infty$ corresponds to the standard Perovskite structure. These materials crystallise in the tetragonal space group I4/*mmm*.

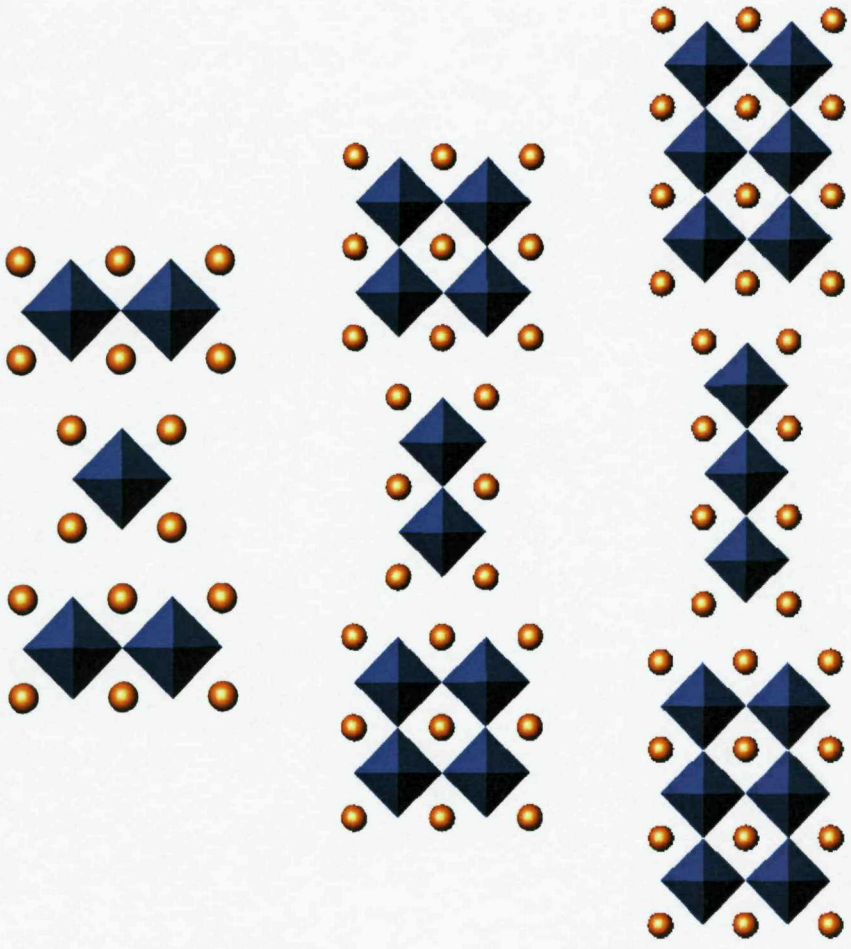

Figure 8 The structures of Sr_2TiO_4, $Sr_3Ti_2O_7$ and $Sr_4Ti_3O_{10}$.

1.8.8 Oxygen Deficiency in Perovskites

The ideal perovskite structure only occurs when all atomic sites are fully occupied. Due to the ability of the perovskite structure to accept cations of varying oxidation states, oxygen deficient perovskites are very common. All oxygen deficient phases can be described as being derived from stacks of AO_{3-x} layers, however the B-cations of the oxygen deficient phases can reside in six, five, four or two coordinate interstices that result from a combination of oxygen atoms and vacancies from the layers above and/or below.

The arrangement of vacancies around each B-cation in an oxygen deficient perovskite is influenced in a similar way to that of B-cation arrangements.

Differences in size, electronic configuration and coordination preferences of both the A and B cations affect the vacancy arrangement and control the manner in which the AO_{3-x} layer stacks. The large variety of vacancy patterns present in different compounds is consequently due to either the replacement of an A or B anion with one in a lower valence state i.e. heterovalent doping or reduction of a B ion present in an ABO_3 perovskite. The latter is the case for the homologous series of $SrFeO_{3-x}$.[63] It has been shown that different compounds with oxygen stoichiometry 3, 2.875, 2.75 and 2.5 can be prepared and hence the oxidation state of Fe varies between +3 and +4. If the B cation can be present with other coordinations than octahedral then vacancy ordered structures might form. The structures of $SrFeO_{2.875}$, $SrFeO_{2.75}$ and $SrFeO_{2.5}$ (=$Sr_8Fe_8O_{23}$, $Sr_4Fe_4O_{11}$ and $Sr_2Fe_2O_5$ respectively) are built up by different arrangements of FeO_6 octahedra, FeO_5 square pyramids and FeO_4 tetrahedra.

Other examples include $Ca_2Mn_2O_5$[64] and $YBaCuFeO_5$[65], they both possessing B-cations which are exclusively 5-coordinate; in the latter there is a large size difference between yttrium (1.19 Å) and barium (1.61 Å), whilst the former contains just one A cation type, calcium (1.34 Å). Although both posses B cations which are exclusively 5-coordinate there is a fundamental difference in the two structures in that each compound has a distinct stacking sequence. This can be attributed to the coordination requirements of the A sites 10,10 in the calcium manganate versus 8,12 in $YBaCuFeO_5$.

A key example of a structure that adopts an oxygen deficient structure is the high-temperature superconductor, $YBa_2Cu_3O_{7-x}$.[66] This non-stoichiometric system is derived from three perovskite ABO_3 unit cells stacked directly on top of each other, to form a material of stoichiometry $A_3B_3O_9$. Copper fills the octahedral corners BO_6, whilst the larger Ba-Y-Ba atoms are positioned in the A sites. Removal of oxygen from the (0,0,½) and (½,0,0) sites give the structure $YBa_2Cu_3O_7$.

The selective removal of oxygen from the sites in the basal plane causes the lattice parameters *a* and *b* to differ resulting in an orthorhombic unit cell (*a* = 3.82 Å, *b* = 3.88 Å, *c* = 11.4 Å). The stacking sequence can be described as:

$BaO\text{-}CuO_2\text{-}Y\text{-}CuO_2\text{-}BaO$

where yttrium is coordinated to 8 oxygen atoms in a distorted cube and barium to 10 oxygen atoms. The copper atoms are in two different coordination environments: square planar and square pyramidal.

1.9 Spin-Crossover

The spin crossover phenomenon was first discovered 60 years ago by Cambi *et al.* when he reported on drastic changes of the magnetic susceptibility in *tris*(N,N-dialkyldithiocarbomato)iron(III) complexes on varying temperature. As a consequence of the splitting of the energy of *d* orbitals into the t_{2g} and e_g sets in a ligand field, octahedral complexes of TM ions with configurations of d^4 to d^7, may exist in high (HS), intermediate (IS) or low spin (LS) states. In weak fields the ground state is high-spin where the multiplicity is a maximum, the *d* electrons being distributed over both t_{2g} and e_g sets whereas strong fields stabilise the low-spin state with minimum multiplicity, the t_{2g} set being completely occupied before electrons are added to the e_g set. In the case of d^6 Co(III), the electronic configurations are HS($t_{2g}^4e_g^2$), IS($t_{2g}^5e_g^1$) and LS(t_{2g}^6 e_g^0). For intermediate fields the energy difference ($\Delta E°_{HL}$) between the lowest vibronic levels of the potential wells of the two states may be sufficiently small such that application of some relatively minor perturbation effects a change in state. This phenomenon is known as the spin-transition (ST) or spin-crossover (SC) and its origin is illustrated in Figure 9.

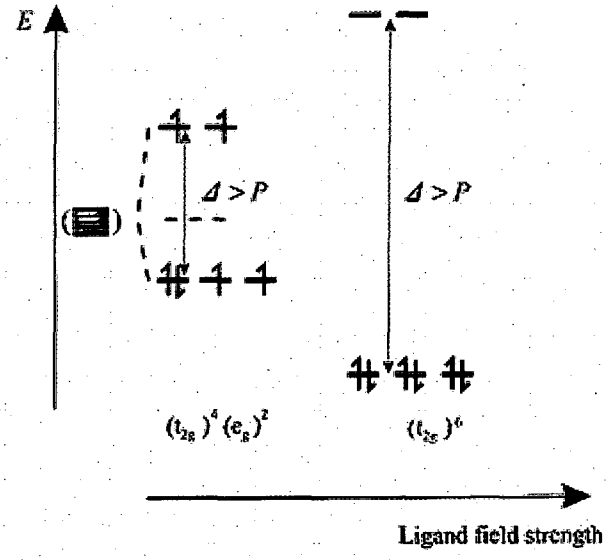

Figure 9 Electronic configuration for a d^6 Co(III) ion, in the LS state, in the HS state and equilibrium between these two states, in the case of thermal spin crossover (Δ stands for the cubic ligand field parameter and P for the mean-spin pairing energy).

A ST will be thermally induced when $\Delta E°_{HL} \approx k_B T$ and when this is met pressure and light induced transitions may also be observed. The ST in iron(II) transition metal complexes are probably the most extensively studied.

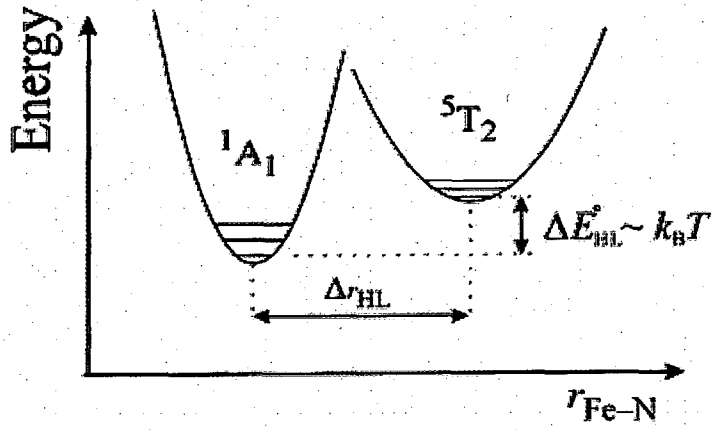

Figure 10 Representation of the potential wells for the $^1A_1$ and $^5T_2$ states of an iron(II) SC system, the nuclear coordinate being the metal-donor atom distance.[67]

From the measurement of the temperature-dependence of the properties of a ST system it is possible to evaluate the relative concentrations of HS to LS states as a function of temperature and thus to construct an ST curve, a plot of the HS molar fraction γ_{HS} *vs.* *T*, (Figure 11).

For systems in solution the behaviour follows a curve similar to that of Figure 11a and may be interpreted as a simple thermal equilibrium involving a Boltzmann distribution over all vibronic levels of the two spin states. In this case the transition occurs at the molecular level without the constraints of lattice interactions.

For solid systems lattice effects become important and the full range of curves Figure 11a-e are exhibited. The transition may be gradual and continuous over an extended temperature range, similar to solution behaviour (Figure 11a), or it may be abrupt and occur with a narrow temperature range (Figure 11b). The transition may be associated with a thermal hysteresis loop (Figure 11c) or be a two-step process (Figure 11d). In certain cases the transition may be incomplete at one or both extremes of the ST curve (Figure 11e). The curves are diagnostic of the nature of the ST and the steepness of the change is indicative of the extent of cooperativity involved in the propagation of the spin change throughout the lattice, i.e. the extent to which the electronic and structural changes in a molecule undergoing ST influence corresponding changes in neighbouring molecules. When this is low the transition will be gradual or a continuous process, but as the cooperativity increases the transition becomes more abrupt and may occur within a very narrow range of temperatures or be associated with a phase change or hysteresis. A transition temperature is defined as that temperature at which the fractions of HS and LS species taking part in the transition are equal. For transitions displaying hysteresis two transition temperatures $T_{1/2}\downarrow$ and $T_{1/2}\uparrow$ define the width of the hysteresis loop (Figure 11).[67]

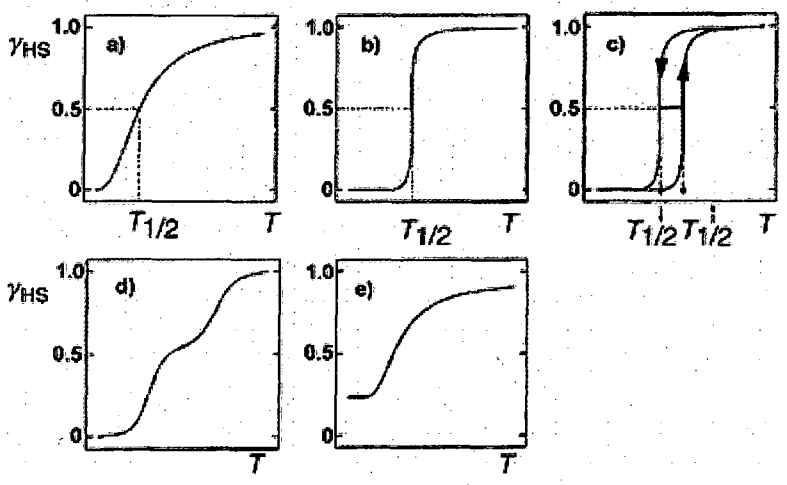

Figure 11 The nature of ST curves for SC systems in the solid state: (a) gradual; (b) abrupt; (c) with hysteresis; (d) with steps; (e) incomplete.[67]

1.9.1 Applications of Spin-Crossover Systems

The term 'molecular materials' refers to molecular-based compounds exhibiting a property, or a set of properties, which can be used in a device, for example display devices, application in optical data processing and information storage. The extreme sensitivity of the electronic properties of spin-crossover systems to relatively minor external perturbations renders them likely candidates for these practical applications.

Two aspects of the spin-crossover phenomenon are of particular interest in this regard. These are the occurrence in some instances of thermal hysteresis in the HS $\rightarrow$ LS $\rightarrow$ HS cycle and the ability of light irradiation to effect changes in spin state. The existence of hysteresis is a prerequisite for molecular bistability, which in turn offers the potential for technical applications in memory and data storage devices. For exploitation in memory devices the bistability must be associated with a response function. In this respect ST systems offer considerable scope since they show two dramatic and readily detectable responses, change in colour and magnetism. The change in colour accompanying a ST is particularly suited to the development of display devices. Ideally, these

applications require that room temperature should fall approximately in the middle of the hysteresis loop, i.e. $\frac{1}{2}(T_{1/2\uparrow} + T_{1/2\downarrow}) \approx 295$ K. Systems meeting this criterion are known and can now be synthesised in a more or less controlled manner. Other criteria such as chemical stability and reproducibility of behaviour for new samples and after cycling through the hysteresis loop must also be met.

The changes of ST behaviour under applied pressure may be exploited in pressure sensors for applications where remote sensing of pressure could be achieved by observation of a colour change in a SC material. The light induced switching phenomena described above offer much promise for application in optical data processing and information storage.

1.9.2 Spin-Crossover in 1,2,4–Triazole Complexes

1,2,4-Triazoles are five-membered heterocyclic compounds, containing three nitrogen atoms in the ring system. The characteristic feature of 1,2,4-triazole derivatives is the stability of the ring system, an inherent property of its aromatic nature. The pKa value of 1*H*-1,2,4-triazole is 2.3.[68] 1*H*-1,2,4-triaozole occurs as three tautomers, since the hydrogen atom can be situated on each of the three ring nitrogen atoms. A consequence of the tautomerism is a variety of coordination modes of 1,2,4-triazole to metal ions. The capability of the ligand to form a bridge between metal ions by establishing a bidentate coordination mode makes them very useful for obtaining polynuclear coordination compounds. By substitution on the nitrogen ring atoms, certain coordination modes can be excluded. Furthermore, by attaching one or more substituents to the ring, the 1,2,4-triazole nucleus can be forced to coordinate in a certain predetermined fashion. In particular the use of chelating substituents can contribute to bringing the ligand to the right conformation for binding two metal ions simultaneously in close proximity (Figure 12).

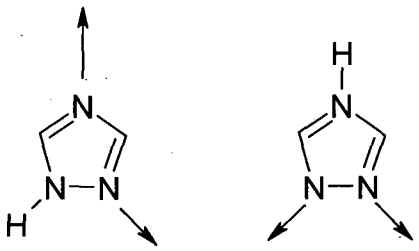

Figure 12 Bidentate coordination modes for 1*H*(4*H*)-1,2,4-triazole.

Triazoles have numerous applications, some triazole derivatives have been reported to act as antimicrobic, antiphlogistic or cytostatic agents.[69] A wide range of triazole compounds exhibit activity against phytopathogenic fungi,[70,71] 5-amino-1,2,4-triazole is the precursor of additives used in photography and products with known anti-corrosion properties.[72,73] In these industrial, medical and biological processes metal ions are involved and their interaction with metal ions is of particular interest.

The ability of azoles, triazoles and tetrazoles to bridge transition metal ions is central to the recent increased interest in their coordination chemistry. From a structural perspective You *et al.*[74] have recently prepared an "open framework" material from cobalt(II) and imidazole, which displays extensive polymorphism and a zeolitic character. While iron(II)[75] coordination polymers with triazoles have been of interest to magnetochemists since many of these compounds show spin crossover behaviour with thermal hysteresis effects. Here a SC driven structural phase transition results from the extensive covalently bridged network, which relays the structural changes at the iron centres. It is perhaps surprising that despite much work in this area, crystallographic structural information is often difficult to obtain. Another point of interest is the ability of these linkages to mediate magnetic interactions and form molecular based magnets. The coordination compounds of 1,2,4-triazoles are described in more detail in Chapter 7.

1.10 Scope of this Work

Layered complex oxides of the transition metals that adopt the K_2NiF_4 structure demonstrate a number of key electronic properties such as superconductivity, oxide ion conductivity and low dimensional magnetic ordering. Such materials have been studied in depth for some transition metal elements, namely Cu, Fe, and Ru but to a very limited extent for other metals e.g. Co(III) and Sc(III). In general, however many materials potentially adopting the K_2NiF_4 structure type, perfect or distorted through ion displacements have not been studied in detail. Many compositions have not been previously synthesised and others are assumed to adopt the perfect tetragonal structure (I4/*mmm*) from poor quality diffraction data. These compounds may show more complex structures when studied in detail or as a function of temperature. Chapters 3, 4 and 5 are concerned with the synthesis and characterization of Co(III), Sc(III) and In(III) containing materials potentially adopting the K_2NiF_4 type structure. In addition to the investigation of Co(III) materials adopting the K_2NiF_4 structure, attempts were made to produce Co(III) compounds with interesting structural and magnetic properties. Chapter 6 reports the results of a detailed investigation into the $Ln_2Ba_6Co_4O_{15}$ phases utilising several lanthanides.

Chapter 7 is concerned with the synthesis and characterisation of new magnetooptic materials, in which the extended structures formed, may show both magnetic coupling interactions and 'cooperative ST effects'. If a material with a ST close to room temperature can be engineered, then such a delicately balanced system may be susceptible to perturbation by other stimuli such as pressure, light or magnetic field.

The work described in this thesis concentrates on the synthesis and characterisation of materials in the solid state, and the synthetic techniques employed have produced polycrystalline oxides or single crystals. The principal technique adopted in the characterisation of polycrystalline materials is PXD. PXD allows initial phase identification and further detailed structural characterisation. Powder Neutron Diffraction (PND) experiments have been

performed on a selection of materials to provide more accurate structural information particularly on the coordination environment surrounding the oxygen atoms. In certain cases neutron diffraction data has also been utilised in determining the magnetic structure of a material. In addition the magnetic properties of several materials have also been investigated using a Vibrating Sample Magnetometer (VSM) as well as a Superconducting Quantum Interference Device (SQUID). Single crystal X-ray crystallography was used to determine the structure of those materials formed as single crystals.

1.11 References

[1] M. A. Subramanian, G. Aravamudan and G. V. Subba Rao, *J. Solid State Chem.*,**31**, 329 (1980).

[2] F. Galasso and W. Derby, *Inorg. Chem.*, **1**, 71 (1962)

[3] J. F. Schooley, W. R. Hosler and M. L. Cohen, *Phys. Rev. Letters.*, **12**, 474 (1964).

[4] V. Ginzburg, *J. Phys. USSR*, **10**, 107 (1946).

[5] W. L. Cherry and R. Adler, *Phys. Rev.*, **72**, 981 (1948).

[6] A. von Hippel, RPTPB, 4660 (1994).

[7] F. Galasso, L. Katz and R. Ward, *J. Am. Chem. Soc.*, **81**, 820 (1959).

[8] General Ceramics, Oxide Thermoelectric Materials Final Rpt., Contract NOBS-78414 (1961).

[9] C. D. Salzberg, *J. Opt. Soc.*, **51**, 1149 (1961).

[10] R. J. Cava, B. Batlogg, J. J. Kajewski, R. Favrovo, L. W. rupp, A. E. White, K. Short, W. F. Pecks and T. Komelan, *Nature*, **332**, 814 (1988).

[11] C. W. Chu, P. H. Hor, R. L. Meng, L. Gao and Z. L. Huang, *Science*, **235**, 567 (1988).

[12] R. P. Liverovich and R. H. Mitchell, *J. Solid State Chem.*, **177**, 2188 (2004).

[13] G. J. Redhammer and G. Roth, *J. Solid State Chem.*, **177**, 2714 (2004).

[14] P. Benzdicka, A. Wattiaux, J. C. Grenier, M. Pouchard and P. Hagenmuller, *Z. Anorg, Allg. Chem.*, **619**, 7 (1993).

[15] H. Lehman and H. K. Muller-Buschbaum, *Z. Anorg. Allg. Chem.*, **470**, 59 (1980).

[16] O. H. Hansteen, H. Fjellvag and B. C. Hauback, *J. Solid State Chem.*, **141**, 411 (1998).

[17] J. C. Grenier, S. Ghodbane, G. Demanzeau, M. Pouchard and P. Hagenmuller, *Mat. Res. Bull.*, **14**, 831 (1979).

[18] W. D. Johnston, R. R. Helkes and D. Sestrich, *Journal of Physics and Solids*, **7**, 1 (1958). R. J. Gummow, D. C. Liles and M. M. Thackeray, *Mat. Res. Bull.*, **28**, 235 (1993).

[19] G. Demazeau, P. Courbin, G. le Flem, M. Pouchard, P. Hagenmuller, J. L. Soubeyroux, I. G. Main and G. A. Robins, *Noveau Journal de Chimie*, **3**, 171 (1979).

[20] C. N. R. Rao, Md. M. Seikh and C. Narayana, *Topp. Curr. Chem*, **234**, 1 (2004).

[21] K. Asai, A. Yoneda, O. Yokokura, J. M. Tranquada, G. Shirane and K. Kohn, *J. Phys. Soc. Jpn.*, **67**, 290 (1998).

[22] M. Jansen and R. Hoppe, *Z. Anorg. Allg. Chem.*, **409**, 152 (1974).

[23] M. Jansen and R. Hoppe, *Z. Anorg. Allg. Chem.*, **398**, 54 (1973).

[24] S. E. Dann and M. T. Weller, *J. Solid State Chem.*, **115**, 499 (1995).

[25] A. Nakatsuka, A. Yoshiasa, N. Nakayama, T. Mizota and H. Takei, *Acta Crystrallogr. C*, **60**, i59 (2004).

[26] V. G. Sathe, A. V. Pimpale, V. Siruguri and S. K. Paranjpe, Journal of Physics: Condensed Matter, 8, 3389 (1996).

[27] R. Hoppe and G. Wingefeld, *Z. Anorg. Allg. Chem.*, **519**, 189 (1984).

[28] P. Niggli, *Zeitschrift fuer Kristallographie, Kristallgeometrie, Kristallphysic, Kristallchemie*, **57**, 253 (1922).

[29] K. Hestermann and R. Hoppe, *Z. Anorg. Allg. Chem.*, **360**, 113 (1968).

[30] A. Pabst, *American Mineralogist*, **23**, 175 (1938).

[31] C. L. Teske and H. Mueller-Buschbaum, *Z. Anorg. Allg. Chem.*, **379**, 113 (1970).

[32] A. F. Wells, Structural Inorganic Chemistry, 5th Ed., Oxford University Press, (1984).

[33] W. Dannhauser and P. A. Vaughan, *J. Am. Chem. Soc.*, **77**, 896 (1955), W. A. Dollase and H. S. C. O'Niel, *Acta Crystallogr. C*, **53**, 657 (1997).

[34] M. Raudsepp, F. C. Hawthorne, X. Z. Zhoul, I. Maartense, A. H. Morrish and Y. L. Luo, *Canadian Journal of Physics*, **65**, 1145 (1987).

[35] H. Effenberger, *J. Solid State Chem.*, **73**, 118 (1988).

[36] C. S. Knee and M. T. Weller, *J. Mater. Chem.*, **6(8)**, 1449 (1996).

[37] K. Knox, *J. Chem. Phys.*, **30**, 991 (1959).

[38] H. M. Park, H. J. Lee, S. H. Park and H. I. Yoo, *Acta. Crystallogr, C,* **59**, 131 (2003).

[39] P. D. Battle, A. I. Coldea, N. A. Jordan, M. J. Rosseinsky and J. Singleton, *J. Mat. Chem.*, **11**, 1656 (2001).

[40] A. M. Glazer, *Acta. Crystallogr, B,* **28**, 3384 (1972).

[41] A. M. Glazer, *Acta. Crystallogr, A,* **31**, 756 (1975).

[42] P. Coppens and M. Eibschuetz, *Acta. Crystallogr*, **19**, 524 (1965).

[43] S. Sasaki, C. T. Prewitt and J. D. Bass, *Acta. Crystallogr, C*, **43**, 1668 (1987).

[44] V. M. Goldschmidt, *Naturwissenhaften*, **14**, 477 (1926).

[45] J. J. Lander, *Acta. Crystallogr.*, **4**, 148 (1951).

[46] J. B. A. A. Elemans, B. van Laar, K. R. van der Veen, B. O. Loopstra, *J. Solid State Chem.*, **3**, 238 (1971).

[47] S. Quezel-Ambrunaz, *Bulletin de la Societe Francaise de Mineralogie et de Cristallographie*, **91**, 339 (1968).

[48] E. A. Wood, *Acta. Crystallogr.*, **4**, 353 (1951).

[49] J. Brous, I. Fankuchen and E. Banks, *Acta. Crystallogr.*, **6**, 67 (1953).

[50] H. D. Megaw, *Proceedings of the Physical Society, London*, **6**, 67 (1946).

[51] A. Wold and R. Ward, *J. Solid State Chem.*, **124**, 230 (1996).

[52] G. Haegg, *Nature*, **135**, 874 (1935).

[53] P. Bezdicka, A. Wattiaux, J. C. Grenier, M. Pouchard and P. Hagenmuller, *Z. Anorg. Allg. Chem.*, **619**, 7 (1993).

[54] G. Bayer, *J. Am. Ceram. Soc.*, **46**, 604 (1963).

[55] A. Arulraj, K. Ramesha, J. Gopalkrishnan and C. N. R. Rao, *J. Solid State Chem.*, **155**, 233 (2000).

[56] T. Nakamoto and J. H. choy, *J. Solid State Chem.*, **20**, 233 (1977).

[57] M. P. Atfield, P. D. Battle, S. K. Bollen, S. H. Kim, A. V. Powell and M. Workman, *J. Solid State Chem.*, **96**, 344 (1992).

[58] P. D. Battle and C. W. Jones, *J. Solid State Chem.*, **78**, 108 (1989).

[59] M. T. Anderson and K. R. Poeppelmeier, *Chem. Mater.*, **3**, 476 (1991).

[60] D. H. Gregory and M. T. Weller, *J. Mater. Chem.*, **4**, 921 (1994).

[61] D. Balz and K. Plieth, *Z. Elektrochem.*, **59**, 545 (1955).

[62] S. N. Ruddlesden and P. Popper, *Acta Crystallogr.*, **11**, 54, 1958.

[63] J. P. Hodges, S. Short, J. D. Jorgensen, X. Xiong, B. Dabrowski, S. M. Mini and C. W Kimball, *J. Solid State Chem.*, **151**, 190 (2000).

[64] K. R. Poeppelmeier, M. E. Leonowicz and J. M. Longo, *J. Solid State Chem.*, **44**, 89 (1982).

[65] L. Er-Rakho, C. Michel, P. Lacorre and B. Raveau, *J. Solid State Chem.*, **73**, 531 (1988).

[66] M. K. Wu, J. R. Ashburn, C. J. Torng, R. L. Meng, L. Gao, Z. J. Huang, Y. Q. Wang and C. W. Chu, *Phys. Rev. Lett.*, **58**, 909 (1987).

[67] P. Gütlich, Y. Garcia and H. A. Goodwin, *Chem. Soc. Rev.*, 2000, **29**, 419.

[68] C. F. Kröger and W. Frieburg, *Chimica*, **21**, 161 (1967).

[69] R. Bohm and C. Karow, *Die Pharmazie*, **4**, 243 (1981).

[70] S. C. Bahel, B. L. Dubey, N. Nath and J. K. Srivastava, *Inorg. Chim. Acta*, 91, L43 (1981).

[71] M. Nadasy, Magy Kem. *Lapja*, **36,** 518 (1981).

[72] D. J. Cash and A. N. Ferguson, *J. Photogr. Sci*, **28** , 121 (1980).

[73] D. L. Smith and H. L. Luss, *Photogr. Sci. Eng.*, **20** , 184 (1976).

[74] Y.-Q. Tian, C.-X. Cai, Y. Ji, X.-Z. You, S.-M. Peng, G.-H. Lee, *Angew. Chem. Int. Ed.*, **41**, 1384 (2002); *Angew. Chem.*, **114**, 1442 (2002);Y.-Q. Tian, C.-X. Cai, X.-M. Ren, C.-Y. Duan, Y. Xu, S. Gao, X.-Z. You, *Chem. Eur. J.*, **9**, 5673 (2003).

[75] O. Kahn, C. Jay Martinez, *Science*, **279**, 44 (1998); Y. Garcia, J. Moscovici, A. Michalowicz, V. Ksenofontov, G. Levchenco, G. Bravic, D. Chasseau, P. Gütlich, *Chem. Euro. J.*, *8*, 4992 (2002).

Chapter Two

Experimental Techniques

2.1 Introduction

A range of techniques were adopted in the characterisation of materials prepared in this work. The primary method was PXD. PND experiments have been performed on selected samples to provide more accurate structural information, particularly on materials containing oxygen. Variable temperature powder and neutron diffraction was undertaken on selected samples in order to investigate phase and structural changes and also spin-crossover. Materials that were formed as single crystals were characterised using single X-ray diffraction techniques. The magnetic properties of several materials have also been investigated using both a Vibrating Sample Magnetometer (VSM) and a Superconducting Quantum Interference Device (SQUID). This chapter provides a summary of the experimental techniques used in this work and describes their applications on a range of materials.

2.2 Synthetic Methods

2.2.1 Direct Solid State Route

The most widely used method for the synthesis of polycrystalline inorganic materials is the direct solid state reaction. This involves heating the components together at high temperatures over an extended period. In the consideration of a solid state reaction, both thermodynamic and kinetic criteria must be satisfied.[1] The temperature of a reaction must therefore be appropriate for the production of a desired phase, and suitably high to facilitate the reaction at a reasonable rate. Routinely used reaction temperatures fall in the range 600 - 1200 °C. The need for high temperatures required in the synthesis of complex oxides may be rationalised by consideration of the nature of the reactant lattices and the degree of structural change necessary for the formation of the new phase. The solid state reaction involves the complete disruption of the structure; the cations in an oxide material are normally coordinated to a large number of oxide ions. In order for these ions to migrate to the interface and form a new structure a considerable amount of energy is

required in order to overcome the lattice energy. Additionally, as the reactant solids can rarely be truly intimately ground, the temperature must promote an appreciable rate of ion diffusion.

Standard direct solid state reactions involve the mixing of the reactant solids, sometimes facilitated by the use of a volatile solvent e.g. ethanol, in an agate pestle and mortar. The reactants are then placed in a crucible (typically constructed of an inert material such as vitreous silica, recrystallised alumina or platinum) to avoid contamination of the sample, and fired at elevated temperatures. The rate of reaction can often be increased by frequent regrinds of the sintered mixture or by pelletisation of the starting materials. Both of these effectively increase the interfacial contact of the reacting species and minimise the distance over which the cations are required to migrate. Typically materials are synthesised from a stoichiometric mixture of the relevant oxides. The use of high temperatures also permits the use of carbonates and other oxo-salts, which readily decompose *in situ*.

Controlling the environment surrounding a reaction is often crucial to its success. In such cases the reactions are carried out in a controlled atmosphere. The use of a tube furnace enables gases such as nitrogen, argon and oxygen to be passed over the reactant mixture. These processes facilitate the partial control of the oxidation states of the metals present in the reaction mixture, preventing or promoting metal oxidation states as required.

2.2.2 The Sol-Gel Method

Chemical methods can be used to further decrease particle size thus enhancing reaction rates. In a typical sol-gel process, the precursor is subjected to a series of hydrolysis and polymerisation reactions to form a colloidal suspension. The particles then condense in a new phase, the gel, in which a solid macromolecule is immersed in a solvent. The sol is made of solid particles with a diameter of a few hundred nm, usually inorganic metal salts, suspended in a liquid phase. The resulting porous gel

is then chemically purified and fired at high temperatures into high purity oxide materials. The sol-gel process allows the synthesis of materials with varying properties: ultra-fine powders, monolithic ceramics and glasses, ceramic fibers, inorganic membranes, thin film coatings and aero gels.

This work primarily used a citrate gel method whereby the nitrate salts of the required starting materials are dissolved in water, followed by the addition of molar equivalents of citric acid and ethylene glycol. Heating of the mixture and evaporation of water results in the formation of a gel, which may be further heated in a crucible to form the complex oxide. The final stage, due to the mixing of various ions at the atomic level, can be carried out at temperatures as low as 700 °C, requiring less time compared to direct solid state routes.

2.2.3 Hydrothermal Synthesis

Many non-oxide inorganic materials may be synthesised by crystallisation from solution. Typical reactions involve the break-up of the lattices of the starting materials and the formation of a new crystal structure. Therefore, in order for some reactions to occur the conditions used must be severe. Traditional solid state chemistry relies on intimate mixing of the reagents, either by simply grinding powders together, or using a sol-gel type technique. Hydrothermal chemistry employs a different approach, more related to geochemical processes that occur naturally. Solutions of the reagents are heated in sealed Teflon-lined autoclaves with an internal volume of 23 mL, a maximum operating temperature of 523 K (250 °C) and a reported maximum operating pressure of over 12000 kPa. As water approaches the boundary to supercritical behaviour, its properties change dramatically. A supercritical fluid is any substance at a temperature and pressure above its thermodynamic critical point. It has the ability to diffuse through solids like a gas, and dissolve materials like a liquid. In this state water exists as small but liquid like hydrogen bonded clusters dispersed within a gas like phase, where physical properties such as gas or liquid like behaviour vary in response to changing

density. Supercritical fluids can be regarded as 'hybrid solvents' with a low viscosity, high diffusion rates and no surface tension. Hydrothermal and solvothermal reactions can be carried out in the supercritical conditions in the autoclaves.

Hydrothermal synthesis has significant advantages over solid-state approaches. Reagents in solution or suspension have greater ion mobility than the solid phases and the combination of heat and pressure enable reactions to occur at much lower temperatures than dry techniques. A further advantage is that the product may form single crystals that are easier to characterise by diffraction than fine powders normally produced by traditional solid state routes. Despite efforts in the area of crystal engineering it is still not possible to predict the outcome of such reactions; however this is not surprising when considering the amount of variables. The hydrothermal reactor is a closed system and reactions may be affected by factors such as time, temperature, pH, and concentration of reagents and the fill level of the reaction mixture. The order in which the reagents are added may also play a role, for example a homogenised mixture will behave differently to one with concentrated areas of reagents.

2.3 Powder X-ray Diffraction

The application of PXD has become a crucial characterisation technique for the solid state chemist. The most widespread use of PXD, and the one that we focus on here, is for the identification of crystalline compounds by their diffraction pattern. It is a non destructive technique that can be used to determine lattice parameters, locations of atoms within a unit cell, sample purity and defects within a crystal structure. It can also identify different phases of a compound if it exists as polymorphs.

This research has concentrated heavily upon PXD to identify the materials synthesised, and determine the purity of the products formed. Initially short scans of approximately 20 minutes allowed phase identifications to be undertaken and

elucidation of the cell parameters of the materials. Longer scans of approximately 13 hrs allowed structural refinement using the Rietveld method.[2,3] Variable temperature powder diffraction techniques were used to study structural changes in the materials.

2.3.1 X-ray Radiation

X-rays were discovered by Wilhelm Röntgen in 1895, for which he was awarded the first Nobel Prize in Physics in 1901. The original records were lost, but a reconstruction of them in Moore and Reynolds (1997)[4] shows that he discovered that in an experiment with high energy electrons, another type of radiation with the following properties was being produced:

- travels in straight lines
- are exponentially absorbed in matter with the exponent proportion to the mass of the absorbing material
- darken photographic plates
- make shadows of absorbing material on photosensitive paper.

In following years, much investigation into Röntgen's discovery was undertaken. Studies of X-rays revealed that they could be polarised, but could not be refracted, leading to controversy over whether X-rays were waves. It was understood that if X-rays were waves then the wavelength must be 10^{-10} m or less. Max von Laue theorised that X-rays could be diffracted if the slits were small enough. In 1912 von Laue proved that X-rays were not particles, but waves of light with very small wavelengths by using a crystal as a diffraction grating. Lawrence Bragg and his father William Henry Bragg used von Laue's discovery and, for monochromatic radiation, were able to show that diffraction could be treated geometrically like a reflection and derived Bragg's law (Section 2.3.2).

The wavelengths of X-radiation commonly used for X-ray diffraction lie between 0.7 and 2.3 Å. This is very close to the interplanar spacing of most crystalline materials. X-rays are produced whenever matter is irradiated with a beam of high-energy charged particles or photons. Provided that the beam of electrons striking a metal plate (anode) is sufficient in energy, an electron from one of the metal atom core orbitals will be ejected. Filling of this vacancy by electron decay from a higher energy orbital occurs with the emission of radiation. Typically the metal atoms are of a high enough atomic number, to yield high-energy photons in the X-ray region. In copper, for example core electron vacancies formed by collision with electrons can be filled by decay from various higher energy electrons and thus the spectrum of X-rays obtained contains a number of intense maxima corresponding to the energies of these various transitions. In addition bombarding a metal target with a focused electron beam accelerated across a high voltage can also produce X-rays. As electrons collide with the atoms in the target and decelerate, a continuous spectrum of X-rays are emitted, which are termed *Bremsstrahlung* radiation. Common anode materials are listed in Table 1.

Table 1 Characteristics of common anode materials.

Material	Atomic No.	Kα/ Å	Char Min[a]/ keV	Opt[b]/ kV	Advantages and Disadvantages
Cr	24	2.291	5.99	40	High resolution for large d-spacing's, particularly organics (high attenuation in air)
Fe	26	1.937	7.11	40	Most useful for Fe-rich materials where Fe fluorescence is a problem (strongly fluoresces Cr in specimens)
Cu	29	1.542	8.98	45	Best overall for most inorganic materials (fluoresces Fe and Co Kα and these elements in samples can be problematic.
Mo	42	0.710	20.00	80	Short wavelength good for small unit cells, particularly metal alloys (poor resolution of large d-spacing).

a. Characteristic minimum excitation potential
b. Optimal operating kV

2.3.2 Powder X-ray Diffraction Theory

The technique of powder diffraction depends on a coherent beam of X-rays impinging on a powdered sample. A polycrystalline sample contains an enormous number of randomly orientated crystallites, typically 10^{-7} – 10^{-4} m in dimension. Many of these will be orientated so as to satisfy the Bragg condition. The effect of this is that each lattice spacing in the crystal will give rise to a cone of diffraction. Diffraction maxima will be observed with the conical angle from the incident beam defined by the Bragg equation. In order that all the reflections are detected it is important that the sample is completely randomly orientated and there is no

preferred crystallite orientation. This is achieved by thorough grinding of the sample using an agate pestle and mortar.

Interaction of X-rays with matter (electrons) creates a secondary 'diffracted' beam according to a mathematical relation called 'Bragg's Law'.[5] The concept of PXD is introduced by considering a scattering situation as shown in Figure 1, in which a plane wave is incident on two parallel planes of atoms, separated by a perpendicular distance *d*.

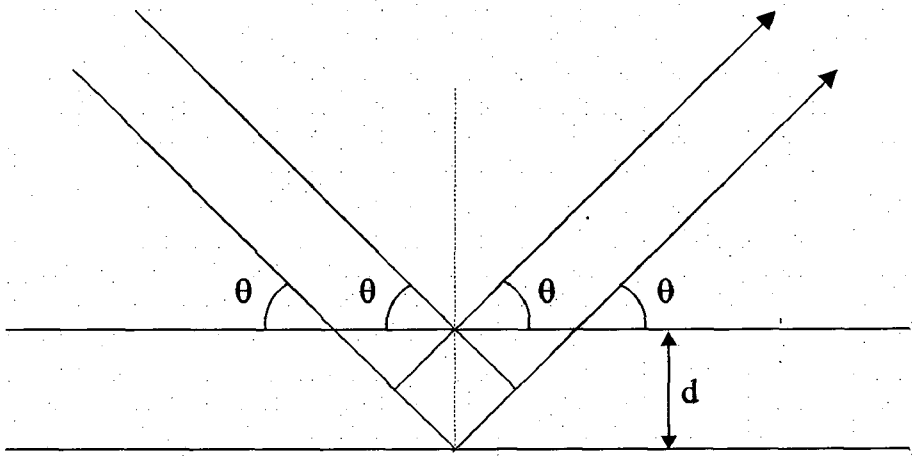

Figure 1 "Reflection" of X-rays from two planes of atoms in a solid.

For constructive interference the path difference between the two diffracted beams must correspond to an integral number of wavelengths. Simple trigonometry yields the Bragg equation:

$$n\lambda = 2d\sin\theta \ (n = 1,2,3\ldots)$$

The angle θ is known as the Bragg angle. At angles other than the Bragg angle, the diffracted beams are out of phase and interfere destructively. The interplanar separations, *d*, in the crystal are calculated by measuring the diffraction maxima, of which only first order diffraction maxima ($n = 1$) are generally seen. Lattice planes

are defined by their Miller indices, *hkl*, the reciprocal values of the fractional positions where the plane cuts the *a*, *b* and *c* axes respectively. If the calculations result in indices with a common factor, i.e. (442) the index is reduced to the simplest set of integers (221). This means that a Miller index refers to a family of parallel lattice planes defined by a fixed translation distances (*d*) in a direction perpendicular to the plane. The crystal system can then be derived from these *d* values by identification of the planes involved (Table 2). In theory, diffraction maxima should be seen for all planes in a structure, but in practice this is not the case. Reflection conditions or systematic absences arise from the symmetry elements such as glide planes and screw axes.[6,7]

Table 2 Equations for *d*-spacing in the different crystal systems.

Crystal system	Expression for d_{hkl}
Cubic	$\frac{1}{d_{hkl}^2} = \frac{h^2+k^2+l^2}{a^2}$
Tetragonal	$\frac{1}{d_{hkl}^2} = \frac{h^2+k^2}{a^2} + \frac{l^2}{c^2}$
Orthorhombic	$\frac{1}{d_{hkl}^2} = \frac{h^2}{a^2} + \frac{k^2}{b^2} + \frac{l^2}{c^2}$
Hexagonal	$\frac{1}{d_{hkl}^2} = \frac{4}{3}\left(\frac{h^2+hk+k^2}{a^2}\right) + \frac{l^2}{c^2}$
Monoclinic	$\frac{1}{d_{hkl}^2} = \frac{1}{\sin^2\beta}\left(\frac{h^2}{a^2} + \frac{k^2\sin^2\beta}{b^2} + \frac{l^2}{c^2} - \frac{2hl\cos\beta}{ac}\right)$
Triclinic	$\frac{1}{d_{hkl}^2} = \frac{1}{V^2}[h^2b^2c^2\sin^2\alpha + k^2a^2c^2\sin^2\beta + l^2a^2b^2\sin^2\gamma + 2hkabc^2(\cos\alpha\cos\beta - \cos\gamma) + 2kla^2bc(\cos\beta\cos\gamma - \cos\alpha) + 2hlab^2c(\cos\alpha\cos\gamma - \cos\beta)]$ where $V = abc(1 - \cos^2\alpha - \cos^2\beta - \cos^2\gamma + 2\cos\alpha\cos\beta\cos\gamma)^{1/2}$

In X-ray diffraction we make use of the repetition of the arrangement of atoms (or motif) in a crystal structure. The repetition produces the diffraction pattern, if there is no repetition then the diffraction pattern is absent as in amorphous materials. Repetition of the motif in a lattice defines its symmetry. Symmetry is a series of replication operations on one surface of a shape/ object by which the entire object may be generated. Crystal structures are based on the symmetry operations used to replicate the structure. All symmetry operations may be defined by several basic movement operations:

- rotation, in which the symbols used are *1,2,3,4,6* for rotation with the number of repeats of the form during one rotation.
- reflection (*m*), in which the form is reflected by mirror reflection across a plane.
- inversion (*i*), in which the form is replicated by projection of all points through a point of inversion; this defines the centre of symmetry.
- rotation-inversion, denoted by $\bar{1}$ for a single rotation/ inversion, which may be combined with rotational operations, i.e. $\bar{3}$ (3 –fold rotation with an inversion at each rotation).
- translation; a lateral movement which replicates the form along a linear axis.

In general, rotation, reflection and inversion operations generate a variety of unique arrangements of lattice points in three dimensions. These translation-free symmetry operations are called point-group elements. Translations are used to generate a lattice from the unit cell (the smallest special group that when tiled in three dimensional space will complete the structure). The translations include a simple translation, a linear translation combined with a mirror operation (glide plane), or a translation combined with a rotational operation (screw axis). A large number of three dimensional structures (the 230 space groups) are generated by these translations acting on the 32 point groups.

All crystal structures can be categorised into one of seven crystal systems with distinct symmetry requirements. Subsequently these can be divided further into 14 Bravais

lattices by including the lattice types primitive (P), body centred (I) or face centred (F-or C convention for cases in which only one face is centred). For each of these systems there are different symmetry arrangements possible (Table 3).

Table 3 The crystal systems and corresponding crystal classes.

Crystal system	Minimum Criteria	Crystal Classes
Triclinic	none	1, -1
Monoclinic	$\alpha = \gamma = 90°$	2, m, 2/m
Orthorhombic	$\alpha = \beta = \gamma = 90°$	2/m2/m2/m, mm2 (2mm), 222
Tetragonal	$a = b \neq c$, $\alpha = \beta = \gamma = 90°$	4, -4, 4/m, 422, 4mm, -42m, 4/m2/m2/m
Trigonal	$a = b = c$, $\alpha = \beta = \gamma \neq 90°$	3, -3, 3m, -32/m, 32
Hexagonal	$a = b \neq c$, $\alpha = \beta = 90° \gamma = 120°$	6, -6, 6/m, 622, 6mm, -6m2, 6/m2/m2/m
Cubic	$a = b = c$, $\alpha = \beta = \gamma = 90°$	23, 2/m-3, 432, -43m, 4/m-32/m

2.3.3 Instrumentation

Two diffractometers were routinely used throughout this work; a Siemens D5000 diffractometer and a Bruker D8 Advance diffractometer. The Siemens D5000 (Figure 2) uses a copper anode and a single crystal monochromator to provide Cu $K_{\alpha 1}$ (λ= 1.54056 Å) radiation. This radiation is collimated by aperture slits before hitting the sample, mounted in a recessed aluminium or plastic sample holder. A standard scintillation counter detects the diffracted X-rays. The incident beam, sample and detector are arranged according to the Bragg Brentano geometry in which the incident beam and takeoff geometry is fixed at a $\theta/2\theta$ relationship by rotating the sample plate at precisely half the rate of the detector through the angular range to be studied. The diffractometer is controlled by a PC, which collects the data.

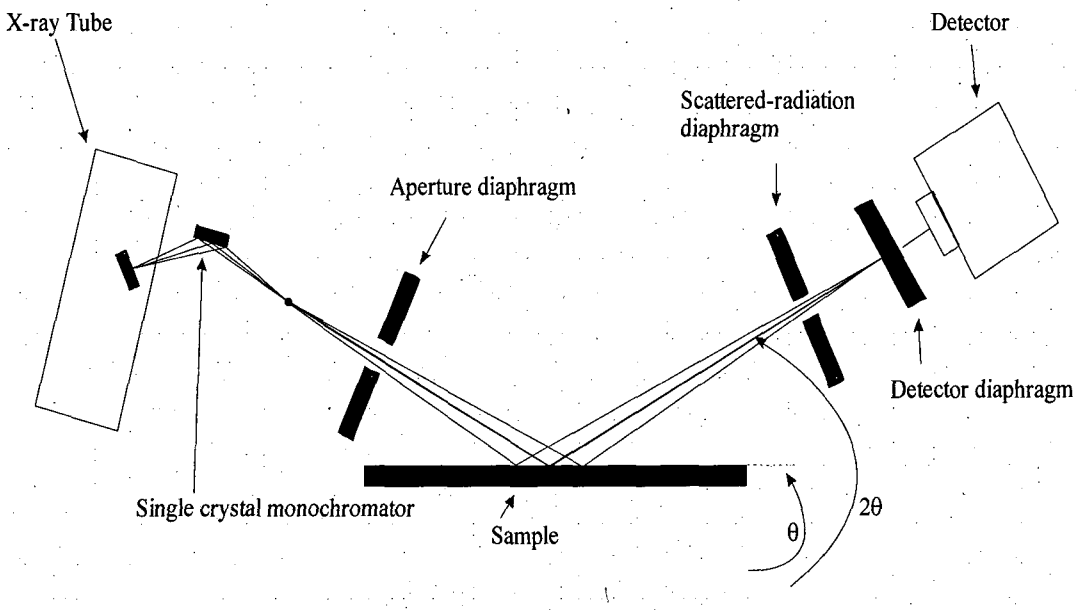

Figure 2 Schematic representation of the D5000 diffractometer.

The Bruker D8 Advance diffractometer uses the same X-ray source, sample mounting and geometry as the D5000 diffractometer. The D8 however, can switch between several types of detector, depending on the sample being characterised. One detector is a standard scintillation detector, similar to that on the D5000. The second detector is a Position Sensitive Detector (PSD); it is comprised of an anode and a cathode, separated by a work gas. At the anode, an intense electric field is applied and the diffracted X-ray photons ionise the detector gas. These electrons are immediately accelerated and have sufficient energy to ionise other argon atoms. A very fast ionisation 'avalanche' occurs and an induced charge arrives on the cathode perpendicular to the impact point of avalanche. The position of this charge is determined by the delay-line method. The charge travels to the left and right along this delay line to both ends. The difference in arrival times of charge at each end allows the position of the induced charge and hence the initial ionisation positions to be calculated. The detector is split into channels and the position of the diffracted beam is measured in channel number. These channels must then be converted into 2θ using a calibration file from a known compound e.g. α-quartz. The advantage of the PSD over the scintillation detector is that the wire covers approximately 7 - 8° in 2θ. This means that data can be collected much more rapidly than the scintillation

detector. The disadvantage is that the resolution is not as good, leading to a broader peak shape in the diffraction pattern.

The third detector is the SOL-X, which is comprised of a semiconductor (Si[Li]) detector and a multi-spectrum analyser. The SOL-X is commonly used when the materials being studied contain first row transition metals such as iron or cobalt. The copper radiation interacts with the transition metals in the sample causing fluorescence (luminescence that is mostly found as an optical phenomenon in cold bodies in which the molecular absorption of a photon triggers the emission of another photon with a longer wavelength, the energy difference between the absorbed and emitted photons ends in molecular vibrations or heat). This results in a very high and thus noisy background, obscuring the smaller peaks. Using the Sol-X it is possible to tune out the fluorescence so that only the diffraction pattern from $CuK_{\alpha 1}$ is observed, resulting in much more accurate structural determinations (Figure 3).

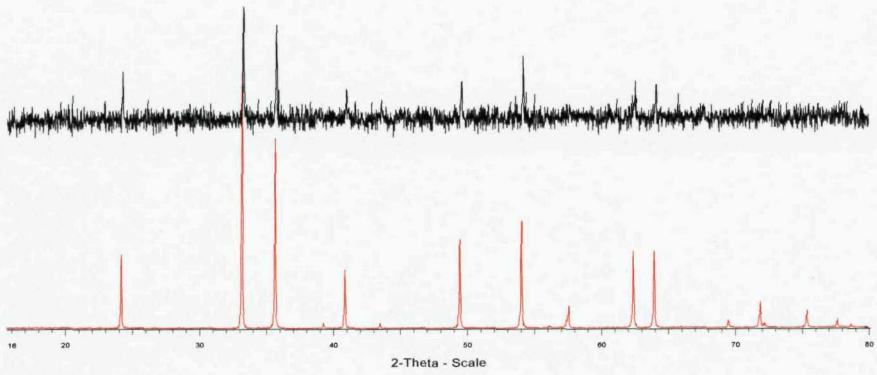

Figure 3 X-ray patterns of Fe_2O_3. The upper pattern is collected with a scintillation counter, demonstrating fluorescence. The lower pattern shows the increased peak discrimination available with the SOL-X detector.

2.3.4 Variable Temperature PXD

The D8 diffractometer is also able to support several different sample stages. Much of this work takes advantage of the Anton Paar HTK-1200 furnace stage (Figure 4). The sample is mounted in a recessed alumina holder. This is then inserted inside a sealed furnace chamber. Incident and diffracted X-ray beams pass through Kapton windows. The chamber can be placed under vacuum or flowing gas if required. The furnace is controlled by a PC, and can operate between room temperature and 1200 °C. The stage can operate with any of the three detectors. In this work the furnace stage is used in conjunction with the Position Sensitive detector.

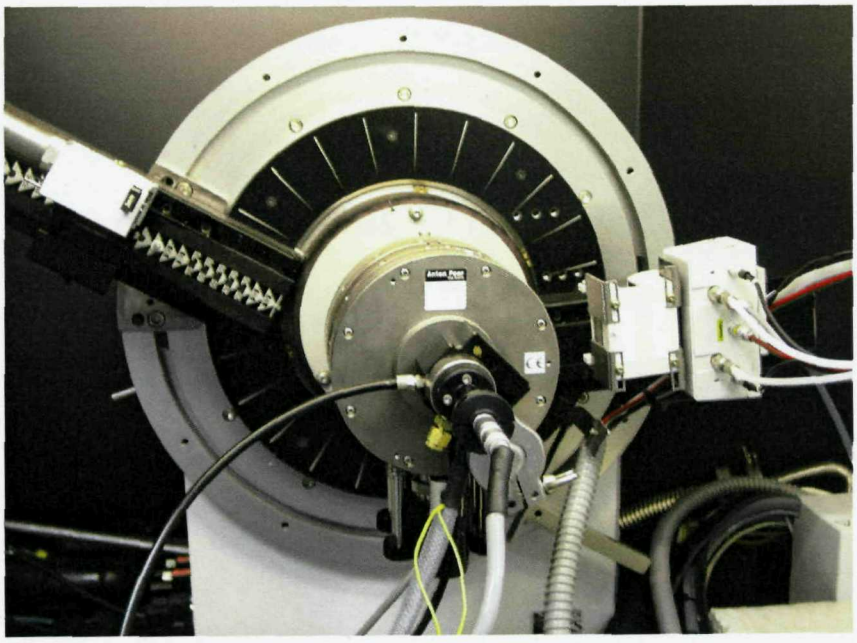

Figure 4 Photograph of the Anton Paar HTK-1200 furnace stage.

2.3.5 Analysis of PXD Data

Data for routine phase identification were acquired typically in the 2θ range 10 – 60° with a step size of 0.02° and scan time of approximately 20 minutes. Following the diffraction experiment the data can be manipulated using software on the PC. Phase identification and purity is accomplished by comparing the data (peaks and relative intensities) from the sample with peaks and relative intensities from a large database, the JCPDS Powder Diffraction File.[8] Following these initial studies, if required, further data can be collected, usually over a larger 2θ range and for a longer period of time enabling full structural refinement using the Rietveld method.

As well as providing information regarding the structure type and cell size, X-ray diffraction permits the resolution of atoms within the structure by considering peak intensities. The intensity of each diffraction maximum is related to the structure factor, *F*. It may be shown that, for any regular arrangement of motionless atoms, *F* is equal to the sum over all the atoms, of a combination of the scattering amplitudes, *f*, and the phases, δ, of each atom[9] giving the expression:

$$F = \sum_{j=1}^{N} [f_j \exp[i\delta_j]$$

In a unit cell, the total phase shift of an atom *j* at a point (x_j, y_j, z_j) from the origin is the sum of the phase shifts in each direction. When the phase shift is evaluated, the structure factor for one unit cell becomes:

$$F_{hkl} = \sum_{j=1}^{N} f_j \exp[2\pi i(hx_j + ky_j + lz_j)]$$

where *h*, *k* and *l* are Miller indices defining the plane from which the reflection occurs.

For very small crystals, it may be shown that the intensity of the scattered beam is proportional to the square of the structure factor:

$$I_{hkl} = kL^2 \left| F_{hkl} \right|^2$$

where k is a scaling constant and L is the Lorentz factor, a geometric function of the method of data collection and hence the instrument used.[9]

In real crystals, the scattered intensity is modified by imperfections in the lattice structure. Defects and substituent disorder causes local structure irregularities, particularly in non-stoichiometric materials. Further changes to the scattering intensity occur as a result of time dependent vibrations (i.e. thermal motion) of the atoms about their mean positions: the atoms in a plane *hkl* are displaced randomly from their ideal in-plane positions, disrupting the in-phase behaviour of their combined scattering. The correction to a structure factor reflected by a plane, *hkl*, takes the form:[9]

$$T_{hkl} = \exp\left[- B_{hkl} \frac{\sin^2 \theta}{\lambda^2} \right]$$

So that for a unit cell, the structure factor becomes:

$$F_{hkl} = \sum_{j=1}^{N} f_j n_j \exp\left[- B_j \frac{\sin^2 \theta_j}{\lambda^2} \right] \exp[2\pi i(hx_j + kx_j + lz_j)]$$

where n_j is the occupation factor of the j^{th} atom, equal to unity in a structure free from vacancies. However, this assumes that the displacements due to thermal motion are equal in all directions (isotropic) which is usually only the case in some highly symmetric positions of cubic space groups.[10] A more rigorous analysis[9,11] describes the anisotropy of thermal motion in the form of an ellipsoid, replacing the above equation with:

$$T_{hkl} = \exp\left[-\frac{1}{4}\left(\begin{matrix} B_{11}h^2a^{*2} + B_{22}k^2b^{*2} + B_{33}l^2c^{*2} \\ +2B_{12}hka^*b^* + 2B_{23}klb^*c^* + 2B_{13}hla^*c^* \end{matrix}\right)\right]$$

There are a number of other expressions for T_{hkl}[9] but the form given here is used to describe the anisotropic temperature factors used in this work. The intensities of the diffracted beams are also governed by the multiplicity of an *hkl* reflection; that is, for a particular *hkl* reflection in a given crystal symmetry class, there are a number of equivalent planes diffracting at the same angle to give an enhanced intensity.

2.4 Powder Neutron Diffraction

Selected samples within this work were investigated using neutrons. The interaction of a neutron with the nucleus of an atom is weak, but not negligible making them a highly penetrating probe. Due to the weak interaction, neutrons are a non-destructive probe. The first neutron diffraction experiments were carried out in 1936[12] following the realisation that neutron motion is governed by wave mechanics. The wavelength of a given neutron is governed by the de Broglie equation:[13]

$$\lambda = \frac{h}{mv}$$

where λ is wavelength, h is Planck's constant, m is mass of a neutron and v is the velocity of a neutron. At 273 K the root mean square of a Boltzman distribution of neutron velocities is 2200 ms^{-1}, which corresponds to a wavelength of approximately 1.55 Å, comparable to interatomic spacing and so moderate velocity neutrons are suitable for diffraction experiments.

Neutrons scatter from materials by interacting with the nucleus of an atom rather than the electron cloud. This means that the scattering power (cross-section) of an atom is not strongly related to its atomic number, unlike X-rays where the scattering

power increases in proportion to the number of electrons in the atom. This has three advantages:

- it is easier to distinguish light atoms, such as hydrogen, in the presence of heavier ones.
- neighbouring elements in the periodic table generally have substantially different scattering cross sections and can be distinguished.
- the nuclear dependence of scattering allows isotopes of the same element to have substantially different scattering lengths for neutrons. Isotopic substitution can be used to label different parts of the molecules making up a material.

Additionally with neutron diffraction there is no angular dependence such as that seen in X-ray diffraction. The result is that reflections can be seen at high angles that would not be seen by X-rays.

The primary requirement for a neutron scattering experiment is a beam of neutrons, there are two principle sources of neutron radiation suitable for diffraction techniques: Constant Wavelength PND and Time of Flight (TOF), both of which were used in this work. Constant wavelength uses conventional nuclear fission reactors, which use the spontaneous decay of uranium to produce neutrons, this then further catalyses uranium fission. TOF uses a synchrotron spallation source, here a very high intensity beam of protons is fired at a heavy metal target, the metal atoms absorb the protons, and then decay releasing many neutrons.

2.4.1 Constant Wavelength PND

In this work PND data were collected on the D1A high resolution instrument at the high flux reactor Institute Laue Langevin (I.L.L) in Grenoble. The nature of the instrumentation is such that the peaks are of near perfect Gaussian nature in the 2θ range 30 – 150°, permitting refinement of complex structures with a volume up to 1000 $Å^3$. The high resolution over a wide range of scattering angles permits the

refinement of up to 150 structural parameters by the Rietveld method. Other features include: a high take-off angle of 122°, giving high resolution at large scattering angles (up to 160°); a bank of 25 high efficiency collimators and counters; an anisotropically squashed germanium monochromator focussing a 250 mm high beam onto only 30 mm; a wide choice of wavelengths, from 1.39 Å to 2.99 Å, quickly available by simple rotation of the focussing monochromator and programmed temperature control for cryostats and furnaces. A schematic diagram of the D1A high resolution PND diffractometer at the I.LL is shown in Figure 5.

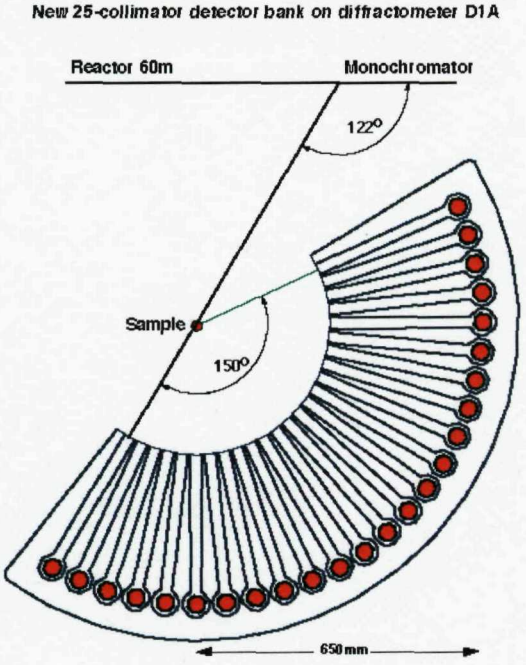

Figure 5 Schematic diagram of the D1A diffractometer.

2.4.2 Time of Flight (TOF) PND

TOF PND data were collected at the ISIS facility at the Rutherford Appleton Laboratory (R. A. L), Oxfordshire. The facility is a synchrotron spallation source, which provides pulses of a range of neutron wavelengths covering the entire neutron spectrum.

Hydrogen gas and caesium vapours are mixed in a reaction chamber, electrical discharge across the chamber results in the formation of H^- and Cs^+ ions. The hydride ions are removed from the chamber by a 665 kV static potential into a linear accelerator; here radiofrequency pulses are used to accelerate the anions up to energy of 70 MeV. The resulting pulse of H^- ions is fired at a thin (0.3 μm) foil of Al_2O_3. This strips the electrons from the ions leaving a pulse of H^+ ions, which are injected, into an H^+ synchrotron ring. Here magnets are used to steer the beam and control the pulse shapes. The injections of H^+ ions into the synchrotron ring happens many times and the number of protons in the storage ring is gradually built up; since the protons are positively charged they repel each other and this limits the maximum size of the pulse. At ISIS the ring can store approximately 2.8×10^{13} protons at any one time. Inside the synchrotron the protons are further accelerated until they reach energy of 800 MeV. The pulse structure inside the ring consists of two rapidly circulating bunches of protons, they each make a complete revolution in 460 ns and the width of the bunch is approximately 100 ns. Once the energy of the protons has reached 800 MeV the pulses are extracted from the ring by a kicker magnet. A kicker magnet is simply an electromagnet that can be switched on and off very rapidly. The rapid change in magnetism 'kicks' the two proton pulses out of the ring, at ISIS the extracted proton beam has a double pulsed structure, with 100 ns long pulses separated by 230 ns, the whole process is repeated every 20 ms. There is a second Kicker magnet which is used to separate the two pulses, one is directed at a heavy metal target made from a series of tungsten plates (clad with tantalum to prevent corrosion), which absorbs the proton and then decays emitting protons, neutrons and gamma radiation. About 30 neutrons are produced for each collision. The other proton pulse is directed to a carbon target and results in the production of muons.

Just as in nuclear reactors the energy of the neutrons can be altered by thermalisation with moderators, and just like reactor sources the instruments are crowded radially around the source target station in order to make maximum use of the neutron flux. The key difference between reactor and spallation sources is that the former produces a continuous supply of neutrons while the latter produces neutrons in short

pulses. Since neutrons with different energies travel at different speeds, a pulsed source easily allows energy determination by measurement of its flight time.

A pulsed neutron source diffractometer operates in a fundamentally different way from a conventional diffractometer. In a conventional diffraction experiment the wavelength is fixed by the monochromator, and the variables are d and the angle of detection θ. In TOF experiments, the detection angle θ is fixed and the variables are d and the wavelength of the neutron, λ. The relationship between TOF and d-spacing is linear and is derived from the de-Broglie's relationship and Bragg's law as shown:

$$\lambda = \frac{h}{P_n}$$

$$= \frac{h}{m_n v_n}$$

$$= 2d \sin\theta$$

where h is Planck's constant, m_n, v_n and p_n are the mass, velocity and momentum of a neutron respectively with d and $\sin\theta$ as derived by Bragg's law. If a primary flight path (moderator to sample) is a distance L_1, a secondary flight path (sample to detector) is L_2 and the corresponding time of flight are t_1 and t_2 then:

$$\frac{h}{m_n}\left[\frac{t_1 + t_2}{L_1 + L_2}\right] = 2d \sin\theta$$

therefore with a total neutron flight path L and time of flight t such that

$$L_1 + L_2 = L \text{ and } t_1 + t_2 = t$$

then

$$t = 2dL\left(\frac{m_n}{h}\right)\sin\theta$$

therefore, for a 12 m instrument like POLARIS, a 1 Å *d*-spacing reflection will be detected in a back scattering bank at a TOF of ~ 5000 μs.

$$\therefore t \propto d$$

2.4.3 TOF Instrument POLARIS

The POLARIS instrument is a high flux, medium resolution diffractometer. POLARIS receives short pulses (< 90 μs) of neutrons from the proton spallation of a uranium or tantalum target, with neutrons of wavelengths down to 0.2 Å suitable for diffraction. The initial burst of neutrons is slowed in a gadolinium poisoned water monchromator at 295 K to give the required tight neutron pulse over a wide range of wavelengths. A schematic representation of POLARIS is shown in Figure 6. On POLARIS backscattered neutrons are detected by 58 ^{3}He detectors giving a resolution of Δd / d of 5 x 10^{-3} and a d spacing range of 0.2 - 3.2 Å. Typical data collection periods on POLARIS for samples of ~ 2 g were 4 - 5 hours. The increased speed of data collection on POLARIS over HRPD makes it a good instrument to use when the highest resolution is not required.

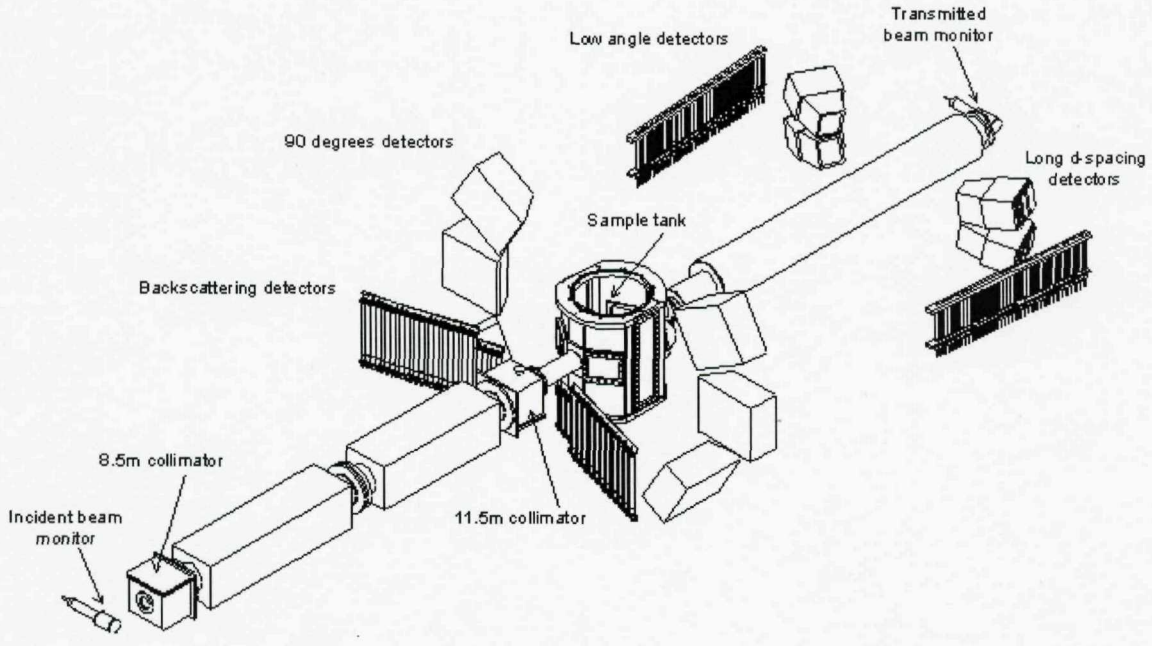

Figure 6 Schematic diagram of the POLARIS diffractometer.

2.4.4 TOF Instrument HRPD

HRPD is a high resolution powder neutron diffractometer (Figure 7), its resolution is quoted as $\Delta d / d = 4.5 \times 10^{-4}$ in backscattering mode. In the back scattering bank a complicated array of ZnS scintillation detectors are fixed at scattering angles of $160° \leq 2\theta \leq 176°$. This leads to the highest available resolution in the *d*-spacing range of ~0.6 - 4.6 Å. HRPD has a path length of 95 m which gives long times of flight and high resolution, however the beam line only takes one in five pulses generated by the source to prevent overlap. This leads to long collection times in the range 8 - 12 hours.

HRPD was designed to handle cell volumes of up to 2500 $Å^3$ with up to 400 structural parameters. This makes it a superb instrument for the study of complicated structures.

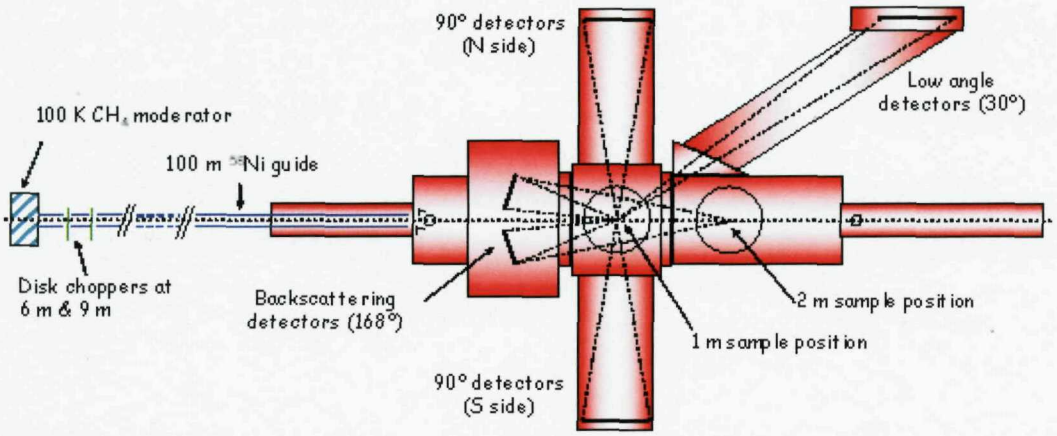

Figure 7 Schematic plan view of the HRPD detector configuration.

On both instruments samples are loaded into vanadium cans of ~ 6 – 12 mm in diameter, as vanadium is largely transparent to neutrons. This can is then mounted within an evacuated sample tank before being exposed to the neutron beam. Data collection is computer controlled. It is also possible to control the sample environment using either the cryostat or furnace. The furnace is capable of operating at temperatures up to 800 °C while the cryostat uses liquid helium to operate down to a base temperature of 2 K. This enables the study of a phase change or magnetic behaviour.

2.5 The Rietveld Method

Sections 2.3 and 2.4 have summarised the collection of three different types of data; PXD, constant wavelength and TOF PND. A method of structural determination is required to analyse the data and determine accurate atomic parameters. Throughout this work the Rietveld refinement method has been used.

In a single crystal diffraction experiment each *hkl* reflection leads to a single diffracted point whose intensity can be easily measured. In a powder diffraction experiment, the X-rays are diffracted from randomly orientated small crystallites,

giving cones of diffracted X-rays. The powder pattern is a one dimensional slice through these rings. Due to the one dimensional nature of the powder pattern full structure factor determination is difficult as much of the information is contained in overlapping peaks. In 1967 H. M. Rietveld[2] originally developed the idea of least squares fitting. Rietveld realised that although many individual reflections did overlap and thus could not be modelled as single entities, they could be fitted using simple peak shape parameters to determine the total intensity and peak shape of overlapping reflections. Today, most experiments aimed at deriving structural information from powder samples exploit the Rietveld method of refinement, and the application of this method has expanded from purely PND data into PXD studies, high resolution synchrotron PXD studies and TOF PND pattern refinement on pulsed machines.

The refinement uses a least squares method to minimise the difference between the observed data and a pattern calculated for a model structure. As the method is one of structure refinement, rather than structure solution, a good starting model is essential. Scale factors and background parameters are the first to be introduced, since the refinement of these parameters involves only coefficients of ordinary or orthogonal polynomials the problem is linear and should immediately converge irrespective of the starting values. Lattice parameters and zero point error are then refined to accurately position diffraction maxima. Initial refinement of the peak shape parameters can also be introduced at this point. After this the atom positions are varied, to locate their position. This varies the peak intensities and improves peak shape. Thermal motion of the located atoms is then calculated by varying the isotropic temperature factors. A final refinement of peak shape is then accomplished, together with further background coefficients, to account for asymmetry or sample broadening effects.

The refinement process is a least squares best fit method. The quantity minimised by the least square method is the function M:

$$M = \sum_i W_i (y_i^{obs} - y_i^{calc})^2$$

W_i is a weighting factor given by $1/y_i^{obs}$, y_i^{obs} is the observed intensity at each step/ point i ($2\theta_1$ for PXD) and y_i^{calc} is the calculated intensity at each step.

For PXD, the calculated intensities y_i^{calc} are determined from the $|F_k|^2$ values collected from the structural model by summing of the calculated contributions from neighbouring Bragg reflections (k) plus a background b_i:

$$y_i^{calc} = s\sum_k L_k |F_k|^2 \phi(2\theta_i - 2\theta_k) P_k A + y_{bi}$$

where s is the scale factor, L_k contains Lorentz polarisation and multiplicity factors, ϕ is a reflection profile function, F_k is the structure factor for the k^{th} Bragg reflection, P_k is the preferred orientation function, A is an absorption factor and y_{bi} is the background intensity at the i^{th} step.

Preferred orientation arises when there is a stronger tendency for the crystallites to be ordered in one way/ set of ways and is defined by:

$$P_k = \left[G_2 + (1 - G_2)\exp\left(-G_1 \alpha_k^2\right)\right]$$

where G_1 and G_2 are refinable parameters and α_k is the angle between the presumed cylindrical symmetry axis and the preferred orientation axis direction.

The background intensity, y_{bi} is modelled by a function that is a cosine Fourier series with a leading constant term:[14]

$$y_{bi} = B_i + \sum_{j=2}^{N} B_j \cos[P * (j - l)]$$

For X-ray, P is the position of the step in 2θ. For TOF, the time is scaled by 180/TMax, where TMax is the maximum allowed by the incident spectrum. Values of B_i and B_j are determined by least squares during the refinement.

Since a comparison of intensities is performed at every point, it is essential for the construction of the calculated profile to accurately describe the peak shape of the Bragg reflections. Peak shape is generally dictated by the instrument; for the Siemens D5000 the peak shape is pseudo-Voigt, and is described by the function:

$$\eta L + (1 - \eta)G$$

where L and G are the Lorentzian and Gaussian contributions to the peak shape and η is the mixing parameter which can be refined as a linear function of 2θ:

$$\eta = N_A + N_B(2\theta)$$

where N_A and N_B are refinable parameters.

The Gaussian (G) and Lorentzian (L) contributions to the peak shape are represented by the equations:

$$G = \frac{(4 \ln 2)^{1/2}}{H_k \sqrt{\pi}} \exp\left(-4 \ln 2 (2\theta_i - 2\theta_k)^2 / {H_k}^2\right)$$

and

$$L = \frac{2}{\pi H_k} \Big/ \left[1 + 4 \frac{(2\theta_i - 2\theta_k)^2}{Hk^2}\right]^{1}$$

where $2\theta_k$ is the calculated position for the k^{th} Bragg peak corrected for the counter zero-point and H_k is the full-width-at-half-maximum (FWHM) of the k^{th} Bragg reflection.

The FWHM, H_k of a peak has been shown to vary with the scattering angle $2\theta_k$ [15] and is modelled as:

$$H_k^2 = U\tan^2\theta + V\tan^2\theta + W$$

where U, V, and W are the refinable parameters and are both instrument and sample dependent. Therefore, this formula can account for peak broadening effects resulting from particle size.

At low scattering angles the peak shape shows marked asymmetry due to the detector and sample heights. This results in the peak maximum shifting to slightly lower angle while the integrated intensity remains unchanged. This can be corrected by the use of a semi-empirical correction factor of the form:

$$1 - \frac{sP(2\theta_i - 2\theta_k)^2}{\tan\theta_k}$$

where P is the asymmetry parameter and s = +1, 0, -1 when $(2\theta_I - 2\theta_k)^2$ is positive, zero or negative.

2.5.1 Criteria of Fit

In any refinement, the parameters that can be varied fall into two distinct groups. The first group are the structural parameters that describe the contents of the unit cell and include the overall temperature factors, coordinates and occupancies of each atom. The second group contains the profile parameters that define the position, shape and full-width-at-half-maximum of each peak and consist of the profile scale factor, unit cell parameters, U, V, W, zero-point, asymmetry and preferred orientation correction. In order to make a quantative assessment of the agreement

between the calculated and observed profiles, a number of reliability factors are defined as follows;

R_p is a parameter showing agreement to the profile.

$$R_{profile} = R_p = \left[\frac{\sum_i \left| y_i^{obs} - y_i^{calc} \right|}{\sum_i y_i^{obs}} \right]$$

R_{exp} is a statistical derivation where N is the number of observables, P is the number of refinable parameters and C is the number of constraints.

$$R_{expected} = R_{exp} = \left[\frac{(N-P+C)}{\sum_i W_i (y_i^{obs})^2} \right]^{\frac{1}{2}}$$

From a mathematical point, R_{wp} is the most meaningful of the R-factors because the numerator is the residual being minimised. For this reason it best reflects the progress of the refinement and is given by:

$$R_{weighted-profile} = R_{wp} = \left[\frac{\sum_i W_i \left| y_i^{obs} - y_i^{calc} \right|^2}{\sum_i W_i (Y_i^{obs})^2} \right]$$

Finally, the chi-squared parameter (χ^2) may be defined as:

$$\chi^2 = \left[\frac{1}{N - P + C} \right]^2 \sum_i W_i \left| y_i^{obs} - y_i^{calc} \right|^2$$

This is the natural measure of the fit and is normally minimised in the refinement. Therefore for a good fit R_{wp} should approach the statistically expected R_e i.e χ^2 should approach unity.

$$= \left[\frac{R_{wp}}{R_{exp}} \right]^2$$

The goodness of fit can also be estimated visually by examining a plot of the profile fit; for a good fit the difference line between calculated and observed should be as flat as possible with fluctuations consistent with noise.

In this work PXD and PND data were analysed using the Generalised Structural Analysis Suite, (GSAS),[14] of Von Dreele and Larson. The R_{wp}, R_p and χ^2 values obtained from Rietveld refinements have been quoted as an indication of the goodness of fit achieved to the data. In addition selected profile fits are shown in the relevant sections of the chapters.

2.6 Single Crystal X-ray Diffraction

The majority of X-ray characterisation carried out in this work was done on powdered samples. However, hydrothermal reactions resulted in crystals, which can be analysed by single crystal X-ray diffraction. This enables complete structural determination of the materials; the main challenge is to obtain a crystal of sufficient size and quality. Diffraction from a single crystal leads to clearly defined points of intensity from each plane, which is easily measured. In contrast a powder consists of randomly oriented crystallites leading to rings of diffraction intensity, with the pattern obtained being one-dimensional slices through the rings.

The angles at which diffraction occurs will depend on the symmetry, unit cell size and contents of the crystal lattice. In general crystals that possess less symmetry

operations require more data to be collected before the structure can be solved. This is because for a highly symmetrical lattice often the incident X-ray beam will produce the same diffraction pattern. Data are collected with the incident beam fired from all unique orientations of the crystal, collecting a portion of the sphere of diffracted beams. The diffracted beams are collected as spots of different intensities by an area detector. The arrangement and intensities of these spots give an indication of the reciprocal lattice. This means spots close together in one direction imply a long *d*-spacing in this particular orientation of the crystal.

The University of Southampton, School of Chemistry has two Bruker Nonius Kappa CCD diffractometers. These run from a single Bruker-Nonius FR591 rotating anode X-ray generator giving molybdenum K_α radiation ($\lambda = 0.71073$ Å). Both devices run crystals at low temperatures (120 K) using a liquid nitrogen cryostream. One diffractometer has a conifocal mirror instead of a monochromator to focus and monochromate the X-ray beam, resulting in a much larger flux (six times greater) enabling shorter collection times. Larger crystals cannot be collected with the more focussed beam. A 95 mm CCD camera collects diffraction data. The crystal is mounted on a glass fibre and fixed in a goniometer, which can orient the crystal in a range of angles to the X-ray beam. The intensities of the diffracted data are measured by an area detector. Initially a single position scan is done to check the quality of the diffraction from the crystal (blurred or doubled diffraction spots indicate twinned crystals). If this is suitable, a series of eight phi/chi scans are made in order to determine the unit cell. The program DirAx[16,17] will suggest a unit cell and give an indication of how well this model fits the collected data. The given unit cell is compared with the database of known cells to see if the structure or isostructural materials have been characterised. If the structure is to be collected then the software package COLLECT[18] is used to calculate the number of frames required and suggests the collection time, based on the unit cell. Collection time is very much dependent on crystal quality and symmetry, usually the full data set is collected with 10 – 30 seconds per frame at each orientation. The program aims to obtain 100% data completeness and further redundancies. The excess of data helps

reduce the impact of any poor quality frames and give better statistical accuracy of results.

In this work, crystal data were solved using the WinGX suite of software,[19] principally using the SHELX-97 program[13,20] and XPREP.[21] This uses direct methods to determine the crystal structure. The data obtained will be a list of the angles at which the reflections occur and their intensities. The intensity results from two sources; the first is a scattering factor that is related to electron density of the atoms, the second is a phase factor, which comes from different planes. The scattering factor of all the atoms in a unit cell can be combined to form a structure factor:

Once the data have been collected, we have a set of reflections *hkl* with their respective intensities. These can be used to construct a picture of the electron density in the unit cell, according to equation:

$$\rho(xyz) = \sum_h \sum_k \sum_l |F_{hkl}| \cos[2\pi(hx + ky + lz) - \alpha_{hkl}]$$

The amplitudes |F(*hkl*)| have been measured, the final exponential term can be calculated for the contribution of each reflection *hkl* to each position *xyz*. However, the phases of the reflections (α) are unknown, so the calculation cannot be carried out immediately. This is known as the *phase problem*.

The Direct method is the most common way of solving this problem relying on statistical techniques. The electron density is the Fourier transform of the diffraction pattern. This means that we add together a set of waves in order to produce the electron density distribution. Each wave has half its value positive and half negative, except for F(000), which is constant and positive. The electron density however is positive or zero; it can have no negative regions. So the waves must be added in such a way so as to concentrate positive regions and cancel out negative regions. Since large numbers of reflections are involved in the complete Fourier transform,

individual phase relationships are not certainties but have to be expressed in terms of probabilities, and the probabilities depend upon the relative intensities.

Direct methods involve selecting those reflections which contribute most to the Fourier transform, working out the probable relationships among their phases, and then trying different possible phases to see how well the probability relationships are satisfied. For the most promising combinations, (assessed by various numerical measures), Fourier transforms are calculated from the observed amplitudes and trial phases, and are examined for recognisable molecular features. Once an approximate model has been produced it can then be refined, and the iterative process can give the positions of all the other atoms. In some case hydrogen atoms will not be resolved due to the small and diffuse electron density. Least square refinement optimises the model and eventually other parameters such as anisotropic temperature factors, which can be included to give a very accurate picture of the crystal structure.

The accuracy of the model is shown by the reliability (R) factors:

$$R_F = \frac{\sum_{hkl}\left(\left|F_{hkl}^{obs}\right| - \left|F_{hkl}^{calc}\right|\right)}{\sum_{hkl}\left|F_{hkl}\right|} x100$$

A good refinement will have an R factor below 5%.

2.7 Magnetic Measurements

Magnetic susceptibility is the quantitative measure of the response of a material to an applied (i.e. external) magnetic field. Diamagnetic materials only have paired electrons. Such materials will be weakly repelled by a magnetic field, as the field will induce an opposite magnetic moment in the substance. Paramagnetic materials (unpaired electrons orientated at random on different atoms), possess a permanent magnetic moment, even in the absence of an external field. When an external field is

applied these materials will tend to be weakly attracted to it as the two fields align. Paramagnetism is weak because the thermal vibration of the atoms moves the magnetic moments of the atoms reducing the alignment.

Diamagnetic susceptibilities are temperature independent, but paramagnetic susceptibilities depend on the temperature of the sample, often in a rather complex fashion. Cooling the substance down allows the individual magnetic moments to interact and greater ordering can occur. Normally, below a critical temperature the individual moments align with each other in a parallel arrangement, giving rise to ferromagnetism, or antiparallel, in which case the material is known as antiferromagnetic. For ferromagnets this critical temperature is known as the Curie point, T_c and in the case of antiferromagnets the Neel point T_N. Since all the individual magnetic moments are interacting in ferromagnets or antiferromagnets the interaction with an external field will be larger. Ferromagnets will be strongly attracted, leading to an increase in susceptibility, whereas the antiferromagnet will behave more like a diamagnet and the susceptibility will drop. The temperature dependence of the magnetic susceptibility of paramagnetic, ferromagnetic and antiferrromagnetic materials is shown in Figure 8.

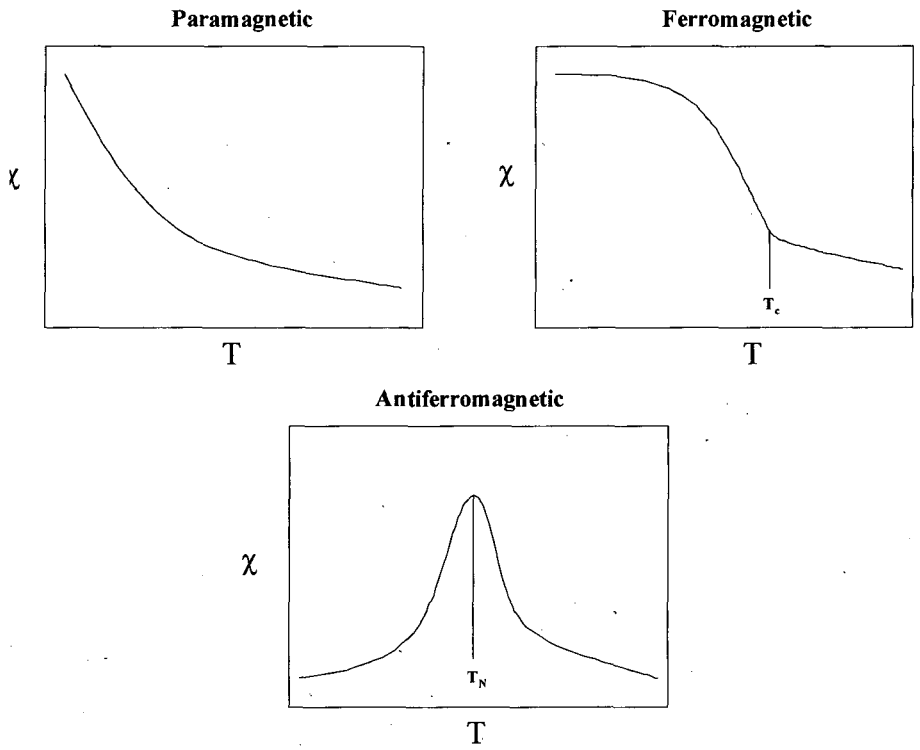

Figure 8 Temperature dependence of the magnetic susceptibility of a) paramagnetic, b) ferromagnetic and c) antiferromagnetic materials.

Ferrimagnetism is found when the magnitudes of the magnetic moments associated with the two AF sublattices are not exactly the same. Then, when the spontaneous anti-parallel alignment occurs at a transition temperature, the material retains a small but permanent magnetic moment rather than a zero one. The simplest example is magnetite, Fe_3O_4, a spinel. The two chemical or structural sublattices are

1) iron(III) ions in tetrahedral coordination to oxygen
2) iron(II) and iron(III) ions in equal proportion to octahedral oxygen coordination.

The result is that the inequivalent magnetic sublattices cannot balance each other out, and a weak moment persists below T_c.

A Superconducting Quantum Interference Device (SQUID) was used to measure the magnetic susceptibility of certain materials. If two superconducting regions are kept

totally isolated from each other the phases of the electron pairs in the two regions will be completely unrelated. If the regions are brought close together then the electrons will be able to tunnel through the space and interact. This is known as Josephson tunnelling and the gap between the superconductors a Josephson junction. A SQUID magnetometer consists of a superconducting ring with Josephson junctions at opposite sides. A magnetic field is applied perpendicular to the ring and this induces a current within the ring. A small quantity of the sample (~ 20 mg) is lowered into the ring and any change in the magnetic field due to the sample is detected as differences in the current around the ring. This enables determination of the magnetic properties of the material (e.g. ferromagnetic) down to temperatures as low as 2 K. The great advantage of this technique over other methods of magnetic analysis such as the Guoy balance is the small sample volume required. SQUID analysis typically uses 20 – 30 mg of material in comparison to 1 or 2 grams.

The magnetic properties of several of the materials included in this thesis were also characterised using Vibrating Sample Magnetometry (VSM). A schematic diagram of the VSM instrument is shown in Figure 9. The sample is loaded into a small magnetically neutral, plastic container which is then placed in a magnetic field between two search coils. The sample is then vibrated rapidly and the temperature dependence of the magnetic susceptibility of the sample measured. When a material is placed within a uniform magnetic field and is made to undergo sinusoidal motion, there is some magnetic flux change. This induces a voltage in the pick up coils, which is proportional to the magnetic moment of the sample.

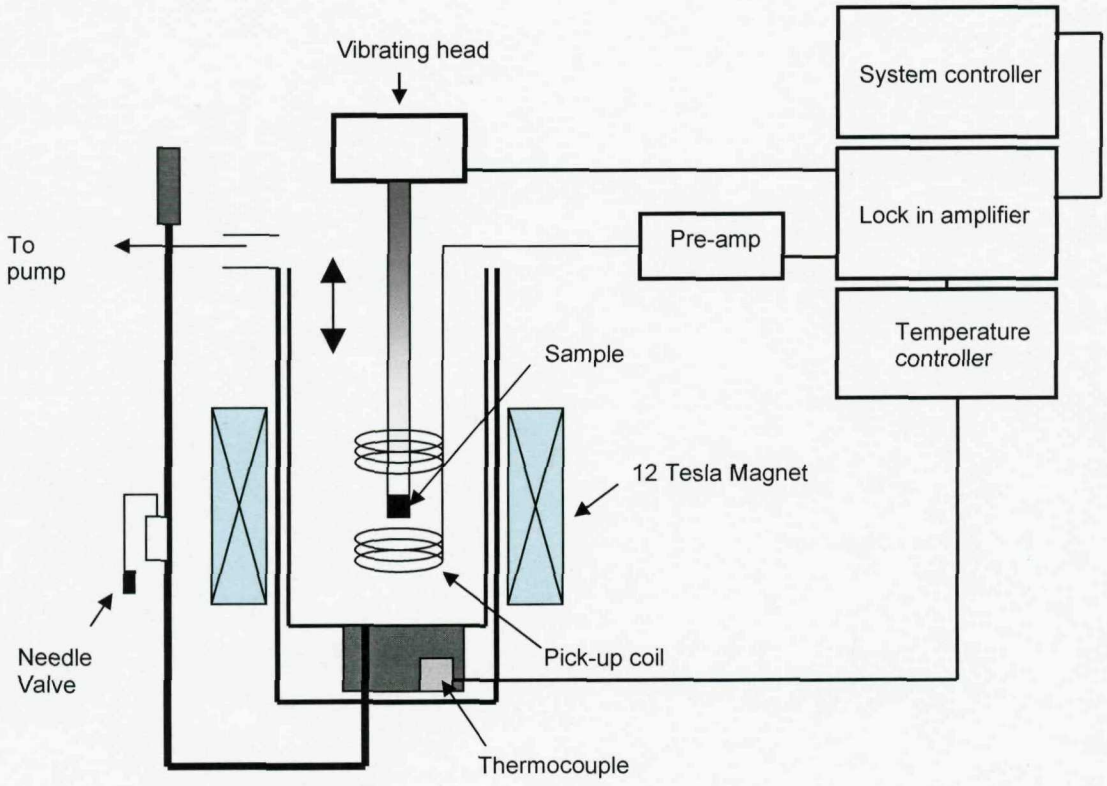

Figure 9 Schematic diagram of the VSM instrument.

The data reveal what type of magnetic behaviour the materials exhibit i.e. paramagnetic, ferromagnetic, antiferromagnetic or superconductivity. For non-interacting paramagnetic materials, the molar magnetic susceptibility, χ, which is related to the number of unpaired electrons present within the compound, may be determined using the Curie equation:

$$\chi = \frac{C}{T}$$

where χ is magnetic susceptibility, C is the Curie constant and T is the temperature. Therefore a plot of $^1/_\chi$ against temperature will yield a straight line through zero.

When we have a weak interaction the behaviour can be described by a modified equation; the Curie-Weiss law:

$$\chi = \frac{C}{T - \theta}$$

where θ is the Weiss constant. The plot of $^1/_\chi$ against temperature for this behaviour will yield a straight line with a gradient related to C and an intercept on the T axis related to θ. In general if θ is positive it implies a dominant ferromagnetic interaction and if θ is negative it implies an antiferromagnetic interaction. The Curie-Weiss law can be re-written as:

$$\chi = \frac{N_A \mu_B{}^2 \mu_{eff}{}^2}{3 k_B (T - \theta)}$$

where N_A is Avogadro's number, μ_B is the Bohr magneton, k_B is the Boltzman constant and μ_{eff} is the magnetic moment. Therefore from the gradient of the line in a plot of $^1/_\chi$ against T we can calculate the magnetic moment.

2.8 Thermal Analysis

Thermal analysis involves the measurement of physical or chemical changes that occur as a function of temperature, the properties examined are usually mass and thermodynamic events. These changes are measured by Thermogravimetric Analysis (TGA). The mass of a sample is recorded as a function of temperature, in a controlled atmosphere the sample can be heated at a rate between 1 and 50 °C per minute. The measurement of the weight loss can give information on the dehydration or decomposition of a material.

Several samples were studied using the Metler Toledo thermal analysis module in the temperature range 25 – 1000 °C in the presence of flowing gas. The instrument is controlled by a PC and enables different heating regimes to be run. In a typical experiment approximately 20 mg of sample was heated under H_2/N_2 to 1000 °C at a

rate of 10 °C per minute. The temperature was held for 30 minutes to ensure any thermal events had occurred before cooling back to room temperature at 20 °C per minute. Data points were recorded every second and displayed in real time. The output from the computer can then be exported for plotting and analysis using other software.

2.9 Infra-red Spectroscopy

IR spectra were recorded on a Perkin Elmer Spectrum One spectrometer in the range 4000 cm^{-1} to 450 cm^{-1}. Samples were mixed with dry KBr and pressed into discs for conventional IR spectroscopy. Diffuse reflectance scans were taken using the micro cup facility and rely on the beam being refocused once it has been scattered by the sample to record the spectra. As the beam does not pass through the sample time spent in sample preparation can be greatly reduced.

2.10 References

[1] A. R. West, '*Solid State Chemistry and its Applications*', John Wiley & Sons (1984).

[2] H. M. Rietveld, *Acta Crystrallogr.*, **22**, 151 (1967).

[3] H. M. Rietveld, *J. Appl. Crystallogr.*, **2**, 65 (1969).

[4] D. M. Moore and R. C. Reynolds, '*X-ray Diffraction and the Identification and Analysis of Clay Minerals*', Oxford University Press, New York (1997).

[5] W. L. Bragg, *Proc. Camb. Phil. Soc.*, **17**, 43 (1913).

[6] A. K. Cheetham and P. Day, '*Solid State Chemistry: Techniques*', Oxford Science Publications, Clarendon Press, Oxford (1988).

[7] T. Hahn, '*International Tables for Crystallography Vol A*', D. Reidel, Dordrecht (1983).

[8] International Centre for Diffraction Data, 12 Campus Boulevard, Newton Square, Pensylvania 19073-3273, U.S.A (1995)

[9] M. J. Buerger, '*Contemporary Crystallography*', Chapter 11, McGraw-Hill (1970).

[10] B. T. M. Willis and A. W. Pryor, '*Thermal Vibrations in Crystallography*', Chapter 4, Cambridge Univeristy Press (1975).

[11] H. A. Levy, *Acta Crystrallogr.*, **9**, 679 (1956).

[12] D. P. Mitchell and P. N. Powers, *Phys. Rev.*, **50**, 486 (1936).

[13] L. J. Farrugia, WINGX, *J. Appl. Crystallogr.*, **32**, 837 (1999).

[14] A. C. Larson and R. B. Von Dreele, Generalized Structure Analysis System, MS-H805, Los Alamos, NM 87545 (1990).

[15] G. Caglioti, A. Paoletti and F. P. Ricci, *Nucl. Instrum. Methods*, **35**, 323 (1958).

[16] A. Duisenberg, *J. Appl, Cryst.*, **25(2)**, 92 (1992).

[17] A. Duisenberg, R. Hooft, A. Schreurs and J. Kroon, *J. Appl. Cryst.*, **33(3)**, 893 (2000).

[18] R. Hooft, COLLECT data collection software, Nonius B. V., 1998.

[19] L. J. Farrugia, *J. Appl. Cryst.*, **32**, 837 (1999).

[20] G. M. Sheldrick, SHELX-97 [Includes SHELXS97, SHELXL97], Programs for Crystal Structure Analysis (Release 97-2), University of Göttingen, Göttingen, Germany, (1997).

[21] XPREP Bruker AXS Inc., Madison, Wisconsin, USA.

Chapter Three

Synthesis and Structural Characterisation of the $LnSrScO_4$ and $LnSrInO_4$ phases and Discussion of the A_2BO_4 oxides

3.1 Introduction

Layered perovskite-type compounds in the Ruddlesden-Popper series $AO(ABO_3)_n$ (n = 1, 2, 3) are interesting materials because of their chemical and physical properties, which include photocatalysis, ability for ion exchange and superconductivity in for example $La_{2-x}Ba_xCuO_4$ and Sr_2RuO_4.[1,2,3] The idealized two dimensional structure of A_2BO_4 oxides (K_2NiF_4-type),[4] consists of perovskite-like, corner linked BO_6 sheets interleaved by rock-salt like AO layers giving a body-centred tetragonal cell. Sheets of BO_6 octahedra sharing four vertices are separated by A cations in nine-fold coordination to O i.e. the large A cations are arranged in layers with nine nearest O neighbors. The BO_6 octahedra are not perfectly regular consisting, typically, of four short in plane B-O distances (equatorial) plus two slightly longer axial B-O interactions.

As with many complex oxide structures built from BO_n polyhedra the potential exists for these units to tilt or rotate around their centres while maintaining the basic structure type. This has been well studied for perovskite ABO_3[5,6,7] structures and to a much more limited extent for the double layer Ruddlesden-Popper phases ($A_3B_2O_7$).[8] Such rotations and tilts of the BO_n polyhedra in these structures generally result in a reduction of the unit cell symmetry but also allow improved coordination to the A type cations. Thus one important factor that determines the structure of the A_2BO_4 compounds is the matching between the perovskite-like BO_6 layers and the rock salt like AO layers. A measure of the bond length matching can be calculated from a version of the Goldschmidt tolerance factor:

$$t = \frac{(r_A + r_O)}{\sqrt{2}(r_B + r_O)}$$

For perovskite structure types, ideal matching between the A cation and one layer of linked BO_6 octahedra occurs for $t \approx 1$ and the structure formed is tetragonal, described in the space group *I4/mmm*. Ganguly and Rao[9] proposed that A_2BO_4 compounds with the t value near the lower limit $t \approx 0.85$ exhibit superlattice

reflection lines in their diffraction patterns associated with a rotation of BO_6 octahedra around the *c* axis or a tilting of BO_6 octahedra in the 100 or 110 direction. This results in orthorhombic deformation of the tetragonal archetype. In these cases two types of orthorhombic distortion have been observed; one is due to the tilting of the BO_6 octahedra resulting in the A*bma* space group, as exemplified by La_2CoO_4. The other is a consequence of displacements in the positions of the rare earth cations and the oxygen anions along the *c* axis generating a structure that can be described in the space group F*mm2* - as for Sm_2CoO_4.[10]

A structural study of the ternary lanthanide orthoscandate perovskites; $LnScO_3$ (Ln = La, Pr, Nd, Sm, Eu, Gd, Tb and Dy) has been undertaken by Liferovich and Mitchell.[11] The structures of these compounds have been determined by PXD at room temperature. These ternary stoichiometric perovskites adopt the space group P*bmn* and contain distorted coordination polyhedron of both Ln and Sc ions, together with strongly tilted ScO_6 octahedra. Because of the decrease in size of lanthanides through the series, the Goldschmidt tolerance factor decreases from 0.843 ($LaScO_3$) to 0.783 (hypothetical $LuScO_3$). In terms of the observed tolerance factor to the critical distortion of the perovskite structure in scandates is just less than $t = 0.841$ (observed in $HoScO_3$). It has also been shown that the coordination polyhedron of the lanthanides in the A-site of the orthorhombic perovskites is best regarded as $^{viii}Ln^{3+}$ rather than $^{xii}Ln^{3+}$. This is because the rotation of the lanthanide in the A-site results in the degeneration of 12 Ln-O bonds to 8 short Ln-O and 4 long Ln-O bonds and determines the first and second coordination spheres for the Ln^{3+} cations. The distortion of the ScO_6 octahedra increases for the orthoscandates of La-Sm and irregularly decreases in the Eu-Ho orthoscandates. The latter shows a poorly developed trend of decreased ScO_6 distortion values towards the heavy lanthanides.

Recently structural studies on $LaInO_3$ have also been undertaken. $LaInO_3$ was synthesised by a solid state reaction method. Rietveld refinements reveal that the compound crystallizes in the P*mna* space group, in which the In atom lies on an

inversion centre and the La atom and one of the O atoms lie on a mirror plane. The structure of $LaInO_3$ is distorted by the in-phase and antiphase tilting of oxygen octahedra in the $a^+b^-b^-$ system of the InO_6 polyhedra. The InO_6 octahedra consist of three types of In-O bond with bond lengths of 2.11(2), 2.164(4) and 2.22(2) Å.[12]

The description of all possible space groups that may occur for A_2BO_4 phases as a result of various octahedral tilts and rotations have been discussed by Hatch and Stokes.[13] In general, however, few materials adopting, or potentially adopting, the K_2NiF_4 structure type have been studied in detail structurally. Indeed many compositions have not been previously synthesised and others are assumed to adopt the perfect tetragonal structure on the basis of poor quality diffraction data. Furthermore, in most cases only the room temperature structures have been investigated.

Of the few previously studied A_2BO_4 complex oxides those adopting the lower symmetry orthorhombic K_2NiF_4-type structure, as a result of octahedral tilts or rotations, include the oxygen deficient $La_{1-x}Sr_{1+x}InO_{4-d}$ ($x = 0 - 0.2$)[14] compounds and $LaSrScO_4$.[15] $La_{0.8}Sr_{1.2}InO_{3.9}$ crystallises in the space group P*bca* and has a calculated *t* value of 0.9, which suggests that the ionic radius of In^{3+} is too large to form a regular square-net perovskite-type layer in association with these A site cations ($La_{0.8}^{3+}Sr_{1.2}^{2+}$). This results in the formation of a perovskite layer that consists of tilted InO_{6-x} octahedra.

$LaSrScO_4$ has been studied using both PXD and dielectric measurements by Kim *et al.*[15] This work targeted Sc^{3+} as the B site ion of A_2BO_4 because Sc^{3+} has the greatest ionic radius among the trivalent 3*d*-transition metal ions and, therefore, was predicted to have the greatest mismatch between the A and B sites. Rietveld profile refinements carried out using the PXD data investigated three different space groups; I4/*mmm*, F*mmm* and A*bma*. On the basis of the lower profile fit R factors obtained for the refinements with the space groups F*mmm* and A*bma* it was concluded that these two space groups offered the best descriptions of the structure

adopted by $LaSrScO_4$. A*bma*, which can accommodate a tilting of the ScO_6 octahedra, was chosen as the most plausible based on the dielectric measurements.

In this work the effect on the K_2NiF_4 structure type on introducing an even greater mismatch in the A and B ion sizes caused by reducing the effective ionic radius of the A site in the series of compounds $LnSrScO_4$ (Ln = La, Ce, Pr, Nd and Sm) and $LnSrInO_4$ (Ln = La and Pr) has been studied. The effect of temperature on the structures and phase behaviors of these materials has also been investigated. Using this information the relationship between A and B cation sizes and choice of structure in the general A_2BO_4 system is discussed.

3.2 The $LnSrScO_4$ (Ln = La, Ce, Pr, Nd and Sm) Phases

3.2.1 Synthesis

The $LnSrScO_4$ (Ln = La, Pr, Nd and Sm) compounds were synthesised by the direct reaction of stoichiometric amounts of Ln_2O_3 (99.99%, Aldrich) (Ln = La, Nd and Sm), Pr_6O_{11} (99.99%, Aldrich), $SrCO_3$ (99.9+%, Aldrich) and Sc_2O_3 (99.9%, Avocado). The lanthanide oxides were dried in air at 800 °C for 24 hours prior to use. The starting materials were intimately ground as a suspension in ethanol, which was subsequently evaporated. The mixed powders were pressed into pellets of 10 mm diameter and 3 mm thickness under 10 tonnes of pressure and these were then fired at 1200 °C for 48 hours. Samples were cooled, ground, reformed into pellets and heated again in air at 1350 °C for 48 hours and the products quenched to room temperature to obtain a single phase product.

$CeSrScO_4$ was synthesised *via* a sol-gel route, whereby stoichiometric amounts of $Ce(NO_3)_3.6H_2O$ (99.99+%, Aldrich), $Sr(NO_3)_2$ (99.9+%, Aldrich) and Sc_2O_3 (99.9%, Avocado) were dissolved in the minimum quantity of 15.8 M nitric acid. Molar equivalents of ethylene glycol and citric acid dissolved in ~ 25 mL distilled water were added to this solution. The mixture was heated and stirred to dryness.

The dry mixture was further decomposed at 220 °C for 5 hours. After decomposition the sample was heated to 400 °C in air for 48 hours and then 1200 °C under 5% H_2/N_2 for a further 48 hours. Following regrinding and pelletisation the sample was annealed under 5% H_2/N_2 for another 48 hours at 1350 °C; these conditions avoid the potential for oxidation of Ce(III) to Ce(IV).

The synthesis of $GdSrScO_4$ and $DySrScO_4$ was also attempted using both the direct route and the sol-gel method, however PXD patterns show that the required phase is not formed and the pattern matches that of $SrGd_2O_4$ and $SrDy_2O_4$. Attempts to prepare $LaBaScO_4$ using the same procedure results in the formation of the required phase as well as the double layered Ruddlesden-Popper phase $La_2BaSc_2O_7$.

3.2.2 Structural Characterisation

3.2.2.1 Variable Temperature PXD Structure Refinement of $LnSrScO_4$

The $LnSrScO_4$ (Ln = La, Ce, Pr, Nd and Sm) compounds were characterised using PXD. Variable temperature PXD data were collected over the 2θ range 10-100° using a step size of 0.018° and the Bruker D8 diffractometer operating with $Cu_{K\alpha 1}$ radiation in conjunction with the PSD detector and an Anton- Paar HTK 1200 furnace stage.

In order to determine the correct structural description for the $LnSrScO_4$ compounds, initial detailed analysis centred on the room temperature data from $LaSrScO_4$. Rietveld[16,17] refinements using the GSAS[18] suite of programmes and PXD data obtained for $LaSrScO_4$ were performed in the different space groups accommodating various octahedral tilts as proposed by Hatch and Stokes.[13] For each structural description the appropriate model was set-up within GSAS and identical numbers of profile parameters refined; the number of atomic positional parameters, which were varied as a function of the structural model are included in Table 1. Table 1 also summarises the degree of success achieved in fitting each of these structural models to the data obtained.

Table 1 Refined lattice parameters and final fit parameters for room temperature $LaSrScO_4$ PXD data in space groups accommodating different octahedral tilts (*e.s.d's are given in parantheses*).

Space Group	Latice Parameters/ Å			χ^2	R_{wp} (%)	Rp (%)	No. of atomic positional parameters varied
	a	*b*	*c*				
I4/mmm	4.0699(1)	4.0699(1)	12.4676(3)	4.35	5.12	3.73	2
A*bma*	5.7615(1)	5.7499(1)	12.4674(2)	2.89	4.17	3.11	5
P*bca*	12.4674(4)	5.7619(3)	5.7499(3)	9.95	7.73	4.94	9
P*ccn*	5.7616(1)	5.7496(1)	12.4676(2)	2.86	4.14	3.09	8
F*mmm*	5.7619(1)	5.7493(1)	12.4674(3)	3.71	4.72	3.45	2

Two space groups model the data better than the others, A*bma* and *Pccn;* of these the higher symmetry A*bma* was chosen as it is a simpler model and requires three less positional parameters to describe the structure. In this A*bma* description, also used by Kim *et al.*, the lanthanum and strontium are fully disordered and situated on (x,0,z), x ~ 0.02, z ~ 0.36; scandium on (0,0,0) and oxygen atoms on (0.25,0.25,z) z ~0.02 and on (x,0,z) x ~ 0.45, z~0.33. As with the I*4/mmm* crystal structure description for K_2NiF_4 phases, the B-type / Sc^{3+} ions occupy sites with a distorted octahedral coordination to oxygen and the Sr^{2+} and Ln^{3+} ions occupy sites having a coordination number of 9, though variation in bond lengths to oxygen are much larger than for the regular tetragonal K_2NiF_4 structure. Final stages of the refinements in the *Abma* description included all global parameters, i.e. histogram scale factor, peak shape, zero point displacement, background parameters and lattice constants; isotropic temperature factors and the atom positions were also varied. As expected for X-ray data, the U_{iso} of the oxygen atoms were high and as a result the thermal parameters of the axial and equatorial oxygen atoms were constrained together. The data in Table 2 summarise this crystallographic model and provides a comparision with the model published by Kim *et al.* Figure 1 shows the results of

the structural refinement in terms of the profile fit achieved for the data collected from $LaSrScO_4$ at room temperature.

Table 2 Refined atomic positions for $LaSrScO_4$ at room temperature (PXD)
Space group Abma; a = 5.7615(1), **5.7657(5)**; *b = 5.7499(1),* **5.7513(4)**; *c = 12.4674(2),* **12.4670(1)** *Å (e.s.d's in parentheses and Kim et al.[15] parameters are highlighted)*

Atom	x	y	z	Occupancy	U_{iso} x 100/Å^2
La/Sr	0.0137(3)	0	0.3565(1)	0.5/ 0.5	1.36(5)
	0.0146(9)		**0.3566(3)**		**0.68**
Sc	0	0	0	1	0.42(8)
					0.50
O1	0.25	0.25	0.0154(9)	1	1.97(21)
			0.0137(6)		**2.54**
O2	0.4353(16)	0	0.3307(6)	1	1.97(21)
	0.4514(85)		**0.3297(28)**		**2.90**

$\chi^2 = 2.80$, $R_p = 3.11\%$, R_{wp} 4.17%

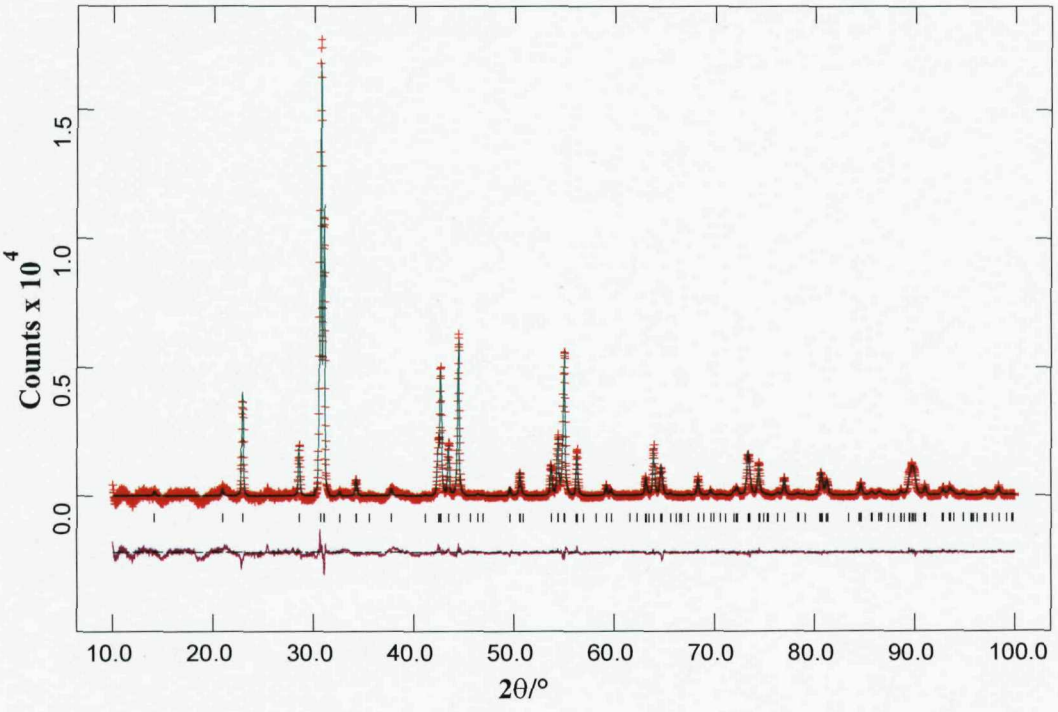

Figure 1 PXD refinement profile fit for orthorhombic $LaSrScO_4$ in the space group A*bma* at room temperature *(crosses indicate observed data, the upper continuous line shows calculated profile, the lower continuous line the difference and tick marks show reflection positions).*

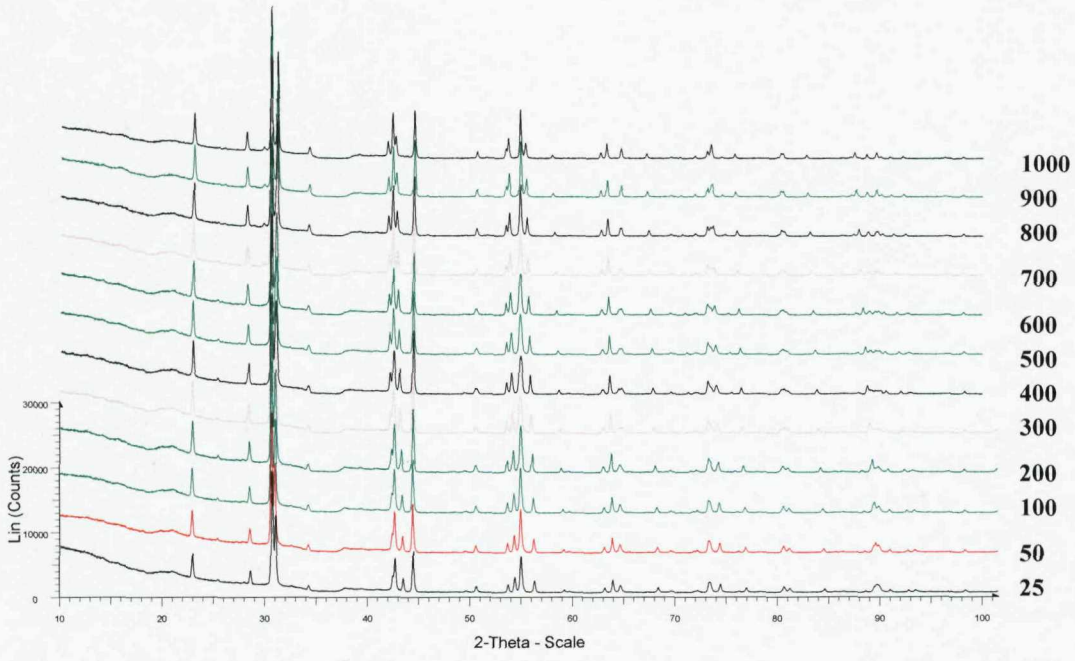

Figure 2 Variable temperature PXD data for $LaSrScO_4$.

Figure 2 shows the variable temperature data obtained for $LaSrScO_4$, the room temperature model was used to successfully fit the diffraction data obtained from $LaSrScO_4$ at temperatures between 25 and 800 °C though above 300 °C the orthorhombicity in the unit cell decreased significantly. Data collected above 800 °C could be fully modelled in the tetragonal space group *I4/mmm* (i.e. a regular tetragonal K_2NiF_4 type structure) with similar fit factors to the orthorhombic space group A*bma* and therefore refinements were undertaken using this simpler crytallographic description.

For the other scandate phases $LnSrScO_4$ (Ln = Ce, Pr, Nd and Sm) a similar analysis was undertaken. Initial modeling of the data collected at room temperature for each lanthanide phase confirmed that the appropriate choice of space group was the orthorhombic A*bma* while at high temperatures the diffraction data from the $PrSrScO_4$ phase could again be modeled in the simpler tetragonal *I4/mmm* description. For all lanthanides and all temperatures for which data were collected,

structure refinements were completed to convergence to include all profile and positional parameters. The unit cells of the *I4/mmm* (a_T x a_T x c_T) and *Abma* descriptions are related *via* the relationship $\sqrt{2}a_T$ x $\sqrt{2}a_T$ x c_T, allowing direct comparison of the values extracted from the refinements.

The refined atomic positions and final fit parameters for all phases at room temperature have been tabulated (Tables 3 – 6), the refined structural parameters as a function of temperature are summarised in Table a/ Appendix A. Table b/ Appendix A details the extracted important interatomic distances and bond angles of these compounds as a function of temperature. The final fit to the profile for the room temperature data are shown in Figures 3 – 6. Variable temperature PXD data for $CeSrScO_4$ were collected under a constant flow of nitrogen with the aim of preventing oxidation of Ce(III) to Ce(IV), however from detailed analysis of the thermodiffractogram and Rietveld refinements using the high temperature data it was clear that above 500 °C the compound started to oxidise. This resulted in the formation of an impurity with a cubic structure (of possible stoichiometry $(Sr^{2+}Ce^{3+})(Ce^{4+}Sc^{3+})O_3$) and data collected above 500 °C from this phase were not analysed further.

Table 3 Refined atomic positions for $CeSrScO_4$ at room temperature (PXD).
Space group Abma; a =5.7606(2), b =5.7459(2) and c =12.3942(4) Å (e.s.d's in parentheses)

Atom	x	y	z	Occupancy	U_{iso} x 100/Å^2
Ce/Sr	0.0162(4)	0	0.3560(1)	0.5/ 0.5	2.65(9)
Sc	0	0	0	1	2.14(15)
O1	0.25	0.25	0.0135(15)	1	2.80(32)
O2	0.4140(22)	0	0.3307(11)	1	2.80(32)

$\chi^2 = 4.99$, $R_p = 4.37\%$, $R_{wp} = 6.22\%$

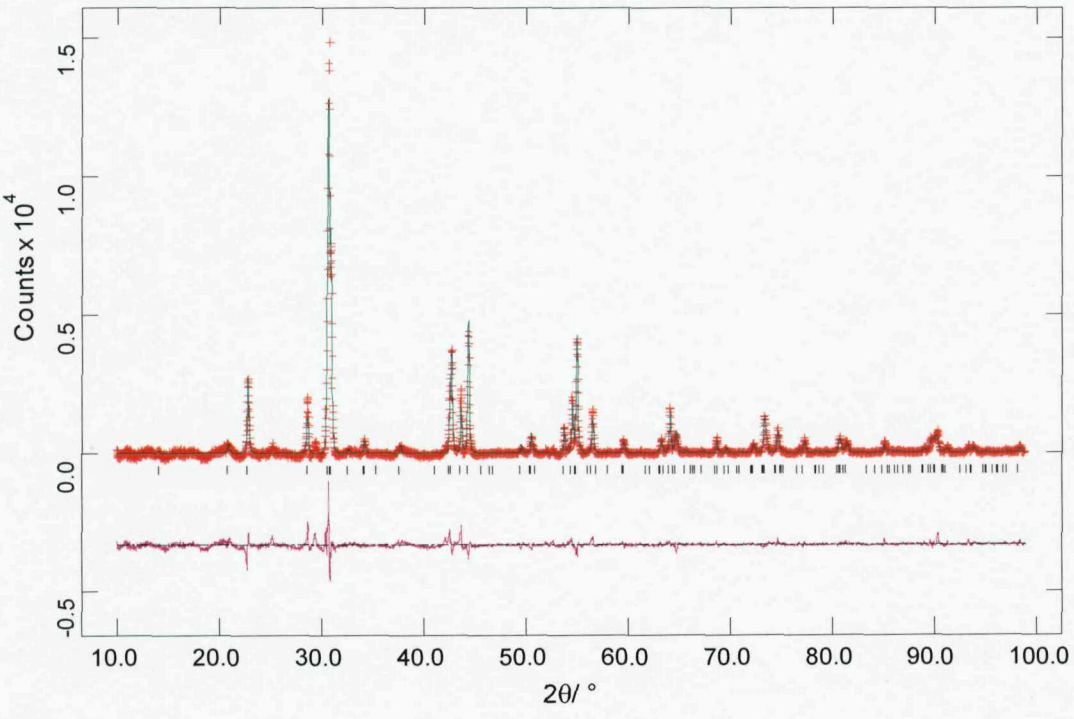

Figure 3 PXD refinement profile fit for orthorhombic $CeSrScO_4$ in the space group A*bma* at room temperature *(crosses indicate observed data, the upper continuous line shows calculated profile, the lower continuous line the difference and tick marks show reflection positions).*

Table 4 Refined atomic positions for $PrSrScO_4$ at room temperature (PXD).

Space group Abma; a = 5.7625(2), b = 5.7339(1) and c = 12.3206(24) Å (e.s.d's in parentheses)

Atom	x	y	z	Occupancy	U_{iso} x 100/Å^2
Pr/Sr	0.0185(4)	0	0.3562(1)	0.5/ 0.5	1.98(8)
Sc	0	0	0	1	1.11(14)
O1	0.25	0.25	0.0198(12)	1	3.27(29)
O2	0.4351(24)	0	0.3358(10)	1	3.27(29)

$\chi^2 = 2.73$, $R_p = 3.46\%$, $R_{wp} = 4.81\%$

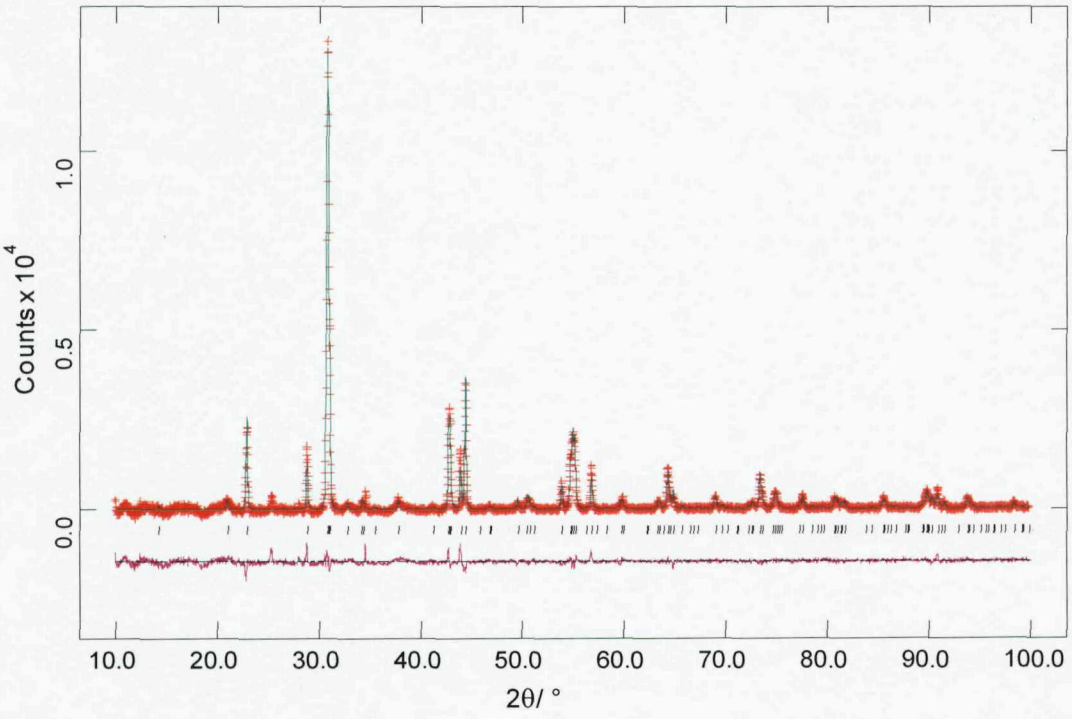

Figure 4 PXD refinement profile fit for orthorhombic $PrSrScO_4$ in the space group A*bma* at room temperature *(crosses indicate observed data, the upper continuous line shows calculated profile, the lower continuous line the difference and tick marks show reflection positions).*

Table 5 Refined atomic positions for $NdSrScO_4$ at room temperature (PXD).

Space group Abma; a = 5.7419(2), b = 5.7008(2) and c = 12.2437(4) Å (e.s.d's in parentheses)

Atom	x	y	z	Occupancy	U_{iso} x 100/Å^2
Nd/Sr	0.0182(4)	0	0.3561(1)	0.5/ 0.5	2.33(5)
Sc	0	0	0	1	0.91(13)
O1	0.25	0.25	0.0177(14)	1	3.54(29)
O2	0.4369(27)	0	0.3240(10)	1	3.54(29)

$\chi^2 = 1.54$, $R_p = 4.12\%$, $R_{wp} = 5.26\%$

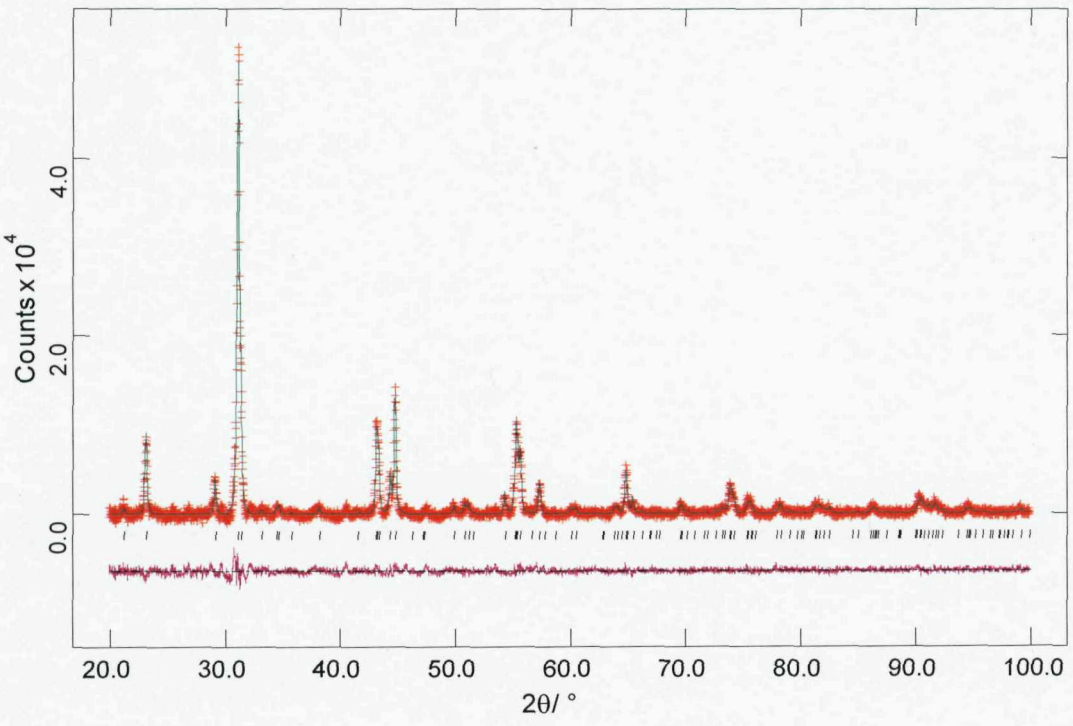

Figure 5 PXD refinement profile fit for orthorhombic $NdSrScO_4$ in the space group A*bma* at room temperature *(crosses indicate observed data, the upper continuous line shows calculated profile, the lower continuous line the difference and tick marks show reflection positions).*

Table 6 Refined atomic positions for $SmSrScO_4$ at room temperature (PXD).
Space group Abma; a = 5.7383(2), b = 5.6994(2) and c = 12.2946(5) Å (e.s.d's in parentheses)

Atom	x	y	z	Occupancy	U_{iso} x 100/Å^2
Sm/Sr	0.0186(5)	0	0.3542(1)	0.5/ 0.5	2.42(8)
Sc	0	0	0	1	1.78(19)
O1	0.25	0.25	0.0252(12)	1	2.3(4)
O2	0.4138(25)	0	0.3357(14)	1	2.3(4)

$\chi^2 = 3.00$, $R_p = 2.83\%$, $R_{wp} = 3.89\%$

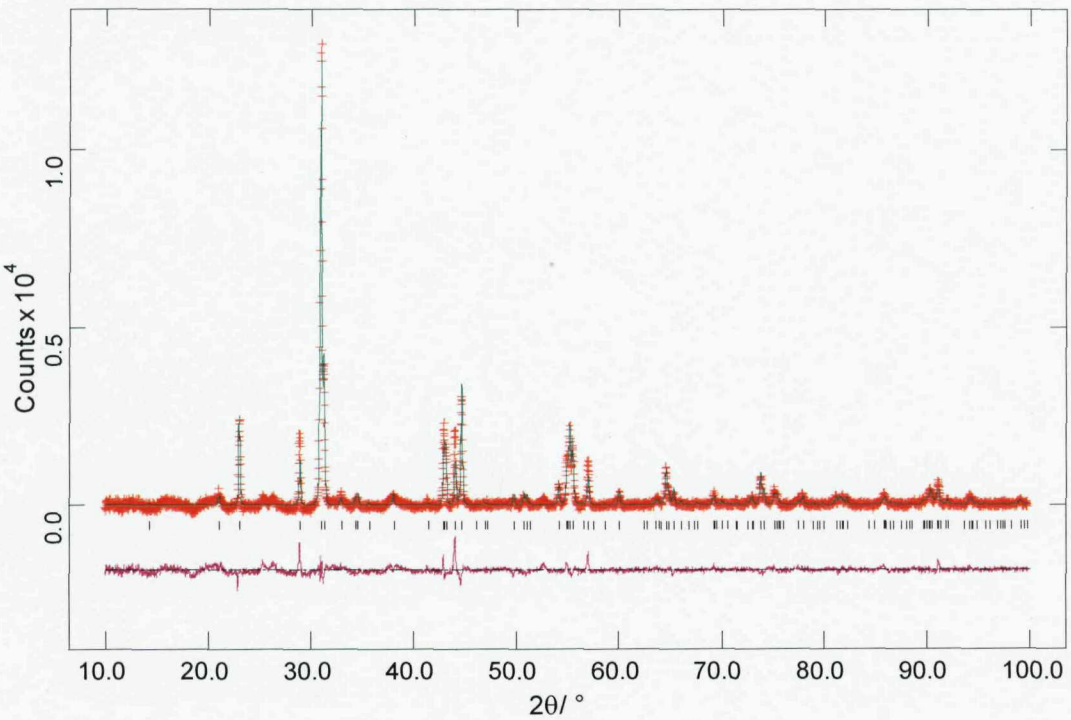

Figure 6 PXD refinement profile fit for orthorhombic $SmSrScO_4$ in the space group *Abma* at room temperature *(crosses indicate observed data, the upper continuous line shows calculated profile, the lower continuous line the difference and tick marks show reflection positions).*

3.2.2.2 Variable Temperature PND Structure Refinement of $LnSrScO_4$ (Ln = La, Pr, and Nd)

In order to determine the exact phase transition and oxygen positions, PND data were collected on selected samples using the high resolution, constant wavelength (λ = 1.909 Å) powder neutron diffractometer D1A at the I.L.L, Grenoble. Approximately 5 g of sample was placed in an 8 mm diameter vanadium can. Data were collected in the temperature range 25 – 1000 °C with a step size 0.1°, over the range 0 – 160° with a collection period of 3 hours.

The PND patterns were analysed using the GSAS suite of programs, and the structural model determined from the PXD refinement (section 3.2.2.1) with Ln^{3+} and Sr^{2+} at half occupancy and Sc^{3+} and O^{2-} at full occupancy. The neutron scattering lengths used were: La = 8.240 , Pr = , Nd = 7.690 , Sr = 7.020, Sc = 12.29 and O = 5.805 fm. Initial stages of the refinement included variation of the background parameters, histogram scale factor, peak shape, lattice parameters and zero point displacement. Isotropic temperature factors and the atom positions were also varied. The thermal parameters of the axial and equatorial oxygen atoms were constrained together.

The final atomic coordinates obtained for $LnSrScO_4$ (Ln = La, Pr and Nd) at room temperature are summarized (Table 7 – 9), the refined structural parameters as a function of temperature are tabulated Table c/ Appendix A. Table d/ Appendix A details the extracted important interatomic distances and bond angles of these compounds as a function of temperature and the final fit to the profile for the room temperature data are shown in Figures 7 – 9. The room temperature model was used to successfully fit the diffraction data obtained from $LaSrScO_4$ at temperatures between 100 and 800 °C; data collected above 800 °C could be fully modelled in the tetragonal space group *I4/mmm* with similar fit factors to the orthorhombic space group A*bma* and therefore refinements were undertaken using this simpler crytallographic description.

A similar analysis was undertaken for $PrSrScO_4$ and $NdSrScO_4$. Initial modelling of the room temperature diffraction data comfirmed that the A*bma* space group was the appropriate choice of space group. For all the phases and all temperatures for which data were collected, structure refinements were completed to convergence to include all profile and positional parameters.

Table 7 Refined atomic positions for $LaSrScO_4$ at room temperature (PND).
Space group Abma; a = 5.7629(4), b = 5.7494(4) and c =12.4833(7) Å (e.s.d's are given in parentheses)

Atom	x	y	z	Occupancy	U_{iso} x 100/Å^2
La/Sr	0.0119(7)	0	0.3562(2)	0.5/ 0.5	0.49(10)
Sc	0	0	0	1	1.28(10)
O1	0.25	0.25	0.0156(5)	1	2.60(12)
O2	0.4405(10)	0	0.3295(5)	1	2.60(12)

$\chi^2 = 11.62$, $R_p = 6.83\%$, $R_{wp} = 9.48\%$

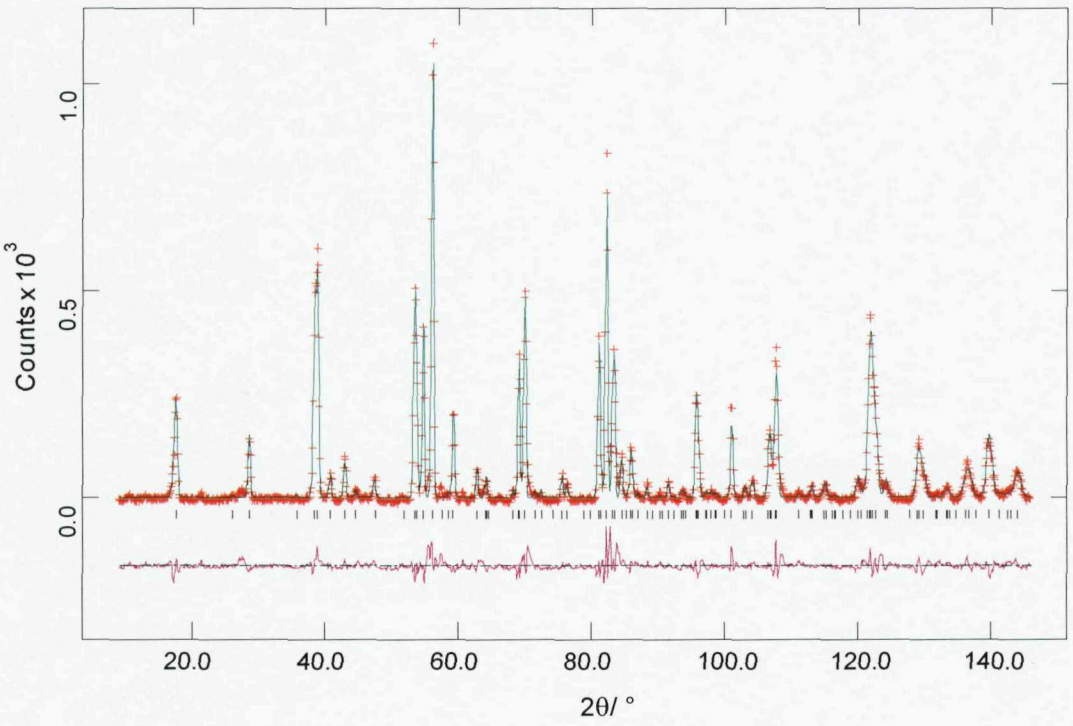

Figure 7 PND refinement profile fit for orthorhombic $LaSrScO_4$ in the space group A*bma* at room temperature *(crosses indicate observed data, the upper continuous line shows calculated profile, the lower continuous line the difference and tick marks show reflection positions).*

Table 8 Refined atomic positions for $PrSrScO_4$ at room temperature (PND).
Space group Abma; a = 5.7648(4), b = 5.7377(4) and c = 12.3377(8) Å (e.s.d's are given in parentheses)

Atom	x	y	z	Occupancy	U_{iso} x 100/Å^2
Pr/Sr	0.0140(13)	0	0.3554(3)	0.5/ 0.5	0.62(16)
Sc	0	0	0	1	1.33(14)
O1	0.25	0.25	0.0176(7)	1	3.37(16)
O2	0.4388(14)	0	0.3251(7)	1	3.37(16)

$\chi^2 = 2.43$, $R_p = 5.21\%$, $R_{wp} = 6.87\%$

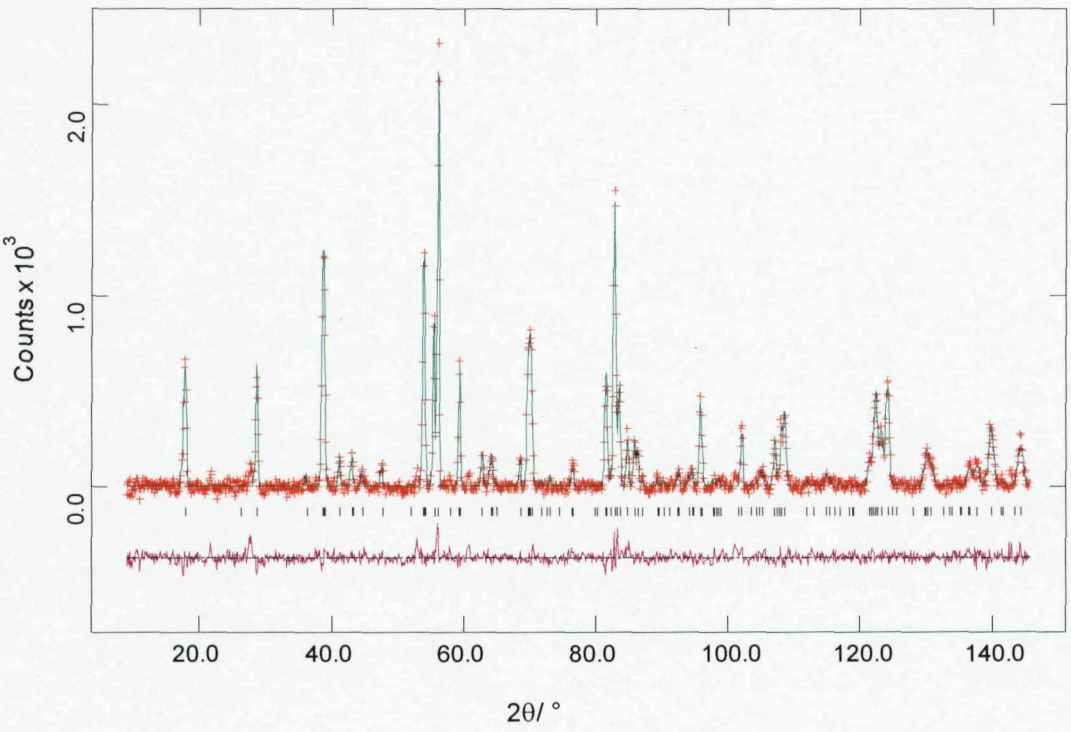

Figure 8 PND refinement profile fit for orthorhombic $PrSrScO_4$ in the space group *Abma* at room temperature *(crosses indicate observed data, the upper continuous line shows calculated profile, the lower continuous line the difference and tick marks show reflection positions).*

Table 9 Refined atomic positions for $NdSrScO_4$ at room temperature (PND).

Space group Abma; a =5.7680(4), b =5.7234(4) and c = 12.2985(7) Å (e.s.d's are given in parentheses)

Atom	x	y	z	Occupancy	U_{iso} x 100/Å^2
Nd/Sr	0.0149(9)	0	0.3561(2)	0.5/ 0.5	0.61(12)
Sc	0	0	0	1	1.28(13)
O1	0.25	0.25	0.0183(6)	1	3.74(14)
O2	0.4364(13)	0	0.3257(7)	1	3.74(14)

χ^2= 5.41, R_p = 6.10%, R_{wp} = 8.13%

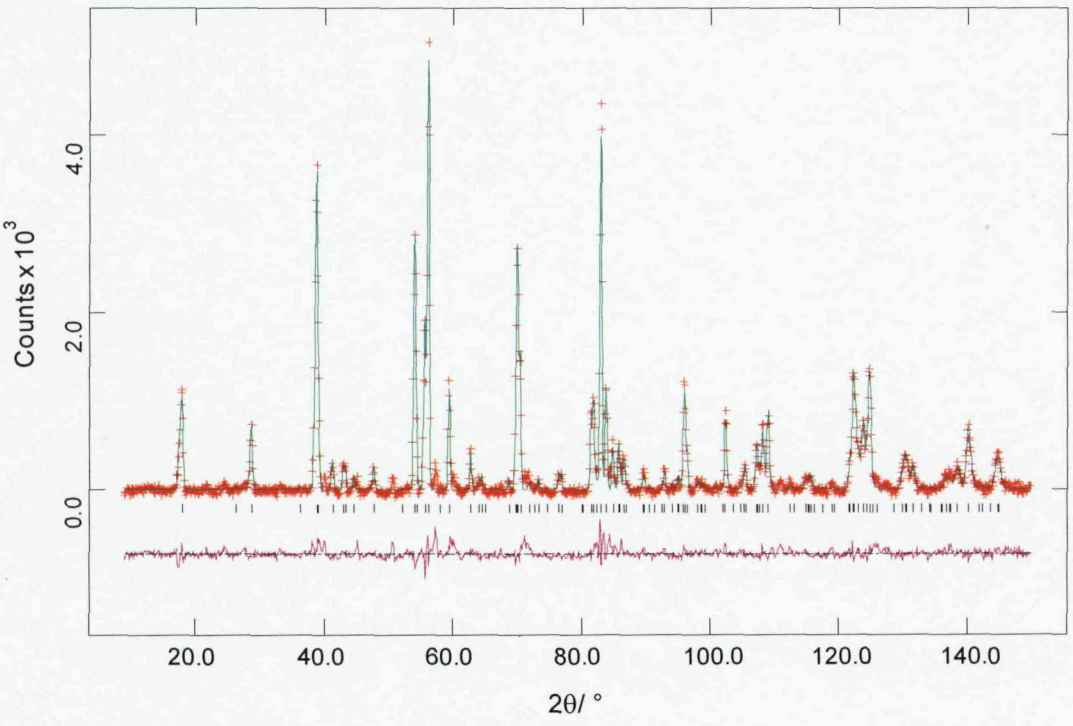

Figure 9 PND refinement profile fit for orthorhombic $NdSrScO_4$ in the space group A*bma* at room temperature *(crosses indicate observed data, the upper continuous line shows calculated profile, the lower continuous line the difference and tick marks show reflection positions).*

3.2.3 Discussion

Analysis of the variable temperature data obtained *via* both PXD and PND allowed elucidation of the structural distortion as a function of temperature for the $LnSrScO_4$ (Ln = La, Ce, Pr, Nd and Sm) systems. The orthorhombic nature of the crystal distortion in these compounds at room temperature results from the tilting of the ScO_6 octahedra within the perovskite layer; Figure 10 displays a polyhedral representation of the structure adopted by $LaSrScO_4$ at room temperature. This behaviour mirrors that reported for $LaSrScO_4$ by Kim *et al.*[15]

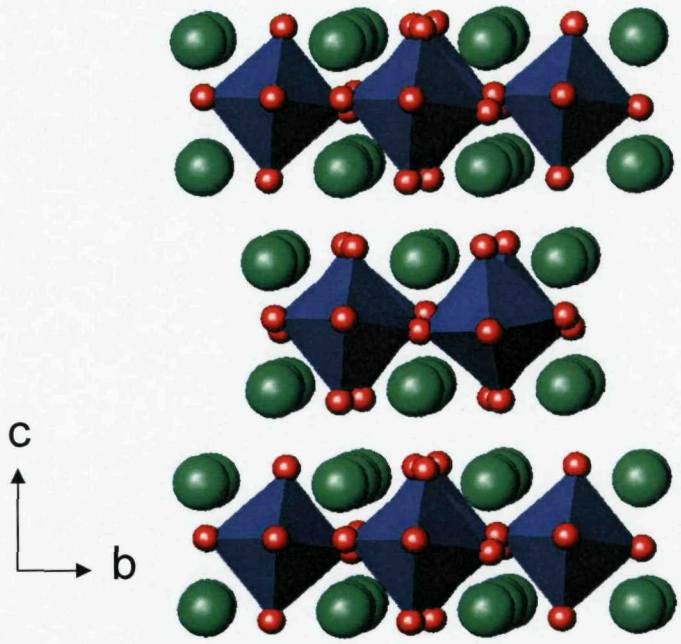

Figure 10 Polyhedral representation of $LaSrScO_4$ at room temperature (*La in green, ScO_6 octahedra in blue and O in red*).

Graphs of the *a* and *b* lattice parameters (converted to a pseudo-orthorhombic description for the highest temperatures) as a function of temperature for $LaSrScO_4$ (Figure 11) and temperature against *b/a* ratio for $LnSrScO_4$ (Ln = La, Ce, Pr, Nd and Sm) (Figure 12) obtained from PXD data have been plotted. It can be seen that in all compounds the level of distortion increases in the temperature range 25 - 300 °C

and then decreases in the temperature range 300 – 1200 °C; for $LaSrScO_4$ and $PrSrScO_4$ the compounds convert to the ideal K_2NiF_4-type structure at approximately 900 and 1100 °C respectively.

Similar graphs using data obtained from PND have also been plotted for $LnSrScO_4$ (Ln = La, Pr and Nd), (Figure 11 and 12), the data mimics that obtained from PXD reconfirming the trends and conclusions drawn from the PXD data. Due to time constraints and limited resources we were unable to obtain data sets for $LaSrScO_4$ and $NdSrScO_4$ at 300 °C and above 1000 °C for $PrSrScO_4$. However, PND data obtained for $PrSrScO_4$ shows that the level of distortion increases in the temperature range 25 – 300 °C and then decreases in the temperature range 300 – 1000 °C.

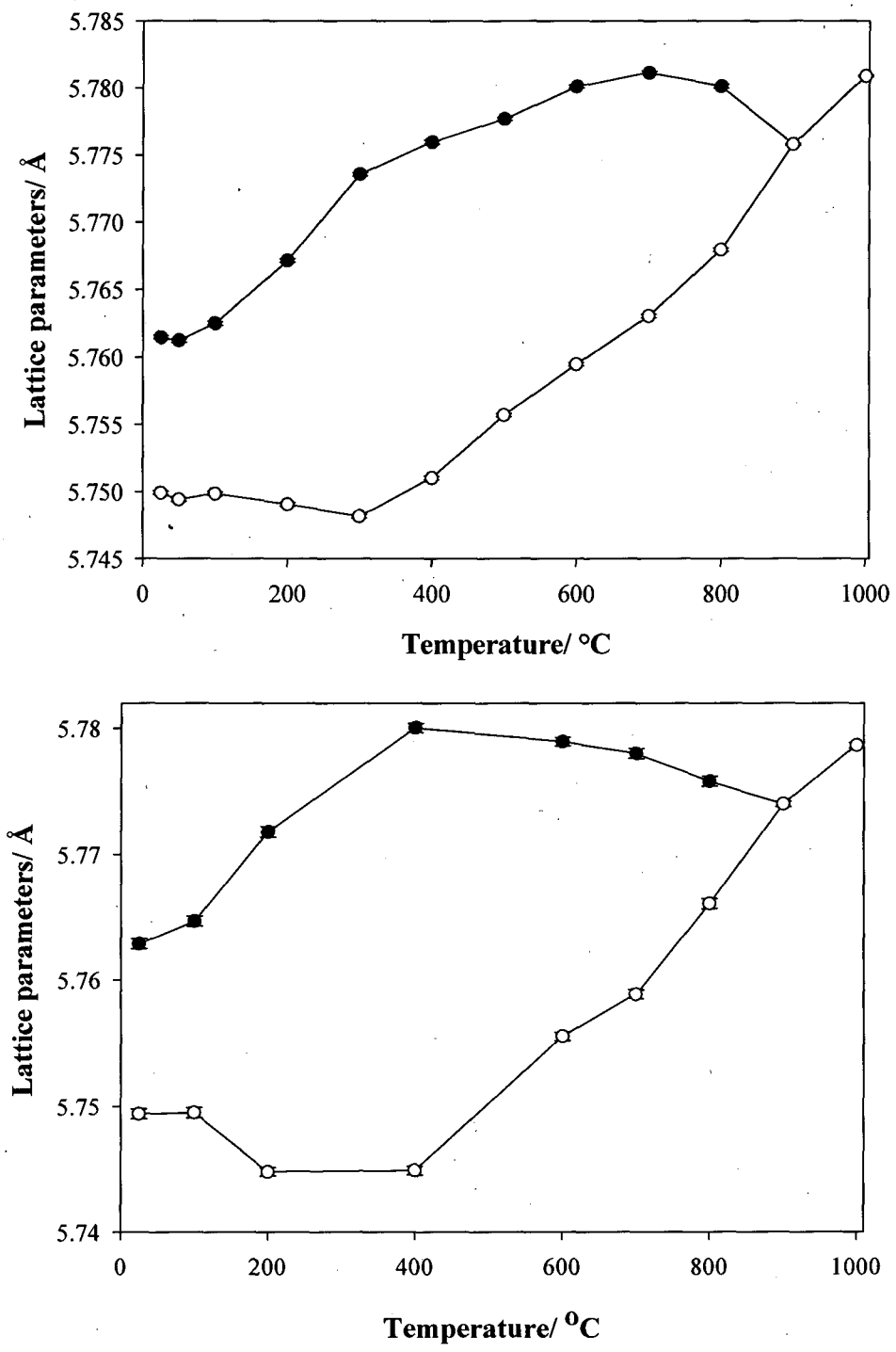

Figure 11 *a* and *b* lattice parameters as a function of temperature for $LaSrScO_4$ as extracted from PXD (top) and PND (bottom) data ; •(a parameter), ○ (b parameter)

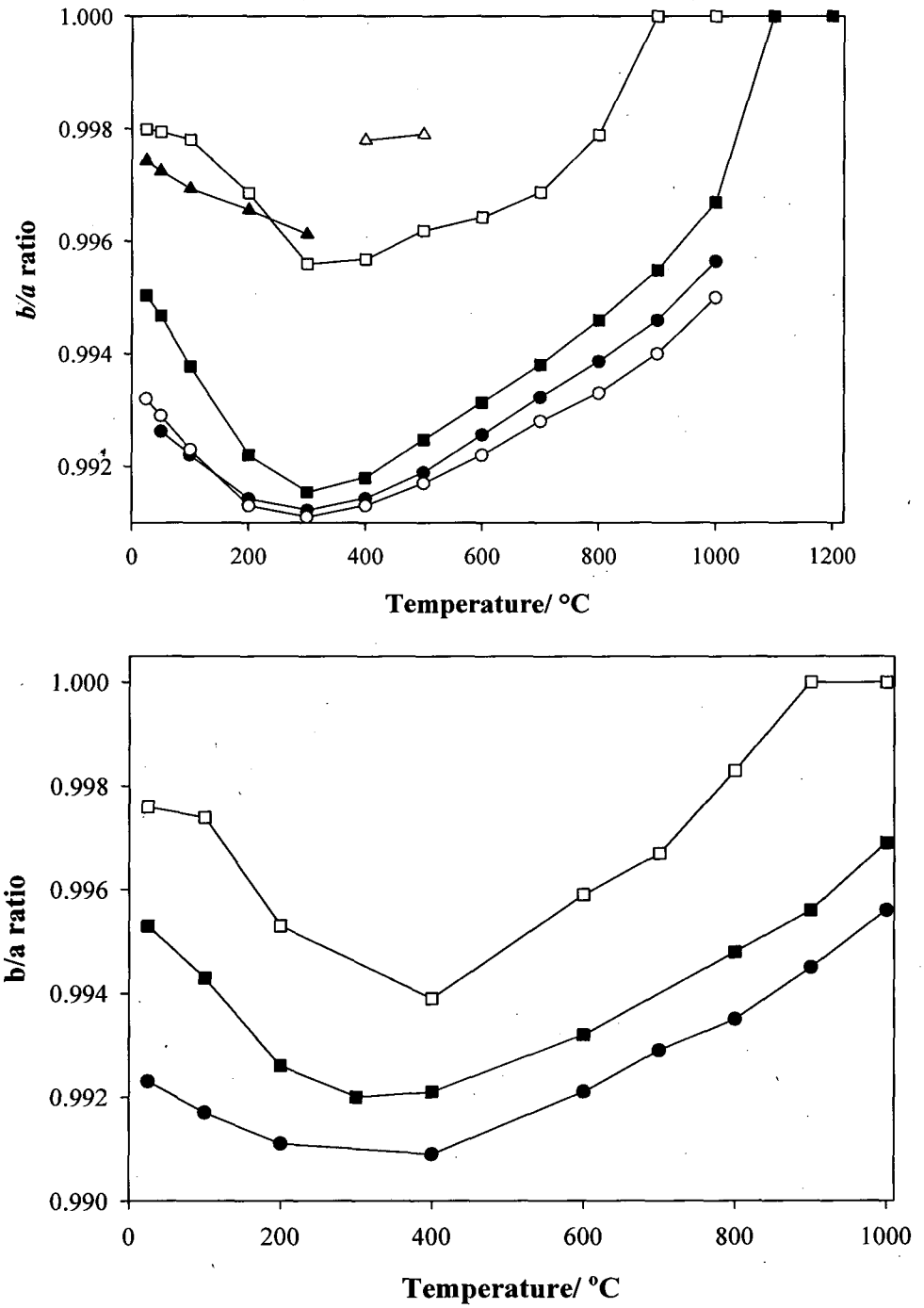

Figure 12 Temperature dependence of the *b/a* lattice parameter ratio for $LnSrScO_4$ as extracted from PXD (top) and PND (bottom) data; □ ($LaSrScO_4$), ▲ ($CeSrScO_4$), Δ (part oxidised $CeSrScO_4$ sample), ■ ($PrSrScO_4$), ● ($NdSrScO_4$), ○ ($SmSrScO_4$).

Octahedral tilting in the A*bma* space group causes the coordination sphere about the Ln^{3+} cation to change dramatically in comparison with the Ln^{3+} coordination sphere in the I*4/mmm* space group; the coordination sphere around the Sc^{3+} is left virtually unchanged. Therefore it is logical to assume that the octahedral tilting is driven by the need to optimise the anion coordination about the A site and particularly the Ln^{3+} cation. The Sc-O-Sc bond angles, which connect the ScO_6 octahedra and provide a measure of the tilting are 169.1(6), 170.6(10), 166.0(8), 167.3(9) and 162.8(9)° for $LaSrScO_4$, $CeSrScO_4$, $PrSrScO_4$, $NdSrScO_4$ and $SmSrScO_4$ respectively in the room temperature PXD structures. This shows a general trend towards an increased tilt of the octahedra as the average ionic radius of the A site cations decreases. In tetragonal K_2NiF_4-type A_2BO_4 oxides, the BO_6 octahedra of the perovskite layer connect with each other at an angle of 180°.

Figure 13 shows the coordination environment of the La^{3+}/Sr^{2+} sites at room temperature and at 1000 °C in $LaSrScO_4$. The effect of the tilting of the octahedra can clearly be seen and the effect is most apparent in the coordination environment of the A site cation. The K_2NiF_4 structure adopted at the highest temperature produces the more regular 1 + 4 + 4 environment for (La,Sr) site with one very short contact (2.35 Å) and 8 further contacts in the range 2.7 - 3.0 Å. The effect of the octahedral tilting at room temperature is to markedly lengthen one of these contacts while shortening the remainder producing an effectively 8 coordinate site. In general, the level of tilting and the asymmetry in the Ln/Sr-O coordination environment increases as the lanthanide cation size decreases. This behavior mirrors that found in many lanthanide compounds with a tendency to move to lower coordination numbers but with shorter contacts as the size of the lanthanide decreases.

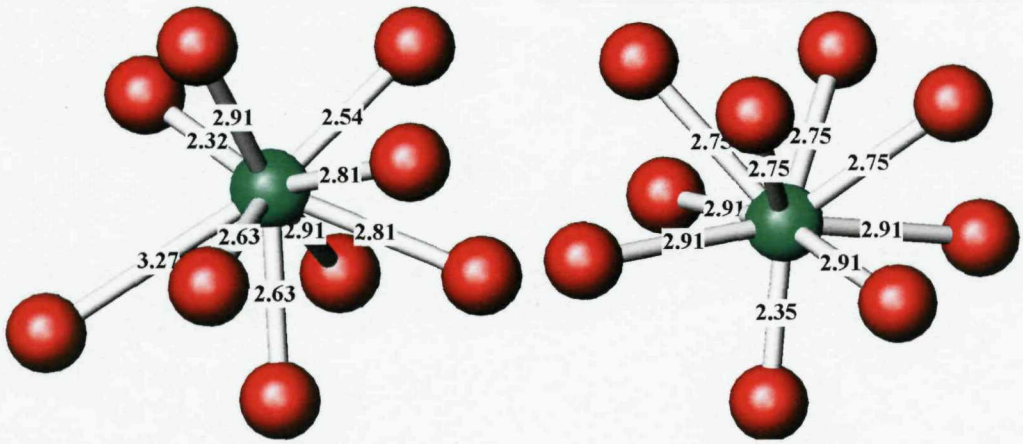

Figure 13 Coordination environment about La^{3+} in $LaSrScO_4$ at room temperature (left) and at 1000 °C (right). Ln/Sr-O bond distances extracted from PND data are labelled.

The variable temperature PXD data show that for all compounds $LnSrScO_4$ (Ln = La-Sm) the degree of octahedral tilt increases on heating to ~ 300 °C before decreasing; for the compounds with the larger lanthanides, Ln = La and Pr this angle reaches 180 °C and the materials become tetragonal. Extrapolation of the data from Ln = Nd and Sm indicate that a similar phase transition would occur for these materials but only at temperatures close to those at which they were synthesised. The origin of this behavior may derive from the competing factors associated with the thermal expansion of different structural elements of the materials. Between room temperature and 300 °C this thermal expansion is accommodated in an increased tilting of the octahedra which allows lengthening of the Sc-O distances; the short Ln-O interactions also increase in length while the longer Ln-O distances decrease as the overall Ln-O coordination geometry becomes more regular.

3.3 The $LnSrInO_4$ (Ln = La and Pr) Phases

3.3.1 Synthesis

The $LnSrInO_4$ (Ln = La and Pr) compounds were synthesised by the direct reaction of stoichiometric amounts of La_2O_3 (99.99%, Aldrich)), Pr_6O_{11} (99.99%, Aldrich), $SrCO_3$ (99.9+%, Aldrich) and In_2O_3 (99.9%, Avocado). The lanthanide oxides were dried in air at 800 °C for 24 hours prior to use. The starting materials were intimately ground as a suspension in ethanol in an agate pestle and mortar. The ethanol was subsequently evaporated. The mixed powders were pressed into pellets of 10 mm diameter and 3 mm thickness under 10 tonnes of pressure and these were then fired at 1200 °C for 48 hours. Samples were cooled, ground, reformed into pellets and heated again in air at 1350 °C for 48 hours and the products quenched to room temperature to obtain a single phase product.

3.3.2 Structural Characterisation

3.3.2.1 Variable Temperature PXD Structure Refinement of $LnSrInO_4$

Variable temperature PXD data were collected on $LaSrInO_4$ in the temperature range 50 – 1000 °C. In order to determine the correct structural description for $LaSrInO_4$ a similar refinement process as for $LaSrScO_4$ was undertaken. Initial detailed analysis centred on the 50 °C data set from $LaSrInO_4$. Rietveld[16,17] refinement using the GSAS[18] suite of programmes and PXD data obtained for $LaSrInO_4$ were performed in the different space groups accommodating various octahedral tilts as proposed by Hatch and Stokes.[13] For each structural description the appropriate model was set-up within GSAS and identical numbers of profile parameters refined; the number of atomic positional parameters, which were varied as a function of the structural model are included in Table 10. Table 10 also summarises the degree of success achieved in fitting each of these structural models to the data obtained.

Table 10 Refined lattice parameters and final fit parameters for 50 °C $LaSrInO_4$ PXD data in space groups accommodating different octahedral tilts (*e.s.d's are given in parentheses*).

Space Group	Latice Parameters/ Å			χ^2	R_{wp} (%)	Rp (%)	No. of atomic positional parameters varied
	a	*b*	*c*				
Abma	5.8788(2)	5.8233(2)	12.5729(4)	6.59	8.28	5.62	5
Pbca	12.5731(3)	5.8788(1)	5.8233(1)	4.64	6.94	4.91	9
Pccn	5.8787(2)	5.8231(2)	12.5727(4)	6.13	7.98	5.38	8
Fmmm	5.8788(2)	5.8230(2)	12.5729(6)	10.57	10.49	6.58	2
Fmmm2	5.8790(2)	5.8232(2)	12.5731(5)	7.71	8.96	5.92	6

The space group that models the data better than the others was found to be P*bca* producing the best refinement statistics. This also corresponds to the model used by Kato *et al.*[14] Table 11 describes the refined atomic parameters for $LaSrInO_4$ at 50 °C. As with the I*4/mmm* crystal structure description for the K_2NiF_4 phases, the B-type / In^{3+} ions occupy sites with a distorted octahedral coordination to oxygen and the Sr^{2+} and Ln^{3+} ions occupy sites having a coordination number of 9, though variation in bond lengths to oxygen are much larger than for the regular tetragonal K_2NiF_4 structure. Final stages of the refinements of the structure in the P*bca* description included all global parameters, i.e. histogram scale factor, peak shape, zero point displacement, background parameters and lattice constants; isotropic temperature factors and the atom positions were also varied. As expected for X-ray data, the U_{iso} on the oxygen atoms were high and as a result the thermal parameters of the axial and equatorial oxygen atoms were constrained together. Figure 14 shows the results of the structural refinement in terms of the profile fit achieved for the data collected from $LaSrInO_4$ at 50 °C.

Figure 15 shows the variable temperature data obtained for $LaSrInO_4$. All variable temperature PXD data collected were modelled in the space group P*bca* and the refined atomic positions and selected bond distances are tabulated (Table e, f and g/

Appendix A). It is however apparent that the P*bca* space group is a poor model for the PXD data sets in the temperature regime 300 – 600 °C, producing negative thermal parameters for the *O1* and *O2* atoms. The structure is the most deformed at 300 °C, therefore the poor model in this range may be a result of the space group no longer being able to accommodate the increased distortion as measured by *c/b*. The poor model may also account for no diffraction intensity observed at the calculated reflection positions that are allowed and unique to the P*bca* description in the PXD data, these reflections are however observed in the PND data. Figure 16 focuses into the region 1 – 4 Å in both the PXD and PND profile fits for $LaSrInO_4$ at 50 °C and 25 °C respectively. It is also apparent from the thermodiffractogram that at 300 °C an intensity grows in at $2\theta = 35°$.

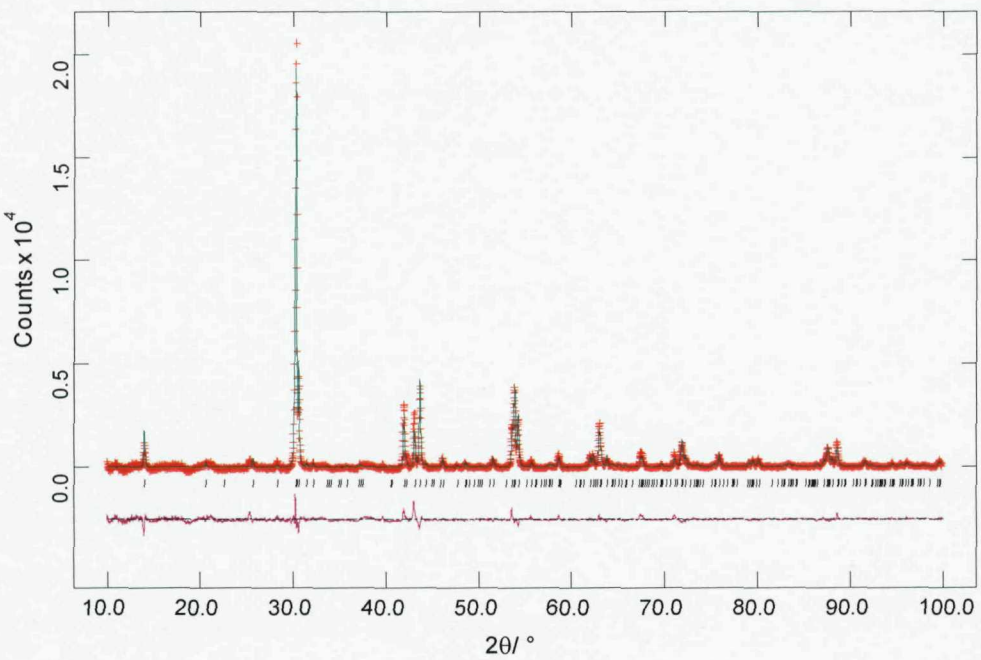

Figure 14 PXD refinement profile fit for orthorhombic $LaSrInO_4$ in the space group P*bca* at 50 °C *(crosses indicate observed data, the upper continuous line shows calculated profile, the lower continuous line the difference and tick marks show reflection positions).*

Table 11 Refined atomic positions for $LaSrInO_4$ at 50 °C (PXD).

Space group Pbca; a = 12.5731(3), **12.5806(8)**; *b* = 5.8788(15), **5.8332(4)**; *c* = 5.8233(1), **5.8332(4)** *Å (e.s.d's are given in parentheses and Kato et al parameters for* $La_{0.8}Sr_{1.2}InO_{3.9}$ *at room temperature are highlighted for comparison)*

Atom	x	y	z	Occupancy	U_{iso} x 100/Å^2
La/ Sr	0.1451(1)	-0.0179(5)	-0.0277(3)	0.5/ 0.5	1.53(8)
	0.1443(1)	**-0.005(1)**	**-0.0043**	**0.4/ 0.6**	**0.59(6)**
In	0.5	0	0	1	0.41(8)
					0.59(7)
O1	0.0146(18)	0.2315(94)	0.2360(9)	1	2.8(4)
	0.032(1)	**0.233(7)**	**0.250(15)**	**0.975**	**1.62***
O2	0.3186(15)	0.0854(27)	0.0200(4)	1	2.8(4)
	0.323(1)	**0.057(4)**	**0.074(4)**	**0.975**	**1.6(7)**

* Uiso x 100/ Å^2 for the O1 site was fixed at the final cycle of refinement.

χ^2 = 4.60, R_p = 4.91%, R_{wp} = 6.94%

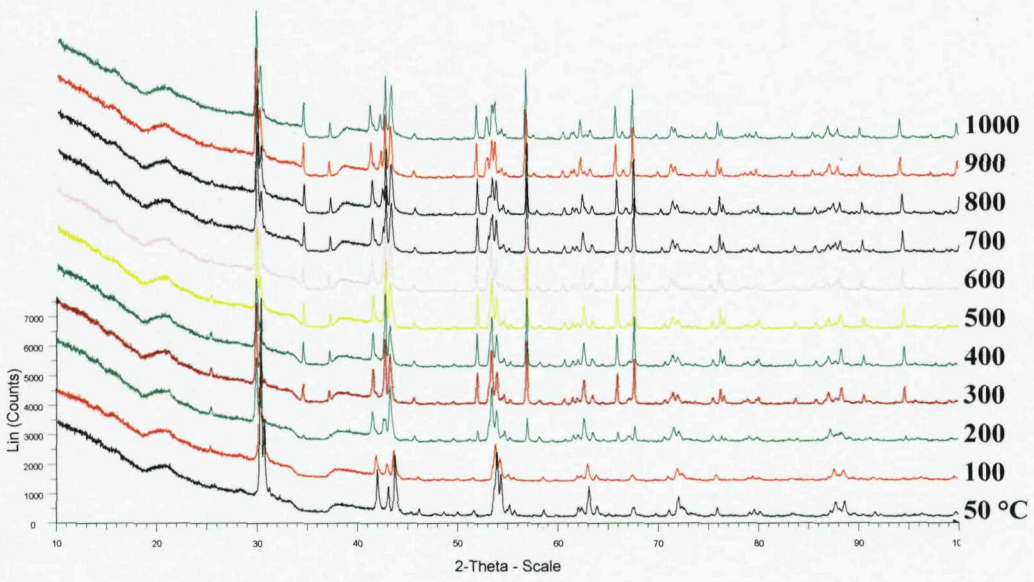

Figure 15 Variable temperature PXD data obtained $LaSrInO_4$.

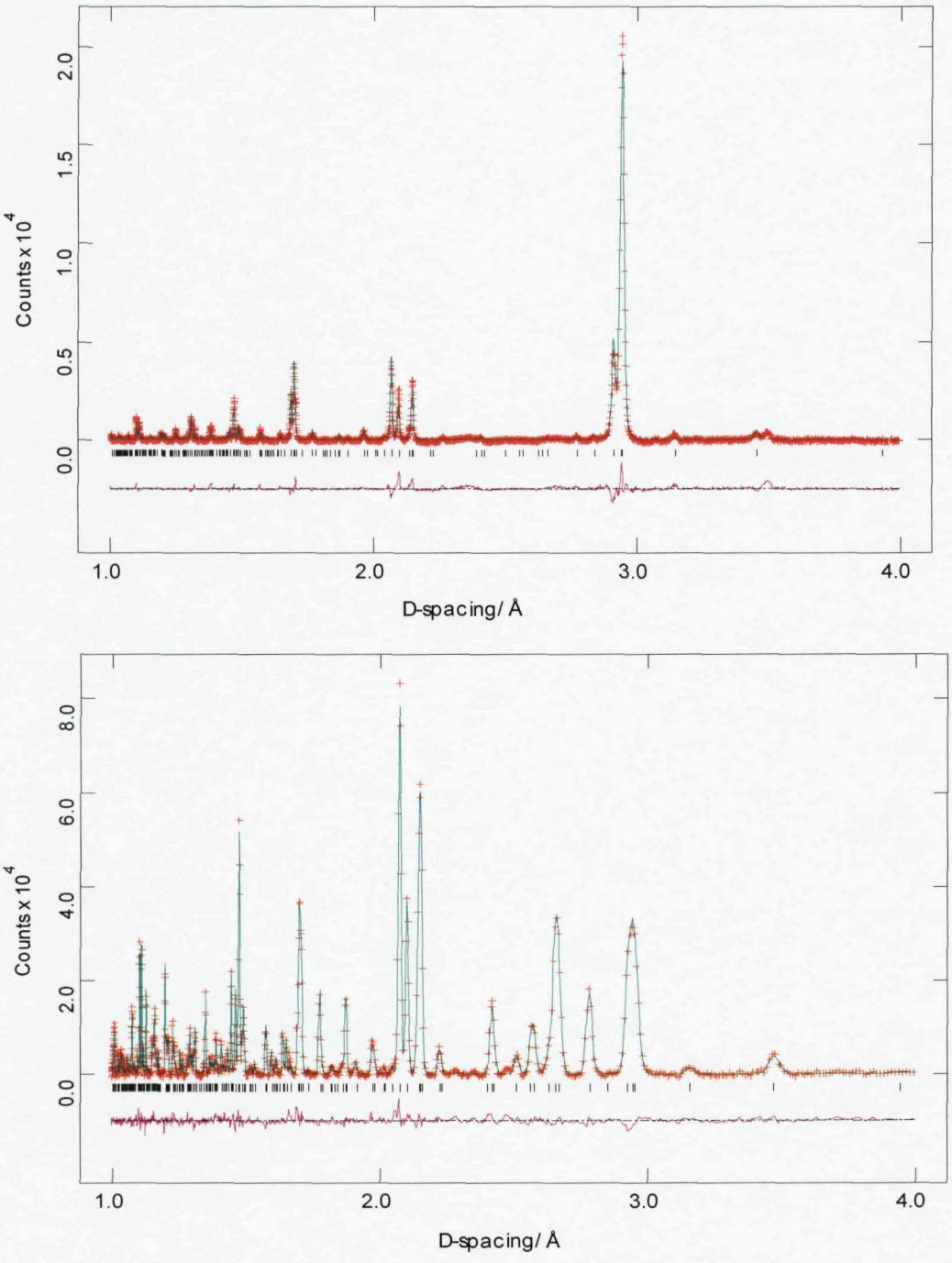

Figure 16 PXD (top) and PND (bottom) profile fits for $LaSrInO_4$ at 50 and 25 °C respectively in the region 1 – 4 Å *(crosses indicate observed data, the upper continuous line shows calculated profile, the lower continuous line the difference and tick marks show reflection positions).*

An even greater A:B cation mismatch was introduced by replacing La^{3+} (1.216 Å) for Pr^{3+} (1.179 Å). Variable temperature PXD data for $PrSrInO_4$ were collected in the temperature range 25 – 1000 °C (Figure 17). Initial Rietveld analysis centred on modelling the 25 °C data set in the P*bca* space group. In order to correctly determine the exact structure adopted for $PrSrInO_4$ a similar initial profile fitting process as for $LaSrInO_4$ was undertaken. Rietveld refinements were performed in the different space groups accommodating various octahedral tilts. For each structural description the appropriate model was set-up within GSAS and identical numbers of profile parameters refined. The number of atomic positional parameters, which were varied as a function of the structural model are included in Table 12. Table 12 also summarises the degree of success achieved in fitting each of these structural models to the data obtained, the thermal parameters for all atoms in each space group are also included.

Taking into account the results obtained from the structural refinements the space groups that model the data better than the others are A*bma*, P*bca* and F*mmm*, of which F*mmm* requires the least positional parameters. When comparing the refinement profile fits for these space groups (Figure 18) it is clear that unlike the P*bca* model the F*mmm* and A*bma* models do not take into account all diffraction intensity present in the PXD pattern. Based on this, the better refinement statistics and atomic temperature factors it would be logical to assume that the P*bca* space group is the correct model. The final refined parameters have been tabulated (Table 13) and the final profile fit is displayed in Figure 19. Refinement of the 50 - 300 °C variable temperature PXD data was attempted in the P*bca* space group. The 50 and 100 °C data were modelled well in the P*bca* space group, however above 100 °C the data can no longer be refined with this model. The exact structure solution of $PrSrInO_4$ as a function of temperature will remain unsolved until PND data are acquired, and further structural work is undertaken.

Table 12 Refined lattice parameters and final fit parameters for 25 °C $PrSrInO_4$ PXD data in space groups accommodating different octahedral tilts *(e.s.d's are in parentheses).*

Space Group	Latice Parameters/ Å			Pr/Sr Ui/Ue x100 Å^2	In Ui/Ue x100 Å^2	O* Ui/Ue x100 Å^2	χ^2	R_{wp} (%)	Rp (%)	No. of atomic positional parameters varied
	a	*b*	*c*							
A*bma*	5.8806(4)	5.8333(4)	12.4361(9)	0.88(19)	0.54(20)	5.7(11)	4.74	7.81	5.23	5
P*bca*	12.4395(7)	5.8832(4)	5.8343(3)	0.43(15)	0.42(16)	3.1(14)	4.36	7.49	5.53	9
P*ccn*	5.881(4)	5.8345(4)	12.4347(10)	1.62(22)	0.53(21)	-5.0(5)	4.68	7.75	5.17	8
F*mmm*	5.8943(4)	5.8404(4)	12.4554(5)	1.42(23)	0.64(26)	5.7(10)	5.98	8.77	5.82	2

O* = All O atoms constrained

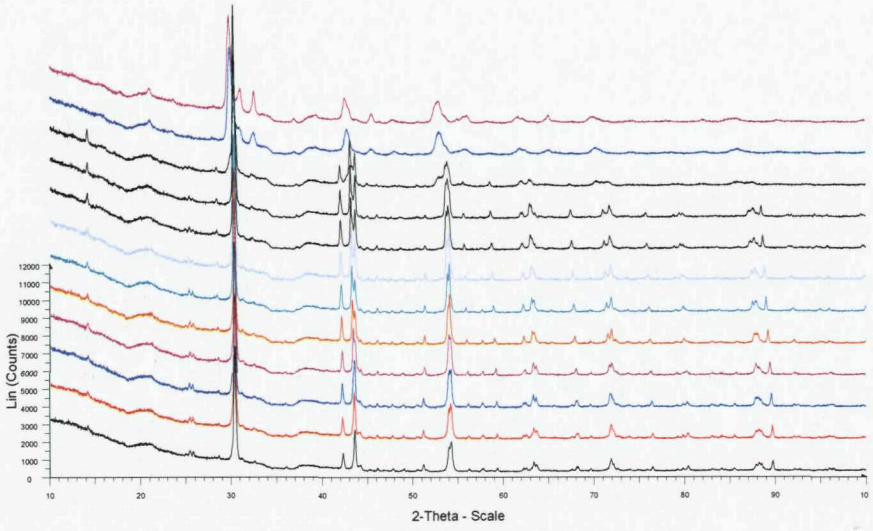

Figure 17 Variable temperature PXD data obtained for $PrSrInO_4$.

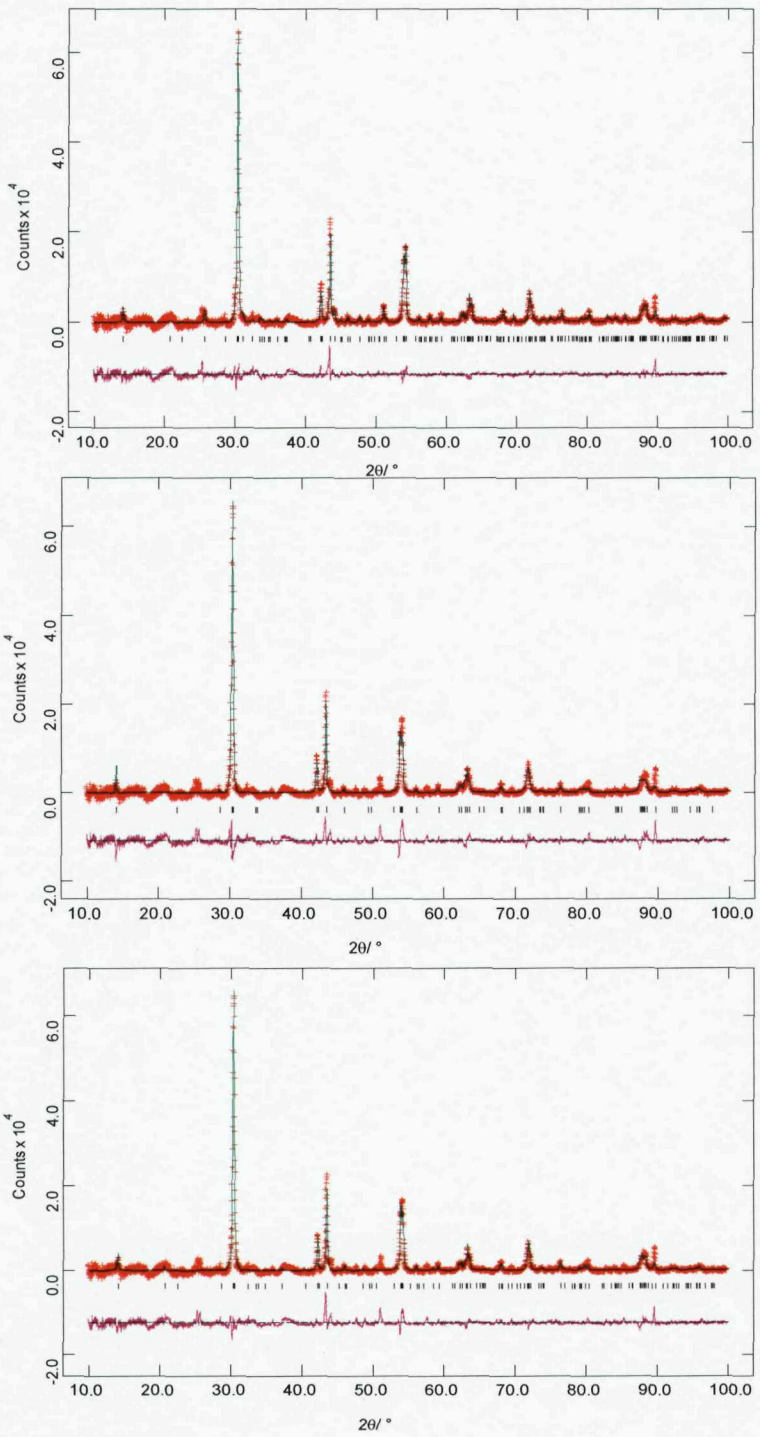

Figure 18 PXD refinement profile fit for orthorhombic $PrSrInO_4$ in the space group P*bca* (top), F*mmm* (middle) and A*bma* (bottom) at 25 °C *(crosses indicate observed data, the upper continuous line shows calculated profile, the lower continuous line the difference and tick marks show reflection positions).*

Table 13 Refined atomic positions for $PrSrInO_4$ at 25 °C (PXD).

Space group Pbca; a = 12.4395(7), b =5.8832(4) and c = 5.8343(4) Å (e.s.d's are given in parentheses)

Atom	x	y	z	Occupancy	U_{iso} x 100/Å^2
Pr/Sr	0.1458(2)	-0.0134(11)	-0.0408(6)	0.5/ 0.5	0.43(15)
In	0.5	0	0	1	0.42(17)
O1	0.010(5)	0.253(12)	0.206(13)	1	3.1(14)
O2	0.305(5)	0.351(11)	0.0274(9)	1	3.1(14)

$\chi^2 = 4.3$, $R_p = 5.53\%$, $R_{wp} = 7.49\%$

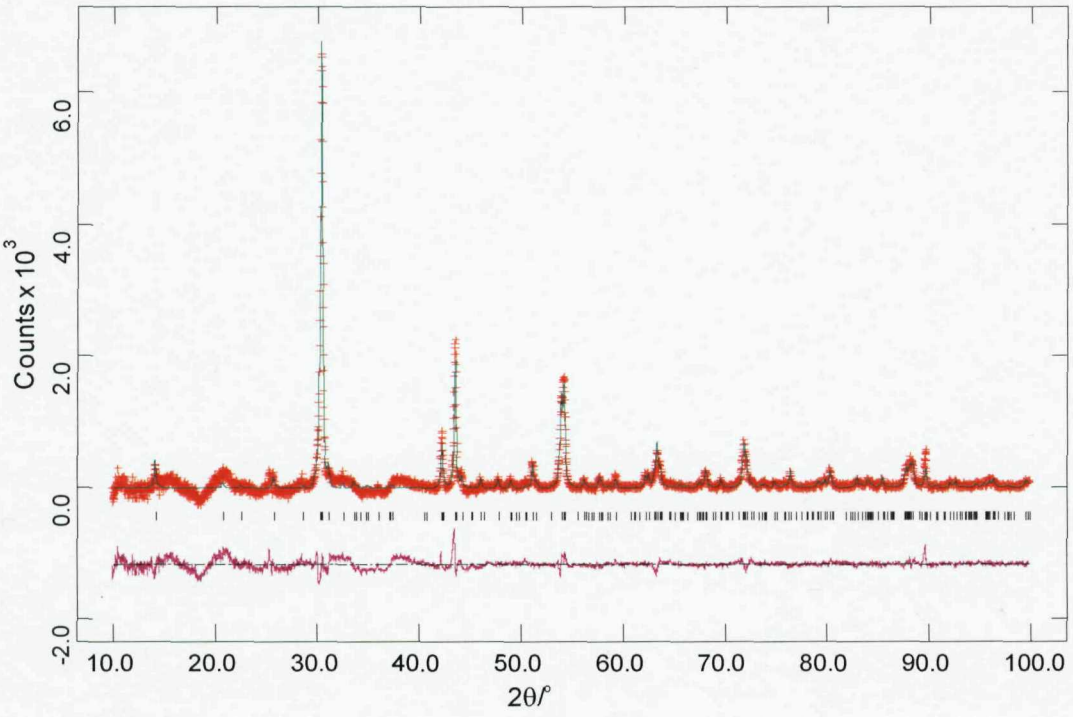

Figure 19 PXD refinement profile fit for orthorhombic $PrSrInO_4$ in the space group P*bca* at 25 °C *(crosses indicate observed data, the upper continuous line shows calculated profile, the lower continuous line the difference and tick marks show reflection positions).*

3.3.2.2 PND Structure Refinement of $LaSrInO_4$

In order to determine the exact structure, space group and oxygen positions adopted by $LaSrInO_4$, room temperature PND data were collected on the high resolution, constant wavelength (λ = 1.909 Å) powder neutron diffractometer D1A at the I.L.L, Grenoble. Approximately 5 g of sample was placed in an 8 mm diameter vanadium can. The powder pattern was collected at steps of $2\theta = 0.1°$, over the range 0 – 160° with a collection period of 3 hours. The structural parameters from the X-ray refinement were used as the starting model. The neutron scattering lengths used were La = 8.240 , Sr = 7.020, In = 4.07 and O = 5.803 fm. Lattice parameters and the background function were the first variables to be introduced. Then a peak shape function was included. Once these were stable the atomic positions and thermal parameters were included in the refinement; Table 14 summarises the refined lattice parameters, atomic positions and final fit parameters. Figure 20 shows the results of the structural refinement in terms of the profile fit achieved for the data collected from $LaSrInO_4$ at room temperature.

Table 14 Refined atomic positions for $LaSrInO_4$ at room temperature (PND).
Space group Pbca; a = 12.6002(5), b =5.8797(3) and c = 5.8435(3) Å (e.s.d's are given in parentheses)

Atom	x	y	z	Occupancy	U_{iso} x 100/Å^2
La/Sr	0.1455 (1)	-0.0134(3)	-0.0309(4)	0.5/ 0.5	1.06(5)
Sc	0.5	0	0	1	0.33(11)
O1	0.0262(2)	0.2156(5)	0.2126(5)	1	1.67(6)
O2	0.3268(2)	0.0769(5)	0.0269(5)	1	1.67(6)

$\chi^2 = 2.34$, $R_p = 5.65\%$, $R_{wp} = 7.34\%$

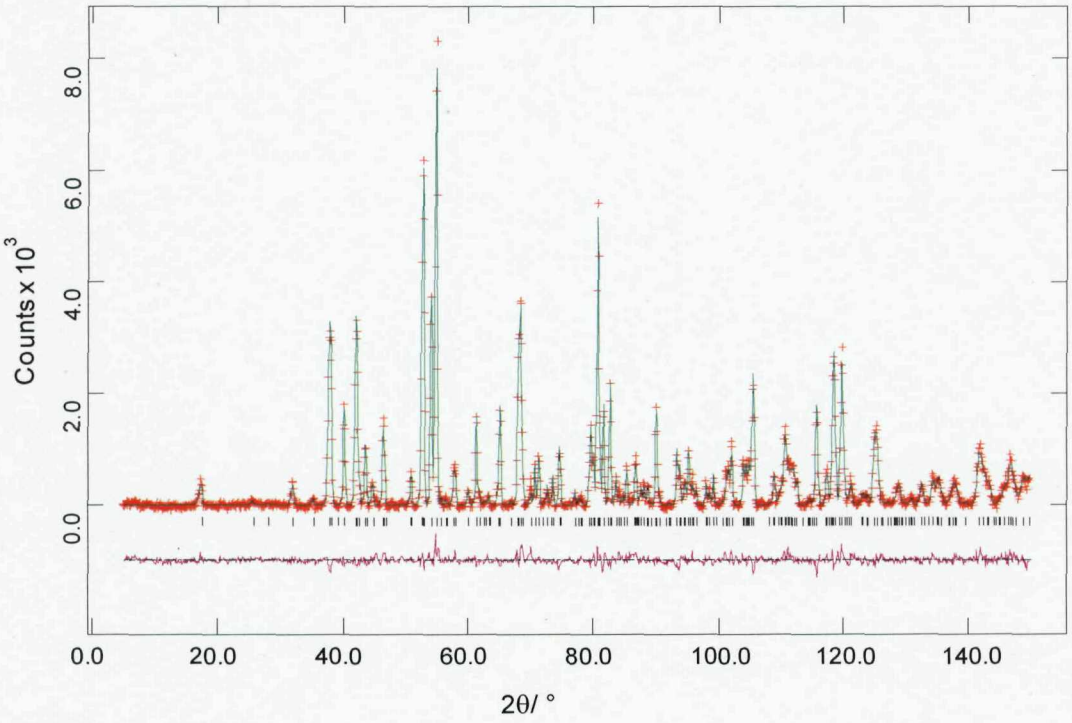

Figure 20 PND refinement profile fit for orthorhombic $LaSrInO_4$ in the space group P*bca* at room temperature *(crosses indicate observed data, the upper continuous line shows calculated profile, the lower continuous line the difference and tick marks show reflection positions).*

3.3.3 Discussion

Analysis of the variable temperature data obtained *via* PXD allowed elucidation of the structural distortion as a function of temperature for $LaSrInO_4$. The variable temperature PXD data obtained for $LaSrInO_4$ in the temperature range 50 – 1000 °C have been described in the space group P*bca*. Rietveld refinement of PND data collected for $LaSrInO_4$ at 25 °C further confirms that the compound does in fact adopt the P*bca* space group. Figure 21 displays a polyhedral representation of the structure adopted by $LaSrInO_4$ at room temperature, the structure was plotted using PND data.

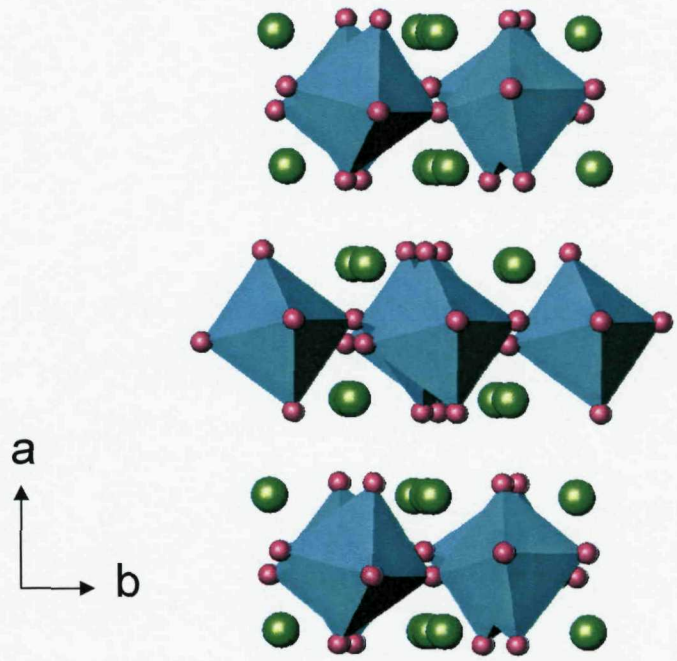

Figure 21 Polyhedral representation of $LaSrInO_4$ at room temperature (*La in green, InO_6 octahedra in light blue and O in purple*).

Graphs of the *b* and *c* lattice parameters as a function of temperature for $LaSrInO_4$ (Figure 22) and temperature against *c/b* ratio for $LaSrInO_4$ and $LaSrScO_4$ (Figure 23) obtained from PXD data have been plotted. Similarly to the $LnSrScO_4$ systems,

it can be seen that the level of distortion of these compound increases on heating to ~ 300 °C before decreasing. Unlike $LaSrScO_4$, $LaSrInO_4$ does not revert to the ideal K_2NiF_4-type structure in the temperature range studied.

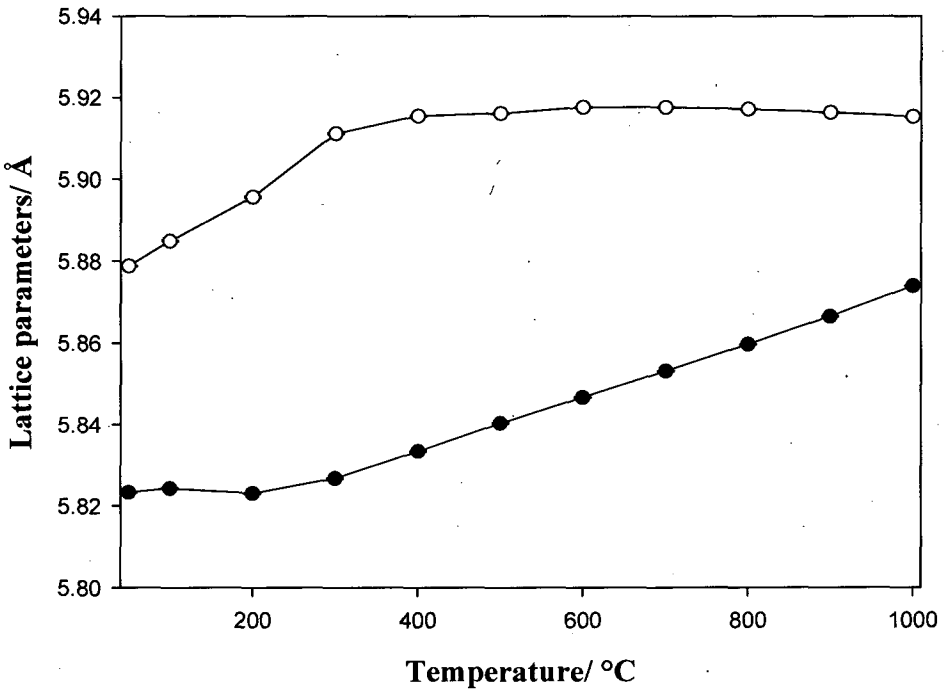

Figure 22 *b* and *c* lattice parameters as a function of temperature for $LaSrInO_4$ as extracted from PXD. ○ (*b* parameter), ●(*c* parameter)

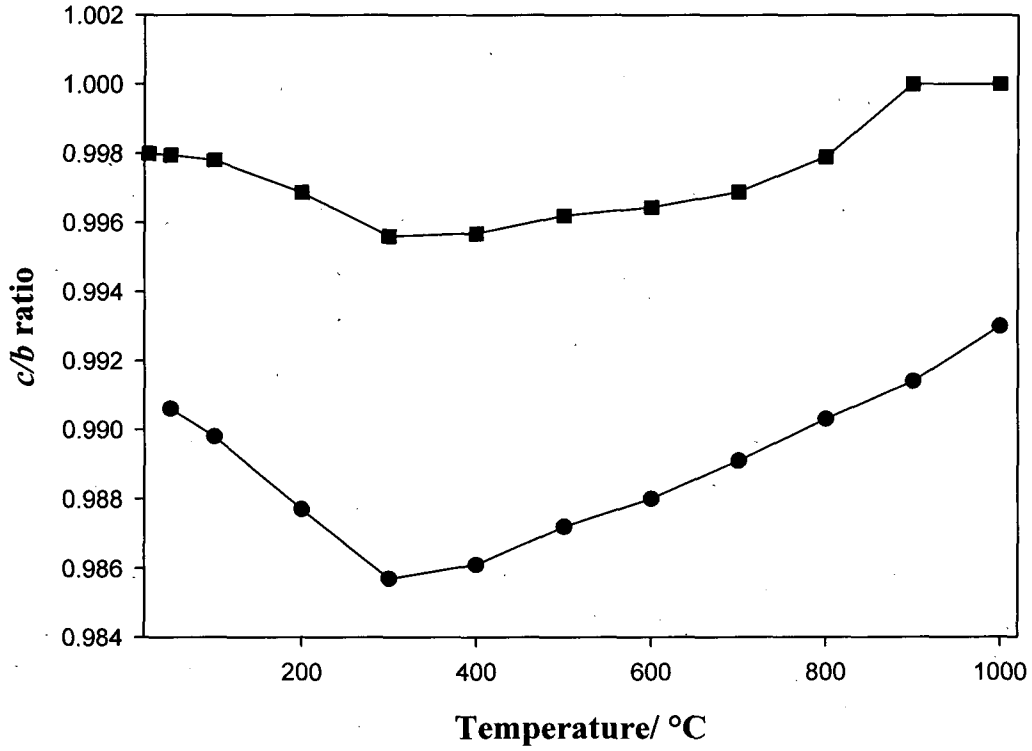

Figure 23 Temperature dependence of the *c/b* lattice parameter ratio for $LnSrInO_4$ (●) and *b/a* for $LaSrScO_4$ (■) as extracted from PXD.

The orthorhombic nature of the crystal distortion in $LaSrInO_4$ arises from both the tilting and deformation of the InO_6 octahedra within the perovskite layer (Figure 21). This causes the coordination sphere about the La^{3+} cation to change considerably in comparison with the La^{3+} coordination sphere in both the A*bma* and I4/*mmm* space groups. The effect of octahedral tilting and deformation of the InO_6 octahedra is evident in the coordination environment of the La^{3+}/Sr^{2+} sites at room temperature (Figure 24), the result is a marked lengthening of three of the La/Sr-O bonds and shortening on average of the remainder. The In-O-In bond which connects the InO_6 octahedra in the structure and provides a measure of the tilting is 166.0(2)°, which is smaller than the Sc-O-Sc bond angle of 169.8(7)° in $LaSrScO_4$ at 50 °C.

It is apparent from the structural studies undertaken that the level of distortion in the $LnSrInO_4$ compounds is higher compared to the $LnSrScO_4$ systems. The increased distortion maybe a result of the larger ionic radii of In^{3+}, hence the structure accommodating a greater mismatch between the A and B cations (La/ Sr = 1.263, Pr/ Sr = 1.244, In = 0.80 and Sc = 0.745 Å).

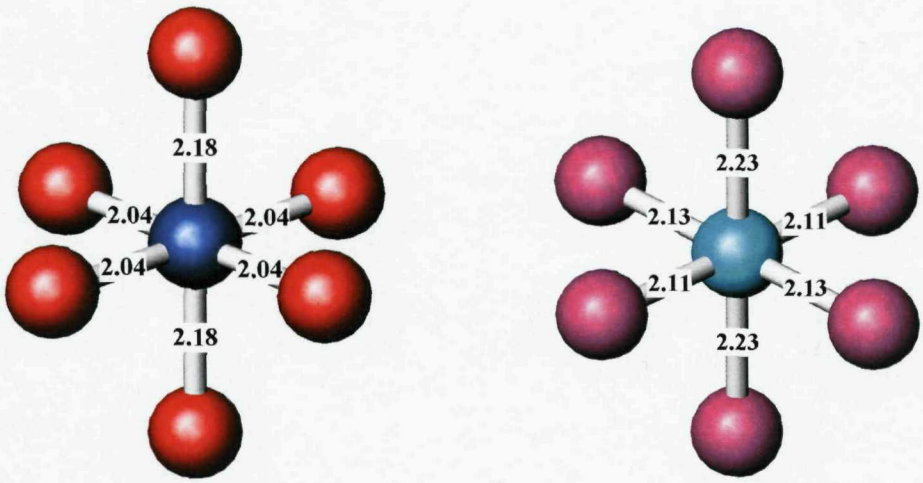

Figure 24 ScO_6 octahedra (left) (*Sc in dark blue and O in red*) and InO_6 octahedra (right) (*In in light blue and O in purple*) in $LaSrMO_4$ (M = Sc and In). Sc-O and In-O bond distances extracted from PND data are labeled.

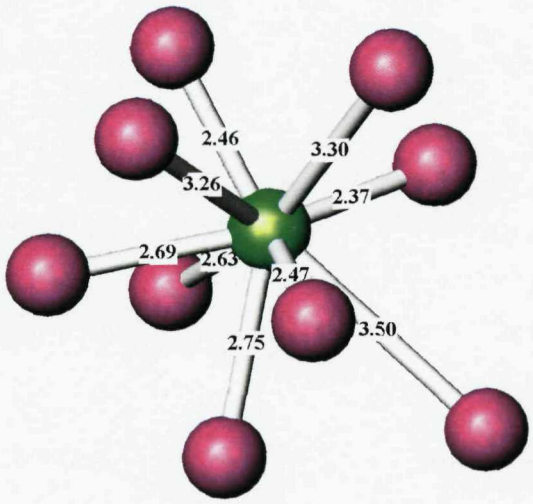

Figure 25 Coordination environment about La^{3+} in $LaSrInO_4$ at 25 °C (*La in green and O in purple*). Ln/Sr-O bond distances extracted from PND data are labelled.

3.4 Structural Distortions in the K_2NiF_4-type Structures

In order to investigate the factors that lead to the choice of structure and drive distortions of the K_2NiF_4-type structure away from an *I4/mmm* description, a further analysis of structural data using that obtained in this work and from literature sources was undertaken. Tolerance factors, *t*, which use the relative sizes of the A and B cation types can provide a reasonable indication of whether a material with the K_2NiF_4 structure-type may have a tendency to distort. However, it should be noted that the value of *t* at which a material chooses to adopt a specific structure type rather than another may depend on additional factors such as spin state, anion type (O^{2-}, F^-, Cl^- and N^{3-} are all known in K_2NiF_4 type structures) and polarization effects.

The regular tetragonal A_2BO_4 structure can react to changes in the relative sizes of A and B. When A is relatively large in comparison with B the network of octahedra is under tension but any tilting of the corner sharing BO_6 units would unfavorably

result in reduction of some A-O distances. In this circumstance the system could lengthen most of the A-O interactions by increasing the interlayer separation but maintaining the regular arrangement of BO_6 units along the *c* direction. The other alternative is to drive the formation of BO_4^{4-} tetrahedra that are coordinated in a regular manner by nine A^{2+} ions e.g. Ba^{2+}. The large ionic radius of the Ba^{2+} ions, effectively isolates the BO_4^{4-} tetrahedra and prevents oxo-bridging and is the primary reason for the isostructural nature of the Ba_2BO_4 (B = Ti,[19] V,[20] Cr[21] and Co[22]) compounds. An important feature of the structure is that the atoms are loosely packed; there is room for eight more oxygen atoms in the unit cell. The atomic arrangement in Sr_2TiO_4[23] and Sr_2FeO_4[24] provides an example of the type of structure Ba_2TiO_4 might adopt if the barium atoms were slightly smaller. The radii of the Sr^{2+} and O^{2-} ions are nearly equal, with the result that Sr_2TiO_4 and Sr_2FeO_4 adopt the K_2NiF_4 structure.

When B is relatively large in comparison with A, the network of octahedra is under compression and this generally leads to a buckling at the shared oxygen apices along the B-O-B directions, which can be accommodated by cooperative rotations of the octahedra. This acts to shorten some A-O distances while lengthening others producing a more compact coordination geometry for the relatively smaller A-type cation.

The three situations, matched A and B, relatively large A, and relatively large B can be discussed in terms of the tolerance factor $t = (r_A + r_O)/\sqrt{2}(r_B + r_O)$ (Figure 26). This expression represents the fit between an A type cation in one perovskite plane to which it is formally 9 coordinated but does not allow for the additional, often very short contact, with the oxygen in the adjacent perovskite layer. Thus when $t = 1$ this would represent a match between A, B and O for just one A to perovskite layer interaction rather than the complete K_2NiF_4 structure.

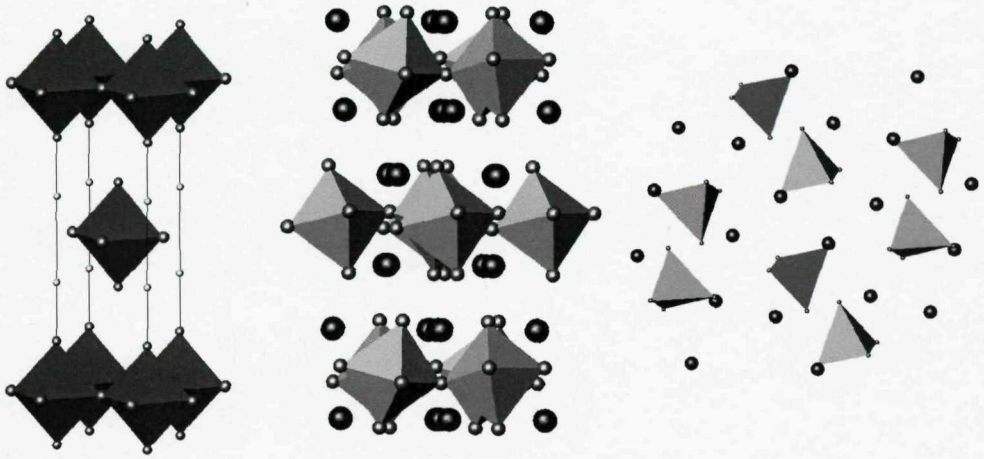

Figure 26 A diagram representing the three possible situations (matched AB; $LaSrFeO_4$ (left), relatively large B; $LaSrInO_4$ (middle) and relatively large A; Ba_2FeO_4 (right)) when in the A_2BO_4 structure-type.

A scatter-plot of K_2NiF_4-type oxide phases as a function of A cation and B cation sizes using Shannon[25] ionic radii is shown in Figure 27 and covers systems where A = Ba, Sr, Ca, Ln and mixtures thereof, and B = Co^{3+}, Sc^{3+}, Ni^{3+}, Al^{3+}, Ga^{3+}, V^{3+}, Cr^{3+}, Fe^{3+}, In^{3+}, Cu^{3+}, Co^{2+}, Ni^{2+} and Cu^{2+}. Lines are plotted on this graph that represent $t = 1$, $t = 0.906$ and $t = 0.8$. It should be noted that no tetragonal compound exists with t >1 which would represent a very large A relative to B; such a system would require the largest A-type cations found in this structure type i.e. Ba^{2+} in combination with the smallest B-type, e.g. Al^{3+} or Co^{3+}. For example $LaBaAlO_4$[26] (t = 1.002) adopts a structure with the space group $P2_12_12_1$ containing discrete AlO_4 tetrahedra and Ba_2TiO_4 (t = 1.012) adopts a structure with the space group $P2_1/c$ also containing discrete tetrahedra of TiO_4. This indicates that the K_2NiF_4 structure cannot accommodate the coordination preferences of both cations for $t > 1$ (using the Shannon set of ionic radii values) and other phases become thermodynamically more stable.

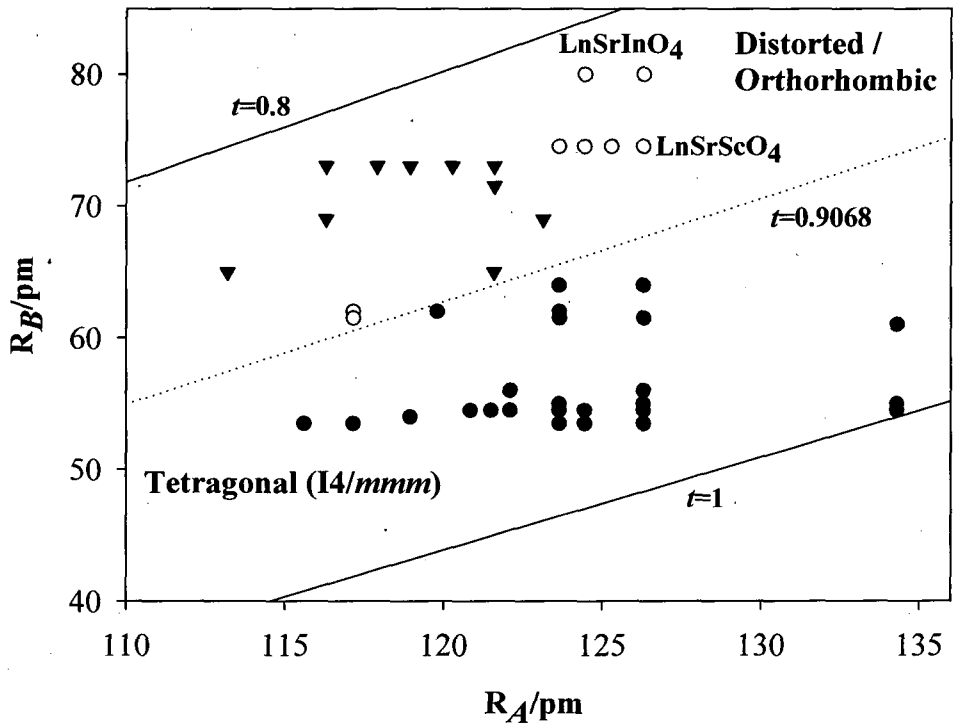

Figure 27 A cationic radii against B cationic radii for compounds adopting the A_2BO_4 structure type; ●(tetragonal A_2BO_4), ○ (distorted A_2BO_4 (B^{3+})), ▼ (distorted A_2BO_4 (B^{2+})).

For values of t above ~ 0.9 all compounds adopt the perfect (I4/*mmm*) A_2BO_4 structure-type; those below this value are distorted. For example tetragonal (I4/*mmm*) $LaBaCoO_4$ (LS) (r_A = 1.343 Å, r_B = 0.545 Å and t = 0.9972) is above the threshold and orthorhombic (A*bma*) La_2CoO_4 (r_A = 1.216 Å, r_B = 0.73 Å and t = 0.8684) is below the threshold. The best value delineating the separation between tetragonal and distorted structure type is equivalent to t = 0.9068 with materials having values lower than this adopting non-I4/*mmm* descriptions. Clearly for a particular B type cation size, and thus size of BO_6 octahedron, there is a minimum A type cation size which can occupy the semi-regular 9-coordinated position; for values smaller than this the BO_6 octahedra tend to tilt, rotate or distort so as to modify the coordination of oxygen to the A-type cation. Generally these lower symmetry structures described in space groups such as A*bma*, F*mmm* and P*bca*

produce a lower number of shorter coordination interactions for the A type cation. $LaSrScO_4$ and $LaSrInO_4$ lie above the $t = 0.9068$ line with $t = 0.878$ and $t = 0.856$ in this diagram consistent with the experimental observation of a tilting/distortion of the BO_6 octahedra.

Using this model it becomes possible to rationalise the high temperature behavior of these materials. The greater thermal vibration that occurs with increased temperature allows the tetragonal K_2NiF_4 structure to accommodate more readily any mismatch between ion sizes, so effectively the t line separating the two regions moves to lower values. Materials with t values close to the line would be expected to transform to the regular tetragonal structure more readily at higher temperatures than those further away, though such arguments would also need to take into account kinetic considerations. This behavior is observed in this work with the two phases with $LaSrScO_4$ and $PrSrScO_4$, transforming to the tetragonal phases on heating to around 900 °C and 1100 °C respectively.

It is also possible to use Figure 27 to predict the stability and structure type of other A_2BO_4 phases. Thus it should be possible to synthesise phases of the type $LnSrCoO_4$ possessing a smaller B cationic radius (r_B = 0.545 Å) for smaller A cations; current work has shown that the smallest lanthanide to fit into a K_2NiF_4-type structure is Gd^{3+} (r_A = 1.107 Å) yielding $GdSrCoO_4$. For the $LnSrScO_4$ systems with a larger B cationic radius (r_B = 0.73 Å) the smallest lanthanide to accommodate the structure type is Sm^{3+}. Attempts to synthesise the pure $LaBaScO_4$ phase was unsuccessful leading to the formation of a mixture of the n = 1 and n = 2 Ruddlesden-Popper phases. By replacing Ba^{2+} with Sr^{2+} the t value increases and a regular *I4/mmm* structure is predicted, however the greater disparity in the La^{3+} and Ba^{2+} ionic radii seems to favor the formation of $La_2BaSc_2O_7$, presumably because the larger Ba^{3+} cation can occupy a site with 12-fold coordination to oxygen.

3.5 Conclusion

The work presented in this chapter has expanded the structural studies of complex A_2BO_4 oxides. The novel $LnSrScO_4$ (Ln = Ce, Pr, Nd and Sm) and $PrSrInO_4$ compounds as well as the previously reported $LaSrScO_4$ and $LaSrInO_4$ have been synthesised. Detailed variable temperature structural analyses on these materials were carried out using PXD and high resolution PND, and the compounds were found to adopt the lower symmetry orthorhombic space groups A*bma* ($LnSrScO_4$) and P*bca* ($LaSrInO_4$) at 25 and 50 °C respectively. The orthorhombic nature of the crystal distortion in the $LnSrScO_4$ compounds at room temperature results from the tilting of the ScO_6 octahedra whereas in $LaSrInO_4$ the distortion arises from both the tilting and deformation of the InO_6 octahedra within the perovskite layer. In all the compounds the level of distortion increases in the temperature range 25 - 300 °C and then decreases in the temperature range 300 – 1200 °C; for $LaSrScO_4$ and $PrSrScO_4$ the compounds convert to the ideal K_2NiF_4-type structure at approximately 900 and 1100 °C respectively. Taking into account tolerance factors and structural data obtained from this work and literature studies, further analysis has been undertaken in order to investigate the factors that lead to the choice of structure and drive distortions of the K_2NiF_4-type structure away from an I*4/mmm* description.

In order to completely understand the structural properties of the $LnSrInO_4$ systems, further work is required. In order to elucidate the correct structural description throughout the temperature range 25 – 1000 °C variable temperature neutron diffraction data on both $LaSrInO_4$ and $PrSrInO_4$ would be beneficial. Also, $LaSrScO_4$ and $PrSrScO_4$ phases need to be studied at elevated temperatures (> 1000 °C) by both PXD and PND in order to conclude whether these structures revert to the ideal K_2NiF_4 structure.

3.6 References

[1] I. Kozo, *Physica C*, **185-189(Pt4)**, 2509, (1991).

[2] J. B. Boyce, F. Bridges, T. Claeson, T. H. Geballe, C. W. Chu, *Phys.Rev. B.*,**35**, 7203, (1987).

[3] K. D. Nelson, Z. Q. Mao, Y. Maeno and Y. Liu, *Science (Washington)*, **306**, 5699, (2004).

[4] D. Balz and K. Plieth, *Z. Elektrochem*, **59**, 545, (1955).

[5] D. I. Woodward and I. M. Reaney, *Acta Cryst.*, **B61**, 387, (2005).

[6] P. M. Woodward, *Acta Cryst.*, **B53**, 44, (1997).

[7] C. J. Howard and H. T. Stokes, *Acta Cryst.*, **B54**, 782, (1998).

[8] H. Shaked and J. D. Jorgensen, *J. Solid State Chem.*, **154**, 361, (2000).

[9] P. Ganguly and C. N. R. Rao, *J. Solid State Chem.*, **53**, 193, (1984).

[10] U. Lehmann and H. Mueller-Buschbaum, *Anorg. Allg. Chem*, **470**, 59, (1980).

[11] R. P. Liferovich and R. H. Mitchell, *J. Solid State. Chem*, **177**, 2188 (2004).

[12] H. M. Park, H. J. Lee, S. H. Park and H. I. Yoo, *Acta Crystallogr.*, **C59**, i131 (2003).

[13] D. M. Hatch and H. T. Stokes, *Phys. Rev. B.*, **39**, 9282, (1989).

[14] S. Kato, M. Ogasawara, M. Sugai and S. Nakata, *Solid State Ionics*, **149**, 53, (2002).

[15] I-S. Kim, H. Kawaji, M. Itoh and T. Nakamura, *Mat. Res. Bull.*, **27**, 1193 (1992).

[16] H. M. Rietveld, *Acta Cryst.*, **22**, 151, (1967).

[17] H. M. Rietveld, *J. Appl. Cryst.*, **2**, 65, (1969).

[18] A. C. Larson and R. B. Von Dreele, Generalised Structure Analysis System, Los Alamos National Laboratory Report, LAUR 86-748 (2000).

[19] L. M. Kovba, L. N. Kykova and E. V. Antiopov, *Koordinatsionnaya Khimiya*, **11**, 1574, (1985).

[20] G. Liu and J. E. Greedan, *J. Solid State. Chem.*, **103**, 228, (1993).

[21] G. Liu, J. E. Greedan and W. Gong, *J. Solid State Chem.*, **105**, 78 (1993).

[22] K. Boulahya, M. Parras, A. Vega and J. M. Gonzalez-Calbet, *Solid State Sciences*, **2**, 57 (2000).

[23] S. N. Ruddlesden and P. Popper, *Acta Crystallogr.*, **10**, 538 (1957).

[24] S. E. Dann, M. T. Weller, D. B. Currie, M. F. Thomas and A. D. AlRawas, *J. Mat. Chem*, **3**, 1231 (1993).

[25] R. D. Shannon, *Acta Cryst.*, **A32**, 751, (1976).

[26] J. A. Bland, *Acta Cryst.*, **14**, 875, (1961).

Chapter Four

Synthesis, Structural and Magnetic Characterisation of the $LnSrCoO_4$ series

4.1 Introduction

Mixed oxides with Ruddlesden-Popper (RP) structures have received considerable attention in recent years due to their interesting magnetic and electrical properties such as superconductivity (e.g. $La_{1.8}Ba_{0.2}CuO_4$[1,2] and Sr_2RuO_4),[3] oxide ion conductivity and low dimensional magnetic ordering. Such materials have been studied in depth for some transition metal elements, namely Cu,[4,5] Fe,[6,7] Cr[8,9] and Ru but to a very limited extent for other metals e.g. Co(III)[10,11,12] and Ni(III).[13] Layered cobalt oxides with structures based on a CoO_2 square net demonstrate a number of unusual electronic and magnetic properties associated with the various spin states of the Co(III) ion and interactions between such centres. These properties appear to derive from the specific electronic states of Co(III) in octahedral environments and the associated co-operative phenomena such as charge ordering spin ordering (magnetism) and conductivity. Many of these properties also appear to be a result of the closeness in energies of the high, intermediate and low spin states of Co(III) in the octahedral environment (d^6, $t_{2g}^4 e_g^2$ (HS), $t_{2g}^5 e_g^1$ (IS), $t_{2g}^6 e_g^0$ (LS)). Thus redistribution of spins among these cobalt centres, sometimes concertedly, leads to major changes in the compounds physical properties. HS and IS Co(III) systems are generally favored at high temperatures and give rise to a high effective moment and metallic phases, conversely at low temperatures insulating phases of LS Co(III) are generally favored. However, in practice the behaviors of Co(III) oxides are much more complex due to phenomena such as multiple sites and coordination environments leading to partial or complete spin ordering, low dimensionalities in the structure and dopant effects. Materials that have been studied in detail include $LaCoO_3$,[14,15] $TlSr_2CoO_5$ and structurally related $LnBaCo_2O_{5+\square}$, $\square \leq 0.5$. $LaSrCoO_4$ and some stoichiometrically closely related phases have also been studied to some degree and show the spin-crossover behavior albeit weakly. Demazeau *et al.*[10] state that $LaSrCoO_4$ undergoes a spin crossover from IS to HS transition near 400 K, which is reflected in their extracted structural data as a weak change in the Co-O distances with a distinct increase in the axial Co-O distance relative to the equatorial Co-O separation. However, their data were collected at a few temperatures and as such any

significant shift in positions is very poorly defined. The spin state and electronic configuration of $LaSrCoO_4$ have been the subject of numerous investigations and discussions over the past 30 years, however its intrinsic magnetic behavior is still controversial.[10,11,12]

The thermally induced spin transition in $LaCoO_3$ has been investigated for nearly five decades, but there are still some aspects that are not fully understood. At low temperatures $LaCoO_3$ is non-magnetic, Co^{3+} ions being in the LS state with 6 electrons in the t_{2g} levels and empty e_g states (LS, $t_{2g}^6e_g^0$, S=0) At ≈ 100 K $LaCoO_3$ undergoes a transition to a magnetic state, the character of which is still under intense debate. Possible states of Co^{3+} that can give rise to the magnetism correspond either to intermediate spin (IS, $t_{2g}^5e_g^1$, S=1) or high spin (HS, $t_{2g}^4e_g^2$, S=2) states. A second transition at ≈ 500 K is accompanied by a further change of paramagnetic properties. The magnetic and electronic transitions are also accompanied by subtle changes in the crystal structure, which is of the rhombohedral perovskite type R*3C* for $LaCoO_3$. The effects are of two types; the ionic radii of Co^{3+} increases from *r*LS = 0.545 Å to *r*IS = 0.56 Å or *r*HS = 0.61 Å. The Co^{3+} ion in IS or HS is Jahn-Teller active and corresponding distortion of the CoO_6 octahedra may arise. A monoclinic distortion of the $LaCoO_3$ structure (space group I*2/a*) and Jahn-Teller distortion of CoO_6 octahedra was found recently by single crystal X-ray diffraction between 100 and 300 K. The Co^{3+} size effect is responsible for the anomalous thermal expansion that reflects the increasing population of magnetic species.[14,15]

In this chapter the results of an investigation of the $LnSrCoO_4$ series where Ln = La-Gd), are reported. The phases synthesised were initially characterised by PXD with more detailed structural characterisation on the compounds performed using Rietveld analysis. The spin-crossover behavior was investigated using variable temperature PXD and PND, and the magnetic behavior of the compounds interpreted.

4.2 Synthesis

Polycrystalline samples of the $LnSrCoO_4$ (where Ln = La, Pr, Nd, Sm, Eu, and Gd) series were prepared using the direct oxide route. The lanthanide oxides were dried in air at 800 °C for 24 hours prior to use. Stoichiometric amounts of Ln_2O_3 (99.99%, Aldrich) (Ln = La, Nd, Sm, Eu and Gd), Pr_6O_{11} (99.99%, Aldrich), $SrCO_3$ (99.9+%, Aldrich) and Co_3O_4 (Aldrich, 99.99%), were ground in an agate pestle and mortar and annealed in air at 970 °C for 48 hours. Following regrinding they were annealed in air at 1150 °C for a further 48 hours and quenched to room temperature.

The synthesis of $LnSrCoO_4$ (where Ln = Tb, Dy and Er) was also attempted using the direct oxide route, however PXD shows the formation of a mixture of phases. Further work concentrated on the formation of $DySrCoO_4$ and the sol-gel method was adopted, whereby stoichiometric amounts of Dy_2O_3 (99.99%, Aldrich), $Sr(NO_3)_2$ (99.9+%, Aldrich) and Co_3O_4 (Aldrich, 99.99%) were dissolved in the minimum quantity of 15.8 M nitric acid. Molar equivalents of ethylene glycol and citric acid dissolved in ~ 25mL distilled water were added to this solution. The mixture was heated and stirred to dryness. The dry mixture was further decomposed for 5 hours at 220 °C. After decomposition, the mixture was heated to 400 °C in air for 48 hours and then at 970 °C for a further 48 hours, with intermediate regrinding at each stage. The powders were pressed into pellets of 10 mm diameter and 3 mm thickness under 10 tonnes of pressure and these were then fired at 1150 °C for 48 hours. The progress of the reactions was monitored using PXD. The results obtained are summarised in Table 1.

Table 1. A summary of the synthetic conditions employed in the synthesis of $LnSrCoO_4$ phases from the constituent starting materials.

Target Phase	Reactants	Conditions		Products
		Temperature (°C)	Duration (hours)	
$LaSrCoO_4$	$SrCO_3+{}^1/_2La_2O_3+{}^1/_3Co_3O_4$	970	48	$LaSrCoO_4$
		1150	48	
$PrSrCoO_4$	$SrCO_3+Pr_6O_{11}+{}^1/_3Co_3O_4$	970	48	$PrSrCoO_4$
		1150	48	
$NdSrCoO_4$	$SrCO_3+{}^1/_2Nd_2O_3+{}^1/_3Co_3O_4$	970	48	$NdSrCoO_4$
		1150	48	
$SmSrCoO_4$	$SrCO_3+{}^1/_2Sm_2O_3+{}^1/_3Co_3O_4$	970	48	$SmSrCoO_4$
		1150	48	
$EuSrCoO_4$	$SrCO_3+{}^1/_2Eu_2O_3+{}^1/_3Co_3O_4$	970	48	$EuSrCoO_4$
		1150	48	
$GdSrCoO_4$	$SrCO_3+{}^1/_2Gd_2O_3+{}^1/_3Co_3O_4$	970	48	$GdSrCoO_4$
		1150	48	
$TbSrCoO_4$	$SrCO_3+{}^1/_2Tb_2O_3+{}^1/_3Co_3O_4$	970	48	$Tb_2O_3+SrTb_2O_4$
		1150	48	$+SrCoO_{2.8}$
$DySrCoO_4$	$SrCO_3+{}^1/_2Dy_2O_3+{}^1/_3Co_3O_4$	970	48	$Dy_2O_3+SrDy_2O_4+$
		1150	48	$SrCoO_{2.8}$
$DySrCoO_4$	$SrCO_3+{}^1/_2Dy_2O_3+{}^1/_3Co_3O_4$	970	48	$Dy_2O_3+Co_3O_4+$
	under O_2	1150	48	unknown phase
$DySrCoO_4$	${}^1/_2Dy_2O_3+Co(NO_3)_2.6H_2O+$	970	48	Dy_2O_3+
	$Sr(NO_3)_2$			$DySrCoO_4+$
				$SrCoO_{2.8}$
		1150	48	$Dy_2O_3+SrDy_2O_4+$
				$SrCoO_{2.8}+SrO$
$ErSrCoO_4$	$SrCO_3+{}^1/_2Er_2O_3+{}^1/_3Co_3O_4$	970	48	$Er_2O_3+SrEr_2O_4+$
		1150	48	$SrCoO_{2.8}$

4.3 Room Temperature PXD Studies of the $LnSrCoO_4$ (Ln = La, Pr, Nd, Eu, Sm and Gd) Systems

4.3.1 PXD Structure Refinement

PXD data at 298 K were collected over the 2θ range 10-100° using a Siemens D5000 diffractometer operating with $Cu_{K\alpha 1}$ radiation. The starting structural model for Rietveld refinement was that proposed by Demazeau *et al*,[10] space group *I4/mmm* with Sr^{2+} and Ln^{3+} at half occupancy and Co^{3+} and O^{2-} at full occupancy. The lanthanum and strontium are situated on (0,0,0.36), cobalt on (0,0,0) and oxygen atom O1 on (0,0.5,0) and O2 on (0,0,0.166). In the crystal structure, the Co^{3+} ions occupy octahedral lattice sites; the Sr^{2+} and Ln^{3+} ions occupy sites having a coordination number of 9 in a 1 + 4 + 4 environment with one very short contact (~ 2.35 Å) and 8 further contacts in the range 2.7 - 3.0 Å. Refinement of the structure introduced the global parameters, i.e. histogram scale factor, peak shape, zero point displacement, background parameters and lattice constants. The isotropic temperature factors and the atom positions were also varied. The atomic parameters and final fit factors have been tabulated (Table 2).

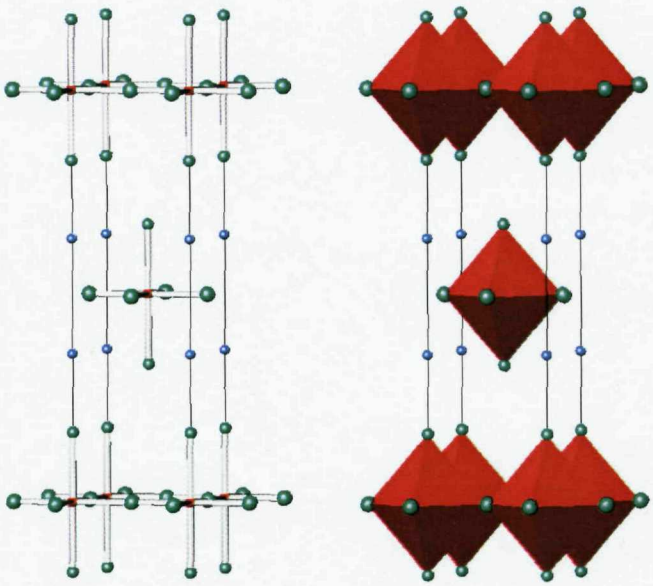

Figure 1 The structure of $LnSrCoO_4$ showing the CoO_6 coordination and the infinite sheets of octahedra.

Table 2 Lattice parameters, selected bond distances and final fit paramters for the $LnSrCoO_4$ phases, as extracted from PXD data obtained from the Siemens D5000 diffractometer at 298 K *(e.s.d's are given in parantheses).*

$LnSrCoO_4$	Ionic radii of Ln^{3+}/ Å	a parameter/ Å	c parameter/ Å	Literature a parameter/ Å	Literature c parameter/ Å	Co-O1/ Å	Co-O2/ Å	χ^2	R_{wp} (%)	R_p (%)
$LaSrCoO_4$	1.216	3.8052(1)	12.4846(3)	3.8052(6)	12.489(2)	1.903(1)	2.072(9)	1.62	7.24	5.60
$PrSrCoO_4$	1.179	3.7817(1)	12.3430(3)	N/A	N/A	1.891(1)	2.060(9)	1.36	7.20	5.74
$NdSrCoO_4$	1.163	3.7716(1)	12.3269(4)	3.7728(5)	12.304(1)	1.886(1)	2.051(7)	1.49	6.98	5.35
$SmSrCoO_4$	1.132	3.7586(1)	12.2079(3)	3.760(5)	12.26(1)	1.879(1)	2.052(9)	1.32	6.41	5.11
$EuSrCoO_4$	1.120	3.7535(1)	12.1791(4)	3.753(5)	12.20(1)	1.877(2)	2.030(10)	1.15	7.11	5.64
$GdSrCoO_4$	1.107	3.7492(1)	12.1344(4)	3.7481(4)	12.160(1)	1.875(1)	2.023(13)	1.16	5.37	4.29

4.3.2 Discussion

The $LnSrCoO_4$ (Ln = La, Pr, Nd, Sm, Eu and Gd) systems have been successfully synthesised and adopt the K_2NiF_4/ n = 1 Ruddlesden-Popper structure, consisting of a single rock-salt layer interleaved with a perovskite layer giving a body-centred tetragonal cell. Sheets of CoO_6 octahedra sharing four vertices are separated by Ln^{3+}/ Sr^{2+} ions in a nine-fold coordination to O^{2-}.

The cell parameters obtained for the series show the expected decrease in size on crossing the lanthanide series from La to Gd (Figure 2). The *c* parameter shows a 0.35 Å reduction and the *a* parameter a 0.056 Å decrease, corresponding to a 10% contraction of the cell volume. The driving force for the observed contraction is clearly the introduction of successively smaller lanthanides onto the A site of the structure. The ionic radius of La^{3+} in 9-fold coordination is 1.216 Å compared with 1.107 Å for Gd^{3+}. Examination of the different structural portions of the materials reveals that the contraction of the *a* and *c* parameters are a result of the shrinkage in the Ln/Sr-O and Co-O bonds. A phase change occurs on the introduction of Tb^{3+} (i.r. = 1.9095 Å), Dy^{3+} (i.r. = 1.083 Å) and Er^{3+} (i.r. = 1.062 Å) and the K_2NiF_4-type structure is no longer stable. A likely explanation for this is that the mismatch between the perovskite Co-O layer and the rocksalt (Sr/Ln)-O layers become too great and $SrLn_2O_4$, Ln_2O_3 and $SrCoO_{2.8}$ form. In addition, the formation of phases with rare earths as small as Tb, Er and Dy in 9-fold coordination is unusual; lower coordinations are usually favoured like the 6-fold sites found in $SrTb_2O_4$, $SrDy_2O_4$ and $SrEr_2O_4$.

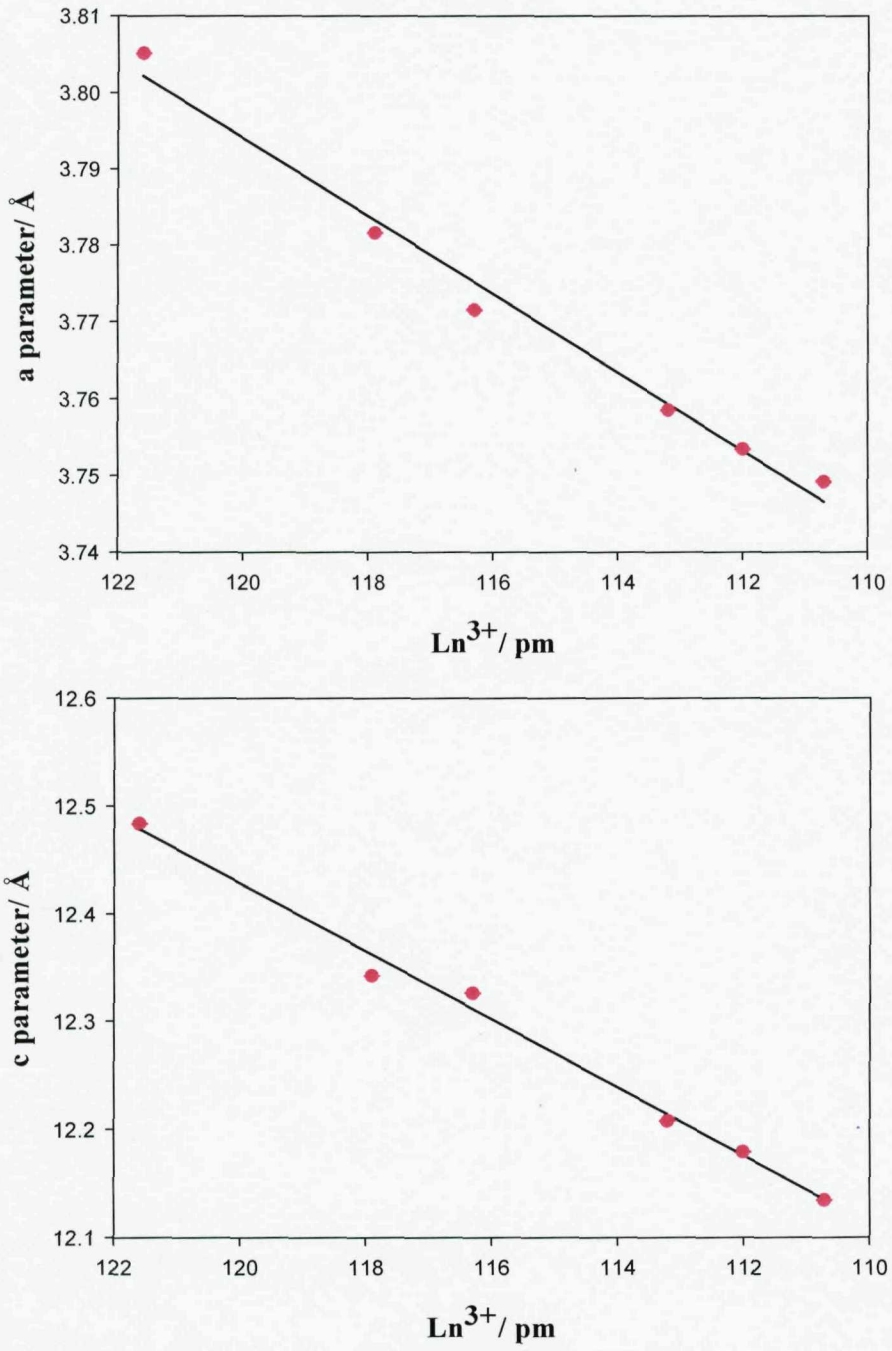

Figure 2 Variation in the lattice constants determined for the series $LnSrCoO_4$ (Ln = La – Gd) as a function of lanthanide ionic radii. Contraction of the *a* parameter is shown in the top diagram and the decrease in the *c* parameter is shown in the bottom diagram.

In all these $n = 1$ Ruddlesden-Popper cobalt compounds, the Co^{3+} ions are in a tetragonally distorted octahedral site within the perovskite blocks, so that there are two different Co-O bond lengths; a shorter Co-O (equatorial) in the *ab* plane and a longer Co-O (axial) along the *c* axis (Figure 3). Both distances decrease as the size of the lanthanide decreases (Figure 4). Jahn-Teller distortions of the

CoO_6 octahedra may arise from the presence of a single (unpaired) electron in the e_g orbitals (IS state). In the Ln/Sr-O layers the Ln/Sr ions are randomly distributed over the 9-coordinated sites and display three different Ln-Sr-O bond lengths. These bond lengths increase as the mean size of Ln/Sr cations get bigger. The shortest distance is to the axial oxygen ion just above it along the *c* axis, which is distinguished as O1, four longer bonds correspond to bonds to O2 oxygen ions from the basal Ln/Sr-O layer and the longest ones are to four oxygen ions O1 in its own Ln/Sr-O layer. As a result these Ln/Sr-O layers are not flat, but slightly corrugated, especially as the mean size of the Ln/Sr ions decreases.

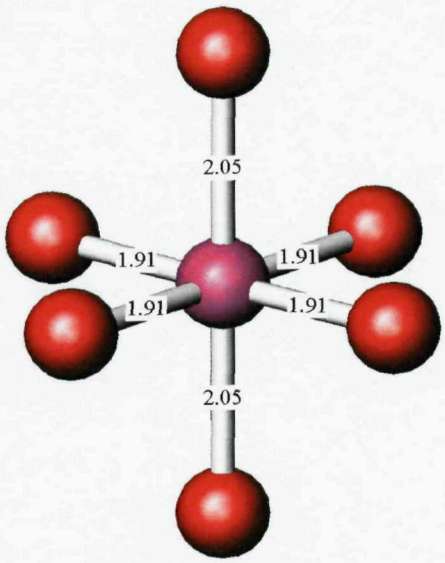

Figure 3 CoO_6 octahedra displaying a shorter Co-O1 equatorial bond in the *ab* plane and a longer Co-O2 axial bond along the *c* axis.

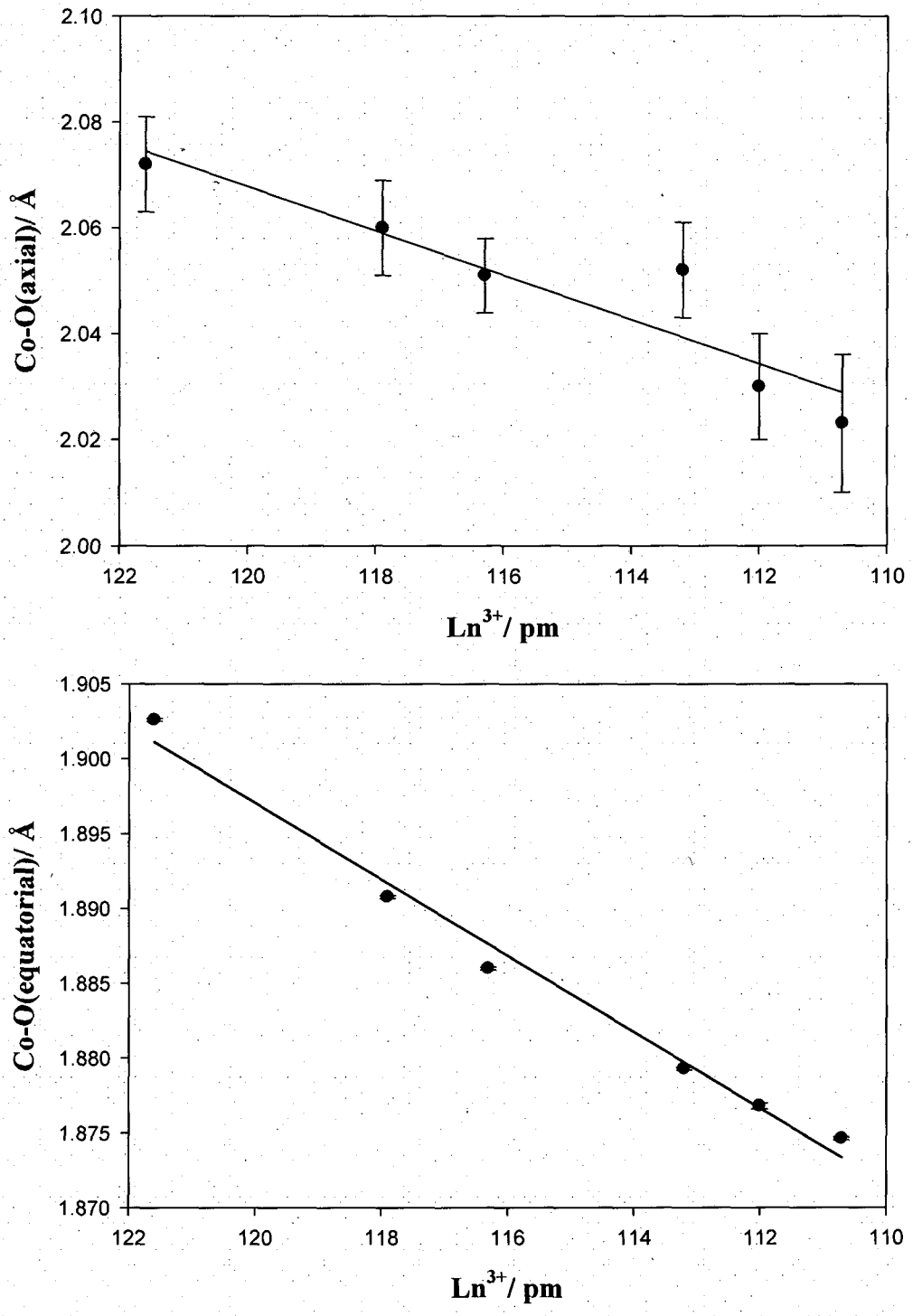

Figure 4 Variation in the Co-O axial (top) and equatorial (bottom) bond distances determined for the series $LnSrCoO_4$ (Ln = La – Gd) as a function of lanthanide ionic radii.

4.4 Magnetic Characterisation

The magnetic behaviour of $LaSrCoO_4$ is already controversial; whilst some authours found a spin glass behaviour,[12] according to other groups the compound is ferromagnetic[16] or paramagnetic.[11] Also it has been proposed that both low spin (t_{2g}^6 e_g^0) and high spin (t_{2g}^4 e_g^2) Co^{3+} ions co-exist in the material. Nevertheless more recent work gives evidence for an intermediate spin (t_{2g}^5 e_g^1) configuration.[14] Here we report the study of the magnetic behaviour of $NdSrCoO_4$. Variable temperature magnetic susceptibility data were collected between 10 and 400 K using a Quantum Design MPMS-5S SQUID magnetometer in an applied field of 100 Oe and from 300 to 870K using an Oxford Instruments VSM heating in a field of 1 kOe.

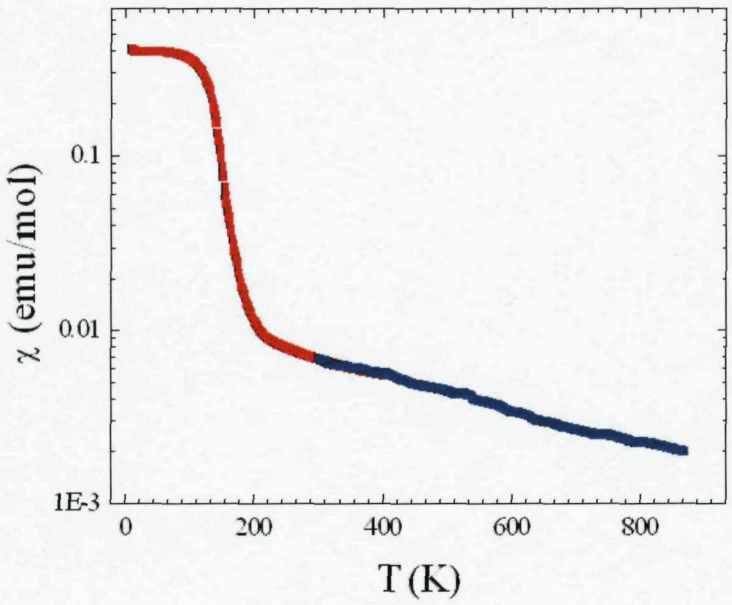

Figure 5 Magnetic susceptibility as a function of temperature for $NdSrCoO_4$ (*red line indicates SQUID data and blue line VSM data*).

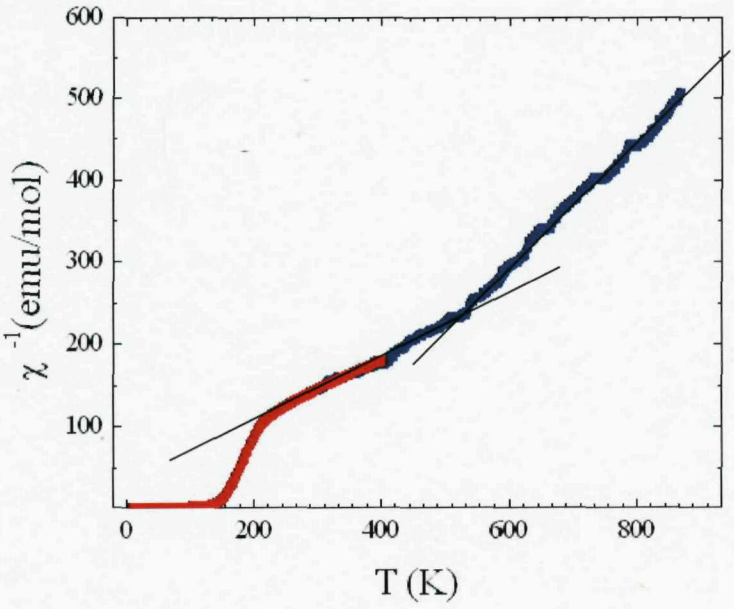

Figure 6 Inverse magnetic susceptibility as a function of temperature for $NdSrCoO_4$ (*red line indicates SQUID data and blue line VSM data*).

Strong variations in the susceptibility behavior are observed at characeteristic temperatures. The χ vs T graph reveals that ferromagnetic ordering sets in at ~ 200 K. Another transition exists at $\approx$ 525 K which may be assigned to a change in Co^{3+} spin state. It is instructive to compare characteristic moments with the measured values. For the intermediate (S = 1) and high (S = 2) spin state the expected effective moments are 2.83 and 4.90 μB respectively. In these systems we would expect a transition from LS (S = 0) $\leftrightarrow$ Intermediate spin (S = 1) $\leftrightarrow$ HS (S = 2). However, the magnetic susceptibility data shows that between 200 – 525 K the calculated effective moment is 4.64 μB suggesting a high spin configuration and > 525 K the calculated effective moment is 3.52 μB i.e. an IS configuration. This does not tie in with what is expected and is due to the magnetic contribution of Nd^{3+}, further work would include the collection of magnetic data on $LaSrCoO_4$ and $GdSrCoO_4$ in which La^{3+} and Gd^{3+} ions do not contribute to the magnetism.

4.5 Variable Temperature PXD and PND Studies of the $LnSrCoO_4$ (Ln = La - Gd) Systems

It is clear from the variable temperature magnetic susceptibility data obtained for $NdSrCoO_4$ that a magnetic transition occurs at ~ 525 K. It is therefore instructive to collect variable temperature PXD and PND data on these systems. This enables the determination of any anomalous behaviour in the lattice parameters and the Co-O axial and equatorial bond distances, owing to changes in the spin state of Co^{3+}. Neutron diffraction data can also be used in determining the magnetic structure of a material. As a result of the magnetic dipole moment associated with neutrons, they can interact with unpaired electrons present in a material. The additional scattering effect of the interaction between the neutrons and unpaired electrons can cause additional peaks to appear in the diffraction profile, which are indicative of the magnetic superstructure of the material. From these peaks it is possible to determine whether a material is ferromagnetic or antiferromagnetic.

4.5.1 Variable Temperature PXD Structure Refinement

Variable temperature PXD data were collected on the $LnSrCoO_4$ series over the 2θ range 10-100° using a step size of 0.018° and the Bruker D8 diffractometer in conjunction with the PSD detector and an Anton-Paar HTK 1200 furnace stage in the temperature range 298 – 873 K. The data were refined using the GSAS suite of programs. The starting point for Rietveld refinements were from the 298 K model as described in section 4.3.1. The atomic positions (Tables 3 - 8) and profile fits (Figures 7 and 8) for a select few $LnSrCoO_4$ phases are described. The lattice parameters and selected bond lengths for all temperatures have been tabulated in Appendix b.

Table 3 Atomic positions and thermal parameters for $LaSrCoO_4$ from 298 K PXD data. *Space group I4/mmm; a = 3.8080(1), c = 12.4883(4) Å (e.s.d's are given in parentheses)*

Atom	x	y	z	Occupancy	U_{iso} x 100/Å^2
La/ Sr	0	0	0.3608(1)	0.5/ 0.5	2.05(5)
Co	0	0	0	1	2.13(10)
O1	0	0.5	0	1	2.67(29)
O2	0	0	0.1663(6)	1	3.03(23)

$\chi^2 = 5.17$, $R_p = 1.99\%$, $R_{wp} = 2.89\%$

Table 4 Atomic positions and thermal parameters for $PrSrCoO_4$ from 298 K PXD data. *Space group I4/mmm; a = 3.7741(1), c = 12.3177(3) Å (e.s.d's are given in parentheses)*

Atom	x	y	z	Occupancy	U_{iso} x 100/Å^2
Pr/Sr	0	0	0.3602 (1)	0.5 /0.5	1.71(5)
Co	0	0	0	1	1.75(10)
O1	0	0.5	0	1	2.73 (33)
O2	0	0	0.1671(7)	1	2.33(25)

$\chi^2 = 1.65$, $R_p = 2.37\%$, $R_{wp} = 3.01\%$

Table 5 Atomic positions and thermal parameters for $NdSrCoO_4$ from 298 K PXD data. *Space group I4/mmm; a = 3.7772(1), c = 12.3115(3) Å (e.s.d's are given in parentheses)*

Atom	x	y	z	Occupancy	U_{iso} x 100/Å^2
Nd/Sr	0	0	0.3603(1)	0.5 /0.5	1.79(8)
Co	0	0	0	1	1.14(10)
O1	0	0.5	0	1	2.61(26)
O2	0	0	0.1666(8)	1	3.47(23)

$\chi^2 = 2.12$, $R_p = 1.60\%$, $R_{wp} = 2.06\%$

Table 6 Atomic positions and thermal parameters for $SmSrCoO_4$ from 298 K PXD data. *Space group I4/mmm; a = 3.7520(1), c= 12.1970(3) Å (e.s.d's are given in parentheses).*

Atom	x	y	z	Occupancy	U_{iso} x 100/Å^2
Sm/Sr	0	0	0.3603(1)	0.5 /0.5	0.94(9)
Co	0	0	0	1	0.67(12)
O1	0	0.5	0	1	0.93(28)
O2	0	0	0.1670(11)	1	2.86(26)

$\chi^2 = 2.14$, $R_p = 1.46\%$, $R_{wp} = 2.93\%$

Table 7 Atomic positions and thermal parameters for $EuSrCoO_4$ from 298 K PXD data. *Space group I4/mmm; a = 3.7575(1), c=12.2000(5) Å (e.s.d's are given in parentheses).*

Atom	x	y	Z	Occupancy	U_{iso} x 100/Å^2
Eu/Sr	0	0	0.3604(1)	0.5 /0.5	2.10(13)
Co	0	0	0	1	1.62(16)
O1	0	0.5	0	1	1.54(35)
O2	0	0	0.1664(9)	1	3.41(31)

$\chi^2 = 1.16$, $R_p = 5.67\%$, $R_{wp} = 7.14\%$

Table 8 Atomic positions and thermal parameters for $GdSrCoO_4$ from 298 K PXD data. *Space group I4/mmm; a = 3.7555(1), c = 12.1554(4) Å (e.s.d's are given in parentheses).*

Atom	x	y	Z	Occupancy	U_{iso} x 100/Å^2
Gd/Sr	0	0	0.3604(1)	0.5 /0.5	1.14(8)
Co	0	0	0	1	1.14(14)
O1	0	0.5	0	1	1.3(4)
O2	0	0	0.1681(14)	1	3.6(4)

$\chi^2 = 1.19$, $R_p = 1.60\%$, $R_{wp} = 2.00\%$

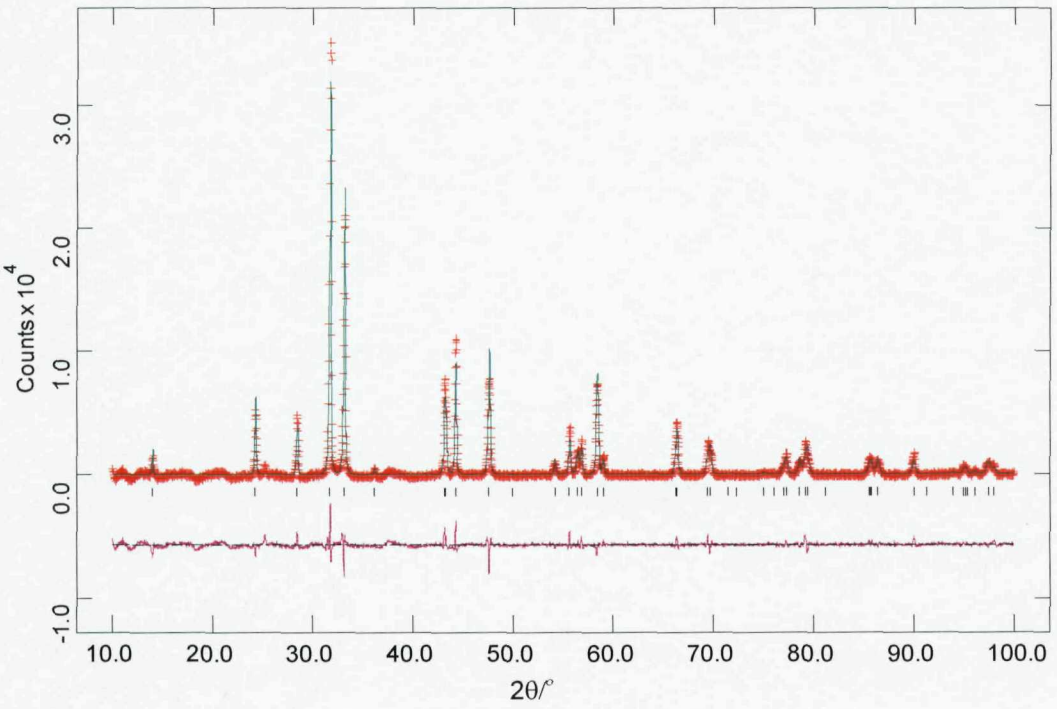

Figure 7 PXD refinement profile for tetragonal $LaSrCoO_4$ at 298 K *(crosses indicate observed data, the upper continuous line shows calculated profile, the lower continuous line the difference and tick marks show reflection positions).*

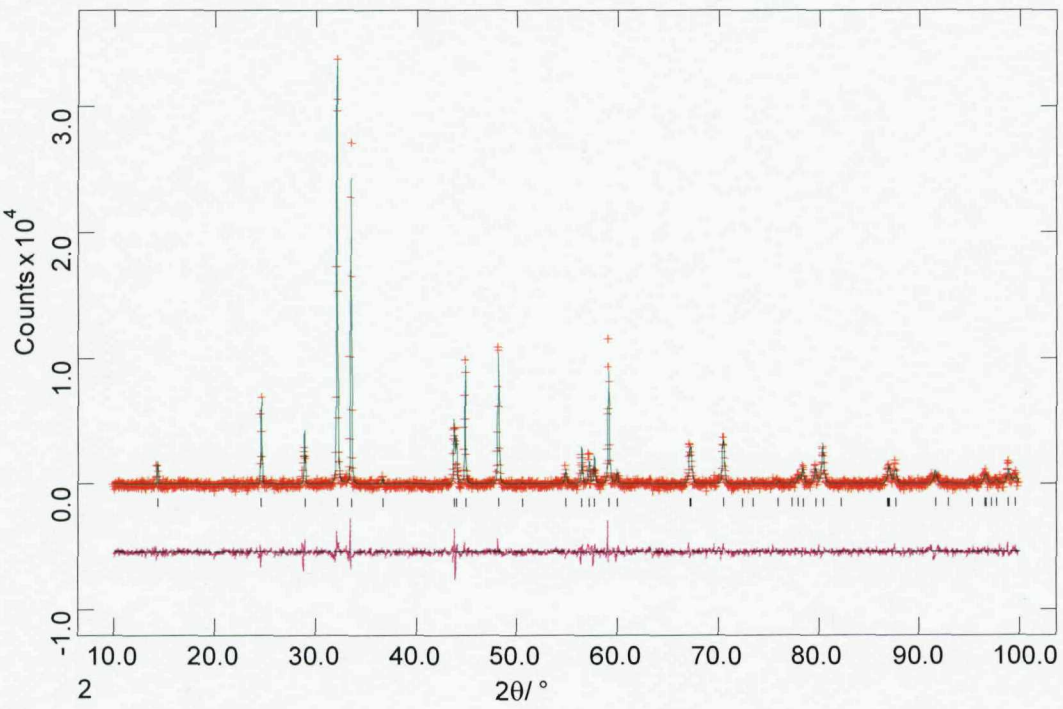

Figure 8 PXD refinement profile for tetragonal $NdSrCoO_4$ at 298 K *(crosses indicate observed data, the upper continuous line shows calculated profile, the lower continuous line the difference and tick marks show reflection positions).*

4.5.2 Variable Temperature PND Structure Refinement of $LnSrCoO_4$ (Ln = La, Nd, ^{154}Sm and ^{160}Gd)

In order to improve the determination of the structure, elucidate exact oxygen positions and investigate the physical properties of these systems; PND data were collected on selected samples using POLARIS at the ISIS facility. Due to the high absorbing power of the common isotopes ^{149}Sm and ^{157}Gd, $SmSrCoO_4$ and $GdSrCoO_4$ samples were synthesised using the isotopic oxides $^{154}Sm_2O_3$ and $^{160}Gd_2O_3$ as the starting materials. The samples were loaded in 6 mm or 8 mm diameter vanadium cans depending upon sample size. Data were collected in the temperature range 2 – 900 K in 50 K intervals. The highest resolution data from the backscattering C bank were used in the strucutural refinement of the data, with the structural parameters from the X-ray refinement used as the starting model. The nuclear scattering lengths used were La = 8.240 , Nd = 7.690 , ^{154}Sm = 9.300, ^{160}Gd = 9.150, Co = 2.490, Sr = 7.020 and O = 5.803 fm. Lattice parameters and the background function were the first variables to be introduced. Then a peak shape function was included. Once these were stable the atomic positions and isotropic thermal parameters were included in the refinement. The atomic positions (Tables 9 - 12) and profile fits (Figures 9 - 12) for a select few $LnSrCoO_4$ phases are described. The lattice parameters and selected bond lengths for all temperatures have been tabulated in Appendix b. The thermal parameters on the Co atom in several of the compounds refine to negative values which may be accounted for by its strongly absorbing nature. The structures were also refined using the A bank data however no additional Bragg (magnetic) reflections were observed.

Table 9 Atomic positions and thermal parameters for $LaSrCoO_4$ from 300 K PND data. *Space group I4/mmm; a = 3.8109(1) and c = 12.4877(1) Å (e.s.d's are given in parentheses).*

Atom	x	y	z	Occupancy	U_{iso} x 100/Å^2
La/Sr	0	0	0.3602(1)	0.5 /0.5	0.19(2)
Co	0	0	0	1	-0.50(5)
O1	0	0.5	0	1	0.41(2)
O2	0	0	0.1643(1)	1	0.73(2)

$\chi^2 = 2.69$, $R_p = 3.76\%$, $R_{wp} = 6.49\%$

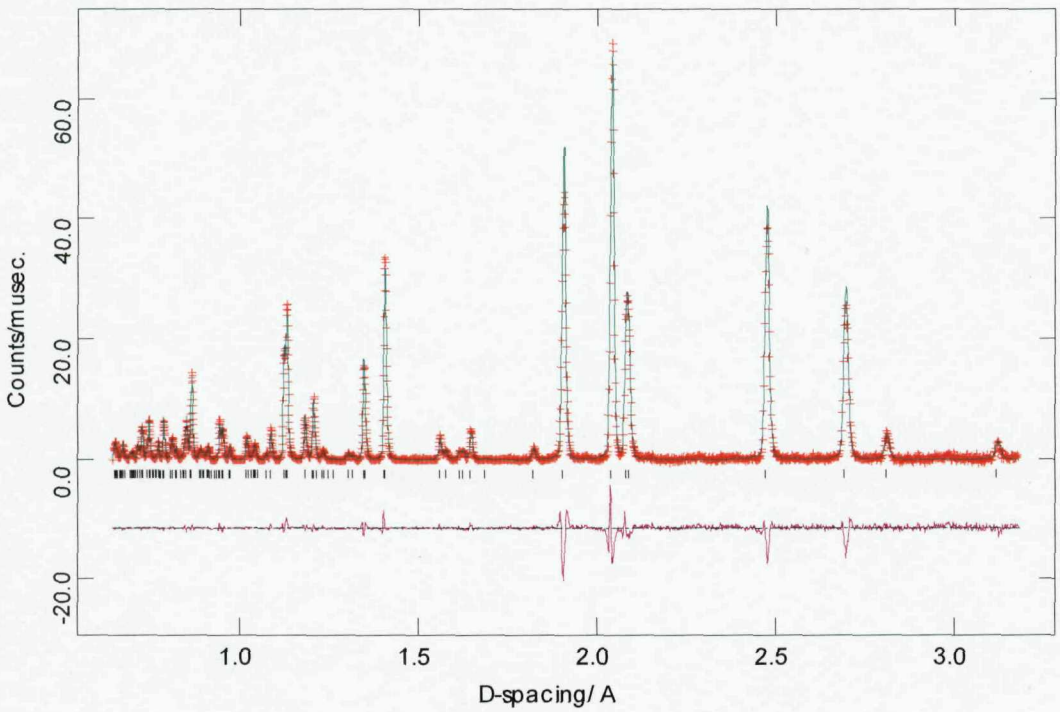

Figure 9 PND refinement profile for tetragonal $LaSrCoO_4$ at 300 K *(crosses indicate observed data, the upper continuous line shows calculated profile, the lower continuous line the difference and tick marks show reflection positions).*

Table 10 Atomic positions and thermal parameters for $NdSrCoO_4$ from 300 K PND data.

Space group I4/mmm; a = 3.7730(4) and c = 12.3046(2) Å (e.s.d's are given in parentheses).

Atom	x	y	z	Occupancy	U_{iso} x 100/Å^2
Nd/Sr	0	0	0.3604(1)	0.5 /0.5	0.21(2)
Co	0	0	0	1	-0.12(5)
O1	0	0.5	0	1	0.54(2)
O2	0	0	0.1645(1)	1	0.84(2)

$\chi^2 = 1.18$, $R_p = 3.14\%$, $R_{wp} = 5.45\%$

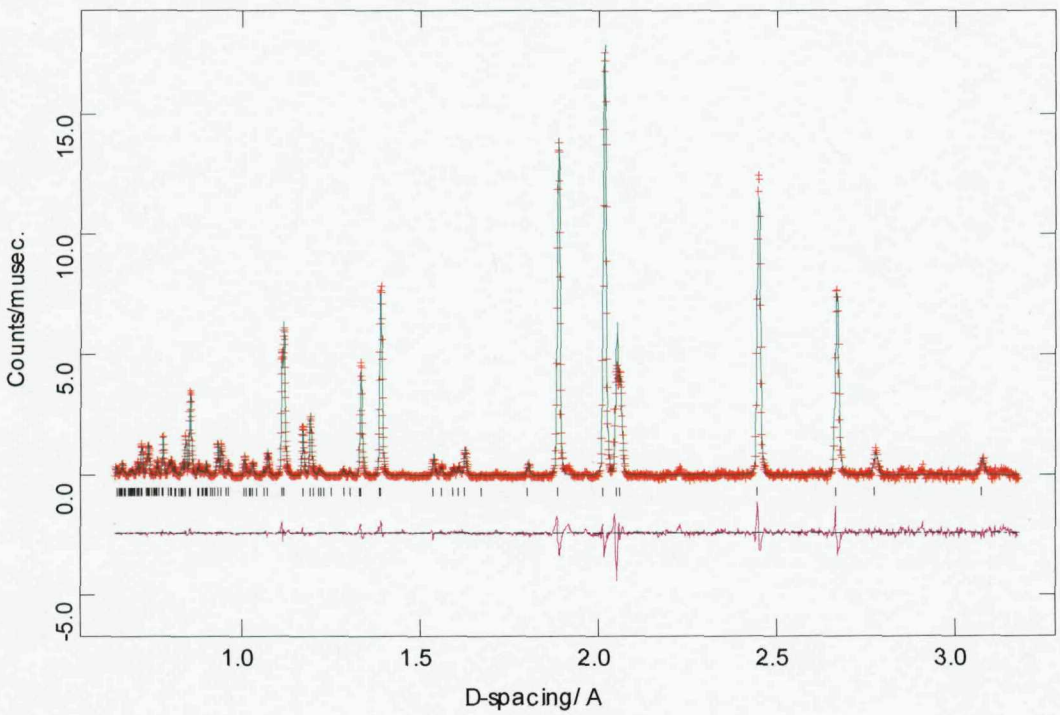

Figure 10 PND refinement profile for tetragonal $NdSrCoO_4$ at 300 K *(crosses indicate observed data, the upper continuous line shows calculated profile, the lower continuous line the difference and tick marks show reflection positions).*

Table 11 Atomic positions and thermal parameters for $^{154}SmSrCoO_4$ from 300 K PND data.

Space group I4/mmm; a = 3.7653(1) and c =12.2328(2) Å (e.s.d's are given in parentheses).

Atom	x	y	z	Occupancy	U_{iso} x 100/Å^2
Sm/Sr	0	0	0.3603(1)	0.5 /0.5	0.16(2)
Co	0	0	0	1	-0.50(5)
O1	0	0.5	0	1	0.55(2)
O2	0	0	0.1655(1)	1	0.85(3)

$\chi^2 = 0.46$, $R_p = 1.74\%$, $R_{wp} = 3.30\%$

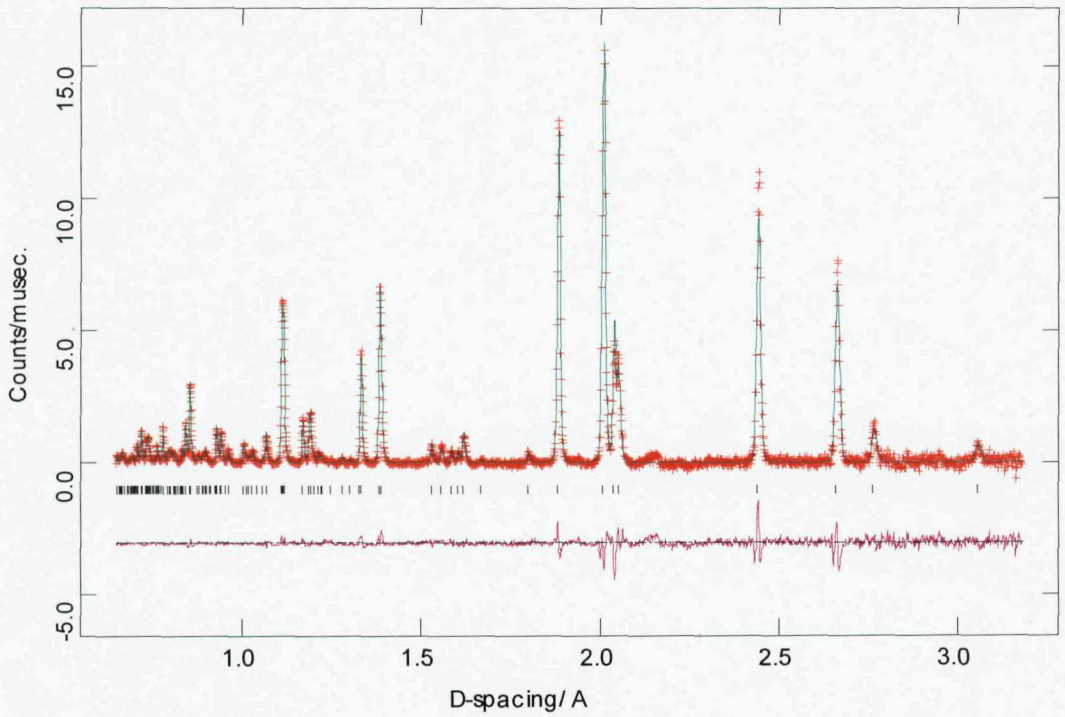

Figure 11 PND refinement profile for tetragonal $^{154}SmSrCoO_4$ at 300 K *(crosses indicate observed data, the upper continuous line shows calculated profile, the lower continuous line the difference and tick marks show reflection positions).*

Table 12 Atomic positions and thermal parameters for $^{160}GdSrCoO_4$ from 300 K PND data.

Space group I4/mmm; a = 3.7561(1) and c = 12.1796(6) Å (e.s.d's are given in parentheses).

Atom	x	y	z	Occupancy	U_{iso} x 100/Å^2
Gd/ Sr	0	0	0.3609(2)	0.5 /0.5	0.07(2)
Co	0	0	0	1	-0.30(5)
O1	0	0.5	0	1	0.56(4)
O2	0	0	0.1663(2)	1	0.74(4)

$\chi^2 = 0.19$, $R_p = 1.28\%$, $R_{wp} = 1.93\%$

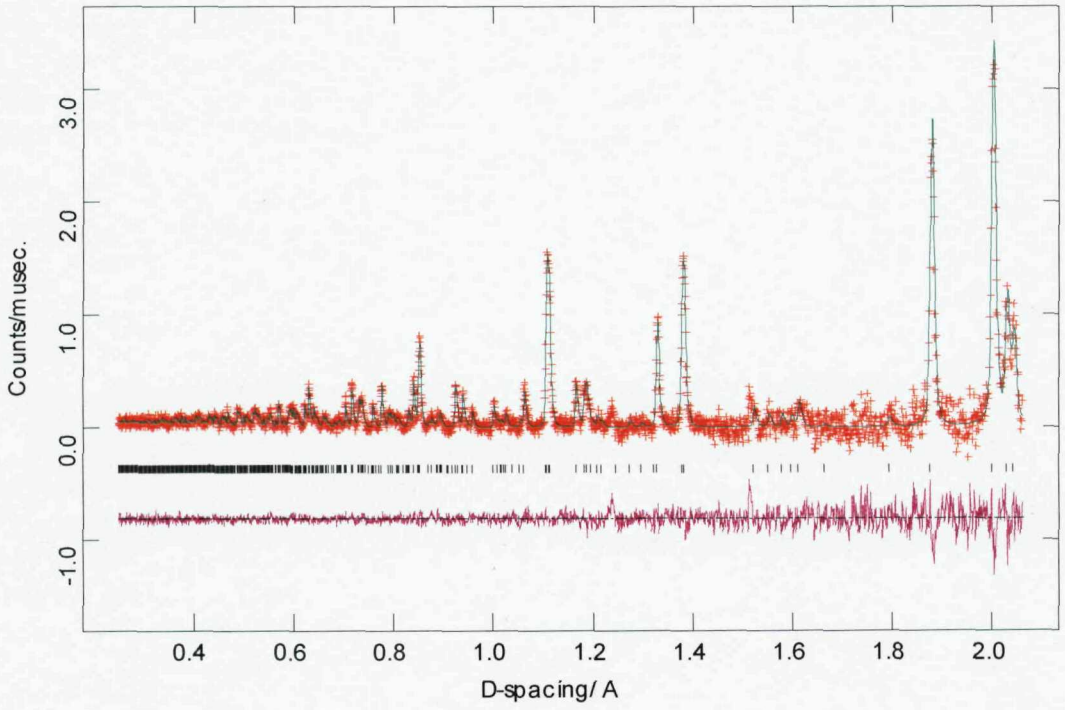

Figure 12 PND refinement profile for tetragonal $^{160}GdSrCoO_4$ at 300 K *(crosses indicate observed data, the upper continuous line shows calculated profile, the lower continuous line the difference and tick marks show reflection positions).*

4.5.3 Discussion

Orbital degeneracy can be created by thermally inducing a spin transition, the ground state of Co^{3+} ions is the LS, (S = 0), (t_{2g}^6, e_g^0), and can be thermally excited to either a HS, (S = 2), ($t_{2g}^4e_g^2$) or an IS (S = 1), ($t_{2g}^5e_g^1$) configuration. Previous studies on $LaSrCoO_4$ by Demazeau *et al.*[11] state that $LaSrCoO_4$ undergoes an IS to HS transition near 400 K. This is reflected in their extracted structural data as a weak change in the Co-O distances with a distinct increase in the axial Co-O distance relative to the axial Co-O separation. In order to determine whether a thermally induced spin transition occurs in the $LnSrCoO_4$ series, variable temperature PXD and PND data were obtained in the temperature range 2 – 900 K. All variable temperature data can be modelled in the *I4/mmm* space group with good refinement statistics, no evidence was found for a lower symmetry structure caused by tilting or twisting of the octahedra as is found in materials such as La_2CoO_4 and Sm_2CoO_4.[17]

Throughout the series the *a* and *c* parameters increase linearly with temperature; the thermal expansion coefficients between 323 and 698 K were calculated using the formula:

$$\frac{\Delta L}{L_o \Delta T} = \alpha$$

where ΔL is the change in *a* or *c* parameter between 323 and 698 K, L_o is the *a* or *c* parameter at 323 K, ΔT is the change in temperature between 323 and 698 K and α is the thermal expansion coefficient. Graphs of the calculated linear thermal expansion coefficients as a function of the ionic radii of the lanthanide have been plotted (Figure 13). Expansion in the *a* direction through the $(CoO_4)_n$ layers of the network generally occurs at the same rate for all compounds. It is observed that the increase in the *c* direction comes from the expansion of the |Ln/Sr-O-Ln/Sr-O| layers between the perovskite blocks. Expansion in the *c* direction is greater than in the *a* direction this is due to the bonds in the *c* direction being much weaker. As the size of the rare earth gets smaller the whole structure shrinks both in the *ab* plane and along *c*, the bigger effect comes from

the contraction of the |Ln/Sr-O-Ln/Sr-O| layers i.e. the structure becomes more rigid. As a result the thermal expansion coefficient decreases as the size of the lanthanide decreases.

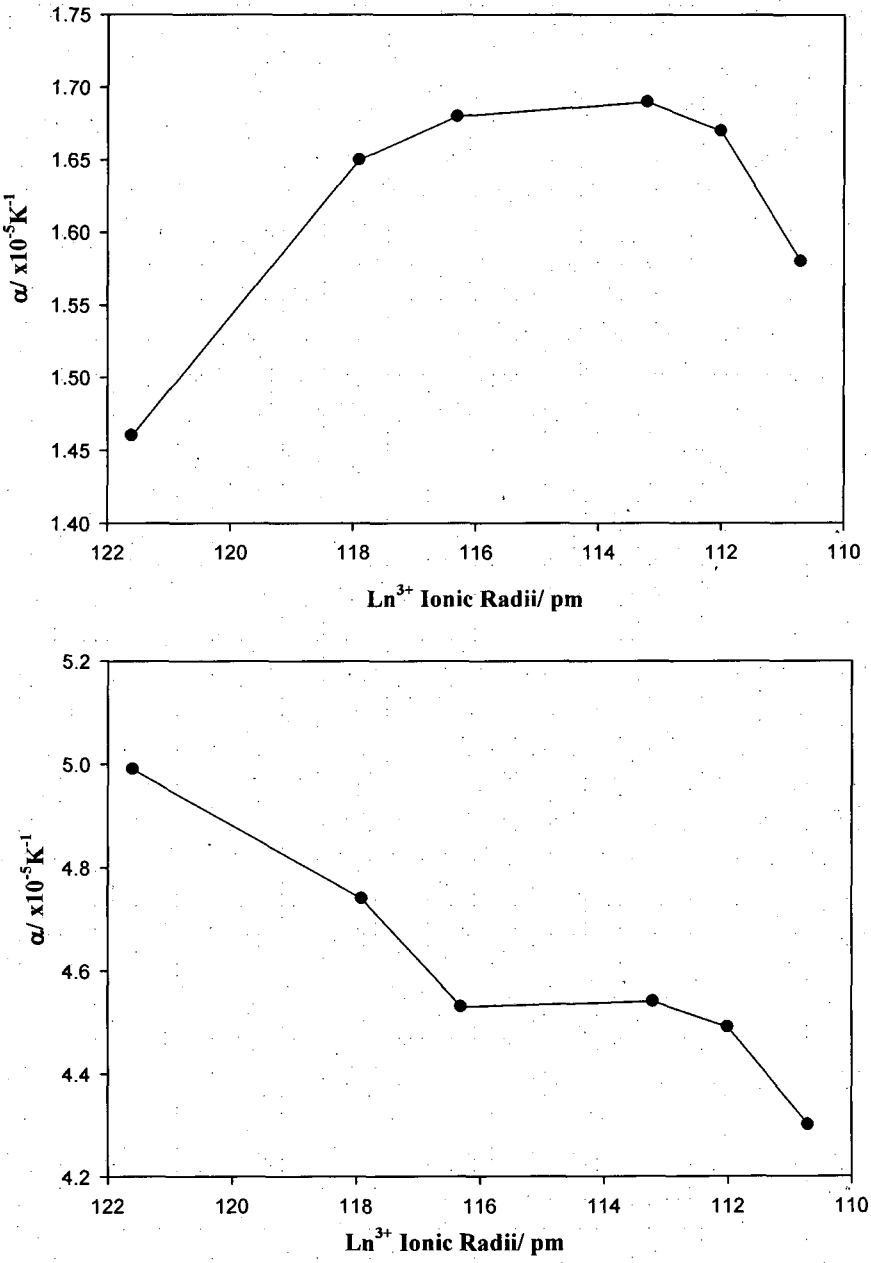

Figure 13 Graphs of Ln^{3+} ionic radii against the thermal expansion coefficients calculated for $LnSrCoO_4$ from PXD *a* (top) and *c* (bottom) parameters in the temperature range 323 – 698 K.

Data extracted from variable temperature PXD and PND Rietveld refinements were used to plot graphs of Co-O(axial) and Co-O(equatorial) bond distances as a function of temperature (Figures 14 - 23), the extracted values agree with

literature data. It is important to note that the PND data is a better representation of the variation of Co-O bond distances due to the inherent ability of PND to accurately determine oxygen positions within the structure. The large shift in the Co-O equatorial bond distance for $^{154}SmSrCoO_4$ between 250 and 300 K and the anomalous Co-O axial and equatorial bond distances for $LaSrCoO_4$ and $NdSrCoO_4$ at 200 K are the result of a change in the sample environment of the compound. The low temperature data were collected in a cryostat and the high temperature data in a hot stage CCR. All compounds generally show a smooth expansion in both the Co-O axial and equatorial bond distances. However, the PXD data show some anomalies in behaviour which are not reciprocated in the PND data with the exception of $GdSrCoO_4$ and are described in Table 13. $GdSrCoO_4$ shows an increased expansion in the axial Co-O bond distance at ~ 650 – 700 K in both PXD and PND data, this could be assigned to a change in the spin state of the Co^{3+} ions.

Table 13 Temperature Regimes of the variation in Co-O axial bond distance as a function of temperature (PXD).

$LnSrCoO_4$	PXD Temperature Range (K)	Comment	PND Temperature Range (K)	Comment
La	298 – 773	Increased expansion at ~425 K	50 – 650	Smooth expansion
Pr	348 – 898	Smooth expansion	N/A	N/A
Nd	298 – 798	Smooth expansion	50 – 600	Smooth expansion
Sm	298 – 773	Smooth expansion	50 – 850	Smooth expansion
Eu	298 – 873	Smooth expansion	N/A	N/A
Gd	298 - 873	Increased expansion at ~700 K	125 - 675	Increased expansion at ~650 K

It is conclusive to say that for $GdSrCoO_4$ the changes that occur in the Co-O(axial) bond distances as the temperature increases are genuine as they occur in both PXD and PND analysis. An explanation for the high transition temperature in $GdSrCoO_4$ can be accounted for by the smaller ionic radii of Gd^{3+}. In the study of $LaCoO_3$ under pressure[18] it was found that the LS to IS transition detected by magnetisation, shifts rapidly to higher temperatures on decreasing the cell volume. The shift could be understood in terms of the volume

dependence of the energy difference Δ_1 between the LS and IS states. Decreasing the size of the lanthanide from La^{3+} to Gd^{3+} acts as a form of internal pressure, and as a result some compression of the Co-O bond length is expected. This contraction would then cause an increase in the energy-level splitting resulting in an upward shift of the transition temperatures.

Following a spin crossover from LS-IS or IS-HS a marked increase in both the axial and equatorial Co-O bond lengths is expected as a result of the movement of electron density from t_{2g} to e_g orbitals which are σ antibonding in character. In these compounds in particular $GdSrCoO_4$, an increased expansion in the Co-O(axial) bond distance is observed, this may suggest that electron density is moving out of the t_{2g} orbitals resulting in a spin transition from IS-HS or LS-IS.

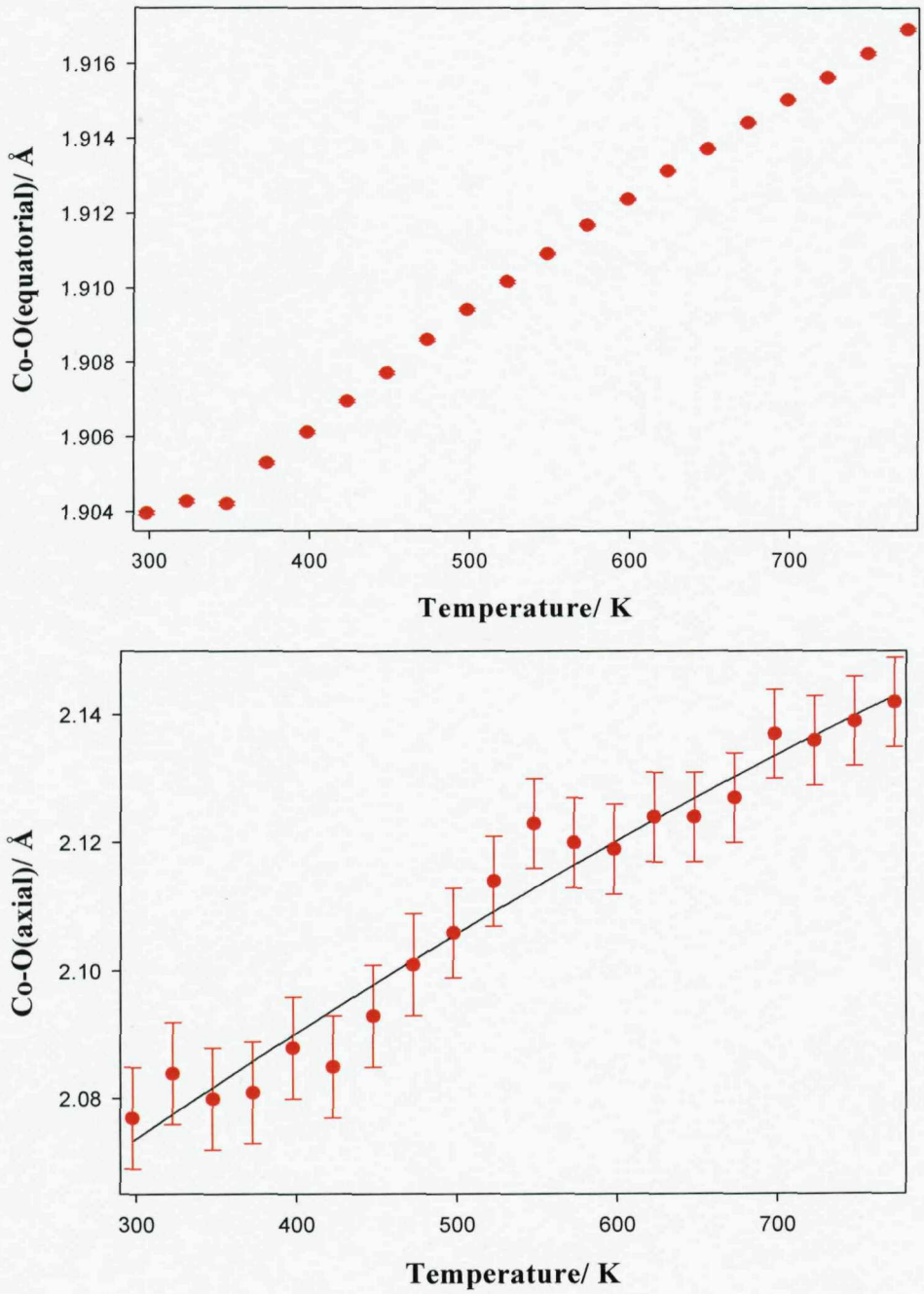

Figure 14 Co-O(equatorial) (top) and Co-O(axial) (bottom) bond distances as a function of temperature for $LaSrCoO_4$ as extracted from PXD data.

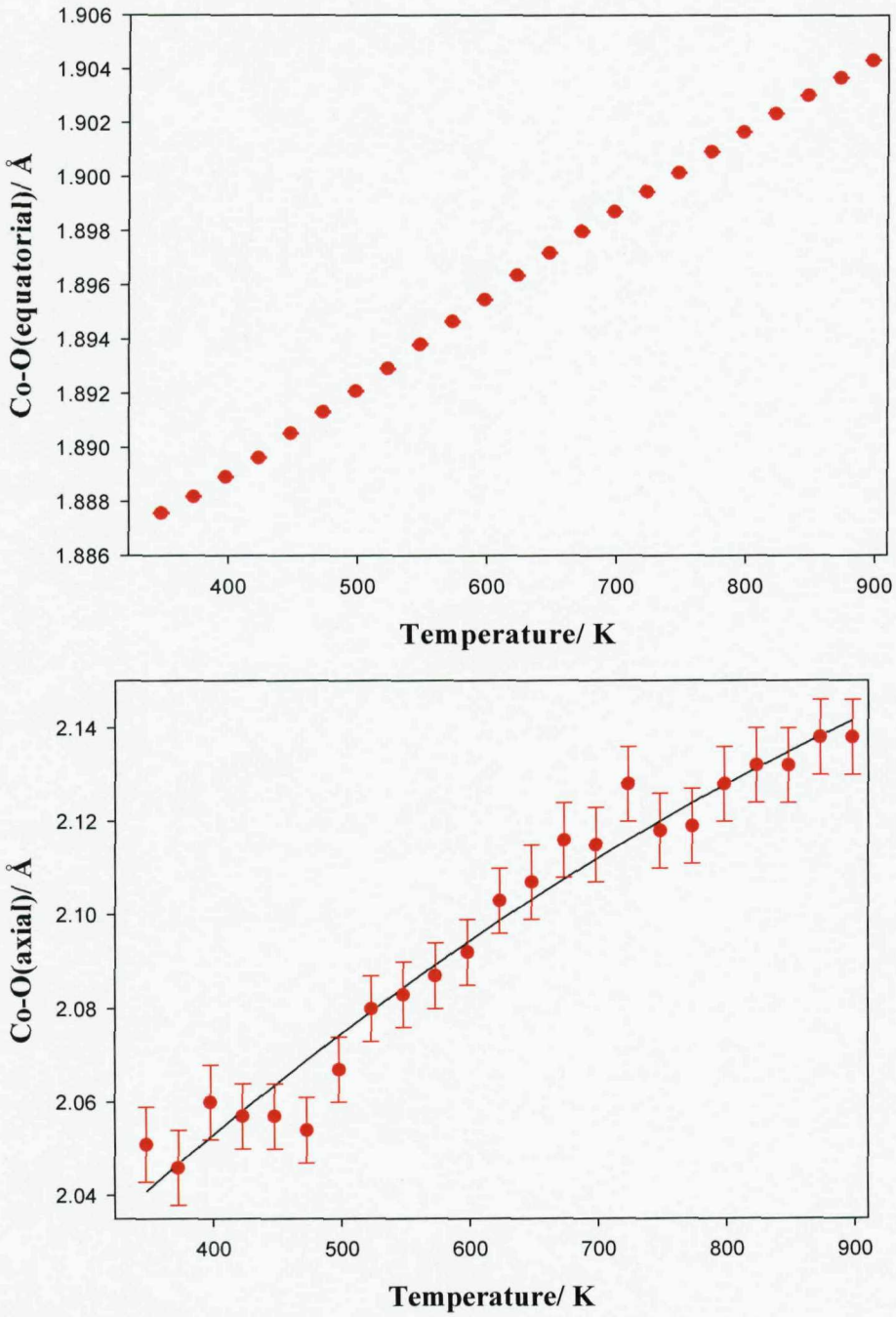

Figure 15 Co-O(equiatorial) (top) and Co-O(axial) (bottom) bond distances as a function of temperature for $PrSrCoO_4$ as extracted from PXD data.

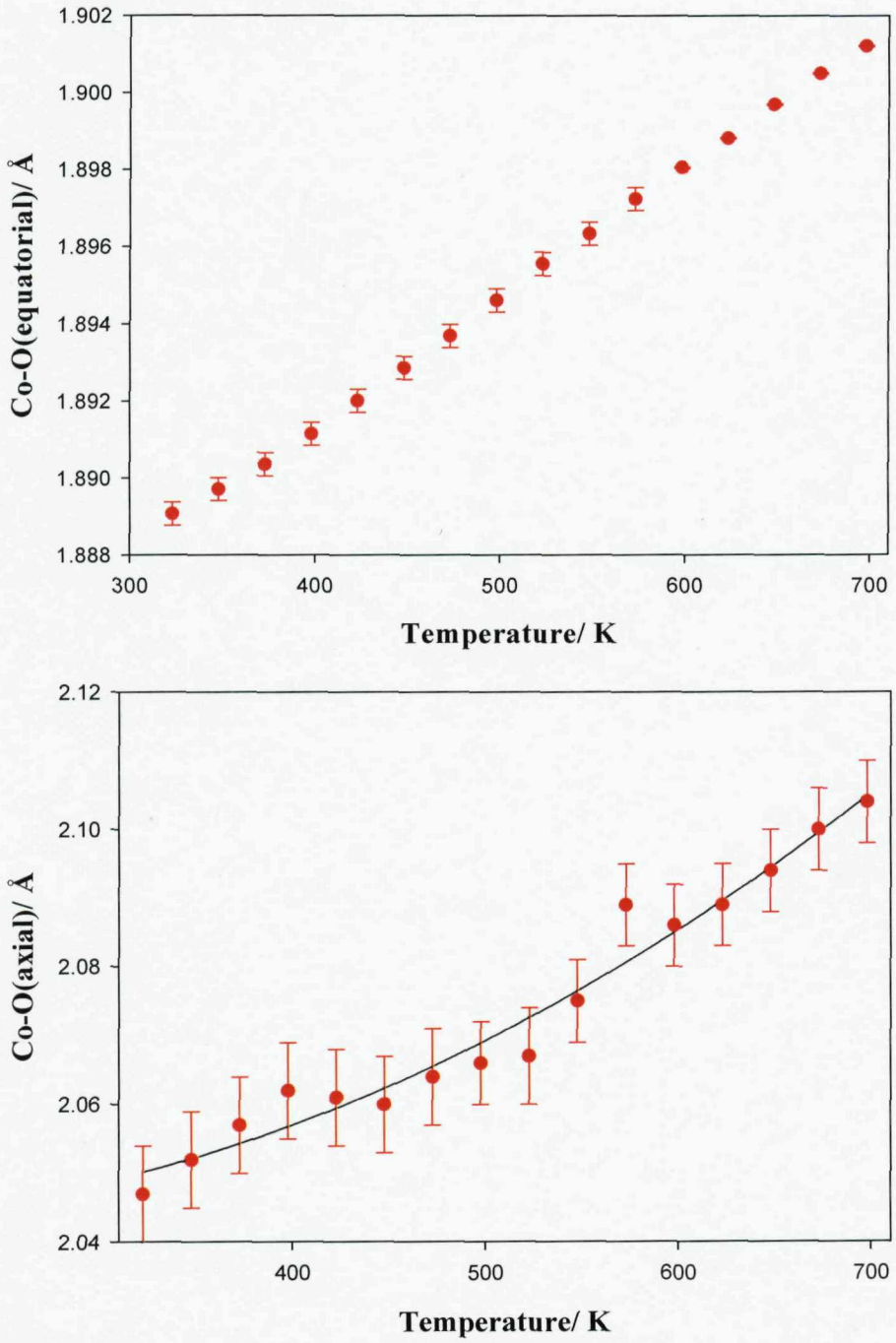

Figure 16 Co-O(equatorial) (top) and Co-O(axial) (bottom) bond distances as a function of temperature for $NdSrCoO_4$ as extracted from PXD data.

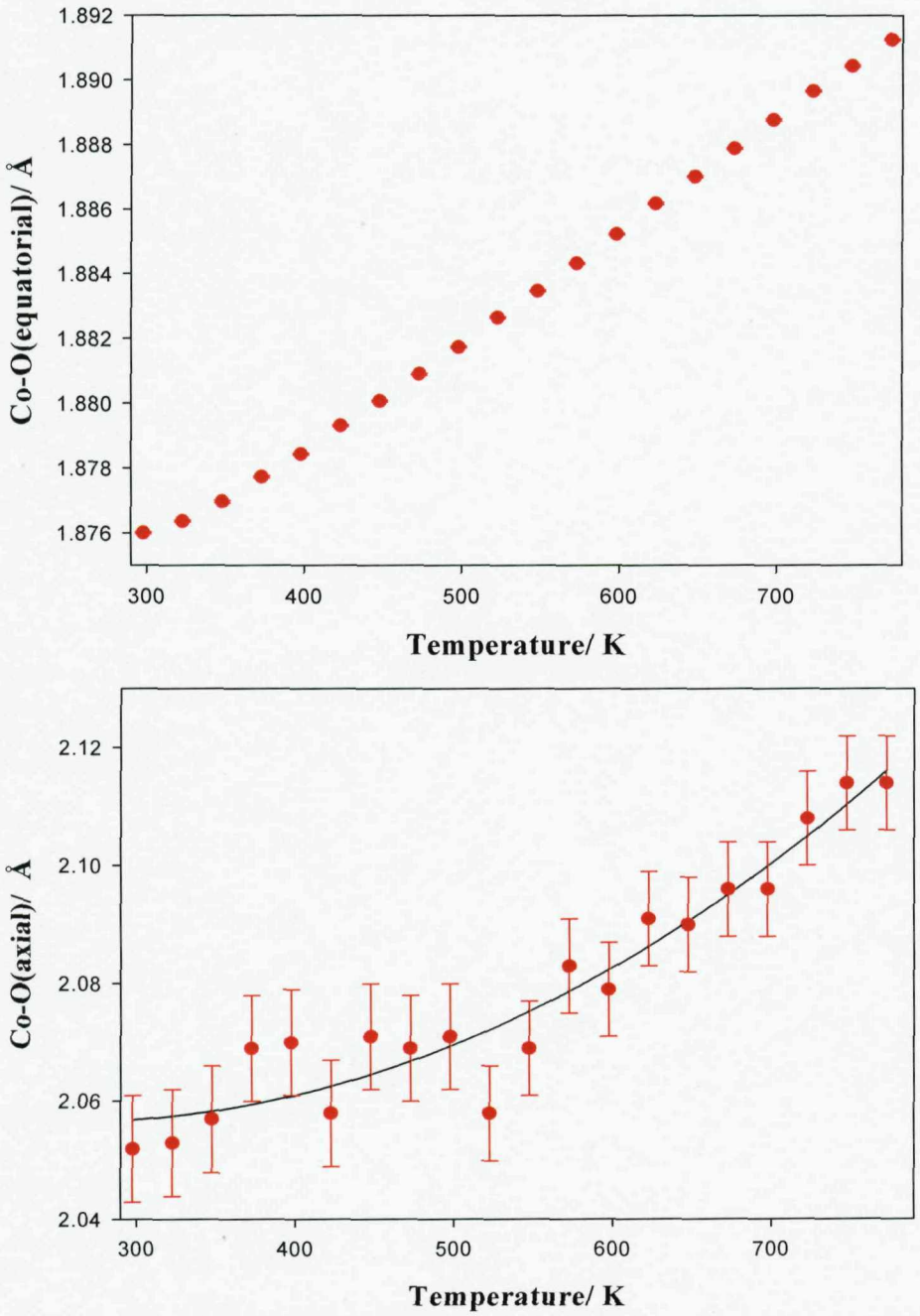

Figure 17 Co-O(equatorial) (top) and Co-O(axial) (bottom) bond distances as a function of temperature for $SmSrCoO_4$ as extracted from PXD data.

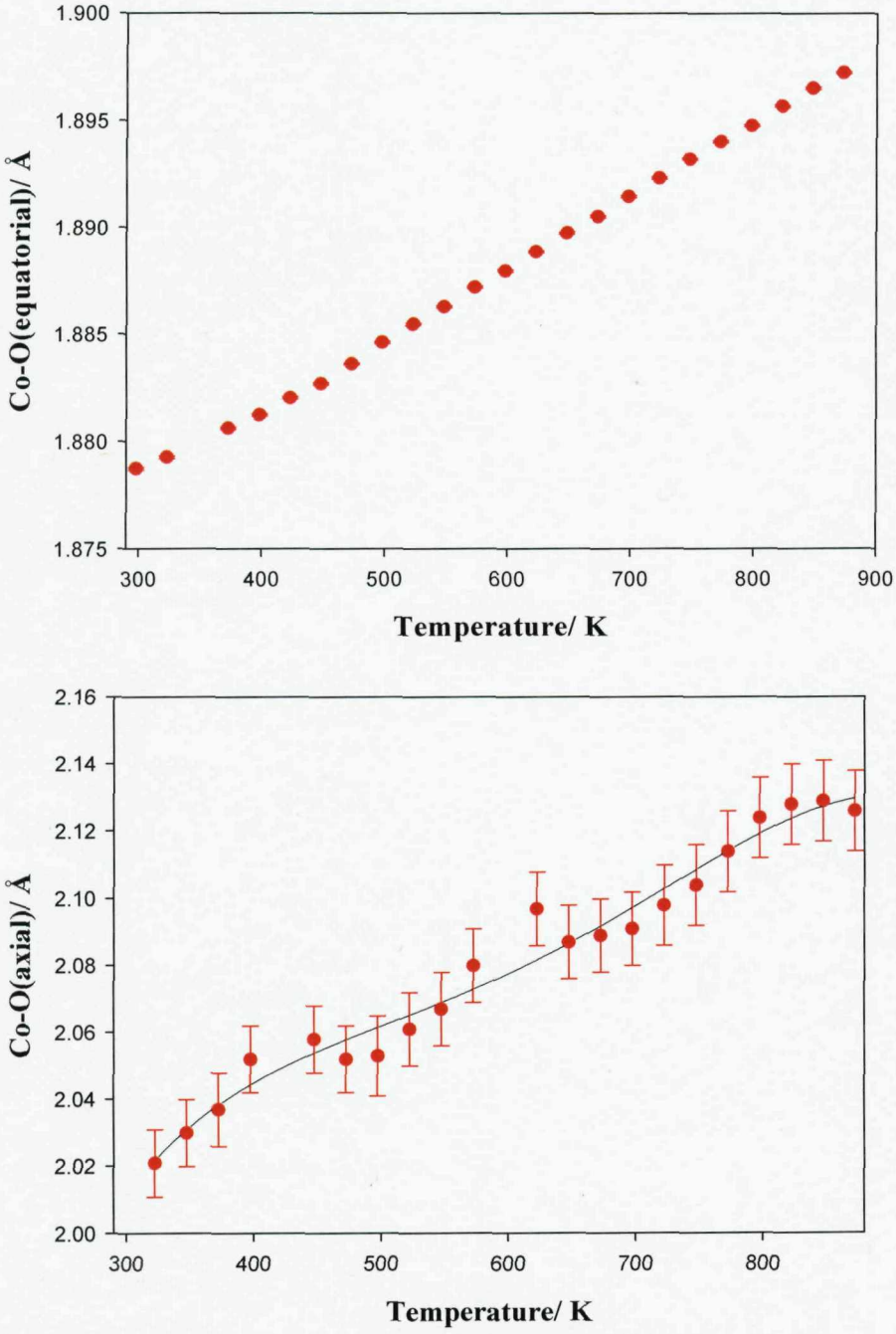

Figure 18 Co-O(equatorial) (top) and Co-O(axial) (bottom) bond distances as a function of temperature for $EuSrCoO_4$ as extracted from PXD data.

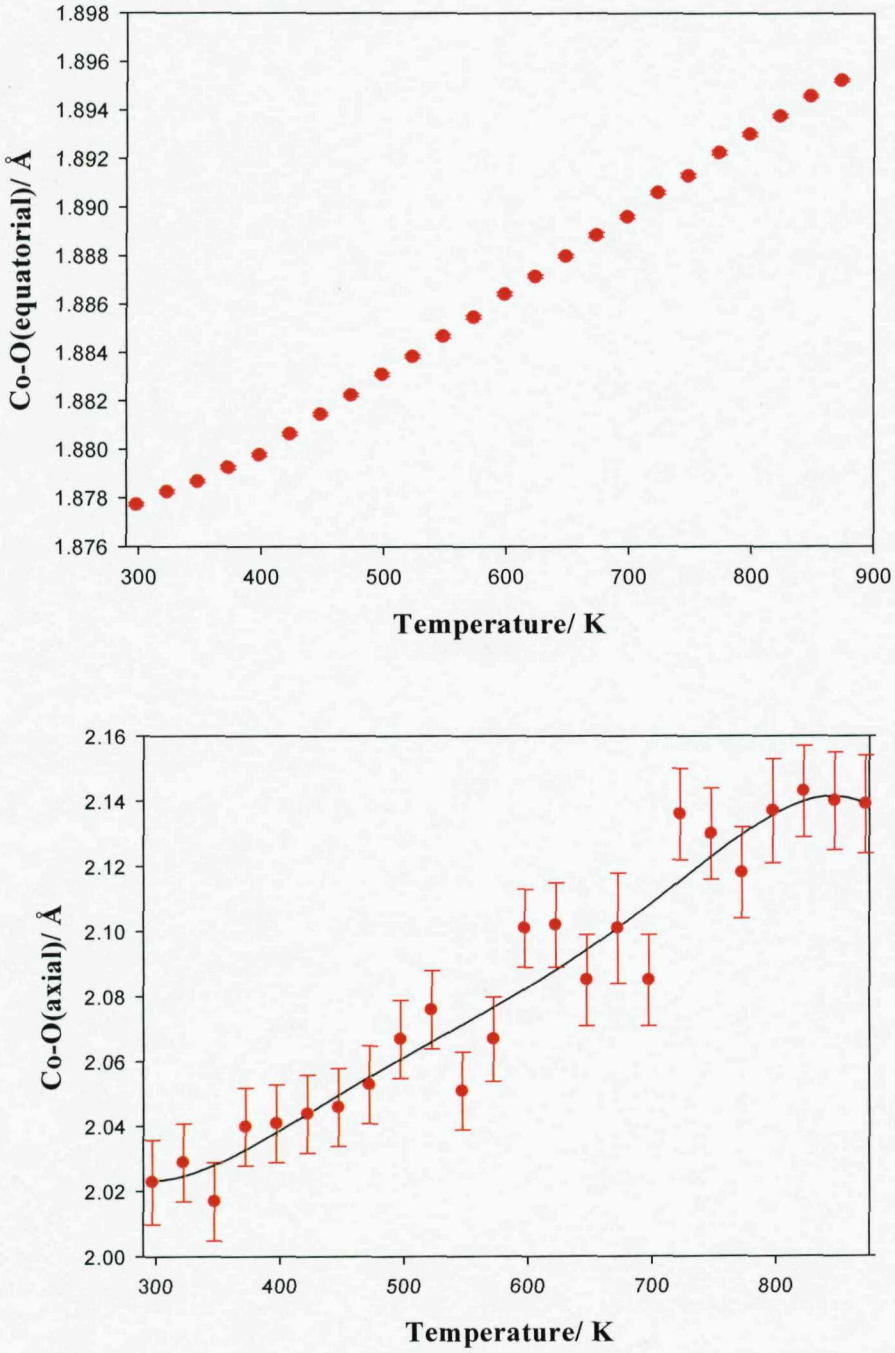

Figure 19 Co-O(equatorial) (top) and Co-O(axial) (bottom) bond distances as a function of temperature for $GdSrCoO_4$ as extracted from PXD data.

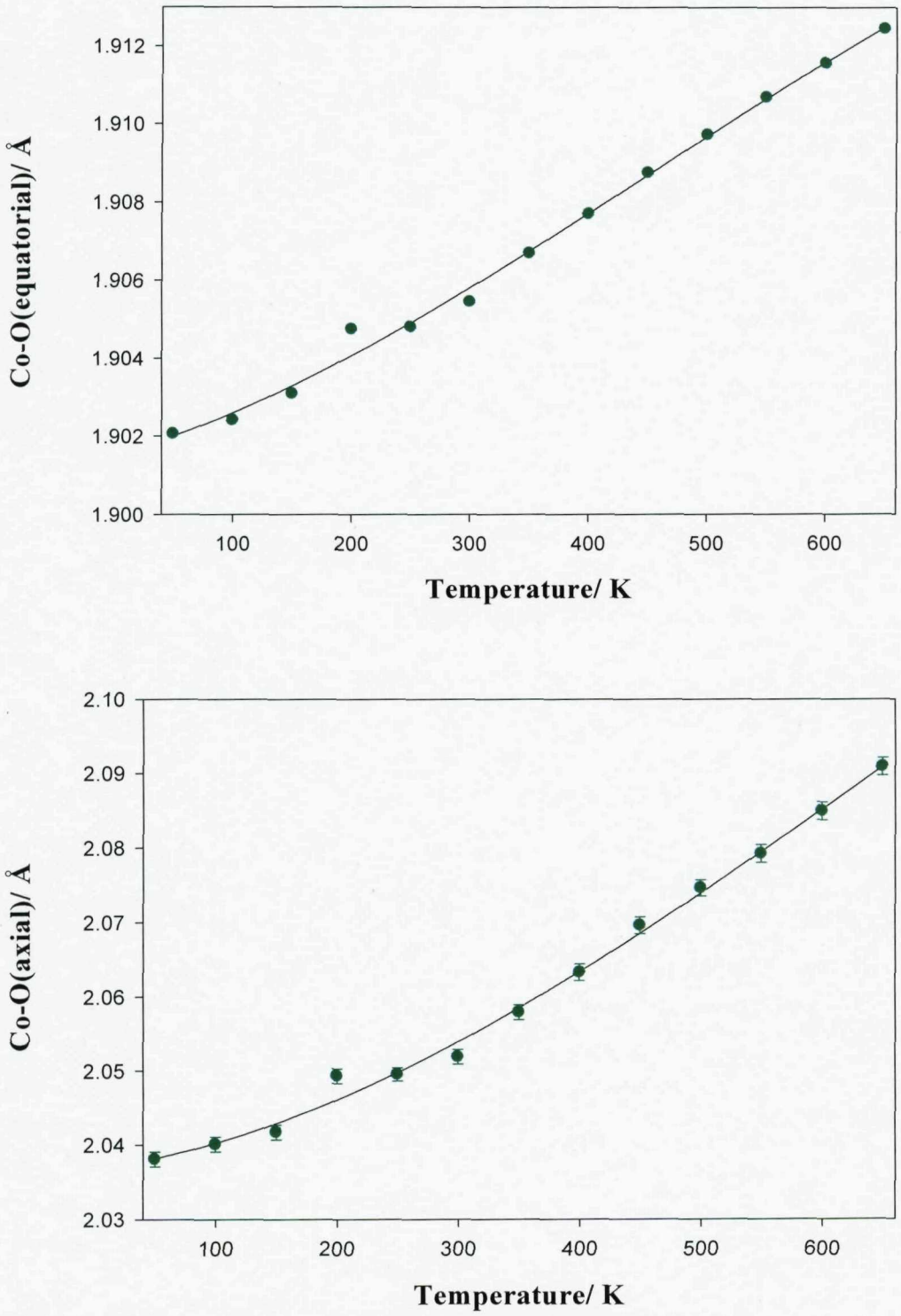

Figure 20 Co-O(equatorial) (top) and Co-O(axial) (bottom) bond distances as a function of temperature for $LaSrCoO_4$ as extracted from PND data.

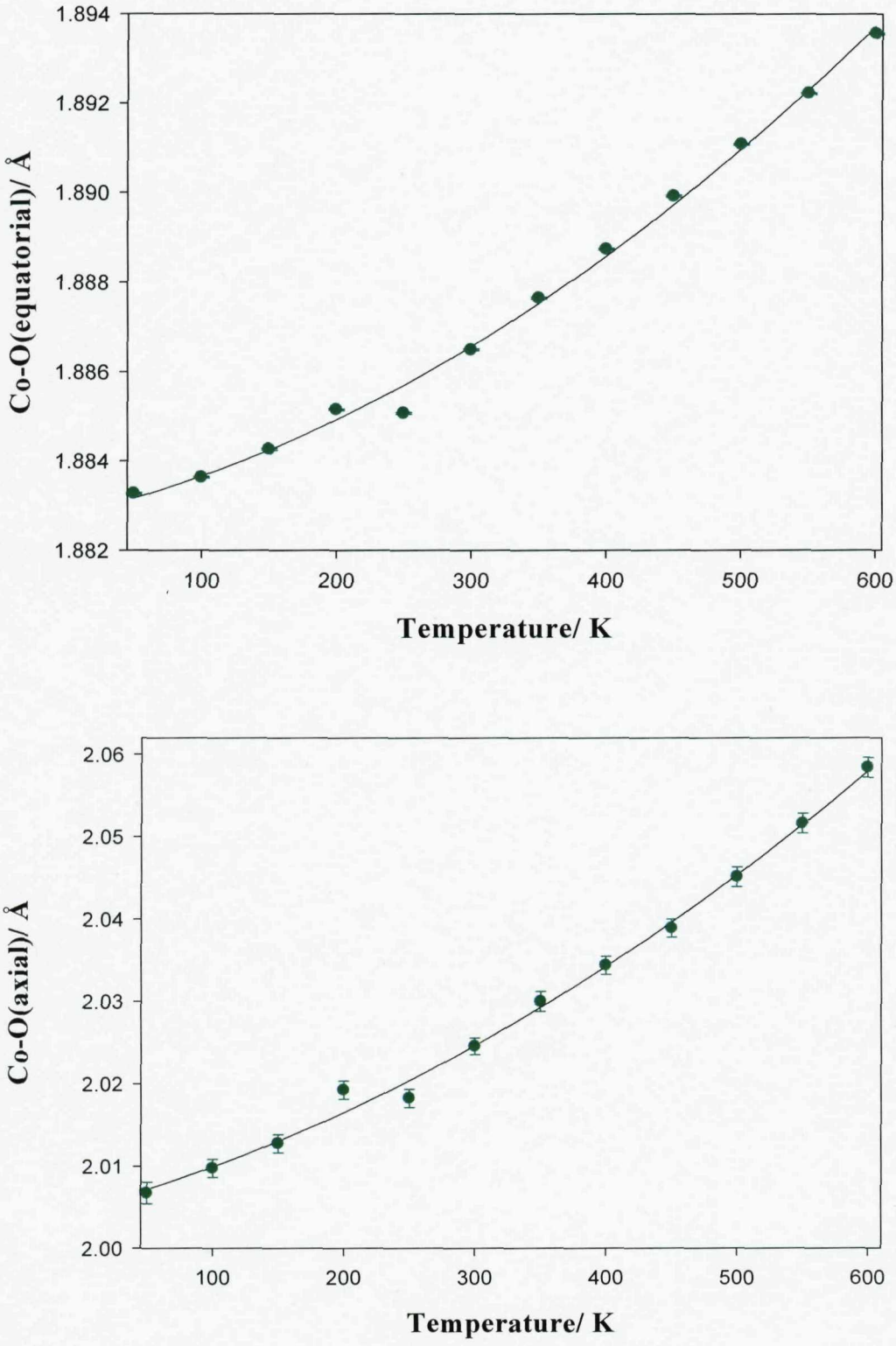

Figure 21 Co-O(equatorial) (top) and Co-O(axial) (bottom) bond distances as a function of temperature for $NdSrCoO_4$ as extracted from PND data.

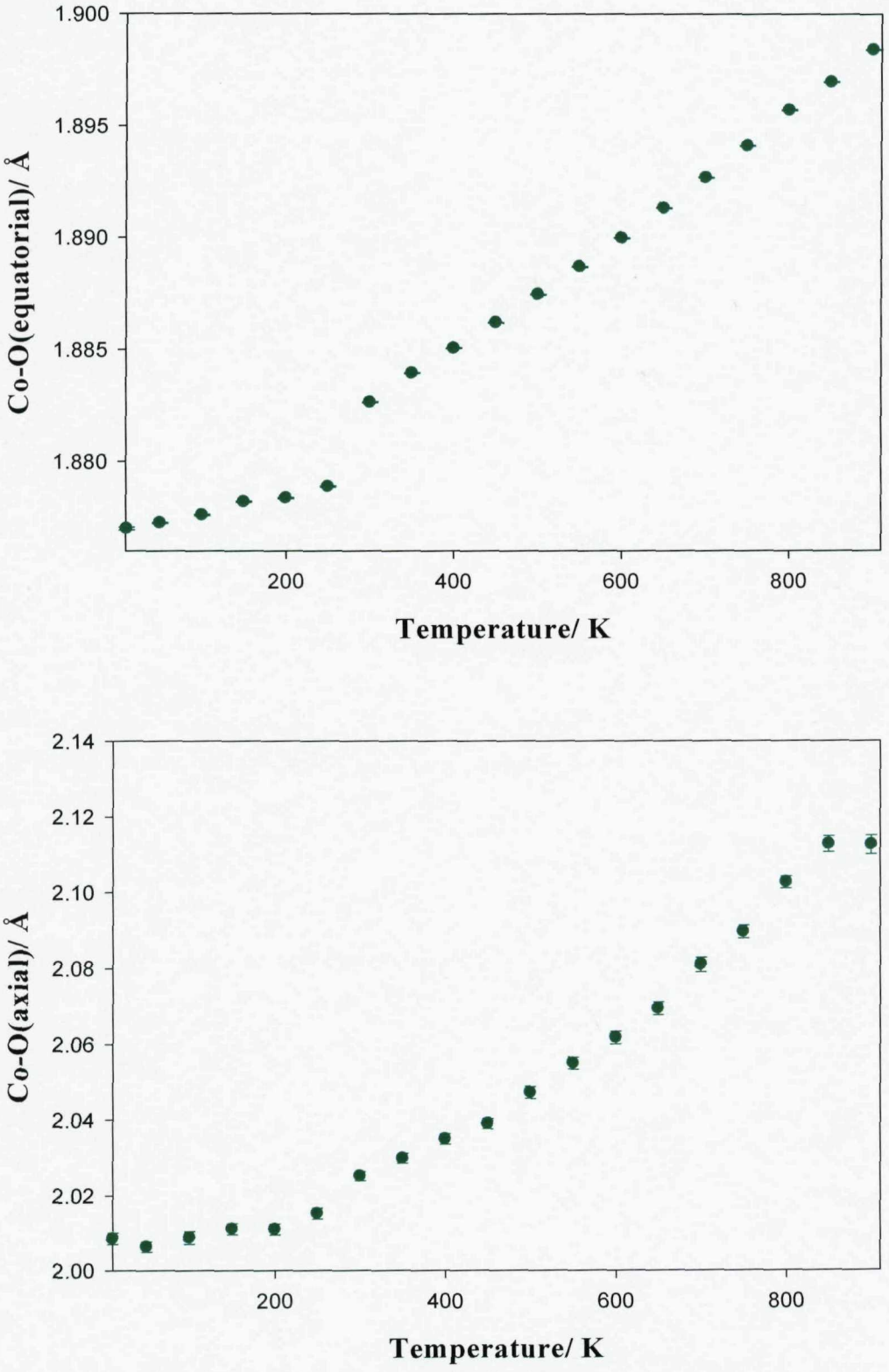

Figure 22 Co-O(equatorial) (top) and Co-O(axial) (bottom) bond distances as a function of temperature for $^{154}SmSrCoO_4$ as extracted from PND data.

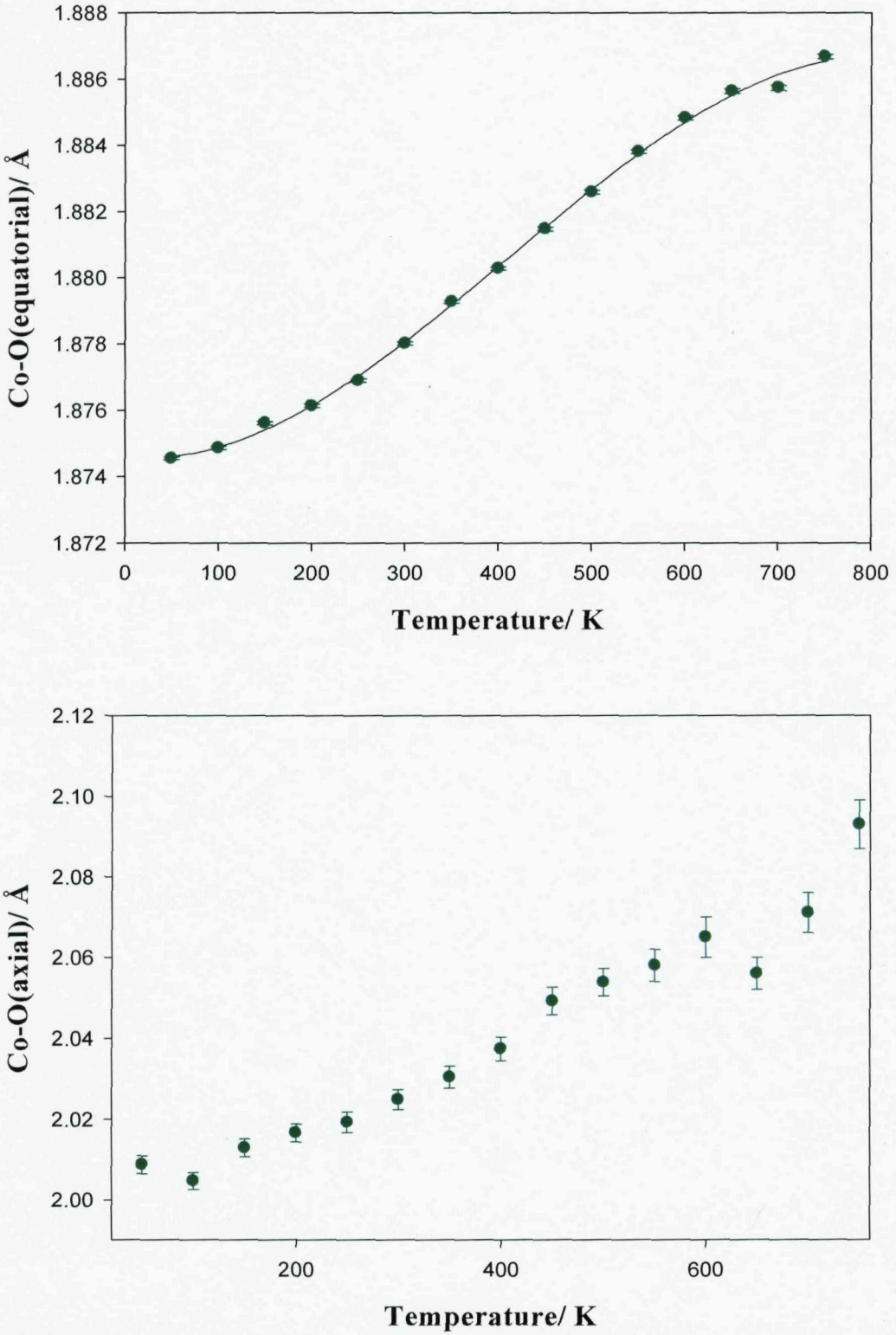

Figure 23 Co-O(equatorial) (top) and Co-O(axial) (bottom) bond distances as a function of temperature for $^{160}GdSrCoO_4$ as extracted from PND data.

4.6 Thermal Analysis

The oxygen content of selected $LnSrCoO_4$ (where Ln = Pr, Sm, Eu and Gd) compounds were studied using the Metler Toledo thermogravimetric analysis module. Samples were heated from room temperature to 1000 °C at 10 °C per minute, held for 30 minutes and cooled back to room temperature at 20 °C per minute. Figure 24 displays the thermogravimetric data obtained for several of these compounds. The oxygen contents were found to be slightly but consistently above 4.00 atoms per formula unit. There does not seem to be a trend in oxygen levels based on different rare earth ionic radii. The reduction of these compounds takes place in two stages giving rise to two plateaus, one at approximately $600 \leq T \leq 1000$ °C which corresponds to a mass loss of approximately 3% and a second plateau at $T \geq 1000$ °C. The first plateau is thought to correspond to metastable phases containing Co^{2+}, the presence of such a phase has been previously noted for $LaSrCoO_{3-x}$ by Hayward and Rosseinsky.[19] The second plateau corresponds to the complete reduction to Ln_2O_3, SrO and Co metal, this was confirmed by PXD on the samples after TGA. From the total weight loss we have calculated the oxygen content of these samples. Results show that there is a small oxygen gain giving rise to $PrSrCoO_{4.07(10)}$, $EuSrCoO_{4.07(10)}$, $SmSrCoO_{4.06(10)}$ and $GdSrCoO_{4.04(10)}$. Although little data has been published that describes oxygen non-stoichiometry for rare-earth strontium doped cobaltates, the K_2NiF_4 structure can accommodate considerable amounts of additional lattice oxygen. Oxygen non-stoichiometry in La_2CuO_4 has been previously investigated and it has been shown that extra oxygen atoms can easily be spread across the network.

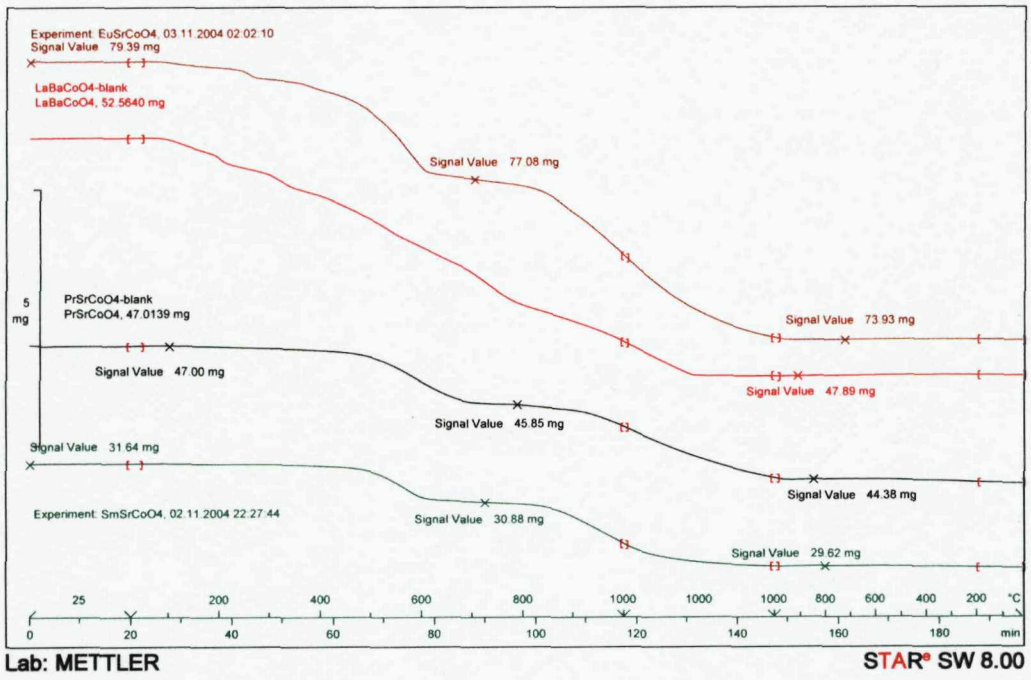

Figure 24 Thermogravimetric data for the reduction of the $LnSrCoO_{4+\delta}$ (where Ln = Pr, Eu and Sm) compounds with 5% H_2 in N_2.

4.7 Comparison with other K_2NiF_4 oxides

It is well known that the transition-metal oxides display a wide variety of complex behaviors. The physical properties of the oxides of the 3*d* transition metals such as Fe, Co and Ni, having a single layered perovskite structure (K_2NiF_4 type), have been studied with interest due to the similarity of these oxides with the superconducting Cu oxides and the fascinating properties that they exhibit. One of these interesting compounds is the Fe-based layered perovskite oxide, $LaSrFeO_4$, whose atomic and magnetic structure was first studied by Souberoux *et al.*[6] using X-ray diffraction, Mössbauer spectroscopy and neutron diffraction in the polycrystalline state. This study as well as earlier papers reported its structure to be orthorhombic ($a \sim 3.87$ Å and $c \sim 12.7$ Å) with space group I4/*mmm*. $LaSrFeO_4$ orders antiferromagnetically below 350 K, the compound exhibits a magnetic structure described by orthorhombic *Cmca*-type symmetry and two magnetic propagation vectors q1 = (½,½,0) and q2 = (-½,½,0) representing the two possible magnetic domains. A collinear antiferromagnetic arrangement of the Fe^{3+} moments confined to the tetragonal

basal plane is found. Bulk magnetic studies on $LaSrFeO_4$ show that the properties of this compound are highly anisotropic, and there is evidence for additional magnetic transitions at lower temperatures (30 and 90 K).[20]

Another interesting K_2NiF_4-type compound is $La_{2-x}Sr_xCuO_4$, which is the simplest copper oxide superconductor and its systematic study has revealed an evolution from the antiferromagnetic (AFM) insulator to a normal metal *via* a superconducting state ($0.07 \leq x \leq 0.24$; $T_c \approx 36$ K for $x = 0.15(1)$). The AFM order is caused by the Cu-moments which are ordered below $T_N = 320$ K. The crystal structure is orthorhombic (*Cmca*) and contains distorted CuO_6 octahedra. The CuO_2 planes are buckled to relieve compressive stress caused by the mismatch of (La,Sr)-O and Cu-O bonds. As x exceeds 0.21 a structural transition into the tetragonal *I4/mmm*, K_2NiF_4-type structure occurs and simultaneously the superconducting transition temperature decreases rapidly.

It is interesting to compare the various transition metal compounds adopting the K_2NiF_4 structure. Table 14 allows a comparison of the axial and equatorial B-O bond lengths for Cu^{3+}, Co^{3+}, Fe^{3+}, Ni^{3+}, Mn^{3+} and V^{3+}. It is expected that as the transition metal (B) ionic radii decrease so do the B-O bond distances, however the data presented in this study shows no such variation. This may be a result of PXD data being collected on different instruments under different conditions. In all cases the B-O axial bond distances are longer than the B-O equatorial. As expected replacing the smaller Sr^{2+} (1.31 Å) for Ba^{2+} (1.47 Å), causes the B-O bond distances to expand. The axial B-O bond distance as a function of temperature for $LaSrBO_4$ (where B = Co^{3+} and Fe^{3+}), $La_{1.8}Sr_{0.2}CuO_4$ and $LaBaCoO_4$ have been compared. The axial Co-O distance increases much more rapidly than the equatorial Co-O distance, this behavior contrasts strongly with that of the compositionally identical $LaSrFeO_4$ which shows almost an invariant axial to equatorial distance ratio. The Co-O axial bond length also increases much more rapidly than the Fe-O and Cu-O with a 1.62, 0.6 and 0.75% expansion respectively in the temperature range 300 – 600 K. The larger expansion in the axial Co-O compared with Fe-O and Cu-O can only be seen when the bond distance is plotted as a function of temperature on the same scale

(Figure 25). $La_{1.8}Sr_{0.2}CuO_4$ contains mainly Cu^{2+} and some Cu^{3+} ions; Cu^{2+} is a true Jahn-Teller species and Cu^{3+} prefers a square planar geometry, as a result the axial bond distances are initially much longer and thus the interactions are weaker. The increasing thermal energy therefore has very little effect on this axial distance i.e. the increased vibrations are pushing the nearest neighbors away first and do not really affect those further away. We are also seeing a similar affect in the Fe^{3+} compound.

This comparison enables us to identify that the Co(III) compounds expand much faster in the axial direction. If low spin Co^{3+} (S = 0), (t_{2g}^6, e_g^0) $dxy^2dzy^2dxz^2$ can be thermally excited to an intermediate-spin (S = 1) ($t_{2g}^5e_g^1$), the electron density would transfer to the dz^2 orbital, this would expand the axial distance faster than a normal thermal effect. This supports the conclusion that a spin crossover is occurring in the $LnSrCoO_4$ compounds.

Table 14 TM-O bond distances for selected compounds.

Compound	TM Ionic radii (Å)	TM-O(equatorial)/ Å	TM-O(axial)/ Å
$LaBaFeO_4$[21]	0.55	1.9605	2.1739
$LaBaCoO_4$*	0.545	1.9307(1)	2.1283(17)
$LaSrCuO_4$[22]	0.54	1.8825	2.243
$LaSrCoO_4$*	0.545	1.9026(1)	2.069(11)
$LaSrFeO_4$*	0.55	1.9359(1)	2.148(22)
$LaSrNiO_4$[23]	0.56	1.9120	2.0494
$LaSrMnO_4$[24]	0.58	1.8930	2.2668
$LaSrVO_4$[25]	0.64	1.9414	2.1335

*extracted from this work

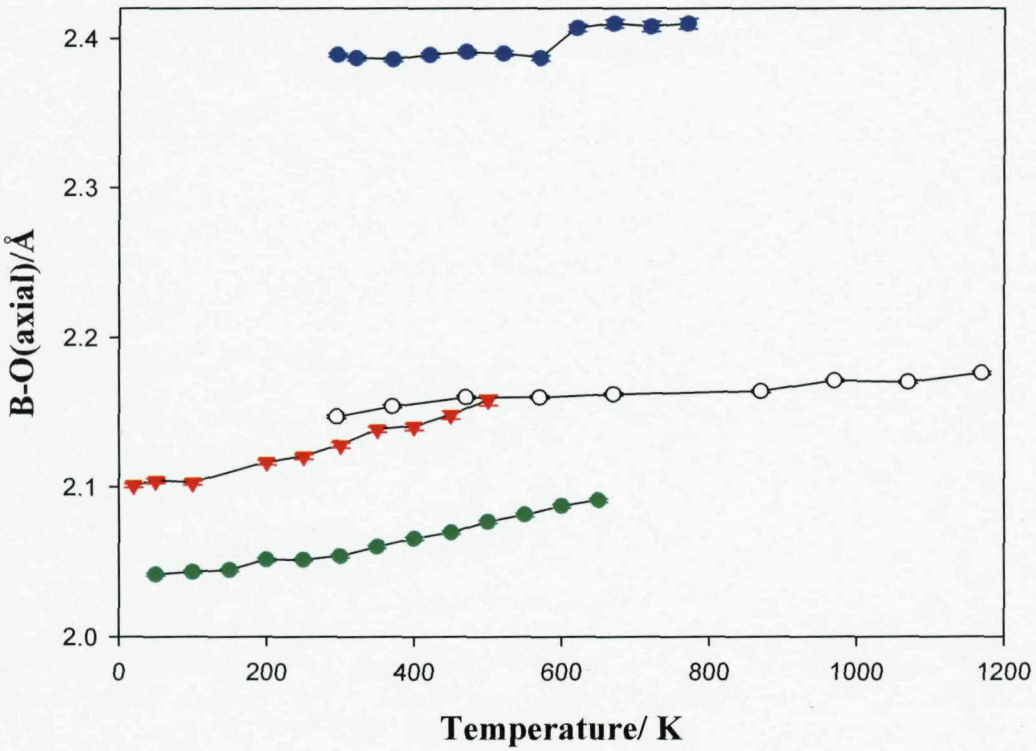

Figure 25 Variation in the B-O axial bond length as a function of temperature (● $LaSrCoO_4$, ▼ $LaBaCoO_4$, ○$LaSrFeO_4$ and ● $La_{1.8}Sr_{0.2}CuO_4$).

4.8 Conclusion

An investigation into the $LnSrCoO_4$ (Ln = La, Pr, Nd, Sm, Eu and Gd) series has been performed. Detailed structural analysis on these materials were carried out using PXD, PND, magnetic susceptibility measurements and TGA on selected samples. The compounds were found to adopt the K_2NiF_4 structure in the I4/*mmm* space group as previously reported. As you go along the lanthanide series from La → Er, the K_2NiF_4 structure is maintained until Tb is incorporated. The mismatch between the perovskite Co-O layer and the rocksalt (Sr/ Ln)-O layers become too great and $SrLn_2O_4$ is formed as result.

Strong variations in the magnetic susceptibility data for $NdSrCoO_4$ were observed, the χ vs T graph shows that ferromagnetic ordering sets in at ~ 200 K, another transition also occurs at ~ 525 K which may be assigned to a spin state transition, however as a result of the magnetic contribution of Nd^{3+} it is inconclusive. Variable temperature PXD and PND data were collected in order

to determine whether these compounds undergo a thermally induced spin-crossover. Throughout the series *a* and *c* parameters increase linearly. The linear thermal expansion in the *a* direction through the $(CoO_4)_n$ layers of the network occurs at approximately the same rate for all the compounds. Expansion in the *c* direction is much greater and is at its highest for $LaSrCoO_4$ decreasing as the size of Ln^{3+} decreases. The graphs of Co-O axial and equatorial bond distances as a function of temperature have been plotted and anomalous behaviour is observed, particularly for $GdSrCoO_4$.

The comparison of the thermal expansion of the axial B-O distances in the compounds; $LaSrCoO_4$, $LaSrFeO_4$, $La_{1.8}Sr_{0.2}CuO_4$ and $LaBaCoO_4$ enabled us to identify that the Co(III) compounds expand much faster in the axial direction. If low spin Co^{3+} (S = 0), (t_{2g}^6, e_g^0) $dxy^2dzy^2dxz^2$ can be thermally excited to an intermediate-spin (IS) (S = 1), $(t_{2g}^5e_g^1)$, the electron density would transfer to the dz^2 orbital, this would expand the axial distance faster than a normal thermal effect. Based on this there is strong evidence that a spin transition occurs in these compounds. With further structural analysis through more beam time and better equipment we would be able to elucidate the structural and magnetic changes in more detail.

4.9 References

[1] I. Kozo, *Physica C (Amsterdam, Neth.)*, **185-189(Pt4)**, 2509 (1991).

[2] J. B. Boyce, F. Bridges, T. Claeson, T. H. Geballe, C. W. Chu, *Phys.Rev. B.*, **35**, 7203 (1987).

[3] K. D. Nelson, Z. Q. Mao, Y. Maeno and Y. Liu, *Science (Washington), DC, U. S)*, **306**, 5699 (2004).

[4] N. Nguyen, J. Choisnet, M. Hervieu and B. Raveau, *J. Solid State Chem.*, **39**, 120 (1981).

[5] G. N. Mazo, S. N. Savvin, E. V. Mychka, Y. A. Dobrovol'skii and L. S. Leonova, Russ. *J. Electrochem.*, **41**, 448 (2005).

[6] J. L. Soubeyroux, P. Courbin, L. Fournes, D. Fruchart and G. Le. Flem, *J. Solid State. Chem.*, **31**, 313 (1980).

[7] C. Bansal, H. Kawanaka, H. Bando, A. Sasahara, R. Miyamoto, Y. Nishihara, *Solid State Commun.*, **128**, 197 (2003).

[8] D. H. Peck, M. Miller, and K. Hilpert, *Solid State Ionics*, **123**, 59 (1999).

[9] J. E. Millburn, and M. J. Rosseinsky, *Chem. Mater.*, **9**, 511 (1997).

[10] G.Demazeau, P. Courbin, I. G. Main and G. Le Flem, *C. R. Acad. Sc.Paris, Section C*, **283**, 61 (1976)..

[11] G. Demazeau, Ph. Courbin, G. Le. Flem, M. Pouchard, P.Hagenmuller, J. L. Soubeyroux, I. G. Main and G. A. Robins, *Noveau Journal de Chimie*, **3**, 171 (1979).

[12] Y. Moritomo, K. Higashi, K. Matsuda and A. Nakamura, *Phys. Rev. B.*, **55**, 14725 (1997).

[13] R. J. Cava, B. Batlogg, T. T. Palstra, J. J. Krajewski, W. F. Jr. Peck, A. P. Ramirez, L. W. Jr. Rupp, *Phys. Rev. B.*, **43**, 1229 (1991).

[14] C. N. R. Rao, Md. M. Seikh and C. Narayana, *Topp. Curr. Chem*, **234**, 1 (2004).

[15] K. Asai, A. Yoneda, O. Yokokura, J. M. Tranquada, G. Shirane and K. Kohn, *J. Phys. Soc. Jpn.*, **67**, 290 (1998).

[16] Y. Furukawae, *et al.*, *J. Phys. Soc. Jpn.*, **62**, 1127 (1993).

[17] U. Lehman and H. Mueller-Buschbaum, *Zeitschrift fuer Anorganische und Allgemeine Chemie*, **470**, 59 (1980).

[18] T. Vogt, J. A. Hriljac, N. C. Hyatt and P. Woodward, *Phys. Rev. B.*, **67**, 140401(R) (2003).

[19] M. A. Hayward and M. J. Rosseinsky, *Chem. Mater.*, **12**, 2182 (2000).

[20] M. H. Jung, A. M. Alsmadi, S. Chang, M. R. Fitzsimmons, Y. Zhao, A. H. Lacerda, H. Kawanaka, S. El-Khatib, H. Nakotte, *J. Appl. Phys.*, **97**, 10A926 – 1 – 10A926 – 3 (2005).

[21] M. Valino, F. Abbattista, D. Mazza and A. Delunas, *Mat. Res. Bull.*, **21**, 733 (1986).

[22] J. B. Goodenough, G. Demazeau, M. Pouchard and P. Hagenmuller, *J. Solid State Chem.*, **8**, 325 (1973).

[23] J. E. Milburn, M. A. Green, D. A. Neumann and M. J. Rosseinsky, *J. Solid State. Chem.*, **145**, 401 (1999).

[24] D. Senff, P. Reutler, M. Braden, O. Friedt, D. Poruns, A. Cousson, F. Bouree, M. Merz, B. Buechner and A. Revcolevschi, *Phys. Rev. Series 3, B, Condensed Matter*, **71**, 024425-1-024425-8 (2005).

[25] J. E. Greedan and W. Gong, *Journal of Alloys Compd.*, **180**, 281 (1992).

Chapter Five

Synthesis, Structural and Magnetic Characterisation of $La_{1+x}Ba_{1-x}CoO_4$

5.1 Introduction

The previous chapter summarised the results obtained in the synthesis and structural investigation of the $LnSrCoO_4$ series using variable temperature PXD, PND and magnetic characterisation. Complex cobalt oxides with structures based on linked $Co(III)O_n$ polyhedra have been shown to exhibit a number of unusual electronic and magnetic properties associated with the various spin states of the Co(III) ion, these properties are derived from the specific electronic states of Co(III) in octahedral environments and the closeness in energies of the HS, IS and LS states. Transitions between these spin states may be thermally induced and lead to major changes in the compound's physical properties. This study revealed that throughout the series the *a* and *c* parameters increase linearly with temperature, i.e. the structures show thermal expansion in this temperature regime, which is understood in terms of the change in ionic radius of Co (or the Co-O bond distance) across the spin state transition. It was also observed that while the Co-O(equatorial) bond distance varies linearly as a function of temperature, the Co-O(axial) bond distance shows some anomalies as discussed in Chapter 4.

A comprehensive literature search has found no reference to the analogous barium containing K_2NiF_4 phases; $LnBaCoO_4$ (where Ln = La, Nd, Pr, Sm, Eu, Gd). Therefore this study concentrates on the synthesis of these compounds, subsequent structural characterisation and effects of temperature on the magnetic and electronic properties.

5.2 Synthesis

Initially the potential for synthesising $LaBaCoO_4$ was investigated by substituting a small amount of the Sr^{2+} for Ba^{2+} i.e. attempting the synthesis of $LaSr_{0.8}Ba_{0.2}CoO_4$, $LaSr_{0.6}Ba_{0.4}CoO_4$, $LaSr_{0.4}Ba_{0.6}CoO_4$, $LaSr_{0.2}Ba_{0.8}CoO_4$ and then finally $LaBaCoO_4$, using the same technique as employed for the synthesis of the $LnSrCoO_4$ systems. It

was found that as the quantity of Ba^{3+} increased the samples required longer annealing times. A polycrystalline sample of the compound $LaBaCoO_4$ was successfully synthesised using the direct oxide route. Stoichiometric amounts of La_2O_3 (99.99%, Aldrich), $BaCO_3$ (99.9+%, Aldrich) and Co_3O_4 (Aldrich, 99.99%), were ground in an agate pestle and mortar and annealed in air at 970 °C for 48 hours. Following regrinding they were annealed in air at 1150 °C for 48 hours, reground and annealed for a further 48 hours at 1150 °C. Compounds with the composition $La_{1+x}Ba_{1-x}CoO_4$ (x = 0.1 and 0.2) were also successfully synthesised using the same experimental technique as for $LaBaCoO_4$. The progress of the reactions were monitored using PXD, the PXD patterns following the final stage of synthesis are displayed in Figure 1.

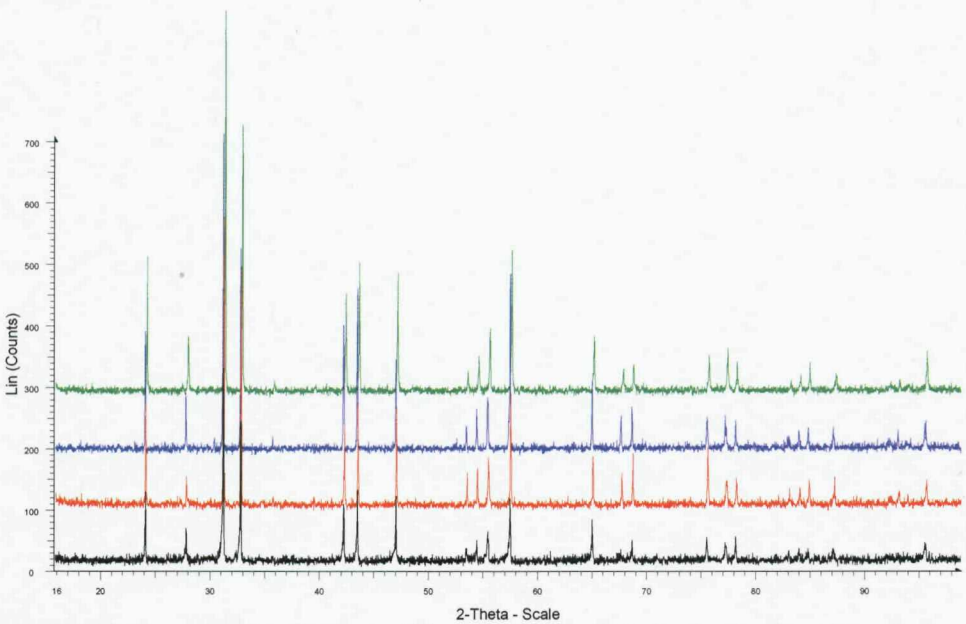

Figure 1 PXD patterns of $LaBaCoO_4$ (*black*), $La_{1.1}Ba_{0.9}CoO_4$ (*red*), $La_{1.2}Ba_{0.8}CoO_4$ (*blue*) and $La_{1.4}Ba_{0.6}CoO_4$ (*green*).

Numerous attempts have been made to substitute La^{3+} for other lanthanides, initial studies looked at synthesising $NdBaCoO_4$ using the same method adopted for the formation of the $LaBaCoO_4$ phase. However, PXD indicated that the compounds contained the phases Nd_2O_3 and $BaCoNd_2O_5$. Later attempts involved investigating the gradual synthesis of $NdBaCoO_4$. Figure 2 displays the PXD patterns obtained for

these phases, it shows that the K_2NiF_4 structure is maintained for $NdBa_{0.2}Sr_{0.8}CoO_4$, $NdBa_{0.4}Sr_{0.6}CoO_4$ and $NdBa_{0.6}Sr_{0.4}CoO_4$ however, there is also an impurity of Nd_2O_3. Attempts to synthesis $LnBaCoO_4$ (where Ln = Pr, Eu and Gd) also proved to be unsuccessful.

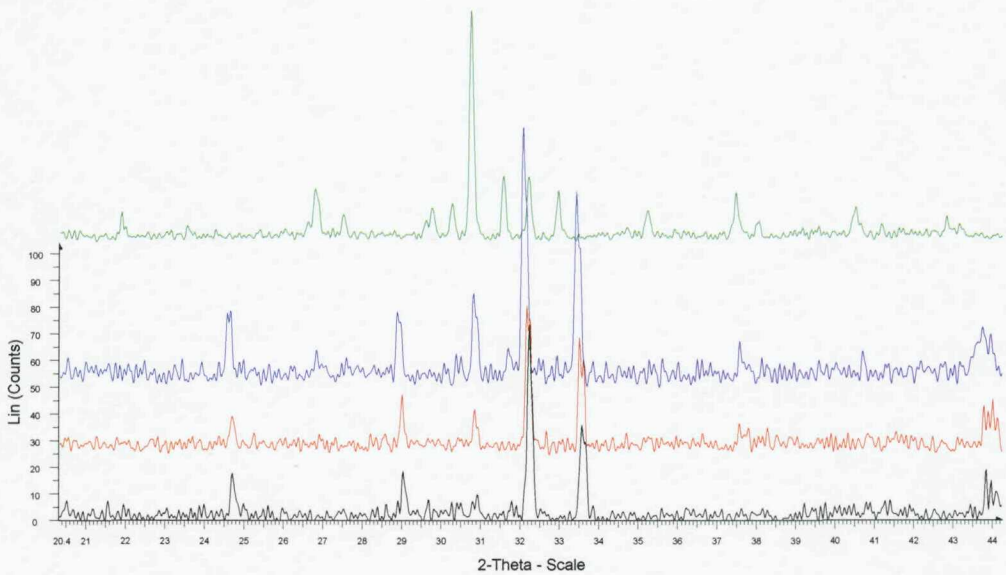

Figure 2 PXD pattern of $NdBa_{0.2}Sr_{0.8}CoO_4$ (*black*), $NdBa_{0.4}Sr_{0.6}CoO_4$ (*red*), $NdBa_{0.6}Sr_{0.4}CoO_4$ (*blue*) and $NdBaCoO_4$ (*green*).

5.3 Structural Characterisation of $LaBaCoO_4$

5.3.1 Variable Temperature PXD Structure Refinement of $LaBaCoO_4$

Room temperature PXD data were collected over the 2θ range 10 - 100° using the D8 diffractometer in conjunction with the Sol-X detector. The starting structural model for Rietveld refinement was that used for $LaSrCoO_4$. Refinement of the structure introduced the global parameters, i.e. histogram scale factor, peak shape, zero point displacement, background parameters and lattice constants. The isotropic temperature factors and the atom positions were also varied. No impurity peaks

with $I/I_0 > 1\%$ were observed showing a single phase product. Figure 3 shows the final profile fit achieved and Table 1 summarises the extracted crystallographic description and lattice parameters at 298 K. Variable temperature PXD data were collected over the 2θ range 10 - 100° using a step size of 0.018° and the Bruker D8 diffractometer in conjunction with the PSD detector and the Anton-Paar HTK 1200 furnace stage in the temperature range 323 – 873 K. The data were refined using the GSAS suite of programs. Table 2 lists the lattice parameters, selected bond distances and final profile fits obtained from Rietveld refinement of the variable temperature data.

Table 1 Refined structural parameters for $LaBaCoO_4$ at 298 K from PXD data.
Space group I4/mmm. a = 3.8589(2) and c = 12.8268(8) Å (e.s.d's are given in parenthesis)

Atom Type	**x**	**y**	**z**	**Occupancy**	**Uiso/Å^2**
La/Ba	0	0	0.362(1)	0.5/0.5	1.94(24)
Co	0	0	0	1	1.7(5)
O	0	0.5	0	1	1.2(15)
O	0	0	0.181(4)	1	2.5(14)

$\chi^2 = 1.09$, $R_p = 18.27\%$, $R_{wp} = 23.62\%$

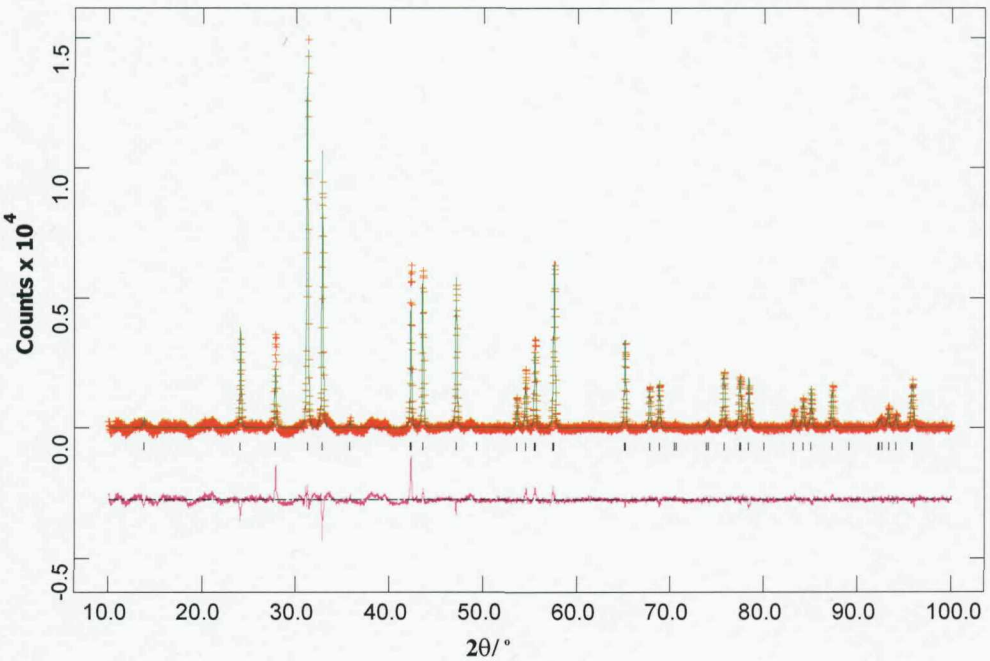

Figure 3 PXD refinement profile for tetragonal $LaBaCoO_4$ at 298 K *(crosses indicate observed data, the upper continuous line shows calculated profile, the lower continuous line the difference and tick marks show reflection positions).*

Table 2 Lattice parameters, selected bond distances and final fit factors for $LaBaCoO_4$ (PXD) (*e.s.d's are given in parantheses*).

Temperature/ ° C	a parameter/ Å	c parameter/ Å	Co-O(1) (ax)/ Å	CoO(2) (eq)/ Å	χ^2	Rwp/ %	Rp/ %
50	3.8548(1)	12.8204(3)	1.927(1)	2.158(12)	3.99	3.65	2.63
100	3.8565(1)	12.8476(3)	1.928(1)	2.162(11)	4.81	3.68	2.60
150	3.8586(1)	12.8818(3)	1.929(1)	2.164(11)	5.14	3.68	2.56
200	3.8609(1)	12.9200(3)	1.930(1)	2.167(11)	5.39	3.68	2.57
250	3.8633(1)	12.9617(3)	1.932(1)	2.160(12)	5.80	3.71	2.55
300	3.8657(1)	13.0039(3)	1.933(1)	2.143(12)	5.79	3.64	2.46
350	3.8680(1)	13.0444(3)	1.934(1)	2.143(12)	5.64	3.54	2.41
400	3.8703(1)	13.0806(3)	1.935(1)	2.147(12)	5.61	3.50	2.36
450	3.8728(1)	13.1131(3)	1.936(1)	2.157(12)	5.61	3.46	2.33
500	3.8752(1)	13.1399(3)	1.937(1)	2.156(12)	5.32	3.37	2.29
550	3.8778(1)	13.1642(3)	1.939(1)	2.163(12)	5.23	3.35	2.26
600	3.8801(1)	13.1853(3)	1.940(1)	2.149(12)	6.01	3.57	2.35

5.3.2 Variable Temperature PND Structure Refinement of $La_{1+x}Ba_{1-x}CoO_4$

In order to improve the determination of the structure and elucidate exact oxygen positions, PND data were collected for $LaBaCoO_4$, $La_{1.1}Ba_{0.9}CoO_4$ and $La_{1.2}Ba_{0.6}CoO_4$ using POLARIS at the ISIS facility. The samples were loaded in 6 mm or 8 mm diameter vanadium cans depending upon sample size. Data were collected in the temperature range 2 – 900 K in 50 K intervals. The highest resolution data from the backscattering C bank was used in the strucutural refinement of the data, with the structural parameters from the X-ray refinement used as the starting model. The nuclear scattering lengths used were La = 8.240, Co = 2.490, Ba = 5.07 and O = 5.803 fm. Lattice parameters and the background function were the first variables to be introduced. Then a peak shape function was included. Once these were stable the atomic positions and isotropic temperature factors were included in the refinement. The structures were also refined using data from the A bank, however no additional Bragg reflections due to magnetic peaks were observed.

Table 3 Refined structural parameters for $LaBaCoO_4$ at 300 K from PND data.
Space group I4/*mmm* a = 3.8614(1) and c = 12.8350(2) Å (*e.s.d's are given in parenthesis*)

Atom Type	x	y	z	Occupancy	Uiso/Å^2
La/Ba	0	0	0.3619(1)	0.5/0.5	0.37(2)
Co	0	0	0	1	0.23(4)
O	0	0.25	0	1	0.70(2)
O	0	0	0.1653(1)	1	1.92(4)

$\chi^2 = 0.86$, $R_p = 1.20\%$, $R_{wp} = 2.59\%$

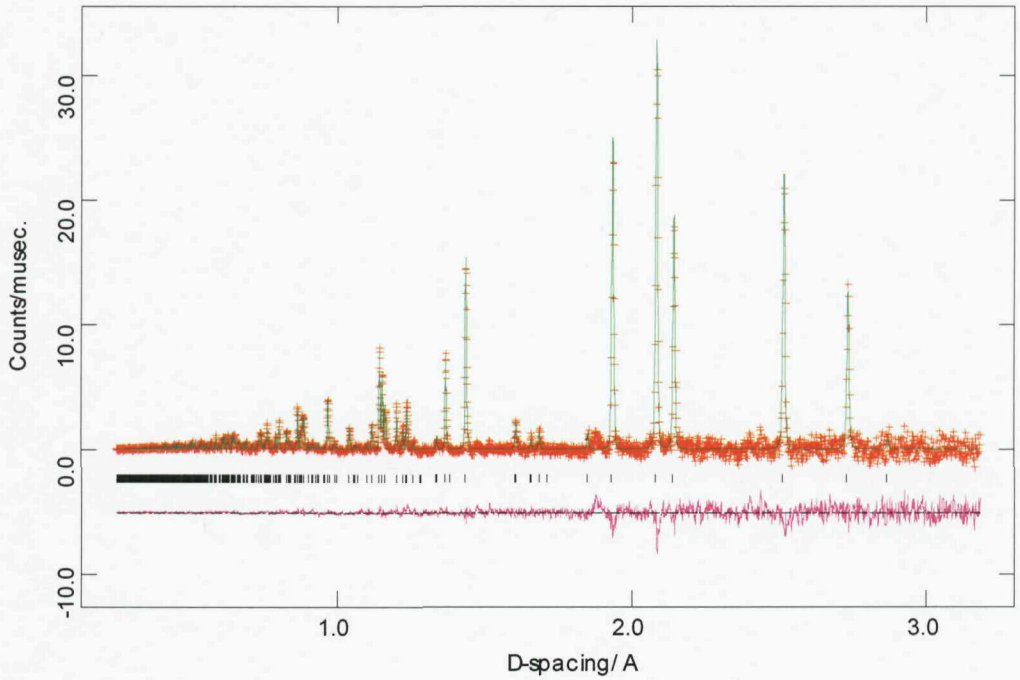

Figure 4 PND refinement profile for tetragonal $LaBaCoO_4$ at 300 K *(crosses indicate observed data, the upper continuous line shows calculated profile, the lower continuous line the difference and tick marks show reflection positions).*

Table 4 Refined structural parameters for $La_{1.1}Ba_{0.9}CoO_4$ at 300 K from PND data.
Space group I4/*mmm*. a = 3.8601(1) *and* c = 12.8329(1) Å *(e.s.d's are given in parenthesis)*

Atom Type	x	y	z	Occupancy	Uiso/Å^2
La/Ba	0	0	0.3615(1)	0.5/0.5	1.54(1)
Co	0	0	0	1	1.31(3)
O	0	0.25	0	1	1.97(2)
O	0	0	0.1659(1)	1	3.45(3)

$\chi^2 = 2.39$, $R_p = 2.20\%$, $R_{wp} = 4.42\%$

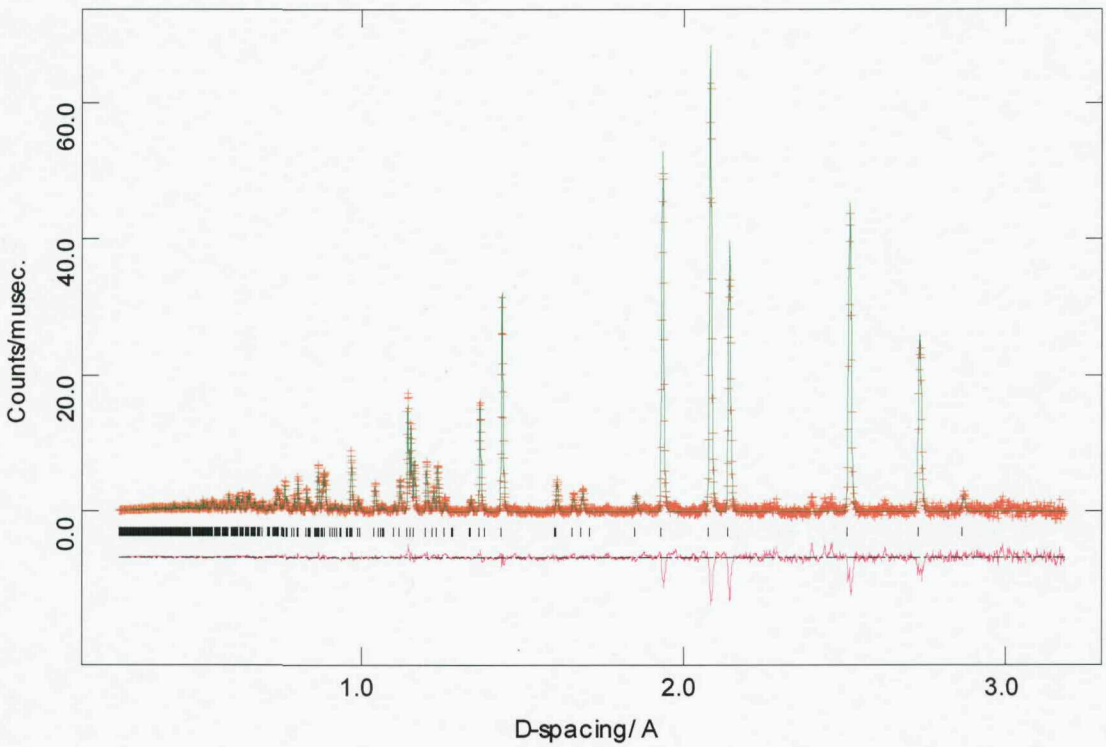

Figure 5 PND refinement profile for tetragonal $La_{1.1}Ba_{0.9}CoO_4$ at 300 K *(crosses indicate observed data, the upper continuous line shows calculated profile, the lower continuous line the difference and tick marks show reflection positions).*

Table 5 Refined structural parameters for $La_{1.2}Ba_{0.8}CoO_4$ at 300 K from PND data.
Space group I4/*mmm* a = 3.8591(6) *and* c = 12.8258(4) Å *(e.s.d's are given in parenthesis)*

Atom Type	x	y	z	Occupancy	Uiso/Å^2
La/Ba	0	0	0.3618(1)	0.5/0.5	0.32(1)
Co	0	0	0	1	0.25(3)
O	0	0.25	0	1	0.68(2)
O	0	0	0.1659(1)	1	1.90(3)

$\chi^2 = 2.41$, $R_p = 2.46\%$, $R_{wp} = 6.09\%$

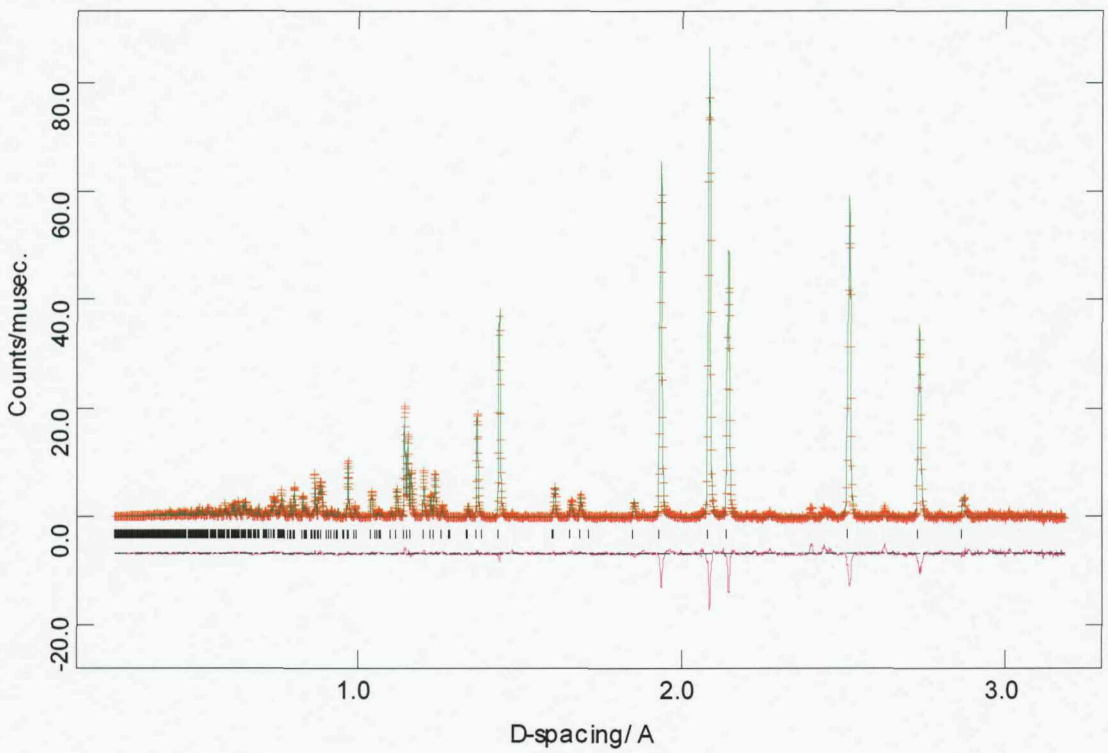

Figure 6 PND refinement profile for tetragonal $La_{1.2}Ba_{0.8}CoO_4$ at 300 K *(crosses indicate observed data, the upper continuous line shows calculated profile, the lower continuous line the difference and tick marks show reflection positions).*

Table 6 Lattice parameters, selected bond distances and final fit factors for $LaBaCoO_4$ (PND) (*e.s.d's are given in parantheses*).

Temperature / K	a parameter/ Å	c parameter/ Å	Co-O(eq)/ Å	Co-O (ax)/ Å	χ^2	Rwp/ %	Rp/ %
20	3.8565(1)	12.7599(3)	2.099(1)	1.928(1)	0.98	2.79	1.28
50	3.8566(1)	12.7612(3)	2.099(1)	1.928(1)	1.02	2.76	1.30
100	3.8571(1)	12.7680(2)	2.099(1)	1.929(1)	0.99	2.73	1.28
200	3.8589(1)	12.7956(2)	2.110(1)	1.929(1)	0.94	2.61	1.25
250	3.8599(1)	12.8148(2)	2.114(2)	1.930(1)	0.89	2.61	1.21
300	3.8614(1)	12.8350(2)	2.122(2)	1.931(1)	0.86	2.59	1.20
350	3.8628(1)	12.8580(2)	2.134(2)	1.931(1)	0.83	2.61	1.17
400	3.8645(1)	12.8836(3)	2.135(2)	1.932(1)	0.92	2.64	1.23
450	3.8667(1)	12.9154(3)	2.143(3)	1.933(1)	1.17	2.81	1.38
500	3.8686(1)	12.9481(4)	2.153(4)	1.934(1)	1.43	2.95	1.52
550	3.8696(1)	12.9654(5)	2.158(4)	1.935(1)	1.62	4.79	1.62
600	3.8709(1)	12.9916(6)	2.174(4)	1.935(1)	2.11	3.33	1.90

5.4 Magnetic Characterisation

The K_2NiF_4 structure type consists of perovskite layers separated by rocksalt layers and is thus magnetically an example of a pseudo-2D square lattice. Magnetic interactions between nearest neighbour B sites are usually very strong and in these materials super exchange through oxygen often results in antiferromagnetic coupling. In the ordered state the moments can point along the *z*-axis (Ising antiferromagnetism) as is in found in K_2NiF_4 and Ca_2MnO_4[1] or can be confined to the *xy* plane (*xy* antiferromagnetism) as observed in most cuprate oxides.[2] $LaSrFeO_4$ is another example of a K_2NiF_4 type material that exhibits *xy* antiferromagnetic behaviour.[3] The interplaner coupling in these structures is much weaker but nonetheless 3D ordering is found.

Magnetic data were collected on an Oxfords Instruments 3001 VSM with a 12 T superconducting magnet. The temperature control (temperature range: 3.6 – 320 K)

was achieved by an Oxford Instruments ITC4 temperature controller. The temperature dependence of the molar magnetic susceptibility of $LaBaCoO_4$ was measured in a field of H = 1 kOe on heating from low temperatures after cooling in a zero magnetic field (ZFC) or in a field of 1 kOe (FC). Figures 7 and 8 show the $\chi_M(T)$ and $1/\chi(T)$ curves obtained for this sample. FC and ZFC susceptibilities are almost the same throughout the temperature range; however at ~ 170 K the two begin to diverge, this may be due to weak antiferromagnetic interactions between the Co centres within the planes. At lower temperatures the ZFC data shows a cusp at ~ 6 K which would indicate further weak possibly interplanar antiferromagnetic coupling, whilst the FC data do not. The expected spin-only effective moment calculated for the Co^{3+} ions in this compound for the intermediate (S = 1) and high (S = 2) spin states are 2.83 and 4.90 μB respectively. This compound can be fitted to the Curie-Weiss equation in the temperature range ~ 6 - 200 K yielding a μ_{eff} of 2.25 μB consistent with the intermediate spin state. Above this temperature the data are very noisy and as a result it is difficult to determine whether there is a change in gradient and thus a change in spin state.

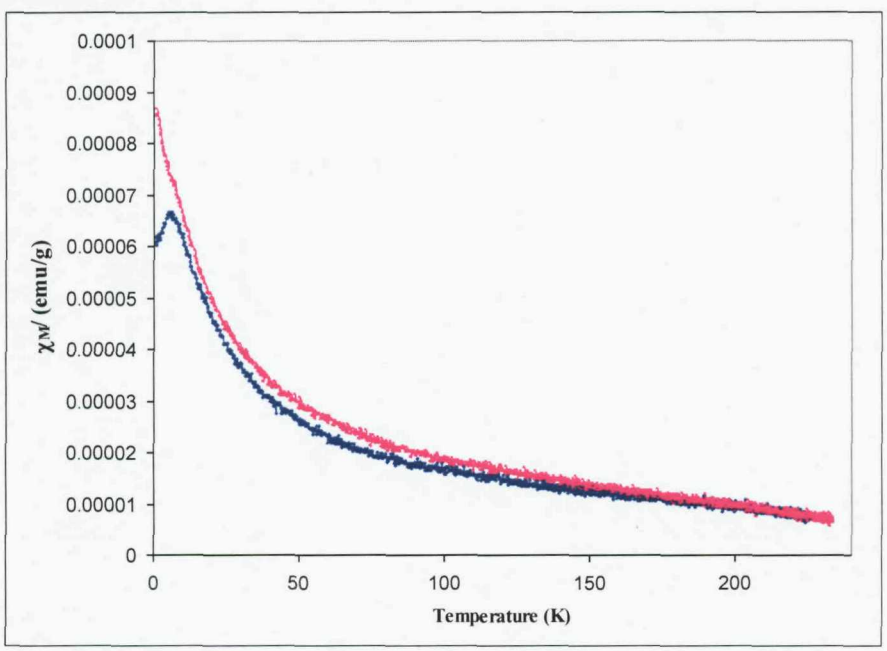

Figure 7 FC (*purple*) and ZFC (*blue*) magnetic susceptibility χ_M of $LaBaCoO_4$ over a temperature range 230 – 1.5 K (*Conversion factor to emu/ mol = 399.17*).

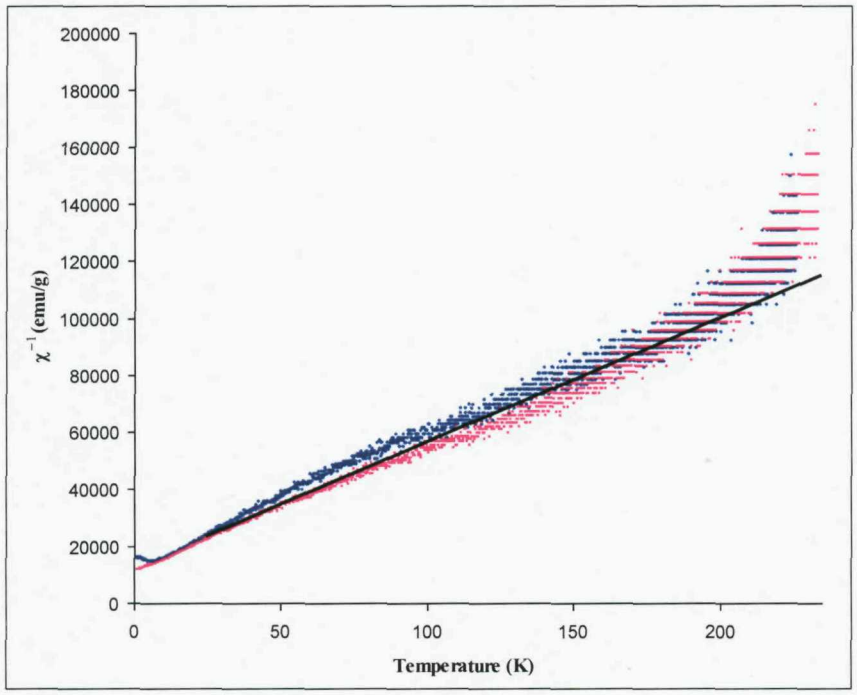

Figure 8 FC and ZFC inverse magnetic susceptibility χ_M of $LaBaCoO_4$ over a temperature range (*Conversion factor to emu/ mol = 399.17*).

5.5 Discussion

At 298 K $LaBaCoO_4$ adopts a regular tetragonal K_2NiF_4 type structure with axially elongated CoO_6 octahedra linked into plane and separated by, disordered 9-coordinated La/Ba cations. No evidence was found for a lower symmetry structure caused by tilting or twisting of the octahedra as is found in materials such as La_2CoO_4 and Sm_2CoO_4.[4] The geometry around the Co^{3+} centre consists of four in plane distances, two Co-O(equatorial), at 1.931(1) Å and two significantly longer axial distances, Co-O(axial), 2.122(12) Å. As expected the CoO_6 octahedra in this structure are much more distorted (greater axial elongation) compared with the analogous $LaSrCoO_4$ compound, in which the Co-O(equatorial) distance is 1.903(1) Å and the Co-O(axial) distance is 2.072(9) Å. If we take into account the study undertaken on structural distortions in Chapter 3, Section 3.4 we can discuss this increased distortion in terms of the tolerance factor $t = (r_A + r_O)/ \sqrt{2}(r_B + r_O)$. If $t \sim$ 0.9 all compounds adopt the perfect (*I4/mmm*) A_2BO_4 structure-type, those below

0.9 all compounds adopt the perfect (*I4/mmm*) A_2BO_4 structure-type, those below this value are distorted, it should also be noted that no compound adopting the K_2NiF_4 structure type exists with $t > 1$. $LaBaCoO_4$ (LS) (r_A = 1.343 Å and r_B = 0.545 Å) has a t value of 0.9972 which is very close to the threshold; $LaSrCoO_4$ (LS) (r_A = 1.263 Å and r_B = 0.545 Å) has a t value of 0.9681 which is well below the threshold, this accounts for the increased distortion in $LaBaCoO_4$. Figure 9 displays the coordination environment about the La^{3+} atoms in both $LaBaCoO_4$ and $LaSrCoO_4$; it is observed that in both structures the A site environment is very similar.

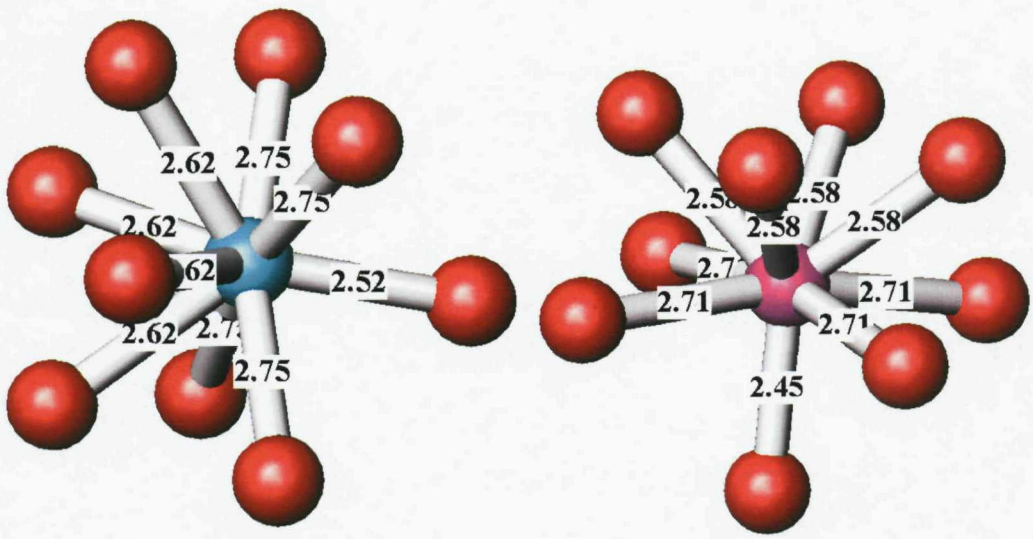

Figure 9 Coordination environment about La^{3+} in $LaBaCoO_4$ (left) and $LaSrCoO_4$ (right). Ln/(Sr/Ba)-O bond distances extracted from PND data are labelled.

Based on the tolerance factor of $NdBaCoO_4$ (t = 0.9875) we would expect this phase to form, however in reality this is not the case. Investigations into the synthesis of $NdBaCoO_4$ show that the compound $BaCoNd_2O_5$ is thermodynamically more stable, this structure adopts the orthorhombic *Pmmm* space group in which Nd^{3+} is in an 8 coordinate site.[5] Presumably, as the size of the lanthanide is reduced the Ln^{3+} ions prefer to adopt sites with smaller coordination. This is commonly seen when synthesising lanthanide compounds e.g. in the $LnSrCoO_4$ series the K_2NiF_4 structure is retained for Gd however for Tb, $SrTb_2O_4$ is thermodynamically more stable with Tb in a 7 coordinate site.

Previous studies by Sánchez-Andujar *et al.* on the phases $La_{1-x}Sr_{1+x}CoO_4$ ($0 \leq x \leq 0.4$) show that the lattice parameter *a* changes very little with the doping degree. Meanwhile the cell parameter *c* increase with *x* as the larger Sr^{2+} (1.31 Å) ion is substituted for La^{3+} (1.216 Å).[6] In the solid solution studies of $La_{1+x}Ba_{1-x}CoO_4$ ($0 \leq x \leq 0.2$) we would expect a decrease in lattice parameters as we substitute the smaller La^{3+} ion for Ba^{3+} (1.47 Å). It can be seen in Tables 1, 3 and 4 both the *a* and *c* lattice parameters are reduced as the amount of La^{3+} is increased. As *x* increases the Co-O(equatorial) bond distances decrease however the Co-O(axial) bond distances increase; the Co-O(axial) distances for $x = 0$, 0.1 and 0.2 are 2.122(2), 2.128(1) and 2.129(1) respectively.

All variable temperature PXD and PND data for $LaBaCoO_4$ was modeled in the *I4/mmm* space group with good refinement statistics. The *a* and *c* parameters increase linearly with temperature. Data extracted from Rietveld refinements of PXD and PND was used to plot graphs of Co-O(axial) and Co-O(equatorial) bond distances as a function of temperature. Figures 10 and 11 summarise the evolution of the Co-O coordination environment on increasing temperature. Inspection of the neutron diffraction data collected above 500 K, i.e. the 550 K and 600 K data sets show additional reflections consistent with slight decomposition of the sample under vacuum conditions of the experiment. However structural information could still be extracted for the main K_2NiF_4 type phase but these data should be treated with caution due to the probable loss of oxygen from the material. Similar to the strontium containing compositions the data from $LaBaCoO_4$ show a distinct increase in the axial Co-O distance relative to the equatorial. There are no well-defined changes in behavior of the two different Co-O distances in the PXD or PND data

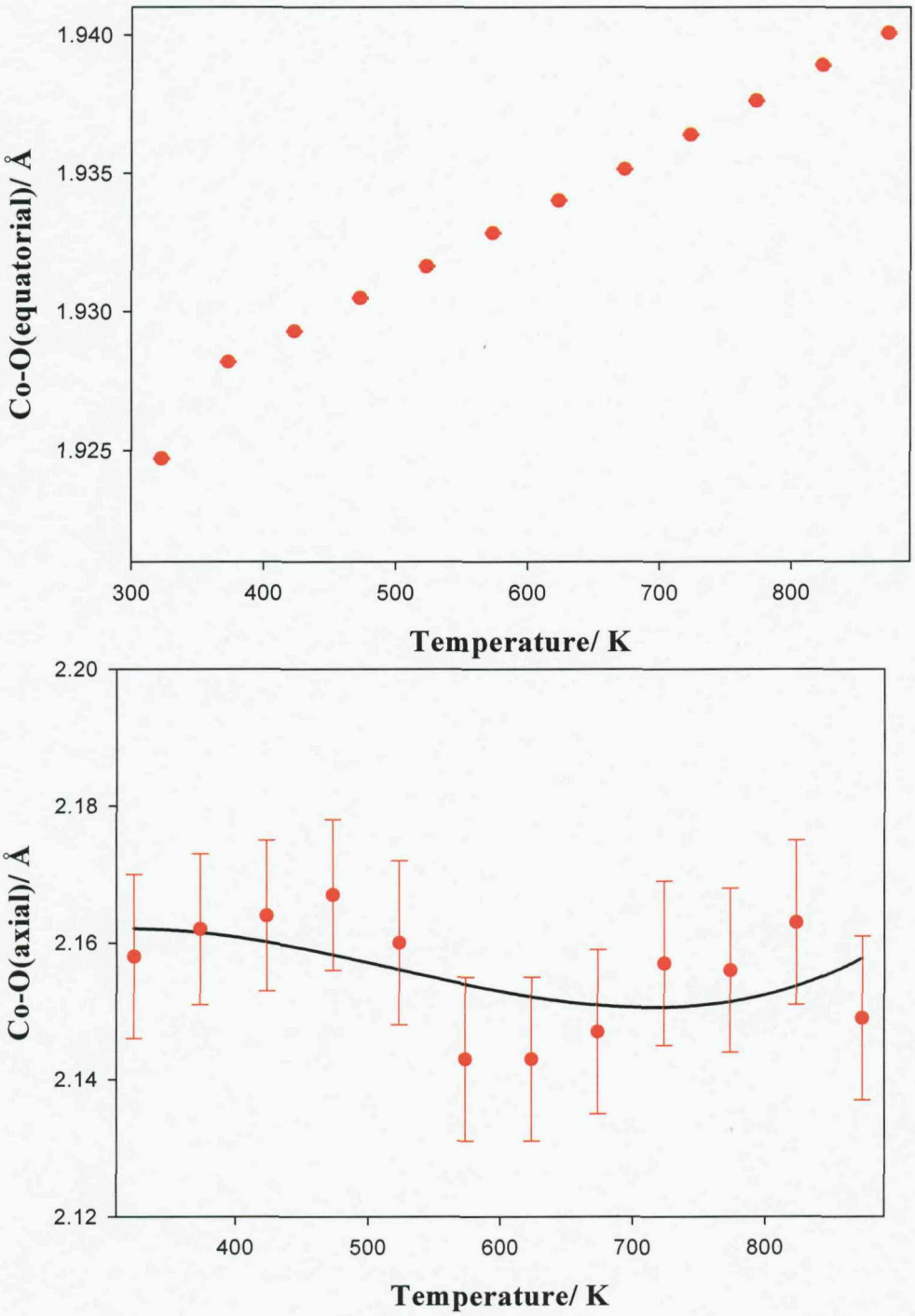

Figure 10 Co-O(equatorial) (top) and Co-O(axial) (bottom) bond distances as a function of temperature for $LaBaCoO_4$ as extracted from PXD data.

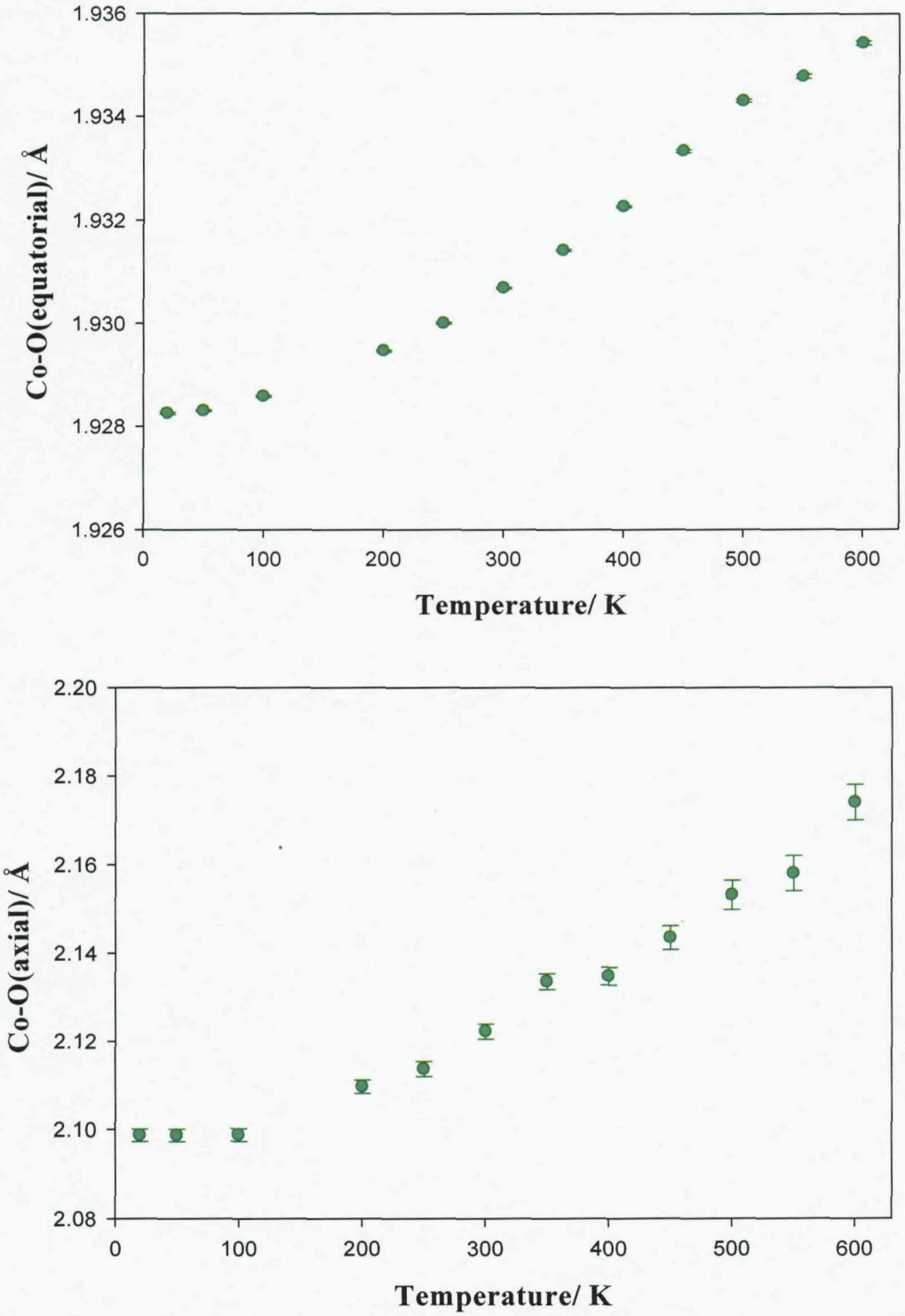

Figure 11 Co-O(equatorial) (top) and Co-O(axial) (bottom) bond distances as a function of temperature for $LaBaCoO_4$ as extracted from PND data.

5.6 Conclusion

The novel compounds $La_{1+x}Ba_{1-x}CoO_4$ (x = 0, 0.1 and 0.2) were synthesised. The compounds adopt the tetragonal K_2NiF_4 structure. The attempted synthesis of the analogous $LnBaCoO_4$ (where Ln = Pr, Nd, Sm and Gd) was unsuccessful. Detailed magnetic and structural analyses were undertaken using PXD, PND and magnetic susceptibility measurements. The CoO_6 octahedra in $LaBaCoO_4$ have a greater axial elongation compared with the CoO_6 octahedra in the analogous $LaSrCoO_4$ compound. This can be accounted for by looking at the *t* values, $LaBaCoO_4$ (LS) (r_A = 1.343 Å and r_B = 0.545 Å) has a *t* value of 0.9972 which is very close to the threshold; $LaSrCoO_4$ (LS) (r_A = 1.263 Å and r_B = 0.545 Å) has a *t* value of 0.9681 which is well below the threshold.

Variable temperature PND and PXD data were collected on $LaBaCoO_4$ in order to determine whether a temperature induced spin transition occurs. In both the PXD and PND data the *a* and *c* parameters increase linearly. Similarly to the strontium containing compositions, $LaBaCoO_4$ shows a distinct increase in the axial Co-O distance relative to the equatorial. There are no well-defined changes in behavior of the two different Co-O distances in the PXD or PND data. FC and ZFC susceptibilities are almost the same throughout the temperature range; however at ~ 170 K the two begin to diverge, this may be due to weak antiferromagnetic interactions between the Co centres within the planes. At lower temperatures the ZFC data shows a cusp at ~ 6 K which would indicate further weak possibly interplanar antiferromagnetic coupling, whilst the FC data do not. This compound can be fitted to the Curie-Weiss equation in the temperature range ~ 6 - 200 K yielding a μ_{eff} of 2.25 μB consistent with the intermediate spin state. Above this temperature the data are very noisy and it is not possible to determine whether any changes in the spin state of Co^{3+} are occurring.

5.7 References

[1] D. E. Cox, G. Shirane, R. J. Birgereau and J. B. MacChesney, *Phy. Rev.*, **188**, 930 (1969); K. Tezuka, M. Inamura, Y. Hinatsu, Y. Shimojo and Y. Morii, *J. Solid State Chem.*, **145**, 705 (1999).

[2] D. Petrigran, S. V. Maleyev, P. Bourges and A. S. Ivanov, *Phy. Rev. B.*, **59**, 1079 (1999).

[3] J. L. Soubeyeroux, P. Courbin, L. Fournes, D. Frouchart and G. Le Flem, *J. Solid State Chem.*, **31**, 313 (1980).

[4] U. Lehman and H. Mueller-Buschbaum, *Anorg. Allg. Chem*, **470**, 59 (1980).

[5] J. C. Burtley, J. F. Mitchell, S. Short, D. Miller and Y. Tang, *J. Solid State Chem.*, **170**, 339 (2003).

[6] M. Sánchez-Andujar and M. A. Señaris-Rodriguez, *Solid State Sciences*, **6**, 21 (2004).

Chapter Six

Synthesis, Structural and Magnetic Characterisation of $Ln_2Ba_6Co_4O_{15}$ (Ln = La, Pr, Nd and Sm)

6.1 Introduction

Layered Co^{3+} oxides with structures based on a CoO_2 square net demonstrate a number of unusual electronic and magnetic properties associated with the various spin states of the Co^{3+} ion and their interaction between linked centres. This species/environment specifically demonstrates mixed spin state behaviours (high, low and intermediate d^6) and crossover between these as a function of temperature and dimensional ordering of these spin arrangements leads to properties associated with orbital ordering. Recent studies have concentrated on layered systems e.g. $LnACoO_4$ adopting the K_2NiF_4 structure type, containing CoO_6 octahedra.

Here we focus our attention on the structural and magnetic properties of the quaternary $Ln_2Ba_6Co_4O_{15}$ (Ln = La, Pr, Nd and Sm) oxides. $Ba_6La_2Co_4O_{15}$ was first synthesised by Mevs and Müller-Buschbaum,[1] and has a fascinating hexagonal one dimensional structure. The compound was first prepared from $Ba(OH)_2$, La_2O_3 and $Co(OAc)_2$ with heating at 1000 °C and laser heating at 1800 – 1900 °C and was investigated by single crystal X-ray diffraction studies. The compound crystallises with hexagonal symmetry in the space group P*63mc*; a = 11.8082 and c = 7.0019 Å. The Co^{3+} ions occupy two kinds of crystallographic sites (*6c* and *2b*) and form a CoO_6 octahedron and three CoO_4 tetrahedra per formula unit connected by corner sharing, and can be regarded as Co_4O_{15} clusters. Thus, this compound may show an anomalous magnetic behaviour reflecting such a structural feature. The literature reports this structure type with Co^{3+} only for La[1] and Pr[2] but for the Fe^{3+} analogue structures containing Ln = La,[3,4] Pr[5] and Nd[6] are known.

Very recently the crystal structure and magnetic properties for the quaternary oxide $La_2Ba_6Fe_4O_{15}$ has been re-investigated.[4] This compound also adopts a hexagonal structure in which four Fe ions per formula unit occupy the sites in one FeO_6 octahedron and three FeO_4 tetrahedra. These polyhedra form a larger Fe_4O_{15} cluster unit by corner sharing. This cluster shows behaviour characteristic of a magnetic tetramer with a ferromagnetic ground state of total spin S_T = 5 by

the antiferromagnetic interaction between Fe^{3+} ions. From the magnetic susceptibility and specific heat measurement, an antiferromagnetic transition was observed at 12.8 K. The magnetic structure was determined by PND at 2.3 K, which indicates that the transition is due to the long range antiferromagnetic ordering of the Fe_4O_{15} clusters. The ordered magnetic moment for each Fe^{3+} ion is determined to be ~ 4 μB. In addition, it is found that the antiferromagnetic structure changes to a ferromagnetic structure of clusters in an applied field of ~2 T (at 1.8 K).[4]

Structural characterisation of the $Ln_2Ba_6Co_4O_{15}$ (Ln = La, Nd and Sm) oxide materials has been performed using both PXD and PND, and the magnetic behaviour of three representative samples have been determined. The attempted synthesis of polycrystalline samples containing Ln = Gd and Dy is also discussed.

6.2 Synthesis

Polycrystalline samples of the series of compounds $Ln_2Ba_6Co_4O_{15}$ (Ln = La, Pr, Nd and Sm) were synthesised using the same method in each case. Stoichiometric amounts of Ln_2O_3 (99.99%, Aldrich) (Ln = La, Nd and Sm), Pr_6O_{11} (99.99%, Aldrich), Co_3O_4 (99.99%, Aldrich) and $BaCO_3$ (99.9+%, Aldrich) were thoroughly ground in an agate pestle and mortar. The lanthanide oxides were dried in air at 800 °C for 24 hours prior to use. The mixture was transferred into alumina crucibles and the samples were annealed in air at 1000 °C for 48 hours. After regrinding, the resulting powder was annealed in air at 1200 °C for a further 48 hours, after which the products were quenched to room temperature to obtain a single phase product.

The attempted synthesis of $Ln_2Ba_6Co_4O_{15}$ (Ln = Gd and Dy) under the same conditions led to the formation of a cubic phase. The PXD pattern (Figure 1) for the Dy containing phase has been indexed and the *a* parameter takes a value of 4.1576 Å indicating the formation of a perovskite phase consistent with $(DyBa)CoO_{3-y}$.

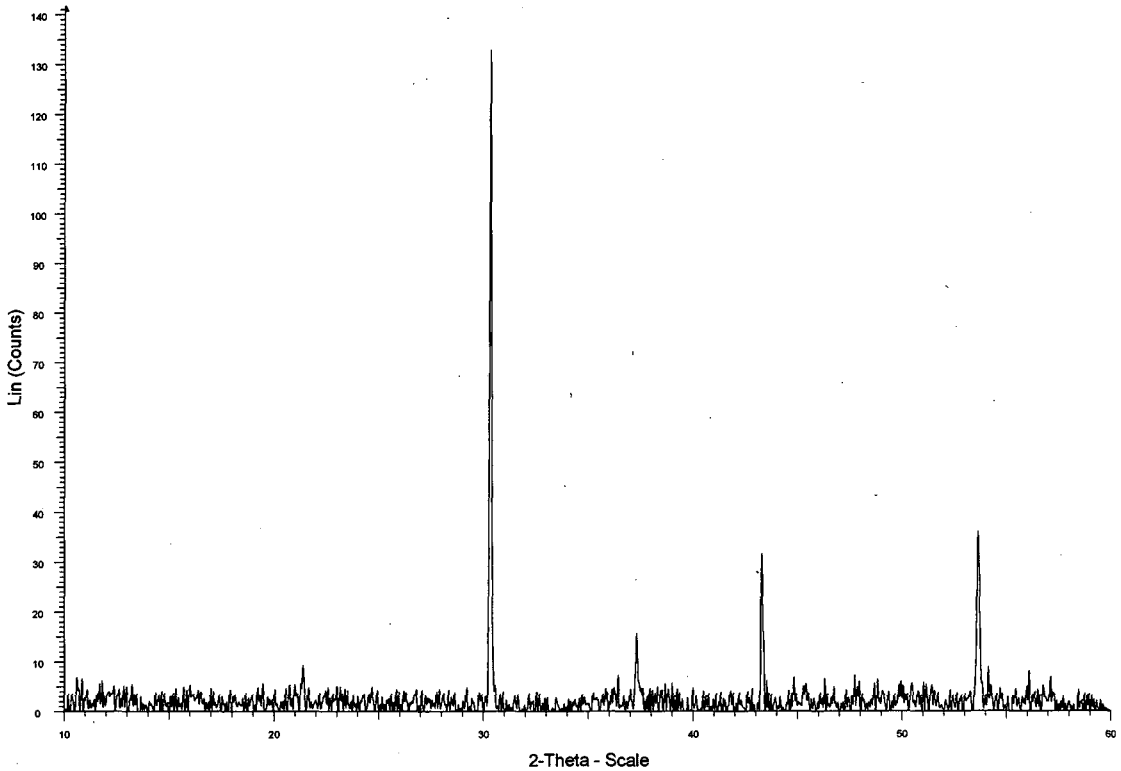

Figure 1 Short scan PXD pattern for the obtained phase when attempting the synthesis of $Dy_2Ba_6Co_4O_{15}$.

6.3 Structural Characterisation

6.3.1 PXD Structure Refinement of $Ln_2Ba_6Co_4O_{15}$ (Ln = La, Pr, Nd and Sm)

Initial characterisation was carried out using PXD. Data were collected in the 2θ range 10 - 60 ° using the D8 diffractometer in conjunction with the PSD detector. The data showed that $Ln_2Ba_6Co_4O_{15}$ (Ln = La, Nd and Sm) are phase pure; however $Pr_2Ba_6Co_4O_{15}$ contained a 22% impurity of an unknown phase, of which the most intense peak occurs at 2θ = 28.7°. Further PXD data were collected on all samples for refinement using the GSAS suite of programs. Scans were collected in the 2θ range 10 – 100° using the D8/ PSD setup. The initial model was that of $La_2Ba_6Co_4O_{15}$ proposed by Mevs *et al.*.[1] Initially lattice parameters, background parameters and zero point were varied. At the next stage of refinement, peak shape parameters were added. Once these parameters were

stable, atom positions and isotropic temperature factors were introduced. However, as a result of fluorescence and possibly preferred orientation effects the refinement diverged and atom positions, peak shape and isotropic temperature factors deviated considerably. Profile fitting and the extraction of structurally meaningful data was therefore prohibited. Using EVA the PXD patterns were compared to the database (JCPDS), from this we were able to conclude that the compounds were phase pure and are of the stoichiometry $Ln_2Ba_6Co_4O_{15}$ (Ln = La, Nd and Sm).

Variable temperature PXD data on the compound $La_2Ba_6Co_4O_{15}$ was collected using the D8 diffractometer with the PSD detector in conjunction with the Anton Paar HTK 1200 furnace stage in the temperature range 25 – 900 °C at 25 °C steps. Scans were collected in the 2θ range 10 - 100° for 6 hours. Figure 2 shows the obtained thermodiffractogram. In the temperature range 25 – 250 °C the data can be refined in the space group *P63mc*, however at 275 °C the phases $Ba_6Co_4O_{12}$ and La_2O_3 begin to form and between 350 - 500 °C the sample comprises of only $Ba_6Co_4O_{12}$ and La_2O_3, then at 825 °C the compound reverts back to the $La_2Ba_6Co_4O_{15}$ phase. Room temperature PXD data were collected on this sample after variable temperature PXD studies. The PXD pattern shows that at this temperature the $La_2Ba_6Co_4O_{15}$ structure is retained.

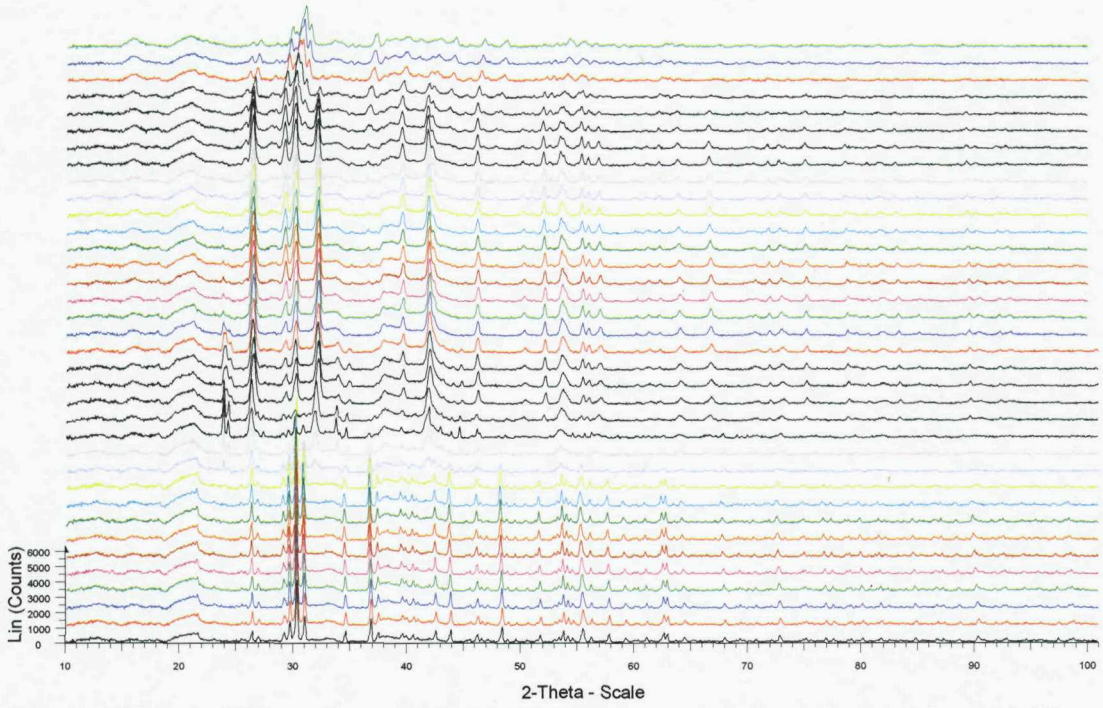

Figure 2 Thermodiffractogram of $La_2Ba_6Co_4O_{15}$ in the temperature range 25 to 900 °C at 25 °C intervals.

6.3.2 PND Structural Characterisation of $Ln_2Ba_6Co_4O_{15}$ (Ln = La and Nd)

In order to structurally characterise these compounds PND data were collected on the compounds $La_2Ba_6Co_4O_{15}$ and $Nd_2Ba_6Co_4O_{15}$ on the high resolution powder diffractometer (HRPD) at the ISIS facility. Approximately 4 g of sample was placed in 8 mm diameter vanadium cans and cooled to 2 K in a standard cryostat and data were collected; further data were collected at 298 K on the candlestick. The PND pattern was analysed, using the GSAS suite of programs, and the structural model was determined from the single crystal refinement as proposed by Mevs *et al.*[1] Initially only the data from Bank 1 were refined. The nuclear scattering lengths used were La = 8.240 , Nd = 7.690 , Co = 2.490, Ba = 5.07 and O = 5.803 fm. Due to the existence of an impurity in the compounds, data were refined with excluded regions. Initial stages of the refinement included variation of lattice parameters, background parameters, histogram scale factor and peak shape. The x, y and z coordinates and the thermal parameters for Ba(4) and Ln were constrained. Atomic and isotropic thermal parameters were introduced to the refinement. The final atomic coordinates and key bond distances and angles are summarised in Tables 1 - 4, and the final fits to the

profile for $La_2Ba_6Co_4O_{15}$ and $Nd_2Ba_6Co_4O_{15}$ at 298 K and 2 K are shown (Figure 4 - 7). The crystal structure of $La_2Ba_6Co_4O_{15}$ is illustrated in Figure 3.

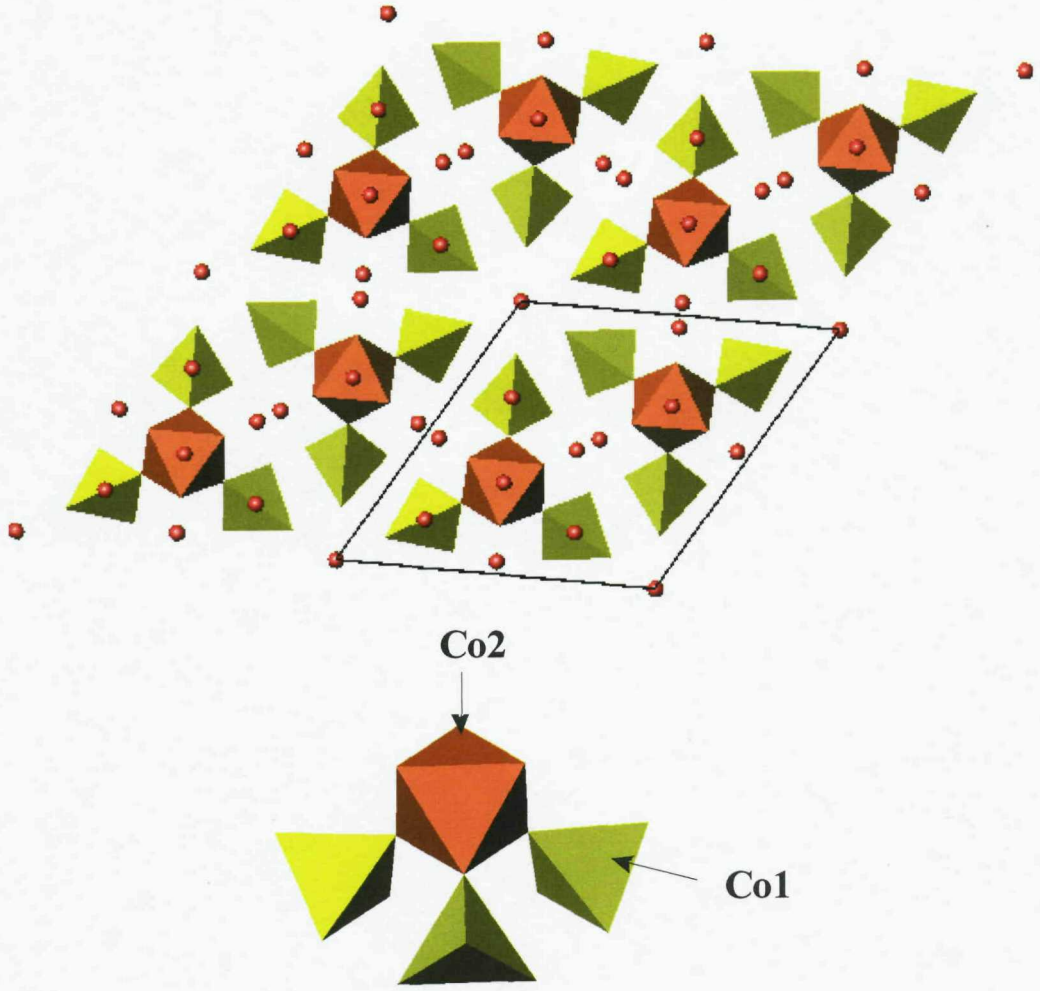

Figure 3 Polyhedral representation of $La_2Ba_6Co_4O_{15}$ (top) and the Co_4O_{15} cluster (bottom) (*CoO_6 octahedra in orange, CoO_4 tetrahedra in yellow and La/Ba atoms in red*).

Table 1 Refined atomic parameters for $La_2Ba_6Co_4O_{15}$ at 298 K from HRPD Neutron data.

Space group P63mc; a = 11.8075(1) and c = 6.9973(1) Å (estimated standard deviations in parentheses).

Atom	x	y	z	U_{eq} x 100/Å^2	Occupancy
Ba1	0	0	0	2.90(16)	1.0000
Ba2	0.3333	0.6667	0.4632(12)	1.46(13)	1.0000
Ba3	0.3503(3)	0.1751(1)	0.6559(12)	1.37(8)	1.0000
Ba4	0.9517(2)	0.4758(1)	0.3202(11)	0.11(4)	0.3333
La1	0.9517(2)	0.4758(1)	0.3202(11)	0.11(4)	0.6667
Co1	0.1744(3)	0.8256(2)	0.6553(17)	0.83(13)	1.0000
Co2	0.6667	0.3333	0.5021(22)	1.22(23)	1.0000
O1	0.4138(1)	0.5862(1)	0.1543(12)	0.87(6)	1.0000
O2	0.7496(1)	0.2504(1)	0.3279(12)	1.46(6)	1.0000
O3	0.6723(2)	0.0679(2)	0.0193(11)	2.00(5)	1.0000
O4	0.8002(3)	0.9001(1)	0.7668(12)	3.42(9)	1.0000

$\chi^2 = 2.52$, $R_p = 6.98\%$, $R_{wp} = 7.94\%$

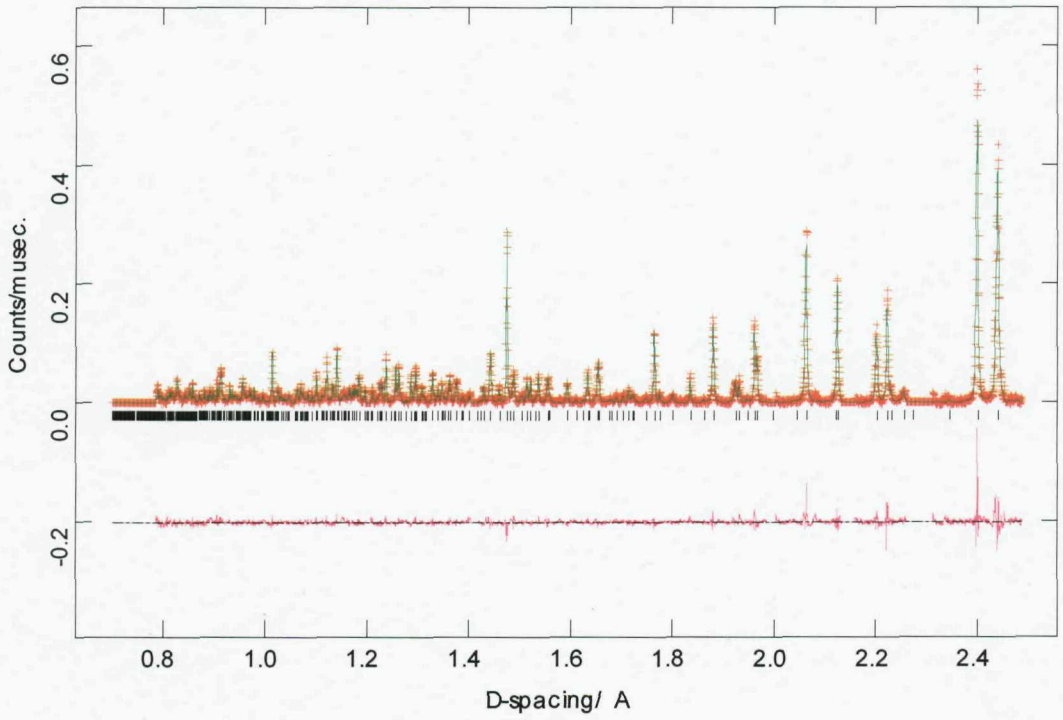

Figure 4 PND refinement profile of $La_2Ba_6Co_4O_{15}$ at 298 K *(crosses indicate observed data, the upper continuous line shows calculated profile, the lower continuous line the difference and tick marks show reflection positions).*

Table 2 Refined atomic parameters for $La_2Ba_6Co_4O_{15}$ at 2 K from HRPD Neutron data. *Space group P63mc; a = 11.7613(1) and c = 6.9583(1) Å (estimated standard deviations in parentheses).*

Atom	x	y	z	U_{eq} x 100/Å^2	Occupancy
Ba1	0	0	0	3.90(24)	1.0000
Ba2	0.3333	0.6667	0.4538(17)	0.79(15)	1.0000
Ba3	0.3518(4)	0.1758(2)	0.6440(18)	1.45(10)	1.0000
Ba4	0.9514(2)	0.4757(1)	0.3091(17)	0.21(8)	0.3333
La1	0.9514(2)	0.4757(1)	0.3091(17)	0.21(8)	0.6667
Co1	0.1736(3)	0.8263(3)	0.6394(24)	0.86(17)	1.0000
Co2	0.6667	0.3333	0.4994(32)	1.45(31)	1.0000
O1	0.4134(2)	0.5866(2)	0.1407(18)	0.95(7)	1.0000
O2	0.7489(2)	0.2511(1)	0.3152(19)	1.40(8)	1.0000
O3	0.6732(2)	0.0676(2)	0.0066(17)	1.96(7)	1.0000
O4	0.7990(4)	0.8995(2)	0.7530(12)	3.79(12)	1.0000

$\chi^2 = 2.12$, $R_p = 4.57\%$ $R_{wp} = 5.20\%$

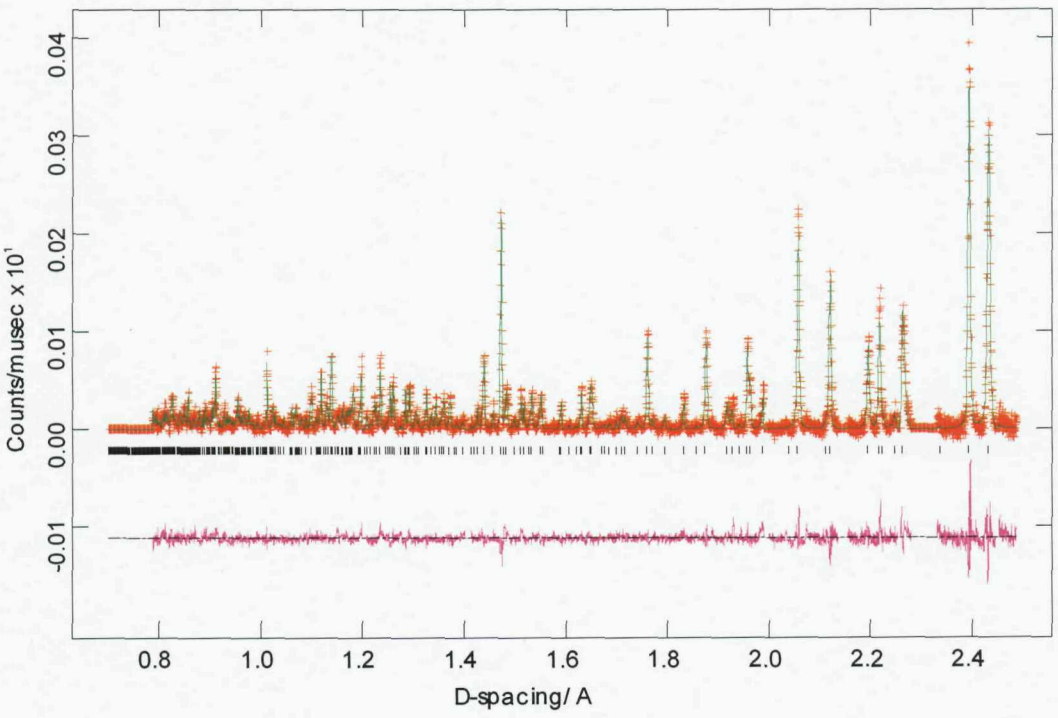

Figure 5 PND refinement profile of $La_2Ba_6Co_4O_{15}$ at 2 K *(crosses indicate observed data, the upper continuous line shows calculated profile, the lower continuous line the difference and tick marks show reflection positions).*

Table 3 Refined atomic parameters for $Nd_2Ba_6Co_4O_{15}$ at 298 K from HRPD neutron data.

Space group P63mc; a = 11.7341(1) and c = 6.9234(1) Å (estimated standard deviations in parantheses).

Atom	x	y	z	U_{eq} x 100/Å^2	Occupancy
Ba1	0	0	0	2.34(19)	1.0000
Ba2	0.3333	0.6667	0.4686(14)	1.22(16)	1.0000
Ba3	0.3519(4)	0.1759(2)	0.6547(14)	1.50(10)	1.0000
Ba4	0.9524(2)	0.4762(1)	0.3185(13)	0.37(5)	0.3333
Nd1	0.9524(2)	0.4762(1)	0.3185(13)	0.37(5)	0.6667
Co1	0.1757(3)	0.8243(3)	0.6521(20)	0.76(17)	1.0000
Co2	0.6667	0.3333	0.5079(30)	1.61(29)	1.0000
O1	0.4133(2)	0.5867(2)	0.1492(14)	1.47(8)	1.0000
O2	0.7484(1)	0.2516(1)	0.3294(15)	1.43(7)	1.0000
O3	0.6713(2)	0.0659(2)	0.0179(13)	1.95(6)	1.0000
O4	0.8023(3)	0.9012(2)	0.7685(15)	3.66(11)	1.0000

$\chi^2 = 3.28$, $R_p = 7.51\%$, $R_{wp} = 8.74\%$,

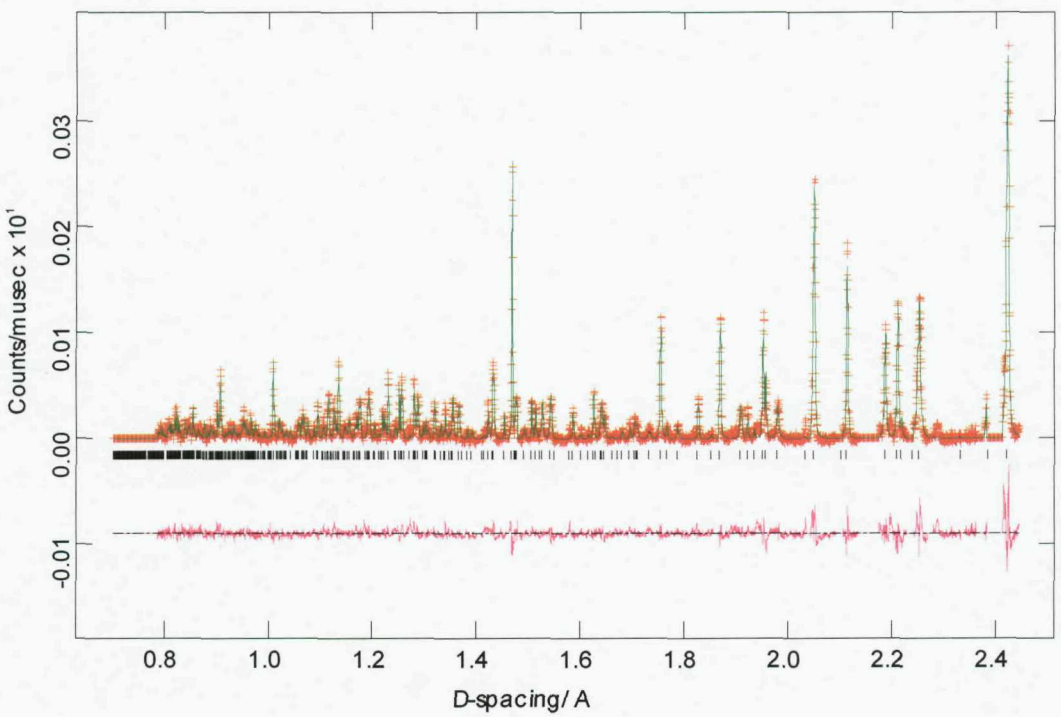

Figure 6 PND refinement profile of $Nd_2Ba_6Co_4O_{15}$ at 298 K *(crosses indicate observed data, the upper continuous line shows calculated profile, the lower continuous line the difference and tick marks show reflection positions).*

Table 4 Refined atomic parameters for $Nd_2Ba_6Co_4O_{15}$ at 2 K from HRPD neutron data. *Space group P63mc; a = 11.7079(1) and c = 6.8975(1) Å (estimated standard deviations in parentheses).*

Atom	x	y	z	U_{eq} x 100/Å^2	Occupancy
Ba1	0	0	0	2.29(21)	1.0000
Ba2	0.3333	0.6667	0.4593(16)	1.00(17)	1.0000
Ba3	0.3535(4)	0.1767(2)	0.6466(16)	0.83(10)	1.0000
Ba4	0.9521(2)	0.4760(1)	0.3045(15)	0.07(5)	0.3333
Nd1	0.9521(2)	0.4760(1)	0.3045(15)	0.07(5)	0.6667
Co1	0.1760(4)	0.8240(4)	0.6467(23)	1.14(14)	1.0000
Co2	0.6667	0.3333	0.4838(31)	1.14(14)	1.0000
O1	0.4131(2)	0.5869(2)	0.1351(17)	1.35(9)	1.0000
O2	0.7481(2)	0.2519(2)	0.3164(17)	1.16(8)	1.0000
O3	0.6720(3)	0.0666(2)	0.0093(15)	1.57(7)	1.0000
O4	0.8017(4)	0.9009(2)	0.7639(17)	3.94(14)	1.0000

$\chi^2 = 3.02$, $R_p = 4.26\%$, $R_{wp} = 4.88\%$

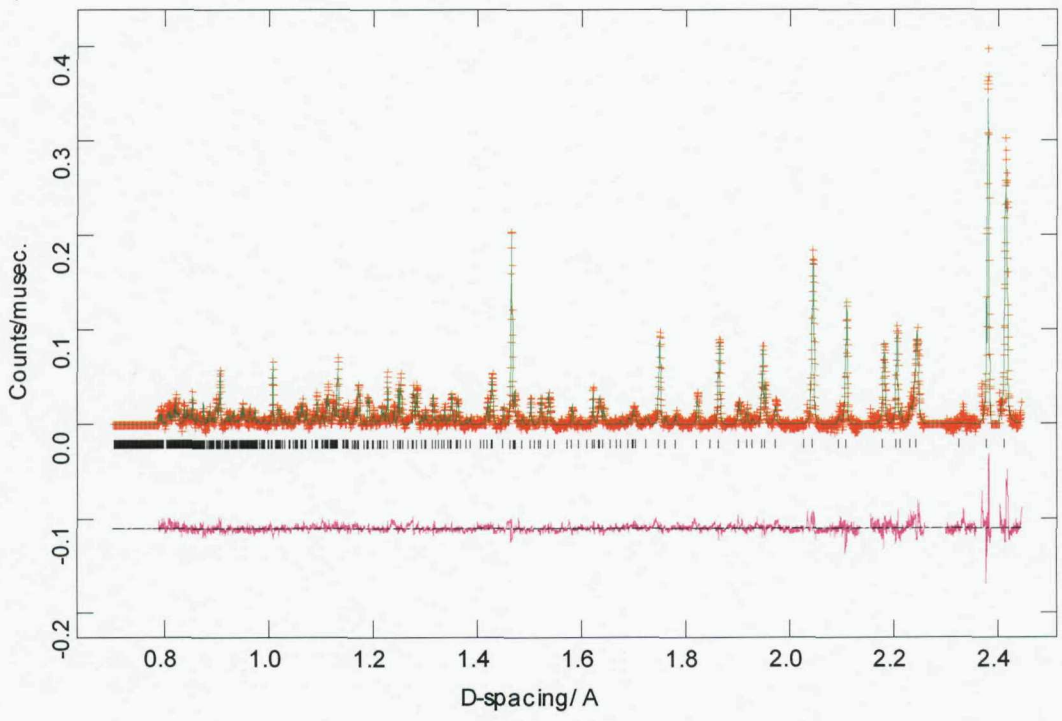

Figure 7 PND refinement profile of $Nd_2Ba_6Co_4O_{15}$ at 2 K *(crosses indicate observed data, the upper continuous line shows calculated profile, the lower continuous line the difference and tick marks show reflection positions).*

Table 5 Key selected bond distances (Å) and bond angles (°) for $La_2Ba_6Co_4O_{15}$ and $Nd_2Ba_6Co_4O_{15}$ at 2 K and 298 K (*e.s.d's are given in parentheses*).

Bond	La (2 K)	La (298 K)	Nd (2 K)	Nd (298 K)
Ba1-O4 x 3	2.700(9)	2.768(6)	2.712(8)	2.736(8)
Ba1-O4 x 3	2.673(9)	2.614(6)	2.587(8)	2.570(7)
Ba2-O1 x 3	2.721(7)	2.717(5)	2.760(8)	2.745(7)
Ba2-O2 x 3	3.022(7)	3.065(6)	2.965(8)	3.000(7)
Ba2-O3 x 6	3.186(2)	3.192(2)	3.172(3)	3.184(2)
Ba3-O1 x 1	2.777(3)	2.802(2)	2.751(3)	2.770(3)
Ba3-O1 x 1	2.778(3)	2.802(2)	2.752(3)	2.770(3)
Ba3-O2 x 1	2.754(6)	2.764(5)	2.741(7)	2.726(6)
Ba3-O3 x 2	2.980(5)	3.005(4)	2.963(5)	2.982(5)
Ba3-O3 x 2	2.891(3)	2.907(2)	2.872(3)	2.872(3)
Ba3-O4 x 1	3.205(4)	3.207(3)	3.215(4)	3.204(3)
Ba3-O4 x 1	3.124(7)	3.127(5)	3.073(7)	3.100(7)
Ba3-O4 x 1	3.204(4)	3.208(3)	3.215(4)	3.203(3)
Ba/Ln-O1 x 1	2.545(4)	2.538(3)	2.535(5)	2.534(4)
Ba/Ln-O1 x 1	2.634(5)	2.660(3)	2.614(6)	2.622(5)
Ba/Ln-O2 x 2	2.522(2)	2.536(1)	2.516(2)	2.524(2)
Ba/Ln-O3 x 2	2.445(3)	2.454(2)	2.446(4)	2.423(3)
Ba/Ln-O3 x 2	2.674(3)	2.673(3)	2.611(4)	2.646(3)
Co1-O2 x 1	1.998(10)	1.968(7)	1.934(11)	1.971(9)
Co1-O3 x 2	1.847(6)	1.867(5)	1.851(7)	1.853(6)
Co1-O4 x 1	1.686(9)	1.713(7)	1.756(10)	1.758(8)
Co2-O1 x 4	1.904(11)	1.960(8)	1.924(12)	1.897(11)
Co2-O2 x 2	2.108(13)	2.088(9)	2.014(13)	2.070(13)
Co1-Co2 x 1	4.103(15)	4.056(11)	3.942(14)	4.041(15)
Co1-Co2 x 1	5.519(19)	5.608(14)	5.583(19)	5.492(18)
Co1-Co2 x 1	5.963(4)	6.003(3)	5.966(4)	5.954(4)
Co1-O2-Co2	179.7(1)	177.9(4)	177.7(7)	178.1(6)
O2-Co1-O3	95.8(3)	96.4(2)	97.1(3)	97.3(2)
O3-Co1-O3	111.3(5)	110.4(4)	111.5(6)	112.7(5)
O2-Co1-O4	114.3(6)	115.0(4)	115.4(6)	114.2(5)
O3-Co1-O4	117.7(2)	117.4(2)	116.3(3)	116.1(2)
O1-Co2-O1	95.7(7)	93.3(5)	93.4(8)	95.8(7)
O1-Co2-O2	173.7(10)	177.2(7)	177.9(11)	174.4(10)
O2-Co2-O2	86.9(7)	89.4(5)	90.4(7)	88.0(7)

6.3.3 Discussion

The PND profile fits for $Ln_2Ba_6Co_4O_{15}$ (Ln = La and Nd) at 298 K and 2 K have been plotted. The X-ray and neutron diffraction data for $Ln_2Ba_6Co_4O_{15}$ (Ln = La, Pr, Nd and Sm) were indexed with a hexagonal unit cell, space group P*63mc*. The diffraction data were analysed using Rietveld analysis and a structural model previously reported. The refined lattice parameters were in good agreement. The extracted lattice parameters and atomic positions are tabulated (Tables 1 – 4). In this structure, the Co^{3+} ions occupy two kinds of crystallographic lattice sites (Co1, *2b*; and Co2, *6c*) and are coordinated by six and four oxygen ions, respectively. One CoO_6 octahedron and three CoO_4 tetrahedra are linked by corner sharing oxygen ions, and thus they form a Co_4O_{15} cluster. Figure 3 displays the crystal structure with a view of the Co_4O_{15} cluster. In this structure the clusters form a triangular-based lattice that resembles a honeycomb. Selected bond lengths and angles have been tabulated (Table 5). The interatomic distances in $La_2Ba_6Co_4O_{15}$ at room temperature between Co1 and O are 1.968(7) Å for Co1-O2, 1.867(5) Å for Co1-O3 and 1.713 Å for Co1-O4, and those between Co2 and O are 1.904(11) Å for Co2-O1 and 2.108(13) Å for Co2-O2. These results indicate that the CoO_6 octahedron and the CoO_4 tetrahedra in both compounds are somewhat distorted in shape. The Ba^{2+} ions occupy three different crystallographic sites (*2a*, *2b*, and *6c*) with four different coordination environments; 6, 8, 10 and 12 coordinate. Figure 8 shows the coordination environment about the Ba^{2+} ions.

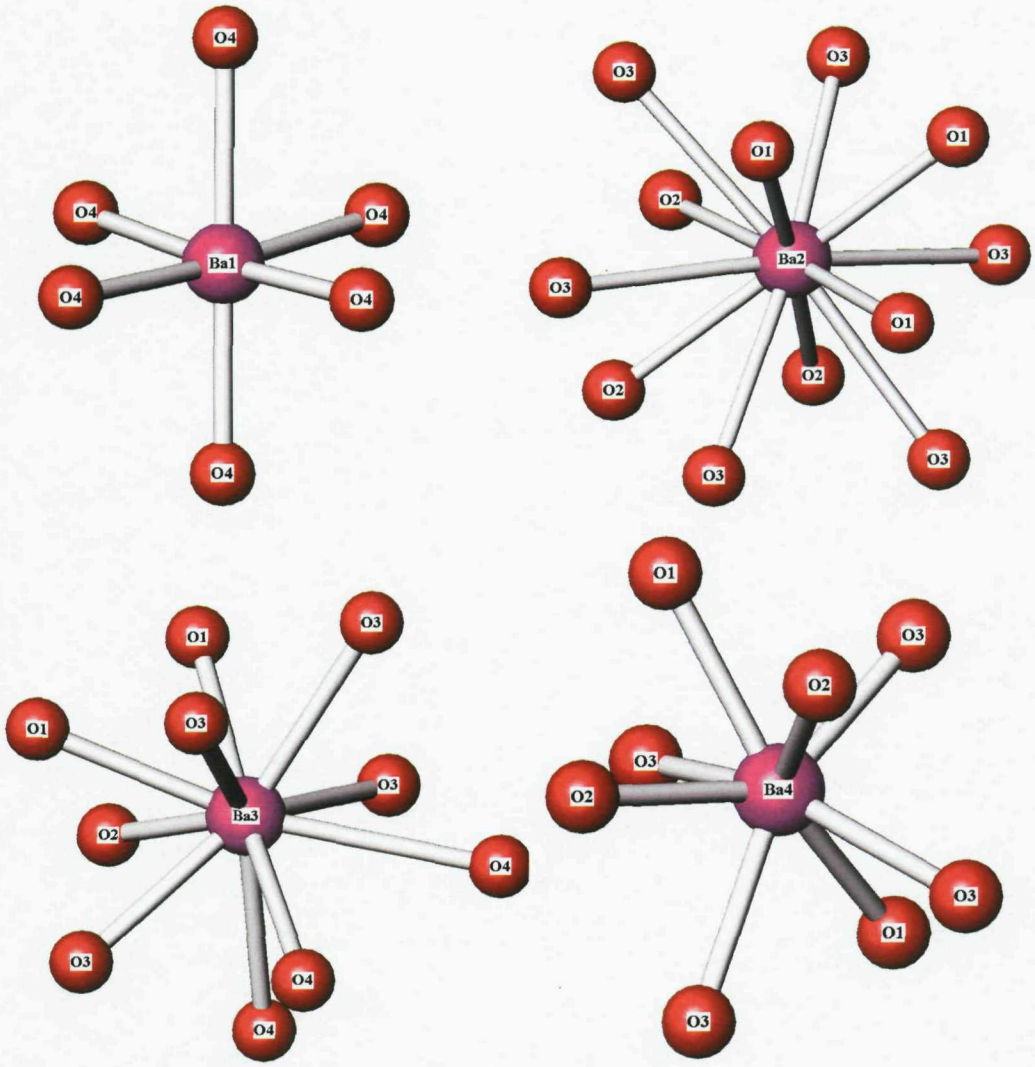

Figure 8 Coordination environments about the three Ba^{2+} and one Ba^{2+}/Ln^{3+} point positions.

In order to determine the presence of magnetic peaks, the structures were refined using PND data from Bank 3 and the same structural model as for structure refinement using Bank 1 data. An additional Bragg reflection that could not be accounted for by the nuclear model was observed in the 2 K data for $Nd_2Ba_6Co_4O_{15}$ (Figures 9 and 10). The low - angle position of the peak suggests that it may be magnetic in origin, associated with the long range ordering of Co^{3+} magnetic moments. This was confirmed by variable temperature scans performed on HRPD, which showed that the reflection vanished in the 298 K data. The magnetic intensities could be indexed on the basis of a magnetic cell related to the nuclear cell by $a_{mag} = 2a$, $b_{mag} = 2b$ and $c_{mag} = c$, however in order

to determine the true magnetic cell we would need to model more magnetic reflections in the data. The lattice parameters of this cell are suggested to be a = 23.4160 and c = 13.7940, with the hkl = 0 3 1 reflection occurring at d = 6.07 Å Additional reflection peaks were also observed in the structurally similar Fe^{3+} compound $La_2Ba_6Fe_4O_{15}$ at 2.3 K. These peaks were indexed using a propagation vector k = (½, 0, 0), i.e. the magnetic until cell is represented by $2a$ x b x c.[4] Doubling of the unit cell parameters are very common in materials which order antiferromagnetically.

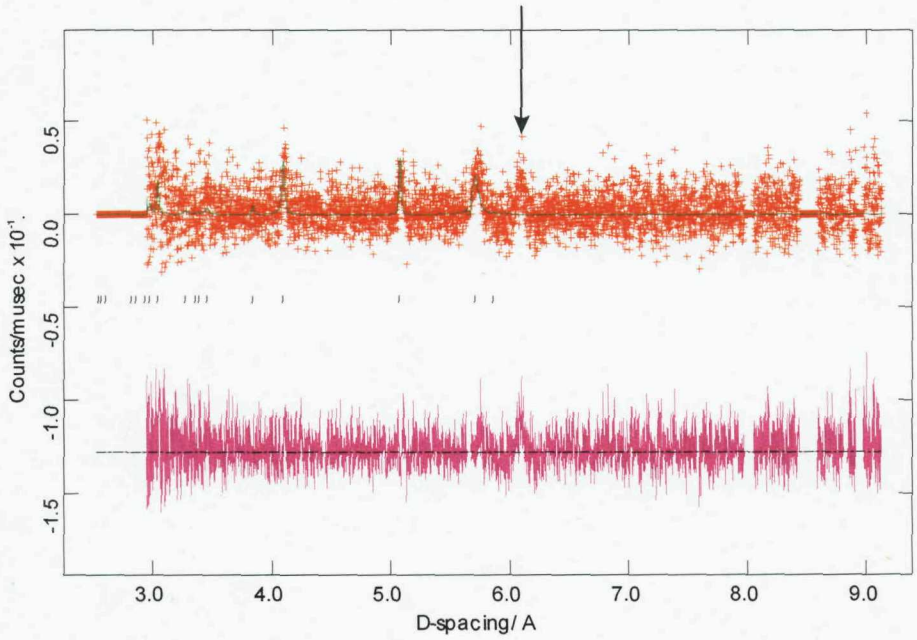

Figure 9 PND refinement profile of $Nd_2Ba_6Co_4O_{15}$ at 2 K as obtained from Bank 3 *(crosses indicate observed data, the upper continuous line shows calculated profile, the lower continuous line the difference and tick marks show reflection positions).*

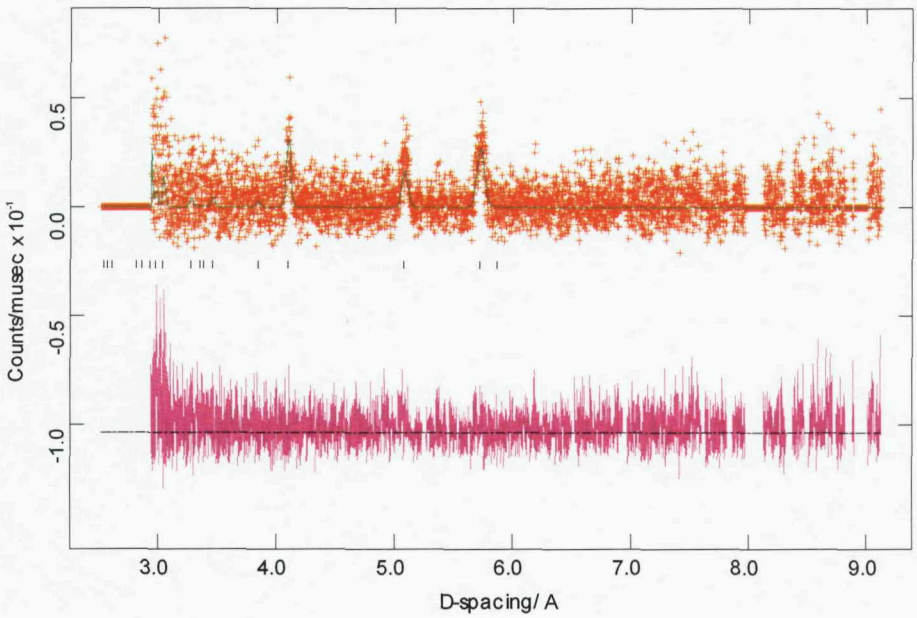

Figure 10 PND refinement profile of $Nd_2Ba_6Co_4O_{15}$ at 298 K as obtained from Bank 3 *(crosses indicate observed data, the upper continuous line shows calculated profile, the lower continuous line the difference and tick marks show reflection positions).*

6.4 Magnetic Characterisation

Magnetic data were collected on an Oxfords Instruments 3001 VSM with a 12 T superconducting magnet. The temperature dependence of the molar magnetic susceptibility of the samples $La_2Ba_6Co_4O_{15}$, $Nd_2Ba_6Co_4O_{15}$ and $Sm_2Ba_6Co_4O_{15}$ was measured in a field of H = 1 kOe on heating from low temperatures after cooling in zero magnetic field (ZFC) or in a field of 1 kOe (FC). Figures 11 - 16 show the $\chi_M(T)$ and $1/\chi(T)$ curves obtained for these samples. Both FC and ZFC magnetic susceptibility data have been collected; the latter provides a means of investigating the effects of the various magnetic interactions. First the sample is cooled to liquid helium temperatures under zero applied field, then a small uniform external field is applied and the net magnetisation is measured while heating the sample at a constant rate. As the particles cool in zero applied field, they will tend to magnetise along a preferred crystal orientation in the lattice, thus minimising the magneto-crystalline energy. Since the orientation of each crystallite varies the net moment of the system will be zero. Even when a small external field is applied the moments will remain

locked into the preferred crystal directions, as temperature increases more thermal energy is available to disturb the system. Therefore more moments will align with the external field direction in order to minimise the Zeeman energy term.

Certain magnetic systems undergoing transitions to ordered ferromagnetic, antiferromagnetic and ferrimagnetic states are reported to show irreversibility, indicated by the difference between their field cooled and zero field cooled susceptibilities. The magnetic susceptibility is larger when the sample is cooled in a magnetic field than when it is cooled in zero magnetic field. The irreversible FC and ZFC magnetic behaviour is one of the characteristic features of a spin-glass.

In $Nd_2Ba_6Co_4O_{15}$ and $Sm_2Ba_6Co_4O_{15}$ the ZFC and FC susceptibilities are almost the same throughout the whole temperature range, however $Nd_2Ba_6Co_4O_{15}$ and $Sm_2Ba_6Co_4O_{15}$ show a cusp in the ZFC susceptibility data at $\approx$ 8.5 and 17.5 K respectively which would indicate a transition to an antiferromagnetic state. These results indicate that a long range antiferromagnetic ordering of Co^{3+} ions occurs at these temperatures. For the La sample there is a large difference between FC and ZFC, indicating some kind of fragile magnetic order. In the region 300 – 90 K the material exhibits a linear variation of χ vs temperature and then undergoes an antiferromagnetic transition $T_{neel} \approx 51$ K before displaying paramagnetic behaviour between 24 - 4 K. Similarly to the Nd and Sm compounds a small cusp is also visible in the La compound at $\approx$ 4 K. These results indicate that as the Co_4O_{15} clusters compress, shown by the decrease in Co1-Co2 bond distances, the 3D ordering temperature increases. In all the compounds there is a difference between the FC and ZFC data at low temperatures suggesting that spin-glass state freezing is occurring in these compounds.

These compounds can be fitted to the Curie-Weiss equation in the temperature range 90 – 300, 50 – 300 and 75 – 300 K yielding Curie constants of 1.44, 2.05 and 1.23 cm^3 K mol^{-1} and μ_{eff} of 6.8, 8.1 and 6.5 μB per formula unit for

spin-only effective moment calculated from the free ion (S = 4/2) for the Co^{3+} ions in these compounds is 9.8 μB per formula unit. Since the ground term is $^5T_2$ we would expect an orbital contribution coming from the free ion ^5D term. However, the octahedral crystal field splitting effectively quenches most of this contribution to the angular momentum, in reality we would therefore expect the effective moment to be up to 1 μB higher than the spin-only value. The experimental values are much smaller than the theoretical values; it is believed that these experimental results reflect the structural characteristics of these compounds i.e. the Co^{3+} ions form a Co_4O_{15} cluster. If the magnetic interaction within the cluster is much stronger than between clusters, it may be possible that the cluster is magnetically isolated. The Weiss constants are -13.75 (La), -6.55 (Nd) and -11.91 (Sm) K, in general these are the same order of magnitude as the average coupling interactions.

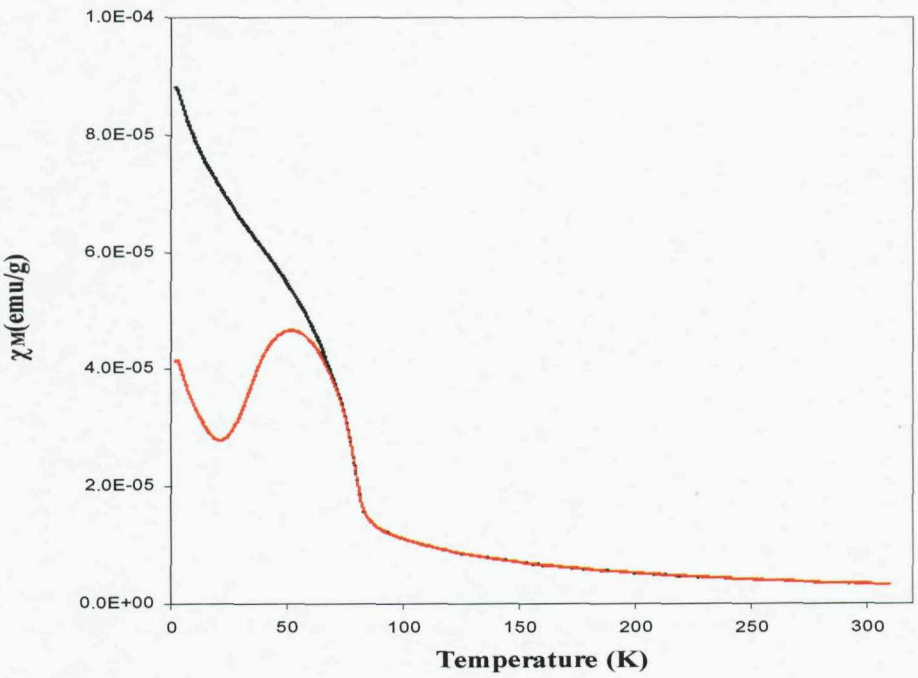

Figure 11 FC (black) and ZFC (red) magnetic susceptibility χ_M of $La_2Ba_6Co_4O_{15}$ over a temperature range 2 - 310 K (*Conversion factor to emu/mol = 1577.52*).

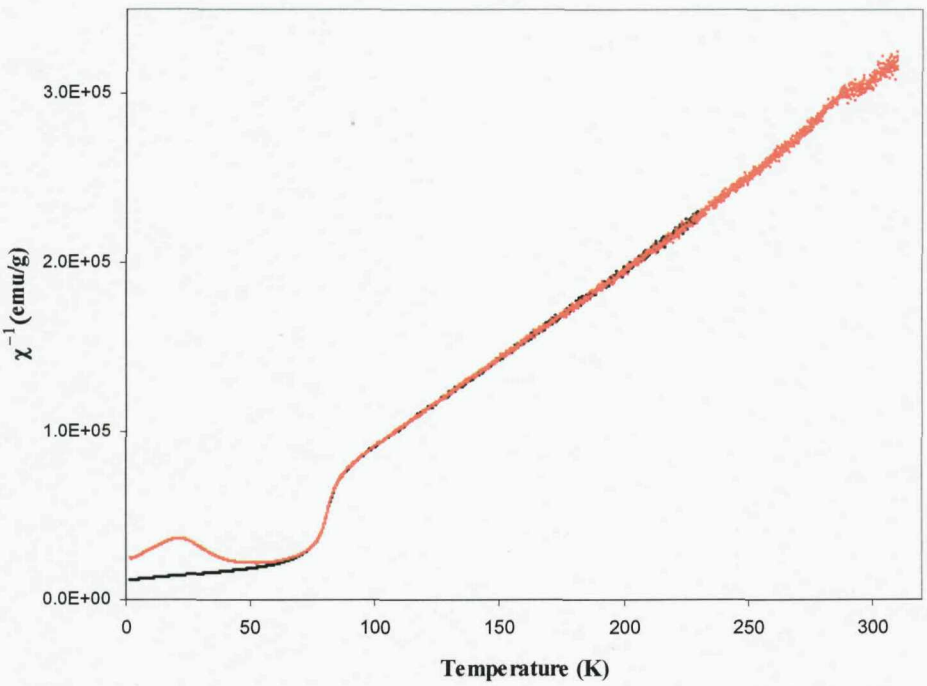

Figure 12 FC (black) and ZFC (red) inverse magnetic susceptibility χ_M of $La_2Ba_6Co_4O_{15}$ over a temperature range 2 - 310 K (*Conversion factor to emu/mol = 1577.52*).

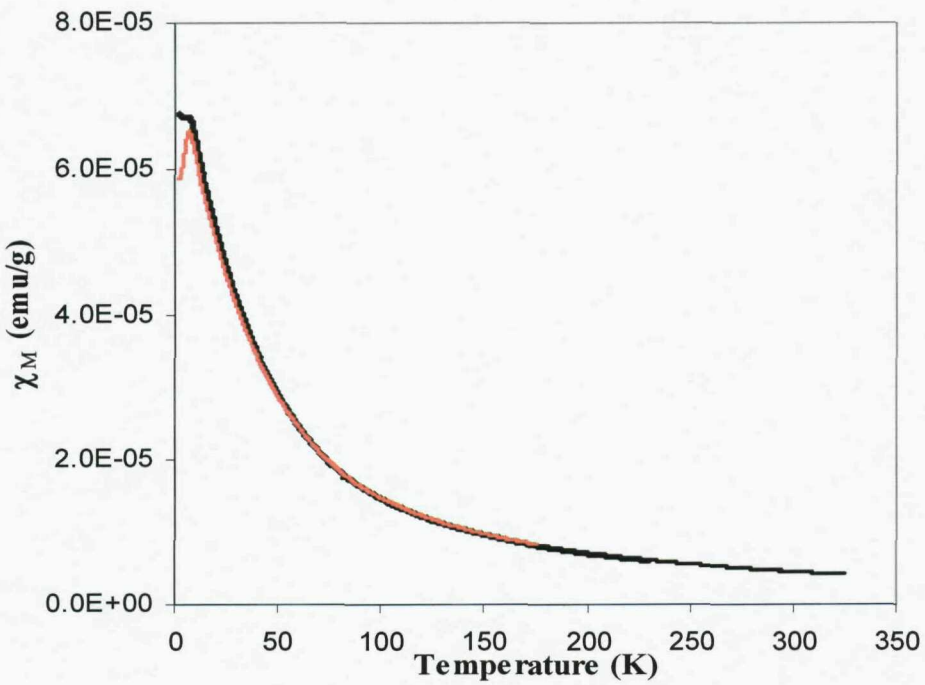

Figure 13 FC (black) and ZFC (red) magnetic susceptibility χ_M of $Nd_2Ba_6Co_4O_{15}$ over a temperature range 2 - 310 K *(Conversion factor to emu/mol = 1588.18).*

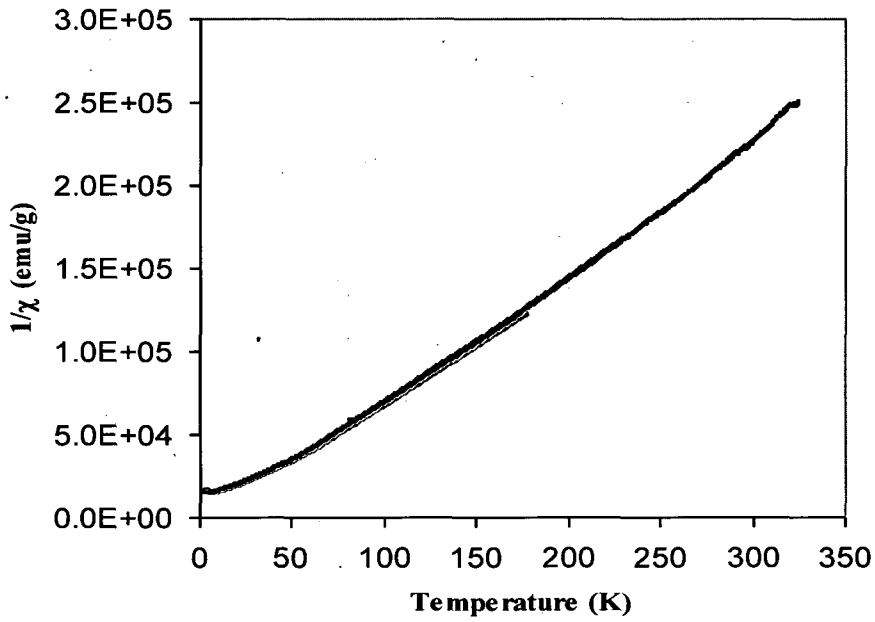

Figure 14 FC (black) and ZFC (red) inverse magnetic susceptibility χ_M of $Nd_2Ba_6Co_4O_{15}$ over a temperature range 2 - 310 K *(Conversion factor to emu/mol = 1588.18).*

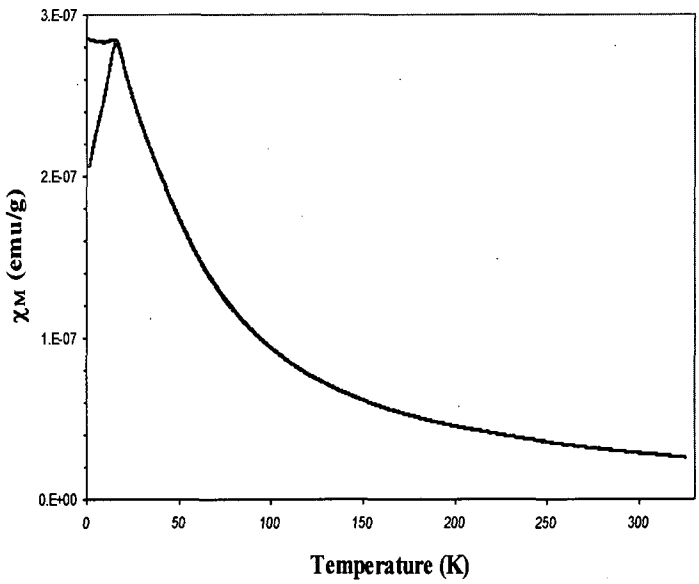

Figure 15 FC (black) and ZFC (red) magnetic susceptibility χ_M of $Sm_2Ba_6Co_4O_{15}$ over a temperature range 2 - 310 K *(Conversion factor to emu/mol = 1600.12).*

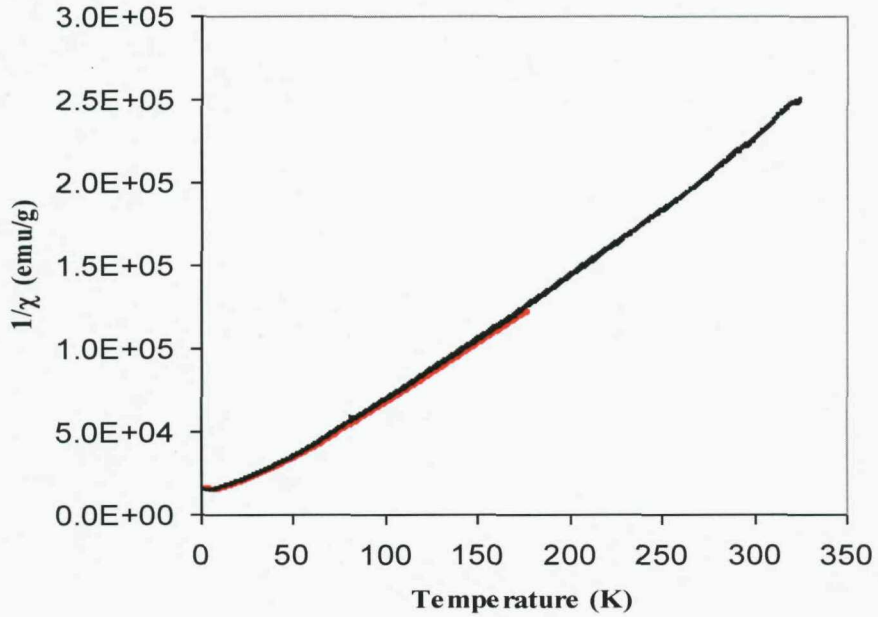

Figure 14 FC (black) and ZFC (red) inverse magnetic susceptibility χ_M of $Nd_2Ba_6Co_4O_{15}$ over a temperature range 2 - 310 K *(Conversion factor to emu/mol = 1588.18).*

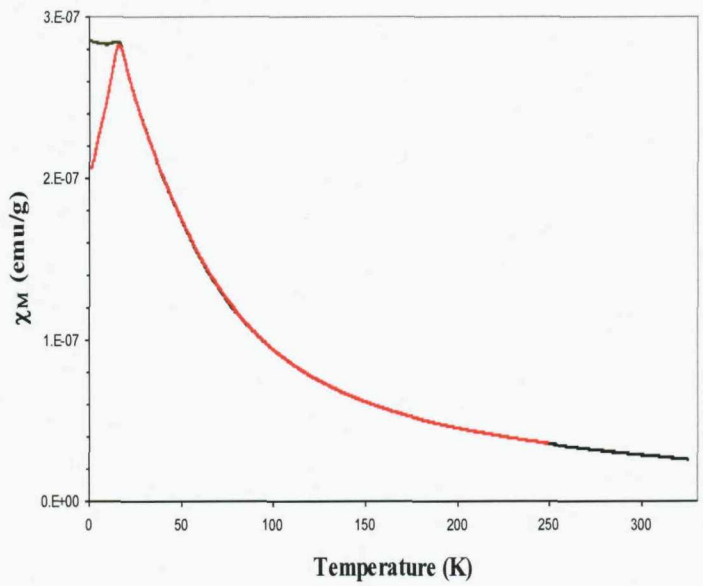

Figure 15 FC (black) and ZFC (red) magnetic susceptibility χ_M of $Sm_2Ba_6Co_4O_{15}$ over a temperature range 2 - 310 K *(Conversion factor to emu/mol = 1600.12).*

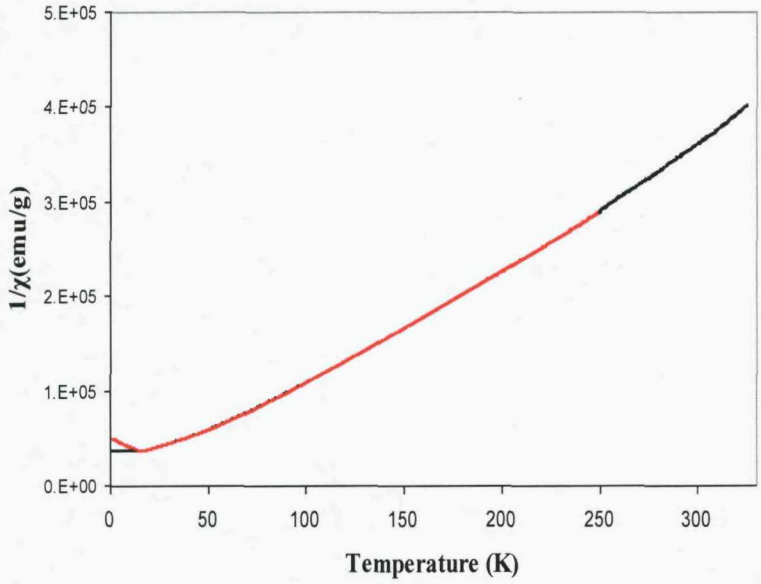

Figure 16 FC (black) and ZFC (red) inverse magnetic susceptibility χ_M of $Sm_2Ba_6Co_4O_{15}$ over a temperature range 2 - 310 K *(Conversion factor to emu/mol = 1600.12).*

6.5 A comparison of $La_2Ba_6Co_4O_{15}$ with $La_2Ba_6Fe_4O_{15}$

The crystal structure and magnetic properties of the quaternary oxide $La_2Ba_6Fe_4O_{15}$ have been investigated by Abe *et al.*.[4] It is useful to compare this compound with the analogous Co^{3+} compound studied in this work. $La_2Ba_6Fe_4O_{15}$ adopts a hexagonal structure with space group $P6_3mc$ in which four Fe^{3+} ions, per formula unit, occupy one FeO_6 octahedron and three FeO_4 tetrahedra sites. Similarly to the Co^{3+} phase, these polyhedra form a larger Fe_4O_{15} cluster by corner sharing. The refined lattice parameters for the Fe^{3+} analogue at 2 K are a = 11.8816(4) and c = 7.0713(1) Å, those obtained for the Co^{3+} phase are clearly much smaller in comparison (a = 11.7613(1) and c = 6.9583(1) Å). This is as expected as d^5 Fe^{3+} (HS) (i.r. = 0.645 Å) is greater than d^6 Co^{3+} (HS) (i.r. = 0.61 Å). The interatomic distances within the $(Fe^{3+}/Co^{3+})_4O_{15}$ clusters have been tabulated (Table 6), in both compounds the octahedra and tetrahedra are distorted and in general the Co_4O_{15} cluster is much more compressed.

Bond	Fe^{3+}	Co^{3+}
Fe/Co1-O2	1.964(6)	1.968(7)
Fe/Co1-O3	1.855(4)	1.867(5)
Fe/Co1-O4	1.813(5)	1.713(7)
Fe/Co2-O1	2.123(6)	2.108(13)
Fe/Co2-O2	1.964(5)	1.904(11)

Table 6 A Comparison of the Fe-O and Co-O bond distances.

The temperature dependence of the inverse magnetic susceptibility for $La_2Ba_6Co_4O_{15}$ shows a poor linearity in the high temperature region and does not obey the Curie Weiss law. In contrast $La_2Ba_6Co_4O_{15}$ was fitted to the Curie Weiss equation in the temperature regime 90 – 300 K. Abe *et al.* estimated the effective magnetic moment from the magnetic susceptibility data at room temperature, and calculated this value to be 8.96 μB, the effective magnetic moment for $La_2Ba_6Co_4O_{15}$ obtained from this work is 6.8 μB. Both experimental effective magnetic moments for the Fe^{3+} and Co^{3+} compounds are much smaller than those previously calculated, with values of 11.83 (S = 5/2) and 9.8 μB (S = 4/2) respectively. Using magnetic susceptibility, specific heat and magnetic entropy measurements Abe *et al.* were able to calculate the exchange integrals for the Fe^{3+} phase and are determined to be J_1 = -35. 1(1) K and J_2 = -3.41(2) K. There are two different types of interaction, one between Fe1 and Fe2 ions and the other between Fe1 and Fe1 ions, $|J_1|$ is 10 times larger which reflects the difference in the interaction pathway i.e. the linear super exchange pathway (Fe1-O-Fe2) and the much weaker super exchange pathway (Fe1-O-O-Fe1). They concluded that the ground state of the Fe_4O_{15} cluster becomes a ferrimagnetic arrangement (S_T = 5 and S' = 15/2). A similar analysis on the Co^{3+} analogue was not undertaken as we were unable to obtain specific heat and magnetic entropy measurements, however based on the similarities between the Fe^{3+} and Co^{3+} compounds we would expect a similar behaviour.

For the Fe^{3+} compound ZFC and FC susceptibilities are almost the same throughout the temperature range. However for the Co^{3+} phase there is a large difference between the ZFC and FC measurements, indicating some kind of

fragile magnetic order. An antiferromagnetic (AF) transition at 12.8 K (Fe^{3+}) and 4 K (Co^{3+}) occurs in both compounds, for the Fe^{3+} compound a specific heat anomaly is also observed at this temperature. The effect of fewer unpaired electrons in d^6 Co^{3+} is observed in the AF temperature; $La_2Ba_6Co_4O_{15}$ orders at a lower temperature, this behaviour is also seen in $FeCl_2$[7] and $CoCl_2$[8] whereby the ordering temperatures are T_N = 23.6 and 9.7 K respectively.

As described in section 6.3.3, additional reflection peaks were observed in the low angle PND data for $Nd_2Ba_6Co_4O_{15}$ at 2 K. Extra Bragg reflections were also observed in the PND data for $La_2Ba_6Fe_4O_{15}$ at 2.3 K by Abe *et al.*, it is important to note that for both compounds these reflections were not observed in the higher temperature data. The reflections in the Fe^{3+} compound were indexed using the propagation vector k = (½, 0, 0) i.e. the magnetic unit cell is represented as 2*a* x *b* x *c*. In the cobalt compound the magnetic cell doubles in both the *a* and *b* directions and is assigned as 2*a* x 2*b* x *c*.

6.6 Conclusion

The crystal structure and magnetic properties of the $Ln_2Ba_6Co_4O_{15}$ (Ln = La, Nd and Sm) phases containing the Co^{3+} ion have been investigated. These compounds have a hexagonal structure with space group P*63mc* and form the Co_4O_{15} cluster. This cluster behaves as a magnetic tetramer. $Nd_2Ba_6Co_4O_{15}$ and $Sm_2Ba_6Co_4O_{15}$ show an antiferromagnetic transition, at 8.5 and 17.5 K respectively, which is due to the long-range antiferromagnetic ordering of the clusters, in which the ordered magnetic moment for each Co^{3+} ion is 4.05 and 3.25 μB. The magnetic susceptibility data for $La_2Ba_6Co_4O_{15}$ is slightly more complex; there is a large difference between FC and ZFC, indicating some kind of fragile magnetic order. In the region 300 – 90 K the material exhibits a linear variation of χ vs temperature and then undergoes an antiferromagnetic transition $T_{neel} \approx 51$ K before displaying paramagnetic behaviour between 24 - 2 K.

In the PND profile for $Nd_2Ba_6Co_4O_{15}$ at 2 K, an additional Bragg reflection was found at lower angles that was not observed at 298 K. This is associated with the

long range ordering of Co^{3+} magnetic moments, the magnetic unit cell is represented as $2a$ x $2b$ x c. The properties of $La_2Ba_6Co_4O_{15}$ have been compared with the literature compound $La_2Ba_6Fe4O_{15}$; both compounds show similarities in structure and magnetic behaviour.

6.7 References

[1] H. Mevs and H. Muller-Buschbaum, *Z. Anorg. Allg. Chem.*, **584**, 114 (1990).

[2] H. Mueller-Buschbaum and H. Uensal, Zeitschrift fuer Naturforschung. Teil B. Anoganische Chemie, Organische Chemie, **51**, 453 (1996).

[3] H. Mevs and H. Mueller-Buschbaum, *Journal of the Less Common Metals*, **157**, 173 (1990).

[4] K. Abe, Y. Doi and Y. Hinatsu, *Chem. Mater*, **18**, 785 (2006).

[5] H. Mueller-Buschbaum and S. Meyer, *Z. Anorg, Allg. Chem*, **623**, 200 (1997).

[6] H. Mevs and H. Mueller-Buschbaum, *Journal of the Less Common Metals,* **158**, 147 (1980).

[7] W. B. Yelon and R. J. Birgeneau, *Phys. Rev. B.*, *5*, 2615 (1972).

[8] J. T. Nicholls, C. Murayama, M. Takahashi, N. Mori, T. Tamegai, Y. Iye and G. Dresselhaus, *Phys. Rev. B.*, **41**, 4953 (1990).

Chapter Seven

Transition Metal Complexes of 1,2,4-triazoles

7.1 Introduction

7.1.1 Coordination Complexes of 1,2,4-Triazoles

Organic inorganic hybrid transition metal halides have received extensive attention in recent years due to their great fundamental and practical interest. The architectures of transition metal halides can be tuned at the molecular level so as to possess unusual electronic properties, various components and potential applications in areas of molecular adsorption, catalysis, electromagnetism and photochemistry. It is therefore vital to synthesise and design novel organic-inorganic hybrid transition metal halides to explore their various properties. A recent advance in this system is the design of coordination frameworks of transition metal halides by the incorporation of various organic structure directing agents. More recently as a result of the introduction of hydrothermal synthesis and various N-containing 1,2,4-triazole organic templating agents, a variety of organic-inorganic hybrid transition metal halide complexes have been isolated with (1D) chain, (2D) layered and (3D) coordination networks.

The first coordination compound with 1,2,4-triazole was described as early as 1900.[1] Until 1970 most papers dealt with copper compounds, especially $[CuCl_2(Htrz)$, $[CuCl(trz)(H_2O)_2]$ and $[Cu(trz)_2]$[2,3,4,5,6] in which trz stands for the deprotonated form of the 1,2,4-triazole. After 1970 a variety of triazole complexes have been reported, some of which show many interesting features especially from a magnetochemistry point of view. In the chain compound $[CuCl_2(Htrz)]$[7] and in the linear trinuclear compound $[Ni_3(Htrz)_6(H_2O)_6](NO_3)_6(H_2O)_2$[8] the triazoles are coordinating in a 1,2-bidentate fashion. The magnetic exchange in both compounds is antiferromagnetic.[5,6,9] Engelfreit *et al.*[10] first described a series of layered structures in which the triazole ligands are bridging through the 2,4-nitrogen atoms. The compounds have a general composition $[M(Htrz)_2(NCS)_2]$ for the divalent metals Mn, Fe, Co, Ni, Cu and Zn. For the Mn, Fe, Co and Ni compounds an antiferromagnetic intralayer exchange is found, while the Cu complex appears to be slightly ferromagnetic. When a substituent is placed at the

4-position, this ligand is forced to coordinate in a monodentate or a 1,2-bidentate fashion, resulting in $[Mn_2(Metrz)_5(NCS)_4]$ (Metrz = 4-methyl-1,2,4-triazole) and $[Co_2(Phtrz)_5(NCS)_4](H_2O)_{2.7}$ (Phtrz = 4-phenyl-1,2,4-triazole). In both dinuclear compounds the metal centres are coupled antiferromagnetically. A series of dinuclear compounds, which show asymmetrical occupation of the terminal coordination sites have also been reported. The compounds have a general composition of $[M_2(Ettrz)_4(H_2O)(NCS)_4](H_2O)_2$ (Ettrz = 4-ethyl-1,2,4-triazole) for M = Mn, Fe, Co, and Ni. In these compounds the metal centres are also coupled antiferromagnetically. Transition metal(II) thiocyanates with 4-t-butyl-1,2,4-triazole give rise to the formation of mono-, di- and tri-nuclear chain compounds.

In 2003 Yan Garcia *et al.* reported $[Cu(hyetrz)_3(CFSO_3)_2.H_2O]$ (hyetrz = 4-(2'-hydroxyethyl)-1,2,4-triazole),[11] the first structurally characterised ferromagnetically coupled Cu(II) chain compound. The coordination polymer consists of a crystallographically independent unit comprising two Cu(II) ions in special positions and another Cu(II) ion in a general position, along with six symmetry independent hyetrz ligands (Figure 1).

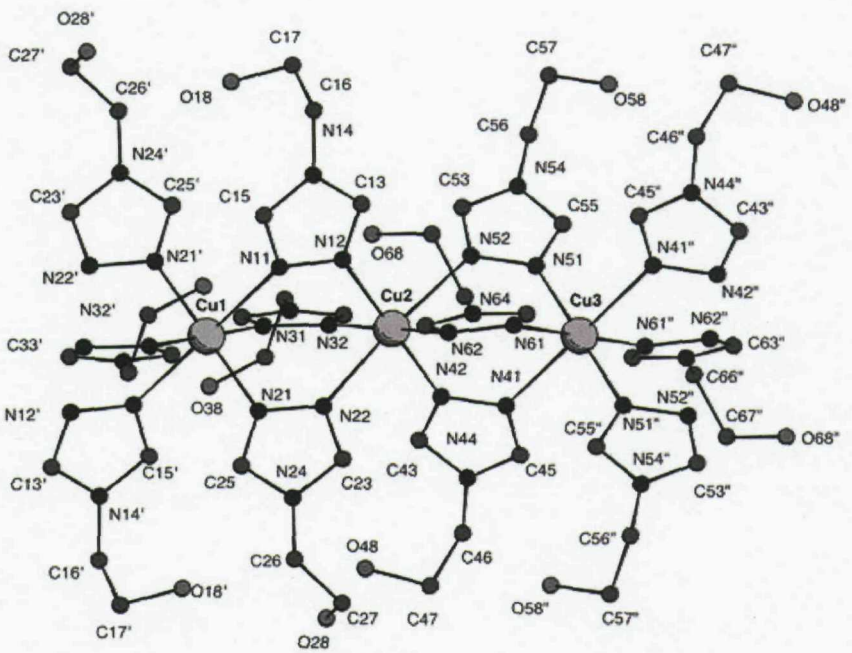

Figure 1 Drawing and atomic labelling system showing the structure of $[Cu(hyetrz)_3](CF_3SO_3)_2 \cdot H_2O$; hydrogen atoms, noncoordinating counter anions, and water molecules have been omitted for clarity.[11]

The reaction between amtrz (amtrz = 4-amino-1,2,4-triazole) in MeCN (0.1 mmol in 10 mL) and an aqueous solution of an appropriate copper salt (0.03 mmol, 2 mL) gave a blue amorphous precipitate. The precipitate was filtered off, washed with 5 mL of MeCN and immediately dissolved in water resulting in a light blue solution. After a few weeks $[\{Cu(amtrz)]_3(BF_4)_2.H_2O\}]$(1) and $[\{Cu(amtrz)_3](BF_4)(SiF_6)_{0.5}.2H_2O\}]$(2) or days $[\{Cu(amtrz)_3]SiF_6).8/3H_2O\}]$(3) crystals appeared. The crystals are composed of linear coordination polymers $[Cu(amtrz)_3]_\infty$ with BF_4 (1), BF_4/SiF_6 (2) and SiF_6 (3) counter ions placed between them as well as different numbers of water molecules (1,2 and 8/3 respectively). The μ-N^1.N^2-1,2,4-triazoles act as bidentate ligands bridging copper(II) ions *via* their nitrogen atoms (Figure 2).[12]

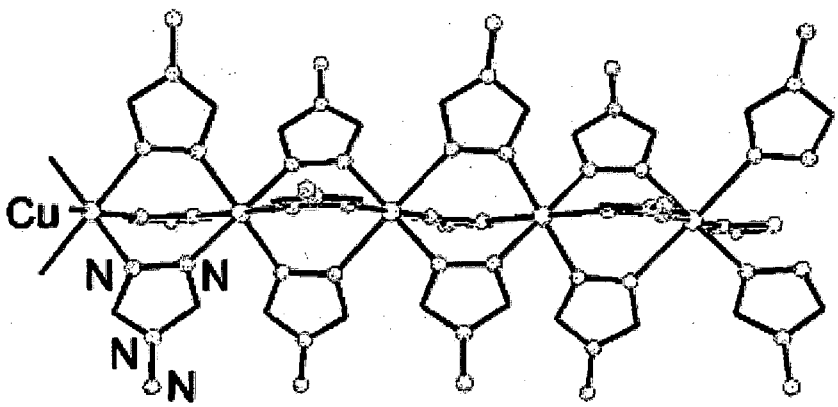

Figure 2 View of the 1-D coordination polymer of $[\{Cu(amtrz)_3]SiF_6).8/3H_2O\}]$. The anions and water solvent molecules have been omitted for clarity.[12]

The first example of a mixed valence trinuclear cobalt derivative with 1,2,4-triazole is the *bis*(μ-3,5-diamino-1,2,4-triazole-N^1,N^2)*bis*(μ-3,5-diamino-1,2,4-triazolato-N^1,N^2)triaquacobalt(II)cobalt(III) trichloride nonahydrate complex.[13] The crystals were obtained by the slow evaporation of a water solution of 3,5-diamino-1,2,4-triazole and cobalt(II) chloride in a 3:1 ratio. The crystals are trigonal, and the structure consists of trimeric units. The chlorine atoms randomly occupy six general positions in the cell, and so do three water

molecules. Six other water molecules are hydrogen bonded to the 3,5-diamino-triazole moieties. In the trimeric cation the three cobalt ions are bridged by six 3,5-diamino-1,2,4-triazole moieties. Each triazole bridges two different cobalt ions with its 1,2-nitrogen atoms. The central cobalt atom is bonded to six nitrogen atoms, with a very short distance (Figure 3). The magnetic properties of the complex agree with the formulation $Co(II)_2Co(III)$, the room temperature effective magnetic moment μ_B = 7.15, agrees with the presence of two uncoupled high-spin octahedral Co(II) ions each with μ_{eff} = 5.1 μ_B, while it would be too small for three Co(II) ions. In fact the range of Co(II) ions is 4.8 – 5.4 μ_B. Furthermore the temperature independence of χT down to *ca.* 100 K rules out any possibility of relevant antiferromagnetic interaction which might reduce the room temperature effective magnetic moment. The observed decrease in χT can be attributed to the thermal depopulation of the excited Kramer's doublets originated by spin-orbit and low symmetry splitting of $^4T_{1g}$ of the two Co(II) ions. Below 20 K μ_{eff} stabilises to 5 μ_B, which agrees with two uncoupled effective S = ½ spins with g = 4.

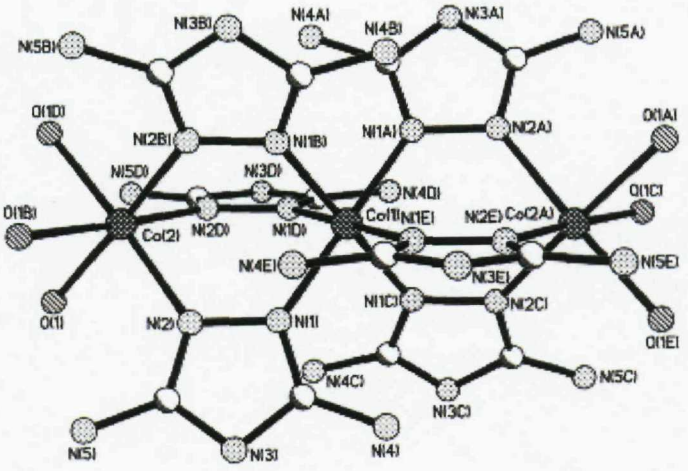

Figure 3 Ortep view of the *bis*(μ-3,5-diamino-1,2,4-triazole-N^1,N^2)*bis*(μ-3,5-diamino-1,2,4-triazolato-N^1,N^2)triaquacobalt(II)cobalt(III) trichloride nonahydrate complex, showing the atom numbering and thermal motion ellipsoids (50%) for the non-hydrogen atoms. The hydrogen atoms are represented as spheres of arbitrary radius. Two water molecules are omitted for clarity.[13]

7.1.2 Objective

Almost all useful magnetic materials are metals, ceramics or other close packed inorganic materials. All these materials are opaque; absorbing strongly across the whole of the visible spectrum. Their electronic structures, which are well described by band theory and contain a continuum of states and excitations, are often non-local. In contrast the electronic spectra of molecular materials and coordination networks are not much different from that observed for isolated 'molecular chromophores'. In such systems we can tailor the electronic behaviour to meet a specific need. Coloured magnets and magnetic materials that change colour as a response to some external stimuli (temperature, pressure, light and magnetic field) have many potential technological applications. Although at present coloured magnets are rare, there is no theoretical conflict between having useful magnetic and optical properties in a single material.

The ability of azoles, triazoles[14] and tetrazoles to bridge transition metal ions is central to the recent increased interest in their coordination chemistry. From a structural perspective You *et al.*[15] have recently prepared an "open framework" material from cobalt(II) and imidazole, which displays extensive polymorphism and a zeolitic character. While iron(II)[16] coordination polymers with triazoles have been of interest to magnetochemists since many of these compounds show spin crossover behaviour with thermal hysteresis effects. Here a spin crossover-driven structural phase transition results from the extensive covalently bridged network, which relays the structural changes at the iron centres. It is perhaps surprising that despite much work in this area, crystallographic structural information is often difficult to obtain. Another point of interest is the ability of these linkages to mediate magnetic interactions and form molecular based magnets.

This chapter is concerned with the synthesis and characterisation of new magnetooptic materials, in which the extended structures formed, may show both magnetic coupling interactions and 'cooperative spin transition effects'. If a material with a spin transition close to room temperature can be engineered, then

such a delicately balanced system may be susceptible to perturbation by other stimuli such as pressure, light or a magnetic field.

Hydrothermal synthesis has been shown to be a highly effective method with which to investigate a wide variety of inorganic materials. Very few coordination compounds of the 1,2,4-triazole ligands have been synthesised using hydrothermal methods. This research concentrated on the synthesis of transition metal (Mn(II), Fe(II), Co(II), Ni(II), Cu(II) and Zn(II)) complexes of the commercially available triazoles; 3-amino-1,2,4-triazole, 4-amino-1,2,4-triazole, 3,5-diamino-1,2,4-triazole, 4-amino-1,2,5-triazole and 4-(-1,2,4-Triazol-1-yl)phenol. Reaction of the 1,2,4-triazoles with $FeCl_2.4H_2O$ led to the formation of Fe_2O_3, which was confirmed by PXD. In hydrothermal reactions these oxides are 'thermodynamic sinks' that is they have such a low 'internal energy', so that once formed it is very difficult to transform them. This is exacerbated by their incredibly low solubility.

Optimisation of the reaction conditions has been conducted in an effort to increase the yield of the crystalline product. The reactions were carried out in Teflon-lined stainless steel autoclaves filled to ~70% capacity and heated under autogenous pressure, with varying reaction times and temperatures. Several of these experiments have been successful and the optimum experimental conditions are described.

7.2 [Co_2Cl(3-amino-1,2,4-triazole)$_3$]

7.2.1 Synthesis

A mixture of $CoCl_2.6H_2O$ (100 mg, 0.42 mmol) and 3-amino-1,2,4-triazole (0.84 mmol) in distilled water (10 mL) was heated at 180 °C under autogenous pressure for 72 hours before being cooled to room temperature. Blue needle-shaped crystals of $Co_2Cl_2(C_2N_4H_3)_3$ were collected by filtration, washed with distilled water and dried. Due to the monophasic nature of this compound we were able to obtain elemental and IR data. Found C 17.68, H 2.19, N 40.00

(outside normal instrument range), Cl 8.37%: $Co_2ClC_6H_9N_{12}$ requires C 17.90, H 2.25, N 41.76, Cl 8.81%. Vibrational spectra (KBr) $\bar{\nu}_{max}$ 3419 (s), 3332 (s), 3141 (m), 2929 (w), 2804 (w), 2703 (w), 2592 (vw), 2483 (w), 2426 (w), 2255 (w), 2094 (vw), 1759 (m), 1614 (s), 1522 (vs), 1426 (s), 1384 (s), 1326 (w), 1282 (s), 1211 (s), 1132 (w), 1094 (m), 1047 (s), 1007 (m), 884 (m), 763 (s), 735 (m), 665 (s), 480 (s) cm^{-1}; Electronic spectra (Diff. Ref. $BaSO_4$ matrix) λ/nm (abs/rel) 320 (0.6), 520 (0.38) ($Co(O_h)$: → $^4T_{1g}(P)$), 620 (0.58) ($Co(T_d)$: → $^4T_1(P)$), 1150 (0.55) ($Co(T_d)$: → $^4T_2(F)$), 1290 (0.58) ($Co(O_h)$: → $^4T_{2g}(F)$). Powder X-ray diffraction, 12 mg sample, Siemens D5000, 5`<`2θ ≤`75°, λ(Cu $k_{\alpha 1}$) d/Å (k-vector), 8.4900 $(1\bar{1}0)$, 5.6917 $(01\bar{1})$, 4.9377 $(2\bar{1}0)$, 4.2819 $(2\bar{2}0)$, 3.7509 $(02\bar{1})$, 2.9948 $(3\bar{2}1)$, 2.8713 $(3\bar{3}0)$, 2.4886 $(4\bar{2}0)$, 2.0332, 1.8832, 1.7619, 1.6632, 1.3844.

7.2.2 Results and Discussion

Crystals of the compound $[Co_2Cl(3\text{-amino-}1,2,4\text{-triazole})_3]$[17] were obtained hydrothermally by the reaction of $CoCl_2.6H_2O$ and 3-amino-1,2,4-triazole. Optical microscopy shows the reaction product to be monophasic and comprised of small blue needle-shaped crystals with a strong blue-pink dichroism. Sample purity was confirmed by PXD. The compound crystallises in a primitive hexagonal cell; a good structural model for $[Co_2Cl(3\text{-amino-}1,2,4\text{-triazole})_3]$ was obtained in the non-polar space group *P6₃/mmc* (#194) (Figure 4), revealing a 3-D coordination network. Details of the crystallographic data collection and refinement parameters are given in Table 1.

Table 1 Crystallographic data and refinement parameters for $[Co_2Cl(3\text{-amino-}1,2,4\text{-triazole})_3]$ *(e.s.d's are given in parantheses).*

Formula Sum	$C_6H_9ClCo_2N_{12}$
Formula Weight	402.56
Temperature/ K	120 K
Wavelength/ Å	0.71073
Crystal System	Hexagonal
Space Group	$P6_3/mmc$
***a*/Å**	9.9655(14)
***b*/Å**	9.9655(14)
***c*/Å**	7.7523(16)
α/°	90
β/°	90
γ/°	120
***U*/ Å^3**	666.74(19)
Z	2
Crystal Size/ mm^3	0.01 x 0.02 x 0.06
Unique reflections	513
Obs. reflections With [$I > 2\sigma(I)$]	388
***R1* [$I > 2\sigma(I)$]**	0.1037
***R1* (all data)**	0.0702
***wR2* (all data)**	0.1316

$R1 = \Sigma||F_o|-|F_c||/\Sigma|F_o|$; $wR2 = [\Sigma w(F_o^2-F_c^2)^2/\Sigma wF_o^4]^{½}$

Table 2 Important derived bond distances and angles for $[Co_2Cl(3\text{-amino-}1,2,4\text{-triazole})_3]$ *(e.s.d's are given in parantheses).*

Bond	Length/ Å	Bond	Angle/ °
Co1 – N1	2.129(5)	Cl1 – Co2 – N2	109.87(10)
Co2 – N2	2.052(7)	C1 – N1 – N1	104.9(4)
Co2 – Cl1	2.287(5)	C1 – N1 – Co1	129.3(4)
N1 – C1	1.318(8)	N1 – N1 – Co1	125.80(12)
N1 – N1	1.385(9)		
C1 – N2	1.320(9)		
C1 – N3	1.328(11)		
N2 – Co2	2.052(7)		

It is clear from this structure that the compound contains two Co(II) ions, three 3-amino-1,2,4-triazole ligands and a chloride ion, in agreement with the results of elemental analysis. The framework is composed of linear $[Co(C_2N_4H_3)_3]_n^{n-}$ chains, in which neighbouring octahedrally coordinated metal ions are linked by three bridging triazole ligands, a motif seen in many other metal-triazole networks.[18] These columns run parallel to the *c*-axis and are arranged in a hexagonal fashion with a second metal ion linking three columns through the coordination of the triazole nitrogen in the 4-position.[19] The fourth site of this tetrahedrally coordinated ion is occupied by the chloride ion (similar to the coordination of Zn(II) in $Zn(C_2N_3H_2)Cl$).[20] Thus the structure contains stacks of CoN_3Cl coordination polyhedra.

Steric considerations require a given stack of CoN_3Cl tetrahedra to be polar, with all Co–Cl bond vectors aligned in the same direction. No steric requirement exists for the relative orientations of neighbouring stacks. Two simple structurally ordered solutions are possible:

A) All the polar stacks align in the same direction, such a structure is described in the polar space group $P6_3mc$, #186.

B) Alternate columns have Co–Cl bonds pointing in opposite directions. This non-polar structure has the same cell parameters and occurs in space group $P\bar{3}m1$, #164.

The */m* symmetry in space group #194 imposes an orientational disorder on the ligand and on the position and orientation of the chloride and tetrahedral cobalt ions. This is consistent with the fact that the crystal structure appears to show a superposition of two triazole orientations. The apparent structural disorder observed in the space group #194 could result from a simple macroscopic twinning of the ordered models A and B, alternatively disorder at a microscopic scales yields model C (a random orientation of stack polarity), which is best described in space group #194. Refinement in both ordered and twinned models gave either unstable or unsatisfactory refinement statistics. Suggesting that the disorder in $[Co_2Cl(3\text{-amino-}1,2,4\text{-triazole})_3]$ is microscopic in origin and model C is the best structural description. Further work would involve diffuse scattering studies which should qualify our model and quantify the extent of any disorder.

Although local orientational disorder of this ligand is known[21] in this case stereo-kinetic considerations suggest that once a particular orientation for a Co^{II} tetrahedron occurs, then that orientation is propagated along the stack as the crystal grows. This type of disorder allows the entire structure to be divided into structurally ordered domains. The division can be described in terms of polar (model A) domains or non-polar (model B) domains. In the likely event of a biased distribution the average domain size of the polar division is inversely related to the size of the non-polar division.

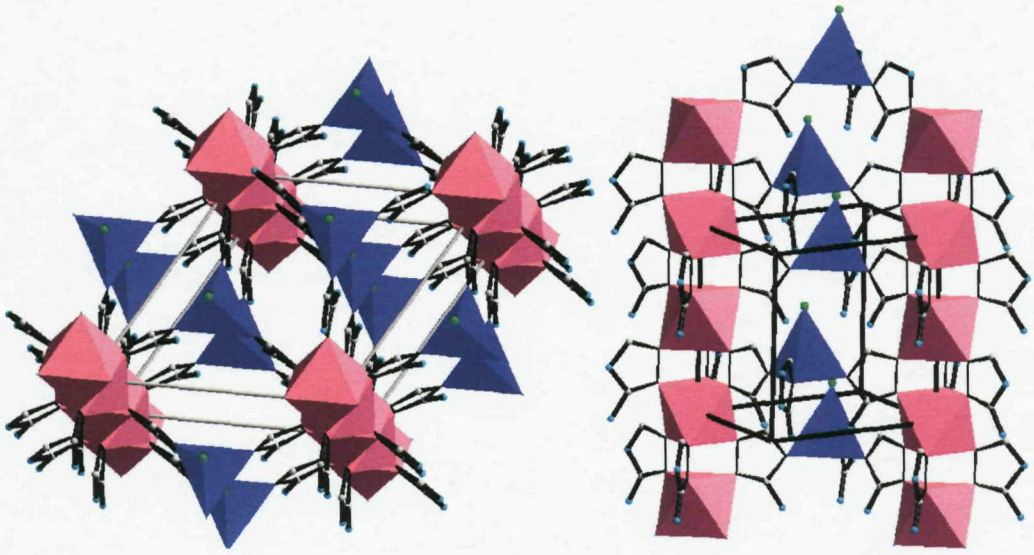

Figure 4 The network structure of $[Co_2Cl(3\text{-amino-}1,2,4\text{-triazole})_3]$, showing a structurally ordered portion with all the ligands having the same (down) orientation. **a)** viewed just off the *c*-axis, showing how the triazole links up Co ions and **b)** viewed nearly perpendicular to *c*-axis (*CuN_6 octahedra in pink, CuN3Cl tetrahedra in dark blue, Cl atoms in green, C atoms in grey and N atoms in light blue*).[17]

7.2.3 Magnetic Susceptibility Measurements of $[Co_2Cl(3\text{-amino-}1,2,4\text{-triazole})_3]$

Field cooled magnetisation measurements (FCM: H = 100 Oe) on $[Co_2Cl(3\text{-amino-}1,2,4\text{-triazole})_3]$ reveal a significant increase in sample magnetisation below ~5 K, typical of an ordered magnetic phase with a spontaneous net moment (Figure 6a). Fitting $\chi(T)$ at high T to Curie-Weiss law gives $C = 2.99(1)$ $cm^3\ mol^{-1}\ K$ and $\theta = -58.2(8)$ K. The Curie constant equates to an $S = {}^3/_2$ ground state for both O_h and T_d Co^{II} ions with an average g-value of 2.31. The negative Weiss constant indicates a dominant antiferromagnetic exchange interaction. Measurements at H = 50 and 200 Oe show a strong field dependence of the susceptibility in the low temperature regime and field independent behaviour above the transition temperature. The FC and zero-field cooled magnetisation (ZFC) show similar behaviour with the onset of a significant moment below 5.3(1) K, while the remnant magnetisation (REM) curve decays to zero by 4.9 K

(Figure 5a). Variable frequency ac susceptibility measurements were performed in the vicinity of the magnetic phase transition (Figure 6). The position of the peak at 3.5 K in both the real and imaginary components is independent of frequency, and corresponds to a transition to a long-range ordered magnetic state with a net moment. We note an unusual feature between 4 and 5.2 K, consisting of two overlapping maxima. The position of the maxima and the shape of this part of the imaginary susceptibility has frequency dependence, suggestive of a 'blocking' temperature and superparamagnetic-like or spin glass-like behaviour. It appears that $[Co_2Cl(3\text{-amino-}1,2,4\text{-triazole})_3]$ shows at least three magnetic phases:

- above 5.3(1) K is a normal paramagnetic state
- between ~ 4 and 5.3(1) K is an intermediate state and
- below ~ 4 K we see the formation of a more conventional long-range ferrimagnetically ordered phase.

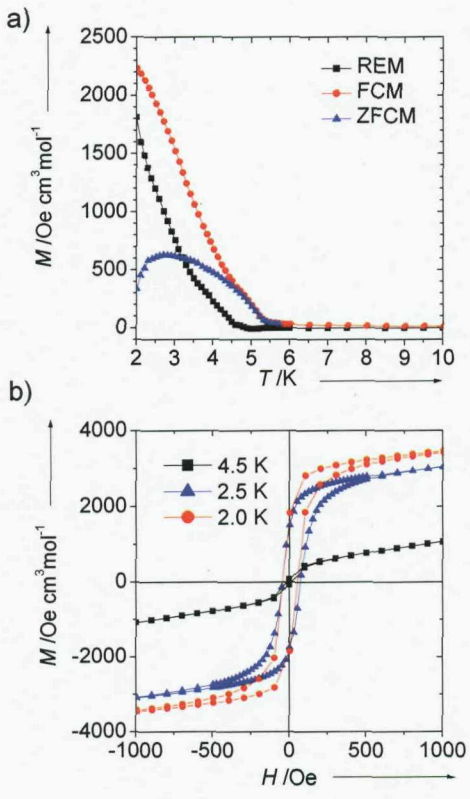

Figure 5 a) FC, ZFC and REM measurements of $[Co_2Cl(3\text{-amino-}1,2,4\text{-triazole})_3]$ **b)** Hysteresis measurements in both the low-temperature and intermediate magnetic phase.[17]

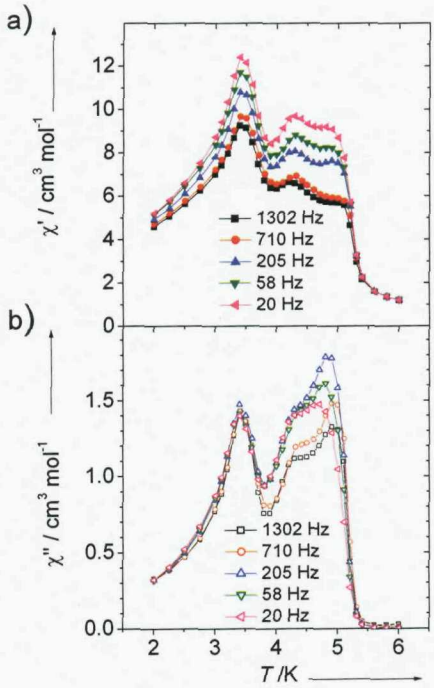

Figure 6 a) The real, in-phase component of the variable frequency ac susceptibility measurement and **b)** the imaginary, out-of-phase component.[17]

Field dependent measurements at 2.0, 3.0 and 3.5 K all show a very rapid increase in $M(H)$ on application of the smallest field; while at 4.0, 4.5, 4.75 and 5.0 K the initial increase in $M(H)$ is not so great; and measurements at 5.5 and 6.0 K reveal characteristic paramagnetic behaviour. Hysteresis measurements at 2 K (Figure 6b) supports the proposed ferrimagnetic order; H_{coer} = 50 Oe, M_{ret} = 1830 Oe cm^3 mol^{-1}. We determine the saturation magnetisation as 3450 Oe cm^3 mol^{-1} (per Co ion), corresponding to 18% of the moment expected for a ferromagnetically aligned sample (using the average g-value determined from the high T susceptibility). The area enclosed by the hysteresis curve is 83.3 mJ mol^{-1}. A similar measurement at 4.5 K shows virtually no remnant magnetisation or cooperativity, consistent with a fast relaxation process. The quoted coupling constants are defined from the pair-wise (or equivalent) Hamiltonian: $\hat{H} = -2J\mathbf{S_1}\cdot\mathbf{S_2}$.

There are three triazole-mediated superexchange interactions (Figure 7); J_1 links O_h Co ions ($d_{(Co\cdots Co)}$ = 3.876 Å) into chains along the c-axis, J_2 and J_3 both link a T_d ion to an O_h ion ($d_{(Co\cdots Co)}$ = 5.886 and 6.329 Å). From previous studies[22,23,24]

we expect antiferromagnetic interactions with $J_1 \sim -7$ cm^{-1} and $J_2 \sim J_3 \sim -2$ cm^{-1}. The 3-D magnetic order is a result of the interchain couplings J_2 and J_3.

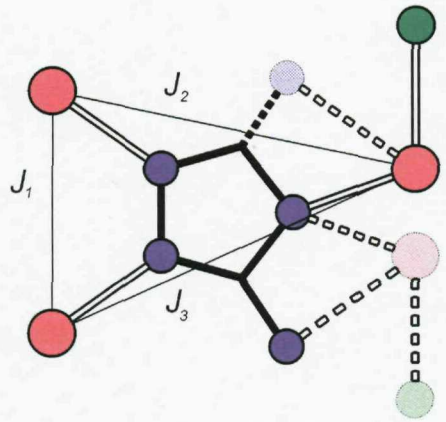

Figure 7 The coordination geometry of the ligand; Co - pink, Cl - green, N - blue, C - black. The alternative ligand orientation shown by dashed bonds and cross-hatched atoms. Also shown are the triazole mediated exchange coupled pathways as described in the text.[17]

A model of the magnetically ordered structure can be built if we assume $J_2 < J_3$. The other possibility ($J_3 < J_2$) yields a qualitatively similar result. In this extended magnetic model, moments connected by J_1 and J_2 have an antiparallel relationship and all of these pair-wise interactions can be satisfied. However, the exact nature of the physical structure of [Co_2Cl(3-amino-1,2,4-triazole)$_3$] is crucial to the overall magnetic ground state. For both the polar model A and the non-polar model B we predict an ordered magnetic structure where $Co^{II}(O_h)$, ions linked by J_1 have alternate spin polarisation, while all Co(II)(T_d) ions in given stack have the same spin polarisation. However, while for model A we expect neighbouring stacks to have opposite spin polarisations, resulting in an overall antiferromagnetic state, for the ordered non-polar structure (model B) we expect topological ferrimagnetic order with all the Co(II)(T_d) stacks having the same spin alignment. Such a structure would have a saturation magnetisation of ~ 8380 Oe cm^3 mol^{-1} per Co ion (assuming $g = 2$ for $Co^{II}(T_d)$). The observed magnetisation corresponds to 41% of the expected value for the ferrimagnetic model (based on structural model B).

The effect of structural disorder on the ground state of [Co_2Cl(3-amino-1,2,4-triazole)$_3$] is quite unusual, the disorder of model C does not result in competing interactions and we do not expect spin glass behaviour. In fact, in the disordered model we still satisfy all J_1 and J_2 pair-wise interactions whilst forming ferromagnetic domains which map directly on the two domains for the non-polar ordered structure (Alternatively we can divide the space into two ordered antiferromagnetic domains which can be mapped onto the structurally polar domains).

So while the structurally ordered models should exhibit straight-forward behaviour (model A - antiferromagnet; model B - topological ferrimagnet) the observed magnetic behaviour is evidence for a more disordered model C structure. We note that the magnetic ordering temperatures for models A and B should be different, and that it is likely that structural domain size can influence T_c. It is well known that when particle size limits domain size, materials can show superparamagnetic behaviour and characteristic blocking temperatures.

The structural properties of [Co_2Cl(3-amino-1,2,4-triazole)$_3$] account for the unusual magnetic behaviour that we observe. In combination the structural data and the magnetic studies all point to a structural model with 1-D order and 2-D orientational disorder. Magnetically the unique structure permits an unusual and distinct intermediate magnetic phase, with little anisotropy and rapid dynamical processes. This material is clearly in need of much further study and both structural and magnetic experiments are required to better qualify and quantify the interplay of structural disorder and magnetic order.

7.3 [CuCl(3-amino-1,2,4-triazole)$_2$.Cl]

7.3.1 Synthesis

A mixture of $CuCl_2.2H_2O$ (100 mg, 8.65 x 10^{-4} mmol) and 3-amino-1,2,4-triazole (1.73 x 10^{-3} mmol) in distilled water (10 mL) was heated at 200 °C under autogenous pressure for 72 hours before being cooled to room temperature. Blue needle shaped crystals of [CuCl(3-amino-1,2,4-triazole)$_2$.Cl] were collected by filtration, washed with distilled water and dried. This compound is not monophasic and therefore we were unable to obtain elemental analysis and IR data.

7.3.2 Results and Discussion

Up to date, the basic copper halide skeletons of hybrid organic-inorganic copper halide complexes generally exhibit several geometrical motifs: cyclic Cu_2X_2 dimeric, cubane tetrameric, zig-zag polymeric and 'stair step' oligomeric structures. Here we describe a zig-zag polymeric structure; crystals of the compound [CuCl(3-amino-1,2,4-triazole)$_2$.Cl] were obtained hydrothermally by the reaction of $CuCl_2.2H_2O$ and 3-amino-1,2,4-triazole in a 1:2 molar ratio respectively in the presence of water. [CuCl(3-amino-1,2,4-triazole)$_2$.Cl] crystallises in the orthorhombic space group P*bcm* with Z = 4 formula units.

In the crystal structure the copper(II) and chlorine atoms form helical chains. The metal ion is in a distorted [4+2] octahedral environment formed by two axial chlorine atoms and four equatorial nitrogen atoms from two separate 3-amino-1,2,4-triazole ligands. The basal plane is formed by four Cu-N bond lengths of 1.996(4) and 2.002(4) Å and the Cu-Cl bond lengths are 2.731(2) and 2.734(2) Å. The distribution of the Cu-N and Cu-Cl distances is the signature for a static Jahn-Teller distortion. The Cl-Cu-Cl bond angle is 174.69(6)° and the Cu-Cl-Cu bond angle is 83.28(6)°. Two 3-amino-1,2,4-triazole ligands *via* the N1 and N3 atoms and one chlorine atom bridge the copper atoms forming a network. Each chain in the structure is separated by chloride ions present in the channels.

Figure 8 displays a view of the crystal structure in the crystallographic *a* axis and Figure 9 the asymmetric unit. The crystallographic data and selected bond angles and bond distance have been tabulated (Tables 3 and 4). The distribution of the Cu-N and Cu-Cl distances are comparable with the complex $[Cu_3Cl_4(btr)_4]Cl_2$ (btr = 4,4′-bitriazole);[25] in the cationic fragments $Cu_3Cl_4^{2+}$ copper atoms are bridged by μ_2 – chlorides and pairs of η^2 – triazolyl groups. The central metal atom has a similarly distorted CuN_4Cl_2 octahedral environment with chlorine atoms in the axial position (Cu-Cl 2.724(7) Å and Cu-N 2.003(2), 2.007(2) Å). The Cu(2) atoms in this structure however display trigonal bipyramidal coordination with one bridging Cu-Cl 2.326(6) and one terminal Cu-Cl 2.257(6) chloride ion in the equatorial plane and only one additional triazole N-donor.

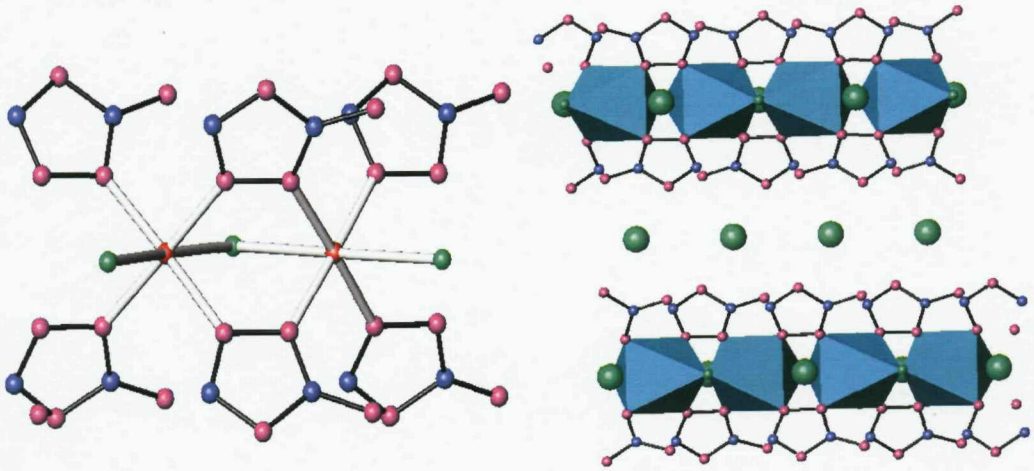

Figure 8 View of [CuCl(3-amino-1,2,4-triazole)$_2$.Cl] in the crystallographic *a* axis *($CuCl_2N_4$ octahedra in light blue, Cl^- ions in green, N atoms in purple and C atoms in dark blue).*

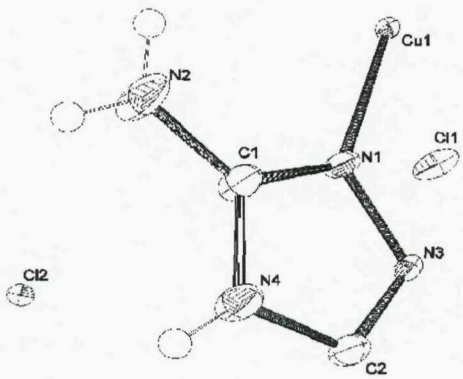

Figure 9 asymmetric unit of $[Cu_5Cl_2(3,5\text{-diamino-triazolate})_3].H_2O$ with thermal ellipsoids at 50% probability. The hydrogen atoms are represented as spheres of arbitrary radius.

Table 3 Crystallographic data and refinement parameters for [CuCl(3-amino-1,2,4-triazole)$_2$.Cl] *(e.s.d's are given in parantheses).*

Formula Sum	C_4 H_8 Cl_2 Cu N_8
Formula Weight	302.62
Temperature/ K	120(2)
Wavelength/ Å	0.71073
Crystal System	orthorhombic
Space Group	P*bcm*
***a*/Å**	7.211(4)
***b*/Å**	7.2544(10
***c*/Å**	20.536(4)
***α*/°**	90
β/°	90
γ/°	90
***U*/ Å^3**	1074.27(60)
Z	4
Crystal Size/ mm^3	0.25 × 0.06 × 0.01
Unique reflections	1269
Obs. reflections With [$I > 2\sigma(I)$]	1221
***R1* [$I > 2\sigma(I)$]**	0.0463
***R1* (all data)**	0.0478
***wR2* (all data)**	0.1057

$R1 = \Sigma|F_o|-|F_c|/\Sigma|F_o|$; $wR2 = [\Sigma w(F_o^2-F_c^2)^2/ \Sigma wF_o^4]^{½}$

Table 4 Important derived bond distances and angles for [CuCl(3-amino-1,2,4-triazole)$_2$.Cl] *(e.s.d's are given in parantheses).*

Bond	Length/ Å	Bond	Angle/ °
Cl(1) – Cu(1)	2.731(2)	Cu(1) – Cl(1) – Cu(1)	83.28(6)
Cu(1) – N(1)	1.996(4)	Cl(1) – Cu(1) – Cl(1)	174.69(6)
Cu(1) – N(3)	2.002(4)	N(1) –N(3) – Cu(1)	125.0(3)
C(1) – N(2)	1.343(6)		
C(1) – N(4)	1.353(6)		
C(2) – N(4)	1.356(6)		
C(2) – N(4)	1.356(6)		
C(2) – N(3)	1.298(6)		
N(1) – N(3)	1.392(5)		

7.4 [Cu_5Cl_2(3,5-diamino-triazolate)$_3$].H_2O

7.4.1 Synthesis

A mixture of $CuCl_2.2H_2O$ (100 mg, 8.65 x 10^{-4} mmol) and 3,5-diamino-1,2,4-triazole (1.73 x 10^{-3} mmol) in distilled water (10 mL) was heated at 200 °C under autogenous pressure for 72 hours before being cooled to room temperature. Colourless needle shaped crystals of [Cu_5Cl_2(3,5-diamino-triazolate)$_3$].H_2O were collected by filtration, washed with distilled water and dried. This compound is not monophasic and therefore we were unable to obtain elemental analysis and IR data.

7.4.2 Results and Discussion

Triangular type copper(II) compounds have generated great interest especially concerning their magnetic and structural characteristics. These systems can be regarded as geometrically frustrated and offer the opportunity to test magnetic exchange models.[26] The concept of magnetic frustration was first introduced by

Toulouse, and is a term applied to the situation wherein a large fraction of magnetic sites in a lattice is subject to competing or contradictory constraints. When frustration arises purely from the geometry or topology of the lattice, it is termed geometric frustration.

Examples of previously reported Cu(II) complexes of the triangular type include $[Cu_3(\mu_3\text{-}OH)(Haat)_3A(H_2O)_2]A\cdot(H_2O)_x$ [A = NO_3, CF_3SO_3, ClO_4; x = 0, 2],[27] where aat = 3-acetylamino-1,2,4-triazole, $[Cu_3(\mu_3\text{-}OH)(aaat)_3(H_2O)_3](NO_3)_2\cdot H_2O$ (**1**) (where Haaat = 3-acetylamino-5-amino-1,2,4-triazole) and $\{[Cu_3(\mu_3\text{-}OH)(aat)_3(\mu_3\text{-}SO_4)]\cdot 6H_2O\}_n$ (**2**). The crystal structure of **1** is built up by discrete trinuclear cations, $[Cu_3(\mu_3\text{-}OH)(aaat)_3(H_2O)_3]^{2+}$, two noncoordinated nitrate anions and one lattice water molecule per cation. This structure is similar to that of the three compounds $[Cu_3(\mu_3\text{-}OH)(aat)_3A(H_2O)_2]A\cdot(H_2O)_x$ [A = NO_3, CF_3SO_3, ClO_4; x = 0, 2] obtained with the related (H)aat ligand. The crystal structure of **2** consists of chains of cyclic trinuclear Cu(II) units of formula $[Cu_3(\mu_3\text{-}OH)(aat)_3(\mu_3\text{-}SO_4)]$. Trimeric $[Cu_3(\mu_3\text{-}OH)(aat)_3]^{2+}$ entitities, of the same type as the cations of **1** are bridged by one tridentate sulfato group, resulting in a one-dimensional network. Part of the chain is presented in Figure 10.[28]

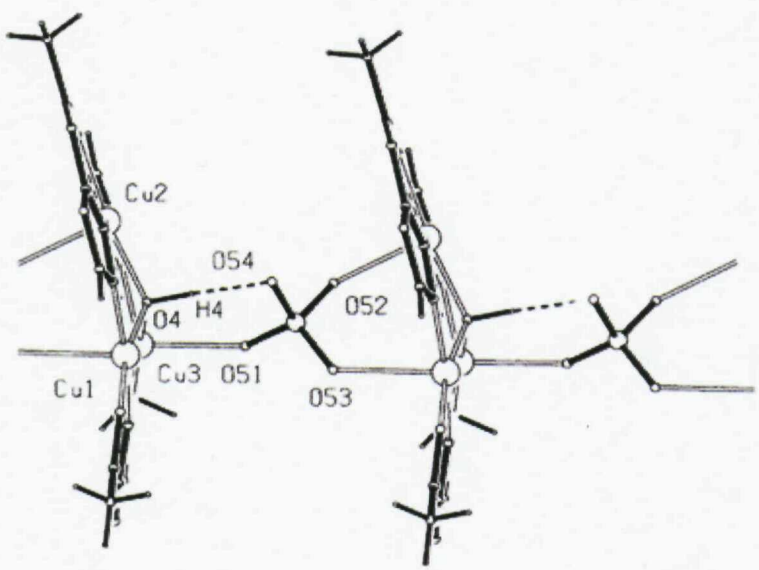

Figure 10 Part of the chain of **2** showing the coordination of the tridentate sulfate anion.[28]

In an attempt to synthesise a geometrically frustrated magnetic material within this work, the copper(I) compound $[Cu_5Cl_2(3,5\text{-diamino-triazolate})_3].H_2O$ was formed. Although not magnetically interesting the fascinating structural properties are described. The crystal structure of $[Cu_5Cl_2(3,5\text{-diamino-triazolate})_3].H_2O$ consists of unusual chains of trinuclear units with a 3,5-diamino-triazole linking the trimeric units. A water molecule stabilises the crystal lattice; Figure 11 displays the asymetric unit of the structure. The trimeric entities are bridged by Cu coordinated to Cl forming a chain (Figure 12), these chains are in turn linked by Cu-Cl in a zig-zag formation to form layers (Figure 13). The Cu-Cl bond length linking the trimeric units is 2.606(5) Å, the Cu-Cl bond lengths within the Cu-Cl zig-zag are 2.699(5) and 2.187(4) Å. The geometry of each copper atom within the trimeric unit is best described as linear with N–Cu–N bond angles in the range 175.7(4) – 179.6(5)°. The Cl-Cu-Cl bond angle is 96.0(2)° and the N-Cu-N bond angle is 143.0(4)°. Relevant bond angles and bond distances are listed in Tables 5 and 6.

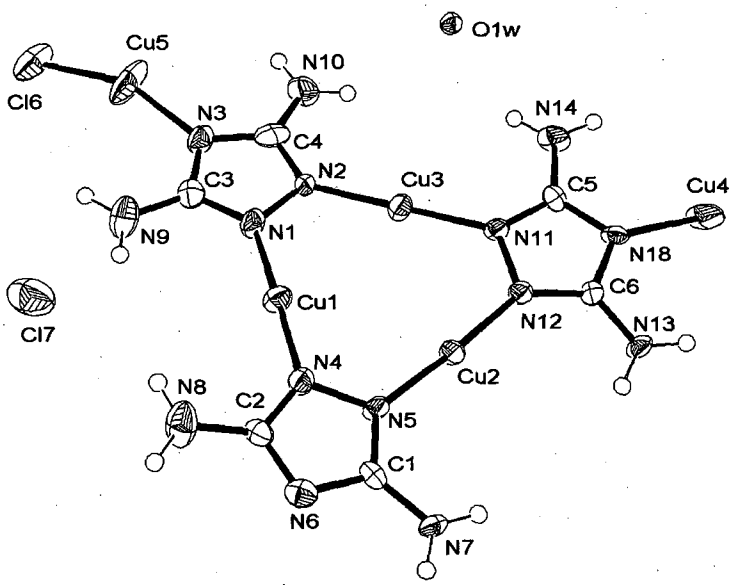

Figure 11 Asymmetric unit of $[Cu_5Cl_2(3,5\text{-diamino-triazolate})_3].H_2O$ with thermal ellipsoids at 50% probability. The hydrogen atoms are represented as spheres of arbitrary radius.

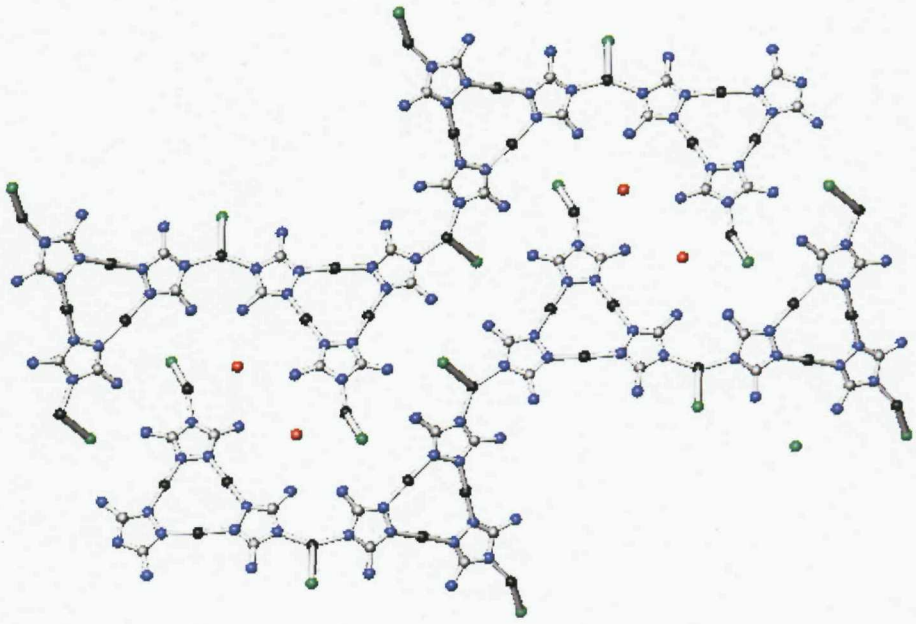

Figure 12 View of the extended network of $[Cu_5Cl_2(3,5\text{-diamino-triazolate})_3].H_2O$ in the *a* axis, hydrogen atoms have been removed for clarity (*C atoms in grey, N atoms in blue, Cu atoms in black, Cl- atoms in green and O atoms in red*).

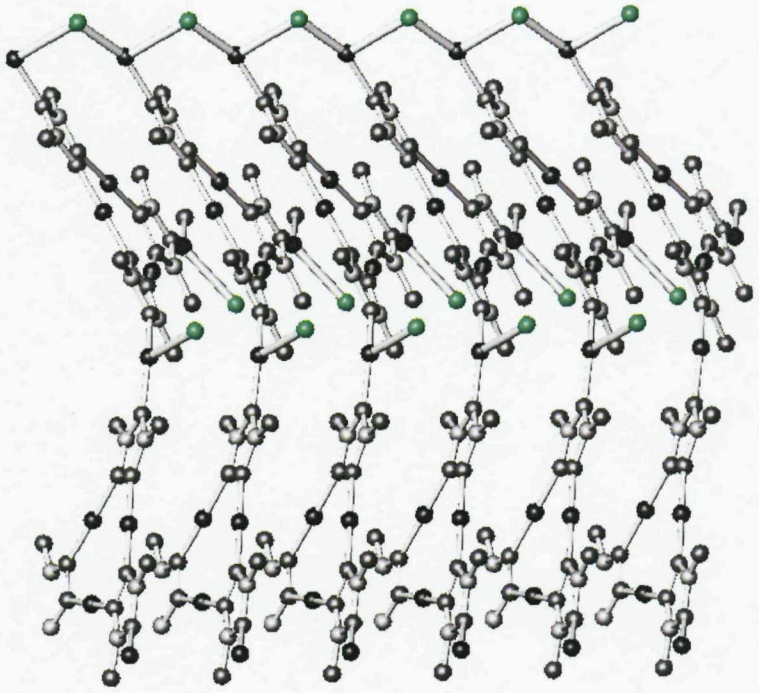

Figure 13 View of the linking of chains *via* Cu-Cl in a zig-zag formation.

Table 5 Crystallographic Data and Refinement Parameters for $[Cu_5Cl_2(3,5\text{-diamino-triazolate})_3].H_2O$ *(e.s.d's are given in parantheses).*

Formula Sum	$C_6H_{14}Cl_2Cu_5N_{15}O$
Formula Weight	700.92
Temperature/ K	120(2)
Wavelength/ Å	0.71073
Crystal System	Monoclinic
Space Group	P*21/c*
***a*/Å**	3.648(2)
***b*/Å**	22.996(4)
***c*/Å**	21.709(10)
α/°	90
β/°	91.70(4)
γ/°	90
***U*/ Å^3**	1820.6(12)
Z	4
Crystal Size/ mm^3	0.2 x 0.05 x 0.05
Unique reflections	3228
Obs. reflections With [$I > 2\sigma(I)$]	2460
R1 **[$I > 2\sigma(I)$]**	0.0837
R1 **(all data)**	0.1085
wR2 **(all data)**	0.2080

$R1 = \Sigma|F_o|-|F_c|/\Sigma|F_o|$; $wR2 = [\Sigma w(F_o^2-F_c^2)^2/\Sigma wF_o^4]^{1/2}$

Table 6 Important derived bond distances and angles for $[Cu_5Cl_2(3,5\text{-diamino-triazolate})_3].H_2O$ *(e.s.d's are given in parantheses).*

Bond	Length/ Å	Bond	Angle/ °
N(11) – Cu(3)	1.867(10)	N(4)-Cu(1)-N(1)	178.6(5)
N(12) – Cu(2)	1.870(9)	N(2)-Cu(3)-N(11)	179.6(5)
N(18) – Cu(4)	1.923(10)	N(12)-Cu(2)-N(5)	175.7(4)
N(1) – Cu(1)	1.875(11)	N(3)-Cu(5)-Cl(6)	155.9(4)
N(2) – Cu(3)	1.861(10)	N(2)-N(1)-Cu(1)	121.3(7)
N(3) – Cu(5)	1.918(10)	N(6)-Cu(4)-Cl(7)	103.7(3)
N(4) – Cu(1)	1.868(10)	Cl(6)-Cu(5)-Cl(6)	96.0(2)
N(5) – Cu(2)	1.872(9)		
N(6) – Cu(4)	1.933(10)		
Cl(6) – Cu(5)	2.187(4)		
Cl(6) – Cu(5)	2.699(5)		
Cl(6) – Cu(4)	2.606(5)		

7.5 Conclusion

Three complex transition metal triazole compounds have been synthesised, showing interesting structural and/ or magnetic features. $[Co_2Cl(3\text{-amino-1,2,4-triazole})_3]$ is an intriguing magnetically coupled coordination network. The implications of the observed ferrimagnetic ordering are discussed in the context of the topological structural disorder. The compound was obtained from a hydrothermal synthesis, crystallising in a primitive hexagonal cell a good structural model for $[Co_2Cl(3\text{-amino-1,2,4-triazole})_3]$ was obtained in the non-polar space group $P6_3/mmc$ (#194), revealing a 3-D coordination network.

Crystals of the compound $[CuCl(3\text{-amino-1,2,4-triazole})_2.Cl]$ were obtained hydrothermally and show a zig-zag polymeric structure. $[CuCl(3\text{-amino-1,2,4-triazole})_2.Cl]$ crystallises in the orthorhombic space group *Pbcm* with Z = 4 formula units.

Although not magnetically interesting the fascinating structural properties of $[Cu_5Cl_2(3,5\text{-diamino-triazolate})_3].H_2O$ have been reported in this chapter. The

crystal structure consists of unusual chains of trinuclear units with a 3,5-diamino-triazole linking the trimeric units. The trimeric entities are bridged by Cu coordinated to Cl forming a chain, these chains are in turn linked by Cu-Cl in a zig-zag formation to form layers.

7.6 References

[1] O. Hantzsch and O. Silberrad, *Chem. Ber.*, **33**, 58 (1900).

[2] I. de Paolini and C. Goria, *Gazz. Chim. Ital.*, **62**, 1048 (1932).

[3] M. J. Campbell, R. Grzeskowiak and M. Goldstein, *Spectrochim. Acta, Part A*: **24**, 1149 (1968).

[4] D. E. Billing, *J. Inorg. Nucl. Chem*, **31**, 137 (1969).

[5] M. Inoue, S. Emori and M. Kubo, *Inorg. Chem.*,**7**, 1427 (1968).

[6] M. Inoue and M. Kubo, *Coord. Chem. Rev.*, **1**, 21 (1976).

[7] J. A. J. Jarvis, *Acta Crystrallogr.*, **15**, 964 (1962)..

[8] C. W. Reimann and M. Zocchi, *Acta Cryst.*, **B27**, 682 (1971).

[9] D. J. Mackey and R. L. Martin, *J. Chem. Soc., Dalton. Trans.*, 702 (1978).

[10] D. W. Engelfriet, G. C. Verschoor and W. Den Brinker, *Acta Crystallogr.*, **B36**, 1554 (1980); D. W. Engelfriet and G. C. Verschoor, *Acta Crystallogr.*, **B37**, 237 (1981).

[11] Y. Garcia, P.J. Konningsbruggen, G. Bravic, D. Chasseau and O. Kahn, *Eur. J. Inorg. Chem.*, 356 (2003).

[12] K. Drabent and Z. Ciumik, *Chem. Commun.*, 1254 (2001).

[13] L. Antolli, A. C. Fabretti, D. Gatteschi, A. Guisti and R. Sessoli, *Inorg. Chem.*, **30**, 4858 (1991).

[14] G. Haasnoot, *Coord. Chem. Rev.*,**200**, 131 (2000).

[15] Y.-Q. Tian, C.-X. Cai, Y. Ji, X.-Z. You, S.-M. Peng, G.-H. Lee, *Angew. Chem. Int. Ed.*, **41**, 1384 (2002); *Angew. Chem.*, **114**, 1442 (2002);Y.-Q. Tian, C.-X. Cai, X.-M. Ren, C.-Y. Duan, Y. Xu, S. Gao, X.-Z. You, *Chem. Eur. J.*, **9**, 5673 (2003).

[16] O. Kahn, C. Jay Martinez, *Science*, **279**, 44 (1998); Y. Garcia, J. Moscovici, A. Michalowicz, V. Ksenofontov, G. Levchenco, G. Bravic, D. Chasseau, P. Gütlich, *Chem. Euro. J.*, *8*, 4992 (2002).

[17] R. Patel, M..T. Weller and D.J. Price, *Dalton Trans.*, **36**, 4034 (2007)

[18] Y. Garcia, P.J. van Koningsbruggen, G. Bravic, D. Chasseau, O. Kahn, *Eur. J. Inorg. Chem.*, 356 (2003), Y. Garcia, P.J. van Koningsbruggen, G. Bravic, P. Guionneau, D. Chasseau, G. L. Cascarano, J. Moscovici, K. Lambert, A. Michalowicz, O. Kahn, *Inorg. Chem.*, **36**, 6357 (1997); L. Antolini, A.C.

Fabretti, D. Gatteschi, A. Giusti, R. Sessoli, *Inorg. Chem.*, **30**, 4858 (1991); K. Drabent, Z. Ciunik, *Chem. Commun.*, 1254 (2001); D. W. Engelfriet, G.C. Verschoor, W. Den Brinker, *Acta Crystallogr.*, **B36**, 1554 (1980).

[19] D.J. Chesnut, A. Kusnetzow, R. Birge, J. Zubieta, *Inorg. Chem.*, **38**, 5484 (1999); J.-P. Zhang, S.-L. Zheng, X.-C. Huang, X.-M. Chen, *Angew. Chem. Int. Ed.*, **43**, 206 (2004); *Angew. Chem.*, **116**, 208 (2003).

[20] J. Krober, I. Bkouche-Waksman, C. Pascard, M. Thomann, O. Kahn, *Inorg. Chim. Acta.*, **230**, 159 (1995).

[21] C.-Y. Su, A.M. Goforth, M.D. Smith, P.J. Pellechia, H.-C. zur Loye, *J. Am. Chem. Soc.*, 126, 3576 (2004).

[22] L.R. Groeneveld, R.A. Le Fêbre, R.A.G. De Graaff, J.G. Haasnoot, G. Vos, J. Reedijk, *Inorg. Chim. Acta*, ***102***, 69 (1985).

[23] W. Vreugdenhil, J.G. Haasnoot, M.F.J. Schoondergang, J. Reedijk, *Inorg. Chim. Acta*, **130**, 235 (1987).

[24] Y.-Q. Tian, C.-X. Cai, X.-M. Ren, C.-Y. Duan, Y. Xu, S. Gao, X.-Z. You, *Chem. Eur. J.*, **9**, 5673 (2003).

[25] A. B. Lysenko, E. V. Gover and K. V. Domasevitch, *Inorg. Chim. Acta.*, **360**, 55 (2007).

[26] (a) *Magnetic Molecular Materials*; Gatteschi, D., Kahn, O., Miller, J. S., Palacio, F., Eds.; Kluwer Academic: Dordrecht, The Netherlands, 1991. (b) Kahn, O.; Pei. Y.; Yournaux, Y. In *Inorganic Materials*; Bruce, D. W., O'Hare, O., Eds.; John Wiley & Sons: Chichester, U.K., 1992. (c) Kahn, O. *Molecular Magnetism*; VCH Publishers: New York, 1993. (d) *Molecule-Based Magnetic Materials: Theory, Techniques, and Applications*; Turnbull, M. M., Sugimoto, T., Thompson, L. K., Eds.; ACS Symposium Series 644; American Chemical Society: Washington, DC, 1996.

[27] S. Ferrer, J. G. Hasnoot, J. Reedjijk, E. Müller, M. Biagini Cingi, M. Lanfranchi, A. M. Manotti Lanfredi and J. Ribas, *Inorg. Chem.*, **39**, 1859 (2000).

[28] S. Ferrer, F. Llonet, I. Bertomen, G. Alzuet, J. Borras, S. Garcia-Granda, M. Lin-Gonzalez and J. G. Hasnoot, *Inorg.Chem.*, **41**, 5821 (2002).

Appendix A

Appendix A

Table a Refined atomic parameters and thermal parameters for $LnSrScO_4$ (PXD) (*e.s.d's are given in parentheses*).

$LaSrScO_4$

Temperature (°C)	a/ Å	b/ Å	c/ Å	Ln/Sr(x)	Ln/Sr(z)	O1(z)	O2(x)	O2(z)	Ln/Sr Ui/Ue x100 Å²	Sc Ui/Ue x100 Å²	O1/O2 Ui/Ue x100 Å²
25	5.7615(1)	5.7499(1)	12.4674(2)	0.0137(3)	0.3565(1)	0.0154(9)	0.4353(16)	0.3307(6)	1.36(5)	0.42(8)	1.97(21)
50	5.7612(1)	5.7494(1)	12.4733(2)	0.0133(3)	0.3565(1)	0.0146(10)	0.4356(16)	0.3309(6)	1.62(5)	0.54(8)	2.14(21)
100	5.7625(1)	5.7498(1)	12.4883(2)	0.0129(3)	0.3565(1)	0.0158(9)	0.4357(16)	0.3310(6)	1.70(5)	1.19(8)	2.18(21)
200	5.7671(1)	5.7490(1)	12.5206(2)	0.0114(4)	0.3563(1)	0.0148(11)	0.4437(18)	0.3317(6)	2.09(5)	0.82(9)	2.77(22)
300	5.7736(1)	5.7482(1)	12.5541(3)	0.0098(5)	0.3562(1)	0.0121(13)	0.4508(21)	0.3308(6)	2.39(6)	1.11(10)	3.58(23)
400	5.7760(1)	5.7510(1)	12.5848(3)	0.0090(5)	0.3560(1)	0.0093(16)	0.4529(22)	0.3310(6)	2.67(4)	1.42(9)	4.12(22)
500	5.7777(1)	5.7557(1)	12.6120(3)	0.0085(5)	0.3559(1)	0.0050(20)	0.4538(22)	0.3307(6)	2.93(4)	1.63(9)	4.38(21)
600	5.7801(1)	5.7595(1)	12.6410(2)	0.0063(6)	0.3559(1)	-0.0130(12)	0.4500(20)	0.3302(6)	3.23(4)	2.43(9)	4.46(23)
700	5.7812(1)	5.7631(1)	12.6718(2)	0.050(6)	0.3558(1)	-0.0139(12)	0.4481(19)	0.3290(5)	3.39(6)	2.61(10)	4.21(24)
800	5.7802(1)	5.7680(1)	12.7031(2)	0.0033(6)	0.3557(1)	-0.0155(11)	0.4465(19)	0.3289(5)	3.58(6)	2.80(10)	4.02(24)
900	4.0841(1)	4.0841(1)	12.7393(2)		0.3555(1)			0.1720(6)	3.67(6)	2.93(11)	6.49(18)
1000	4.0877(1)	4.0877(1)	12.7696(2)		0.3555(1)			0.1716(6)	3.79(6)	2.93(11)	6.54(18)

$CeSrScO_4$

Temperature (°C)	a/ Å	b/ Å	c/ Å	Ln/Sr(x)	Ln/Sr(z)	O1(z)	O2(x)	O2(z)	Ln/Sr Ui/Ue x100 Å²	Sc Ui/Ue x100 Å²	O1/O2 Ui/Ue x100 Å²
25	5.7606(2)	5.7459(2)	12.3942(4)	0.0162(4)	0.3560(1)	0.0135(15)	0.4140(22)	0.3307(11)	2.65(9)	2.14(15)	2.80(32)
50	5.7607(2)	5.7449(2)	12.3989(4)	0.0162(4)	0.3558(1)	0.0128(15)	0.4170(22)	0.3328(11)	2.28(8)	1.61(15)	2.36(32)
100	5.7624(2)	5.7448(2)	12.4125(4)	0.0158(4)	0.3558(1)	0.0122(16)	0.4172(22)	0.3332(11)	2.75(32)	1.91(15)	2.75(32)
200	5.7660(2)	5.7462(2)	12.4467(4)	0.0144(5)	0.3553(1)	0.0117(17)	0.4182(23)	0.3339(11)	2.96(9)	2.15(16)	3.61(34)

Temperature (°C)	a/ Å	b/ Å	c/ Å	Ln/Sr(x)	Ln/Sr(z)	O1(z)	O2(x)	O2(z)	Ln/Sr Ui/Ue x100 Å^2	Sc Ui/Ue x100 Å^2	O1/O2 Ui/Ue x100 Å^2
300	5.7712(2)	5.7488(2)	12.4857(4)	0.0130(5)	0.3550(1)	0.0103(18)	0.4228(22)	0.3333(10)	3.17(10)	2.36(16)	3.49(33)
400	5.7649(3)	5.7523(3)	12.5451(5)	0.0102(8)	0.3536(1)	0.0105(21)	0.4055(24)	0.3383(13)	4.16(9)	2.81(18)	4.2(4)
500	5.7798(3)	5.7680(3)	12.5744(5)	0.0076(8)	0.3505(1)	0.076(24)	0.3929(23)	0.3388(15)	4.97(9)	1.17(16)	5.7(4)

$PrSrScO_4$

Temperature (°C)	a/ Å	b/ Å	c/ Å	Ln/Sr(x)	Ln/Sr(z)	O1(z)	O2(x)	O2(z)	Ln/Sr Ui/Ue x100 Å^2	Sc Ui/Ue x100 Å^2	O1/O2 Ui/Ue x100 Å^2
25	5.7625(2)	5.7339(1)	12.3206(24)	0.0185(3)	0.3562(1)	0.0198(12)	0.4351(24)	0.3358(10)	1.98(8)	1.11(14)	3.27(29)
50	5.7634(2)	5.7327(1)	12.3261(4)	0.0018(4)	0.3560(1)	0.0185(12)	0.4348(23)	0.3362(10)	1.97(8)	0.93(14)	2.88(29)
100	5.7667(2)	5.7308(2)	12.3417(4)	0.0177(4)	0.3559(1)	0.0193(12)	0.4350(23)	0.3355(10)	2.07(8)	1.10(14)	3.18(29)
200	5.7736(2)	5.7286(1)	12.3760(4)	0.0174(4)	0.3557(1)	0.0199(12)	0.4376(23)	0.3354(10)	2.52(9)	1.53(15)	3.66(30)
300	5.7785(2)	5.7296(2)	12.4097(4)	0.0162(4)	0.3557(1)	0.0207(11)	0.4381(22)	0.3348(9)	2.56(9)	1.48(15)	2.00(30)
400	5.7809(2)	5.7335(2)	12.4402(4)	0.0155(4)	0.3554(1)	0.0019(1)	0.4457(24)	0.2240(17)	2.79(10)	1.69(15)	3.55(29)
500	5.7824(1)	5.7389(1)	12.4698(4)	0.0140(5)	0.3551(1)	0.0214(11)	0.446(23)	0.3347(9)	3.10(9)	2.02(15)	3.46(29)
600	5.7847(1)	5.7450(1)	12.4989(4)	0.0129(5)	0.3550(1)	0.0223(10)	0.4473(24)	0.3345(8)	3.35(9)	2.00(15)	3.40(29)
700	5.7867(1)	5.7508(2)	12.5278(4)	0.0134(5)	0.3548(1)	0.0206(12)	0.4496(25)	0.3343(8)	3.69(10)	2.43(16)	4.21(30)
800	5.7876(1)	5.7563(1)	12.5565(4)	0.0124(6)	0.3548(1)	0.0184(13)	0.4498(27)	0.3337(9)	3.71(10)	2.61(16)	4.48(32)
900	5.7884(2)	5.7623(2)	12.5866(5)	0.0114(7)	0.3549(1)	0.0165(17)	0.4446(31)	0.3345(10)	3.93(12)	2.93(19)	4.8(4)
1000	5.7878(2)	5.7687(2)	12.6208(4)	0.0095(8)	0.3548(1)	0.0192(14)	0.4397(28)	0.3327(9)	4.29(8)	3.36(17)	4.4(4)
1100	4.0874(1)	4.0874(1)	12.6570(4)		0.3546(1)			0.1700(11)	4.21(8)	4.69(19)	8.25(31)
1200	4.0890(1)	4.0890(1)	12.6944(4)		0.3548(1)			0.1696(11)	4.09(7)	4.52(19)	8.68(33)

$NdSrScO_4$

Temperature (°C)	a/ Å	b/ Å	c/ Å	Ln/Sr(x)	Ln/Sr(z)	O1(z)	O2(x)	O2(z)	Ln/Sr Ui/Ue x100 Å^2	Sc Ui/Ue x100 Å^2	O1/O2 Ui/Ue x100 Å^2
25	5.7419(2)	5.7008(2)	12.2437(4)	0.0182(4)	0.3561(1)	0.0177(14)	0.4369(27)	0.3240(10)	2.33(5)	0.91(13)	3.54(29)
50	5.7617(2)	5.7191(2)	12.2904(5)	0.0179(4)	0.3564(1)	0.0187(15)	0.4409(30)	0.3235(11)	2.41(6)	0.99(15)	3.76(32)
100	5.7611(2)	5.7162(2)	12.2988(5)	0.0182(4)	0.3562(1)	0.0193(14)	0.4386(28)	0.3251(11)	2.19(6)	0.96(16)	3.09(32)
200	5.7689(2)	5.7194(2)	12.3366(5)	0.0189(4)	0.3560(1)	0.0221(12)	0.4379(16)	0.3262(10)	2.23(7)	0.87(16)	2.66(31)
300	5.7735(2)	5.7228(2)	12.3678(5)	0.0163(5)	0.3557(1)	0.0166(15)	0.4372(26)	0.3285(11)	2.50(7)	0.79(15)	3.40(33)
400	5.7763(2)	5.7268(2)	12.3955(5)	0.0158(5)	0.3557(1)	0.0137(17)	0.4376(27)	0.3281(10)	2.65(7)	0.98(15)	4.22(33)
Temperature (°C)	**a/ Å**	**b/ Å**	**c/ Å**	**Ln/Sr(x)**	**Ln/Sr(z)**	**O1(z)**	**O2(x)**	**O2(z)**	**Ln/Sr Ui/Ue x100 Å^2**	**Sc Ui/Ue x100 Å^2**	**O1/O2 Ui/Ue x100 Å^2**
500	5.7787(2)	5.7319(2)	12.4223(5)	0.0156(5)	0.3554(1)	0.0116(20)	0.4363(28)	0.3267(11)	2.88(7)	1.32(16)	4.7(4)
600	5.7793(2)	5.7363(2)	12.4443(5)	0.0146(6)	0.3551(1)	0.0120(22)	0.4339(30)	0.3281(12)	3.05(8)	1.35(17)	4.8(4)
700	5.7809(2)	5.7417(2)	12.4705(5)	0.0131(7)	0.3548(1)	0.0075(27)	0.4385(31)	0.3275(11)	3.30(8)	1.39(17)	4.9(4)
800	5.7822(2)	5.7467(2)	12.4973(5)	0.0125(8)	0.3546(1)	0.0041(38)	0.446(4)	0.3271(12)	3.66(9)	1.89(18)	6.4(4)
900	5.7831(2)	5.7518(2)	12.5254(6)	0.0125(9)	0.3543(1)	0.0013(35)	0.450(4)	0.3278(13)	3.91(10)	2.21(20)	6.7(5)
1000	5.7838(2)	5.7586(2)	12.5581(6)	0.0099(11)	0.3540(1)	-0.0081(35)	0.445(4)	0.3271(13)	4.39(10)	2.67(21)	6.3(5)

$SmSrScO_4$

Temperature (°C)	a/ Å	b/ Å	c/ Å	Ln/Sr(x)	Ln/Sr(z)	O1(z)	O2(x)	O2(z)	Ln/Sr Ui/Ue x100 Å^2	Sc Ui/Ue x100 Å^2	O1/O2 Ui/Ue x100 Å^2
25	5.7383(2)	5.6994(2)	12.2946(5)	0.0186(5)	0.3542(1)	0.0252(12)	0.4138(25)	0.3357(14)	2.42(8)	1.78(19)	2.3(4)
50	5.7392(2)	5.6986(2)	12.2952(5)	0.0195(5)	0.3543(1)	0.0236(12)	0.4177(24)	0.3368(13)	1.96(8)	1.02(18)	1.38(35)
100	5.7426(2)	5.6986(2)	12.2984(5)	0.0192(5)	0.3542(1)	0.0252(11)	0.4169(23)	0.3363(13)	1.97(8)	1.05(18)	1.08(34)
200	5.7514(2)	5.7015(2)	12.3025(5)	0.0185(5)	0.3546(1)	0.0228(12)	0.4224(24)	0.3372(12)	2.02(18)	1.29(18)	1.77(34)

Temperature (°C)	a/ Å	b/ Å	c/ Å	Ln/Sr(x)	Ln/Sr(z)	O1(z)	O2(x)	O2(z)	Ln/Sr Ui/Ue x100 Å^2	Sc Ui/Ue x100 Å^2	O1/O2 Ui/Ue x100 Å^2
300	5.7573(2)	5.7059(2)	12.3166(5)	0.0193(5)	0.3546(1)	0.0228(12)	0.4244(24)	0.3381(13)	2.24(8)	1.84(19)	2.41(34)
400	5.7611(2)	5.7109(2)	12.3368(5)	0.0191(5)	0.3544(1)	0.0219(13)	0.4254(24)	0.3389(13)	2.47(8)	1.95(19)	2.51(34)
500	5.7641 (2)	5.7165(2)	12.3590(5)	0.0194(50	0.3543(1)	0.0224(13)	0.4269(25)	0.3395(13)	2.63(9)	2.24(20)	2.9(4)
600	5.7673(2)	5.7224(2)	12.3828(5)	0.0183(5)	0.3542(1)	0.0226(13)	0.4261(25)	0.3398(13)	2.98(9)	2.79(21)	3.4(4)
700	5.7692(2)	5.7279(2)	12.4063(6)	0.0177(5)	0.3541(1)	0.0234(14)	0.4331(27)	0.3395(13)	3.29(9)	3.02(21)	4.2(4)
800	5.7722(2)	5.7334(2)	12.4295(6)	0.0170(6)	0.3539(1)	0.0226(15)	0.4353(29)	0.3393(13)	3.61(10)	3.39(22)	5.1(4)
900	5.7739(2)	5.7390(2)	12.4561(5)	0.0163(6)	0.3537(1)	0.0217(16)	0.4342(29)	0.3389(13)	3.75(10)	3.59(22)	5.5(4)
1000	5.7763(2)	5.7457(2)	12.4856(6)	0.0144(7)	0.3533(2)	0.0227(16)	0.4348(31)	0.3387(13)	4.04(11)	4.17(24)	5.3(5)

Table b Key bond distances and angles for $LnSrScO_4$ as extracted from PXD data (*e.s.d's are given in parantheses*).

$LaSrScO_4$

Temperature (°C)	Sc-O(1)/ Å	Sc-O(2)/ Å	Ln/Sr-O(1)x2/Å	Ln/Sr-O(1)x2/Å	Ln/Sr-O(2)/Å	Ln/Sr-O(2)x2/Å	Ln/Sr-O(2)/Å	Ln/Sr-O(2)/Å	Sc-O(1)-Sc/°
25	2.145(7)	2.044(1)	2.801(8)	2.630(7)	2.445(9)	2.909(1)	2.378(7)	3.353(9)	169.1(6)
50	2.141(7)	2.043(1)	2.795(9)	2.636(8)	2.449(9)	2.913(1)	2.381(8)	3.344(9)	169.8(7)
100	2.143(7)	2.045(1)	2.809(8)	2.627(7)	2.452(9)	2.914(1)	2.384(7)	3.332(9)	168.9(6)
200	2.131(8)	2.044(1)	2.810(10)	2.635(8)	2.504(10)	2.911(1)	2.386(8)	3.284(10)	169.6(7)
300	2.143(8)	2.042(1)	2.796(12)	2.655(11)	2.555(11)	2.913(1)	2.371(8)	3.235(11)	171.5(9)
400	2.144(8)	2.041(1)	2.780(14)	2.679(13)	2.572(12)	2.913(1)	2.376(8)	3.220(11)	173.4(11)
500	2.152(7)	2.040(1)	2.716(170	2.749(18)	2.583(12)	2.914(1)	2.374(8)	3.216(11)	176.1(14)
600	2.166(7)	2.047(1)	2.608(10)	2.866(10)	2.576(11)	2.919(1)	2.374(7)	3.220(11)	170.7(9)

Temperature (°C)	Sc-O(1)/ Å	Sc-O(2)/ Å	Ln/Sr-O(1)x2/Å	Ln/Sr-O(1)x2/Å	Ln/Sr-O(2)/Å	Ln/Sr-O(2)x2/Å	Ln/Sr-O(2)/Å	Ln/Sr-O(2)/Å	Sc-O(1)-Sc/°
700	2.187(7)	2.048(1)	2.610(9)	2.874(10)	2.576(11)	2.923(1)	2.365(7)	3.227(10)	170.1(8)
800	2.195(7)	2.051(1)	2.605(8)	2.889(9)	2.578(11)	2.925(1)	2.368(7)	3.230(11)	168.9(8)
			Ln/Sr-O(1)x4/Å		Ln/Sr-O(2)/Å	Ln/Sr-O(2)x4/Å			Sc-O(1)-Sc/°
900	2.192(7)	2.042(1)	2.749(1)		2.337(8)	2.909(1)			180
1000	2.191(8)	2.044(1)	2.753(1)		2.350(8)	2.911(1)			180

$CeSrScO_4$

Temperature (°C)	Sc-O(1)/ Å	Sc-O(2)/ Å	Ln/Sr-O(1)x2/Å	Ln/Sr-O(1)x2/Å	Ln/Sr-O(2)/Å	Ln/Sr-O(2)x2/Å	Ln/Sr-O(2)/Å	Ln/Sr-O(2)/Å	Sc-O(1)-Sc/°
25	2.156(13)	2.041(1)	2.773(13)	2.652(11)	2.312(13)	2.918(2)	2.387(13)	3.486(13)	170.6(10)
50	2.128(13)	2.040(1)	2.768(13)	2.659(12)	2.326(13)	2.912(2)	2.407(13)	3.462(13)	171.1(10)
100	2.124(13)	2.040(1)	2.767(14)	2.663(12)	2.330(13)	2.912(2)	2.414(13)	3.459(13)	171.5(11)
200	2.121(13)	2.040(1)	2.774(15)	2.670(13)	2.343(13)	2.912(2)	2.420(14)	3.448(13)	171.8(12)
300	2.129(13)	2.040(1)	2.774(16)	2.683(14)	2.381(13)	2.911(2)	2.408(13)	3.417(13)	172.8(13)
400	2.100(16)	2.040(2)	2.802(19)	2.688(17)	2.287(14)	2.923(3)	2.482(16)	3.491(14)	172.6(15)
500	2.120(18)	2.044(1)	2.818(22)	2.735(20)	2.232(14)	2.944(3)	2.471(19)	3.556(14)	174.6(17)

$PrSrScO_4$

Temperature (°C)	Sc-O(1)/ Å	Sc-O(2)/ Å	Ln/Sr-O(1)x2/Å	Ln/Sr-O(1)x2/Å	Ln/Sr-O(2)/Å	Ln/Sr-O(2)x2/Å	Ln/Sr-O(2)/Å	Ln/Sr-O(2)/Å	Sc-O(1)-Sc/°
25	2.058(13)	2.047(2)	2.813(10)	2.600(8)	2.409(13)	2.892(2)	2.408(13)	3.378(13)	166.0(8)
50	2.054(12)	2.045(2)	2.803(10)	2.613(9)	2.417(13)	2.890(2)	2.417(12)	3.376(18)	167.2(8)
100	2.065(12)	2.046(2)	2.813(10)	2.609(9)	2.419(13)	2.889(2)	2.410(12)	3.378(13)	166.6(8)
200	2.069(12)	2.048(2)	2.825(10)	2.609(9)	2.439(13)	2.887(2)	2.439(13)	3.364(13)	166.2(8)
300	2.081(12)	2.050(2)	2.840(10)	2.602(8)	2.452(13)	2.889(2)	2.407(12)	3.353(13)	165.6(8)
400	2.089(11)	2.050(1)	2.838(11)	2.614(9)	2.501(13)	2.888(1)	2.391(11)	3.307(13)	166.4(8)

Temperature (°C)	Sc-O(1)/ Å	Sc-O(2)/ Å	Ln/Sr-O(1)x2/Å	Ln/Sr-O(1)x2/Å	Ln/Sr-O(2)/Å	Ln/Sr-O(2)x2/Å	Ln/Sr-O(2)/Å	Ln/Sr-O(2)/Å	Sc-O(1)-Sc/°
500	2.086(11)	2.054(1)	2.868(10)	2.600(8)	2.503(13)	2.891(1)	2.400(11)	3.307(13)	165.0(7)
600	2.057(2)	2.090(10)	2.884(10)	2.594(8)	2.526(13)	2.893(1)	2.399(11)	3.295(13)	164.4(7)
700	2.056(2)	2.096(11)	2.873(11)	2.613(9)	2.537(14)	2.895(1)	2.398(11)	3.270(14)	165.6(8)
800	2.108(11)	2.054(2)	2.860(12)	2.629(10)	2.545(15)	2.899(2)	2.395(11)	3.272(15)	167.1(9)
900	2.053(2)	2.114(12)	2.852(15)	2.640(13)	2.516(16)	2.905(2)	2.411(13)	3.297(16)	168.2(11)
1000	2.058(2)	2.145(12)	2.888(14)	2.616(12)	2.499(15)	2.914(2)	2.399(12)	3.317(15)	166.2(10)
Temperature (°C)	**Sc-O(1)/ Å**	**Sc-O(2)/ Å**	**Ln/Sr-O(1)x4/Å**		**Ln/Sr-O(2)/Å**	**Ln/Sr-O(2)x4/Å**			**Sc-O(1)-Sc/°**
1100	2.044(1)	2.151(14)	2.750(1)		2.337(14)	2.907(1)			180
1200	2.045(1)	2.153(14)	2.753(1)		2.351(15)	2.908(1)			180

$NdSrScO_4$

Temperature (°C)	Sc-O(1)/ Å	Sc-O(2)/ Å	Ln/Sr-O(1)x2/Å	Ln/Sr-O(1)x2/Å	Ln/Sr-O(2)/Å	Ln/Sr-O(2)x2/Å	Ln/Sr-O(2)/Å	Ln/Sr-O(2)/Å	Sc-O(1)-Sc/°
25	2.035(2)	2.186(12)	2.783(12)	2.599(10)	2.419(15)	2.890(2)	2.262(12)	3.378(15)	167.3(9)
50	2.043(2)	2.201(13)	2.796(13)	2.602(11)	2.462(17)	2.899(2)	2.254(24)	3.360(17)	167.0(10)
100	2.043(2)	2.180(13)	2.801(13)	2.603(10)	2.452(16)	2.894(2)	2.276(13)	3.373(16)	166.7(10)
200	2.049(3)	2.174(13)	2.832(11)	2.591(9)	2.445(15)	2.894(2)	2.296(13)	3.384(15)	164.7(8)
300	2.043(2)	2.152(13)	2.798(13)	2.628(11)	2.453(15)	2.893(2)	2.322(13)	3.370(15)	168.5(10)
400	2.040(2)	2.161(13)	2.778(15)	2.652(13)	2.460(15)	2.896(2)	2.323(13)	3.367(15)	170.5(12)
500	2.040(2)	2.184(13)	2.767(17)	2.672(15)	2.457(16)	2.901(2)	2.307(14)	3.377(16)	171.9(14)
600	2.041(2)	2.173(15)	2.779(19)	2.670(17)	2.447(17)	2.903(2)	2.326(15)	3.383(17)	171.1(14)
700	2.039(2)	2.181(14)	2.750(2)	2.705(21)	2.483(18)	2.905(2)	2.314(15)	3.348(17)	174.7(19)
800	2.039(1)	2.183(16)	2.727(32)	2.736(30)	2.533(22)	2.904(3)	2.303(16)	3.302(21)	177.1(27)
900	2.039(1)	2.177(16)	2.711(29)	2.763(28)	2.550(24)	2.903(3)	2.310(17)	3.283(23)	179.0(24)
1000	2.043(2)	2.195(16)	2.646(28)	2.842(29)	2.537(23)	2.911(3)	2.305(17)	3.297(22)	174.3(25)

$SmSrScO_4$

Temperature (°C)	Sc-O(1)/ Å	Sc-O(2)/ Å	Ln/Sr-O(1)x2/Å	Ln/Sr-O(1)x2/Å	Ln/Sr-O(2)/Å	Ln/Sr-O(2)x2/Å	Ln/Sr-O(2)/Å	Ln/Sr-O(2)/Å	Sc-O(1)-Sc/°
25	2.045(2)	2.078(17)	2.864(11)	2.573(9)	2.278(14)	2.885(2)	2.412(17)	3.479(14)	162.8(9)
50	2.042(2)	2.061(16)	2.847(11)	2.585(9)	2.297(14)	2.880(2)	2.420(16)	3.459(14)	163.8(8)
100	2.046(2)	2.069(15)	2.865(10)	2.573(8)	2.294(13)	2.881(2)	2.415(15)	3.464(13)	162.6(8)
200	2.044(2)	2.052(15)	2.844(11)	2.587(9)	2.333(14)	2.879(2)	2.423(15)	3.435(14)	164.2(8)
300	2.046(2)	2.041(15)	2.844(11)	2.592(9)	2.341(14)	2.879(2)	2.436(16)	3.430(14)	164.2(9)
400	2.046(2)	2.033(15)	2.842(11)	2.602(9)	2.348(14)	2.880(2)	2.446(15)	3.428(14)	164.8(9)
500	2.048(2)	2.028(15)	2.850(11)	2.604(9)	2.356(14)	2.881(2)	2.454(16)	3.421(14)	164.5(9)
Temperature (°C)	**Sc-O(1)/ Å**	**Sc-O(2)/ Å**	**Ln/Sr-O(1)x2/Å**	**Ln/Sr-O(1)x2/Å**	**Ln/Sr-O(2)/Å**	**Ln/Sr-O(2)x2/Å**	**Ln/Sr-O(2)/Å**	**Ln/Sr-O(2)/Å**	**Sc-O(1)-Sc/°**
600	2.050(2)	2.028(15)	2.860(12)	2.601(10)	2.358(14)	2.885(2)	2.461(16)	3.420(140	164.3(9)
700	2.053(2)	2.029(16)	2.874(12)	2.597(10)	2.403(16)	2.884(2)	2.450(16)	3.378(16)	163.7(9)
800	2.053(2)	2.032(16)	2.874(14)	2.605(11)	2.421(16)	2.886(2)	2.447(16)	3.363(16)	164.3(10)
900	2.053(2)	2.042(16)	2.874(14)	2.614(12)	2.420(16)	2.889(2)	2.445(16)	3.366(16)	164.9(11)
1000	2.056(3)	2.049(17)	2.896(15)	2.606(12)	2.435(17)	2.894(2)	2.441(17)	3.353(17)	164.2(11)

Table c Refined atomic parameters as extracted from PND data for $LnSrScO_4$ (*e.s.d's are given in parentheses*).

$LaSrScO_4$

Temperature (°C)	a/ Å	b/ Å	c/ Å	Ln/Sr(x)	Ln/Sr(z)	O1(z)	O2(x)	O2(z)	Ln/Sr Ui/Ue x100 Å^2	Sc Ui/Ue x100 Å^2	O1/O2 Ui/Ue x100 Å^2
25	5.7629(4)	5.7494(4)	12.4833(7)	0.0119(7)	0.3562(2)	0.0156(5)	0.4405(10)	0.3295(5)	0.49(10)	1.28(10)	2.60(12)
100	5.7647(4)	5.7495(4)	12.5041(7)	0.0111(7)	0.3560(2)	0.0152(3)	0.4421(9)	0.3274(5)	0.73(10)	1.39(10)	2.79(12)
200	5.7718(4)	5.7448(4)	12.5219(7)	0.0101(8)	0.3560(2)	0.0145(5)	0.4467(10)	0.3269(5)	0.75(10)	1.63(11)	3.21(12)
400	5.7800(3)	5.7449(3)	12.5885(7)	0.0081(8)	0.3559(2)	0.0129(6)	0.4489(10)	0.3272(5)	1.16(11)	1.92(12)	3.53(12)
600	5.7789(3)	5.7555(3)	12.6471(7)	0.0053(9)	0.3558(2)	0.0110(7)	0.4521(10)	0.3274(5)	1.64(11)	2.23(12)	4.17(12)
700	5.7780(4)	5.7589(3)	12.6669(7)	0.0046(10)	0.3556(2)	0.0099(7)	0.4533(11)	0.3272(5)	1.86(11)	2.32(12)	4.29(12)
800	5.7661(4)	5.7758(4)	12.7097(7)	0.0018(12)	0.3555(2)	0.0054(11)	0.4569(13)	0.3269(5)	2.35(12)	2.46(12)	4.75(13)
900	4.0828(2)	4.0828(2)	12.7437(7)		0.3559(2)			0.1719(6)	2.61(13)	2.76(14)	6.14(14)
1000	4.0861(2)	4.0861(2)	12.7700(7)		0.3560(2)			0.1720(6)	2.79(13)	3.02(14)	6.42(14)

$PrSrScO_4$

Temperature (°C)	a/ Å	b/ Å	c/ Å	Ln/Sr(x)	Ln/Sr(z)	O1(z)	O2(x)	O2(z)	Ln/Sr Ui/Ue x100 Å^2	Sc Ui/Ue x100 Å^2	O1/O2 Ui/Ue x100 Å^2
25	5.7648(4)	5.7377(4)	12.3377(8)	0.0140(13)	0.3554(3)	0.0176(7)	0.4388(14)	0.3251(7)	0.62(16)	1.33(14)	3.37(16)
100	5.7694(4)	5.7365(4)	12.3530(8)	0.0135(14)	0.3560(3)	0.0188(7)	0.4403(14)	0.3261(7)	0.84(17)	1.16(15)	3.37(17)
200	5.7752(4)	5.7324(4)	12.3791(8)	0.0111(15)	0.3555(3)	0.0182(7)	0.4422(14)	0.3251(8)	1.07(18)	1.30(15)	3.87(18)
300	5.7785(4)	5.7323(4)	12.4043(9)	0.0115(15)	0.3561(3)	0.0177(7)	0.4422(13)	0.3257(7)	1.01(18)	1.60(16)	3.68(17)
400	5.7809(5)	5.7352(5)	12.4309(10)	0.0107(16)	0.3556(4)	0.0170(8)	0.4399(14)	0.3252(8)	1.49(20)	1.79(17)	4.02(18)

Temperature (°C)	a/ Å	b/ Å	c/ Å	Ln/Sr(x)	Ln/Sr(z)	O1(z)	O2(x)	O2(z)	Ln/Sr Ui/Ue x100 Å^2	Sc Ui/Ue x100 Å^2	O1/O2 Ui/Ue x100 Å^2
600	5.7839(5)	5.7445(5)	12.4873(10)	0.0095(19)	0.3546(5)	0.0160(9)	0.4437(16)	0.3271(9)	1.81(21)	2.33(19)	5.00(20)
800	5.7854(6)	5.7555(6)	12.5456(13)	0.0087(24)	0.3541(5)	0.0147(11)	0.4415(18)	0.3267(10)	2.52(26)	2.56(22)	5.55(25)
900	5.7869(7)	5.7615(7)	12.5760(14)	0.0077(26)	0.3540(5)	0.0146(12)	0.4424(19)	0.3263(10)	2.76(28)	2.36(23)	5.64(27)
1000	5.7847(7)	5.7670(7)	12.6089(14)	0.0020(31)	0.3543(6)	0.0128(15)	0.4453(22)	0.3267(11)	3.13(30)	2.63(24)	6.19(30)

$NdSrScO_4$

Temperature (°C)	a/ Å	b/ Å	c/ Å	Ln/Sr(x)	Ln/Sr(z)	O1(z)	O2(x)	O2(z)	Ln/Sr Ui/Ue x100 Å^2	Sc Ui/Ue x100 Å^2	O1/O2 Ui/Ue x100 Å^2
25	5.7680(4)	5.7234(4)	12.2985(7)	0.0149(9)	0.3561(2)	0.0183(23)	0.4364(13)	0.3257(7)	0.61(12)	1.28(13)	3.74(14)
100	5.7704(4)	5.7227(4)	12.3142(7)	0.0144(9)	0.3563(2)	0.0189(6)	0.4376(12)	0.3252(7)	0.65(12)	1.33(13)	3.67(14)
200	5.7746(3)	5.7232(3)	12.3422(7)	0.0141(9)	0.3560(2)	0.0182(6)	0.4376(12)	0.3252(7)	0.85(12)	1.36(12)	3.73(14)
400	5.7803(3)	5.7278(3)	12.3943(7)	0.0122(10)	0.3558(2)	0.0176(6)	0.4367(11)	0.3257(7)	1.22(13)	1.90(13)	4.12(15)
600	5.7827(3)	5.7371(3)	12.4467(7)	0.0112(10)	0.3551(2)	0.0159(6)	0.4386(11)	0.3254(7)	2.02(14)	2.22(14)	4.87(15)
700	5.7828(4)	5.7419(4)	12.4723(7)	0.0110(11)	0.3553(2)	0.0155(7)	0.4394(12)	0.3264(7)	2.28(15)	2.04(14)	5.16(15)
800	5.7858(3)	5.7485(3)	12.5032(7)	0.0096(12)	0.3549(3)	0.0151(7)	0.4406(13)	0.3268(7)	2.55(15)	2.37(14)	5.56(16)
900	5.7852(4)	5.7535(4)	12.5314(8)	0.0086(12)	0.3550(3)	0.0148(8)	0.4418(13)	0.3264(7)	2.80(15)	2.57(14)	5.78(16)
1000	5.7859(4)	5.7602(4)	12.5642(8)	0.0064(14)	0.3554(3)	0.0135(8)	0.4447(13)	0.3267(7)	3.23(16)	2.66(14)	6.05(17)

Table d Key bond distances and angles as extracted from PND data for $LnSrScO_4$ (*e.s.d's are given in parantheses*).

$LaSrScO_4$

Temperature (°C)	Sc-O(1)/ Å	Sc-O(2)/ Å	Ln/Sr-O(1)x2/Å	Ln/Sr-O(1)x2/Å	Ln/Sr-O(2)/Å	Ln/Sr-O(2)x2/Å	Ln/Sr-O(2)/Å	Ln/Sr-O(2)/Å	Sc-O(1)-Sc/°
25	2.044(1)	2.180(7)	2.812(5)	2.628(5)	2.496(7)	2.910(1)	2.330(7)	3.312(7)	169.09(34)
100	2.044(1)	2.184(7)	2.815(5)	2.632(5)	2.510(7)	2.909(1)	2.327(7)	3.300(7)	169.33(35)
200	2.044(1)	2.191(7)	2.815(6)	2.546(7)	2.546(7)	2.906(1)	2.322(7)	3.272(7)	169.8(4)
400	2.044(1)	2.196(6)	2.815(6)	2.649(6)	2.573(7)	2.906(1)	2.330(7)	3.253(7)	170.9(4)
600	2.044(1)	2.200(6)	2.815(7)	2.661(7)	2.607(8)	2.911(1)	2.338(7)	3.217(8)	172.2(5)
700	2.043(1)	2.205(6)	2.811(8)	2.672(7)	2.617(8)	2.912(1)	2.335(7)	3.206(8)	173.0(5)
800	2.041(1)	2.214(7)	2.786(11)	2.705(10)	2.650(10)	2.920(1)	2.333(8)	3.163(10)	176.1(8)
			Ln/Sr-O(1)x4/Å		Ln/Sr-O(2)/Å	Ln/Sr-O(2)x4/Å			Sc-O(1)-Sc/°
900	2.041(1)	2.190(7)	2.756 (2)		2.345(8)	2.909(1)			180
1000	2.043(1)	2.197(10)	2.749(2)		2.349(9)	2.911(1)			180

$PrSrScO_4$

Temperature (°C)	Sc-O(1)/ Å	Sc-O(2)/ Å	Ln/Sr-O(1)x2/Å	Ln/Sr-O(1)x2/Å	Ln/Sr-O(2)/Å	Ln/Sr-O(2)x2/Å	Ln/Sr-O(2)/Å	Ln/Sr-O(2)/Å	Sc-O(1)-Sc/°
25	2.045(1)	2.186(9)	2.813(7)	2.613(8)	2.477(10)	2.906(2)	2.267(10)	3.337(10)	167.8(5)
100	2.047(1)	2.176(9)	2.822(7)	2.600(8)	2.490(10)	2.904(2)	2.288(11)	3.328(11)	167.0(4)
200	2.047(1)	2.190(10)	2.831(8)	2.603(9)	2.518(11)	2.903(2)	2.271(11)	3.307(11)	167.3(5)
300	2.047(1)	2.188(9)	2.823(8)	2.606(8)	2.517(11)	2.903(2)	2.290(11)	3.311(11)	167.7(5)
400	2.047(1)	2.200(10)	2.827(9)	2.613(9)	2.510(12)	2.906(2)	2.286(12)	3.321(12)	168.1(5)

Temperature (°C)	Sc-O(1)/ Å	Sc-O(2)/ Å	Ln/Sr-O(1)x2/Å	Ln/Sr-O(1)x2/Å	Ln/Sr-O(2)/Å	Ln/Sr-O(2)x2/Å	Ln/Sr-O(2)/Å	Ln/Sr-O(2)/Å	Sc-O(1)-Sc/°
600	2.048(1)	2.184(11)	2.839(11)	2.632(11)	2.535(14)	2.905(2)	2.300(12)	3.291(14)	168.8(6)
800	2.048(1)	2.200(13)	2.843(14)	2.649(14)	2.527(17)	2.912(2)	2.301(15)	3.299(17)	169.6(8)
900	2.050(1)	2.210(13)	2.850(15)	2.651(15)	2.540(18)	2.916(2)	2.298(16)	3.289(16)	169.7(9)
1000	2.048(1)	2.208(14)	2.851(18)	2.648(18)	2.588(22)	2.920(3)	2.306(17)	3.239(22)	171.0(11)

$NdSrScO_4$

Temperature (°C)	Sc-O(1)/ Å	Sc-O(2)/ Å		Ln/Sr-O(1)x2/Å	Ln/Sr-O(2)/Å	Ln/Sr-O(2)x2/Å	Ln/Sr-O(2)/Å	Ln/Sr-O(2)/Å	Sc-O(1)-Sc/°
25	2.044(1)	2.175(9)	2.804(6)	2.601(7)	2.460(8)	2.900(1)	2.281(9)	3.358(9)	167.4(4)
100	2.045(1)	2.182(8)	2.811(6)	2.596(6)	2.472(8)	2.900(1)	2.279(9)	3.350(8)	167.0(4)
200	2.045(1)	2.187(8)	2.813(6)	2.604(6)	2.475(8)	2.900(1)	2.280(9)	3.350(8)	167.4(4)
400	2.046(1)	2.192(8)	2.822(6)	2.609(6)	2.482(8)	2.903(1)	2.291(9)	3.348(8)	167.8(4)
600	2.046(1)	2.202(8)	2.823(7)	2.630(7)	2.499(8)	2.907(1)	2.286(9)	3.332(9)	168.9(4)
700	2.046(1)	2.193(9)	2.822(8)	2.634(7)	2.503(9)	2.907(1)	2.303(9)	3.325(9)	169.1(5)
800	2.048(1)	2.193(9)	2.831(8)	2.638(8)	2.519(9)	2.910(1)	2.307(9)	3.311(10)	169.4(5)
900	2.048(1)	2.201(9)	2.834(8)	2.640(8)	2.531(10)	2.913(1)	2.306(9)	3.299(10)	169.6(5)
1000	2.048(1)	2.200(9)	2.830(9)	2.643(9)	2.561(11)	2.916(2)	2.316(10)	3.270(11)	170.5(6)

Table e Refined atomic parameters for $LaSrInO_4$ (PXD) *(e.s.d's are given in parantheses).*

$LaSrInO_4$												
Temperature (°C)	**a/ Å**	**b/ Å**	**c/ Å**	**La/Sr(x)**	**La/Sr(y)**	**La/Sr(z)**	**O1(x)**	**O1(y)**	**O1(z)**	**O2(x)**	**O1(y)**	**O2(z)**
50	12.5731(3)	5.8788(1)	5.8233(1)	0.1451(1)	-0.0179(5)	-0.0277(3)	0.0146(18)	0.2315(94)	0.236(9)	0.3186(15)	0.0854(27)	0.020(4)
100	12.5820(5)	5.8849(2)	5.8243(2)	0.1452(1)	-0.0178(5)	-0.0253(4)	0.0117(20)	0.2559(123)	0.243(7)	0.3177(15)	0.0962(26)	0.003(4)
200	12.5827(5)	5.8956(2)	5.8231(2)	0.1451(1)	-0.0167(6)	-0.0170(5)	0.0155(16)	0.2179(50)	0.2327(51)	0.3208(14)	0.0936(26)	0.0445(31)
300	12.5670(4)	5.9111(2)	5.8268(1)	0.1440(1)	-0.0161(5)	-0.0072(8)	0.0167(14)	0.2190(43)	0.2470(58)	0.3168(14)	0.0886(25)	0.0594(23)
400	12.5825(4)	5.9154(2)	5.8334(1)	0.1439(1)	-0.0142(6)	-0.0001(14)	0.0131(16)	0.2062(32)	0.2559(42)	0.3171(14)	0.0904(24)	0.0598(22)
500	12.6105(4)	5.9161(2)	5.8404(2)	0.1441(1)	-0.0160(6)	-0.0031(12)	0.0089(19)	0.1997(27)	0.2585(36)	0.3205(14)	0.0890(24)	0.0621(21)
600	12.6433(3)	5.9176(2)	5.8467(1)	0.1441(1)	-0.0153(6)	0.0044(12)	0.0091(19)	0.1965(27)	0.2594(35)	0.3189(13)	0.0843(24)	0.0630(21)
700	12.6748(4)	5.9176(1)	5.8531(1)	0.1442(1)	-0.0161(6)	0.0065(11)	0.0077(20)	0.2024(33)	0.2521(44)	0.3191(13)	0.0774(25)	0.0552(25)
800	12.7063(4)	5.9171(1)	5.8596(1)	0.1443(1)	-0.0144(6)	0.0051(12)	0.0111(20)	0.2057(36)	0.2446(48)	0.3217(13)	0.0688(25)	0.0560(25)
900	12.7395(4)	5.9163(1)	5.8664(1)	0.1445(1)	-0.0074(10)	0.0029(14)	-0.0192(15)	0.2043(32)	0.2389(48)	0.3233(13)	0.0623(23)	0.0615(25)
1000	12.7788(4)	5.9153(1)	5.8739(1)	0.1447(1)	-0.0079(10)	0.0045(13)	-0.0103(25)	0.1886(25)	0.2433(37)	0.3262(13)	0.0583(25)	0.0664(24)

Table f Refined thermal parameters for $LaSrInO_4$ (PXD) *(e.s.d's are given in parantheses).*

Temperature (°C)	La/Sr Ui/Ue x100 Å^2	In Ui/Ue x100 Å^2	O1/O2 Ui/Ue x100 Å^2
50	1.53(8)	0.41(8)	2.8(4)
100	1.65(9)	0.67(9)	2.5(4)
200	2.88(10)	1.60(10)	0.4(4)
300	2.15(9)	0.98(9)	-1.0(4)
400	2.73(10)	1.37(10)	-1.2(4)
500	3.07(10)	1.47(10)	-1.1(4)
600	3.52(11)	1.52(10)	-0.8(4)
700	3.66(11)	1.68(10)	0.4(4)
800	3.91(12)	1.82(10)	0.8(5)
900	4.64(11)	1.78(9)	0.7(5)
1000	4.83(12)	2.17(11)	0.9(5)

Table g Key bond distances and angles as extracted from PXD data for $LaSrInO_4$ (*e.s.d's are given in parantheses*).

Temperature (°C)	In-O(1)/ Å	In-O(1)/ Å	In-O(2)/ Å	La/Sr-O(1)/Å	La/Sr-O(1)/Å	La/Sr-O(1)/Å	La/Sr-O(1)/Å	La/Sr-O(2)/Å	La/Sr-O(2)/Å	La/Sr-O(2)/Å	La/Sr-O(2)/Å	La/Sr-O(2)/Å	In-O(1)-In/°
50	1.990(4)	2.170(4)	2.337(19)	2.650(4)	2.750(4)	2.640(4)	3.04(4)	2.288(18)	3.585(17)	2.394(16)	3.273(20)	2.675(20)	166.0(21)
100	2.050(7)	2.110(7)	2.364(20)	2.680(6)	2.750(6)	2.650(5)	3.00(6)	2.295(18)	3.651(16)	2.344(16)	3.287(24)	2.682(24)	168.2(29)
200	2.027(33)	2.154(33)	2.346(18)	2.658(24)	2.809(25)	2.586(24)	3.045(23)	2.323(17)	3.644(16)	2.365(15)	3.329(17)	2.632(17)	164.4(12)
300	1.962(30)	2.209(30)	2.383(17)	2.736(25)	2.769(26)	2.583(27)	2.973(25)	2.293(16)	3.622(15)	2.425(14)	3.366(14)	2.609(14)	166.1(12)
400	1.903(25)	2.263(25)	2.381(16)	2.678(31)	2.858(30)	2.649(31)	2.877(31)	2.295(15)	3.608(13)	2.437(13)	3.351(13)	2.628(13)	171.2(17)
500	1.843(17)	2.609(23	2.381(17)	2.609(23)	2.892(22)	2.681(24)	2.928(22)	2.308(16)	3.622(15)	2.420(14)	3.349(15)	2.635(15)	168.5(12)
600	1.828(16)	2.354(16)	2.372(17)	2.698(23)	2.919(23)	2.590(22)	2.928(22)	2.313(16)	3.595(14)	2.440(14)	3.326(15)	2.653(15)	167.9(11)
700	1.883(21)	2.301(20)	2.351(17)	2.688(26)	2.940(26)	2.593(25)	2.688(26)	2.312(17)	3.552(15)	2.466(14)	3.266(17)	2.703(17)	168.1(13)
800	1.940(24)	2.257(23)	2.329(17)	2.708(25)	2.918(25)	2.546(24)	2.979(25)	2.322(16)	3.489(14)	2.525(14)	3.278(17)	2.681(17)	165.6(13)
900	1.971(27)	2.250(25)	2.309(16)	2.783(22))	3.155(20)	2.435(22)	2.800(22)	2.340(16)	3.385(13)	2.581(14)	3.346(17)	2.663(17)	161.4(11)
1000	1.885(20)	2.330(18)	2.281(16)	2.695(27)	2.889(24)	2.494(25)	3.136(27)	2.379(16)	3.358(16)	2.601(15)	3.366(14)	2.634(17)	162.7(11)

Appendix B

Appendix B

Table a Lattice parameters, selected bond distances and final fit factors for $LaSrCoO_4$ (PXD) (*e.s.d's are given in parantheses*).

Temperature/ °C	a parameter/ Å	c parameter/ Å	Co-O(eq)/ Å	Co-O (ax)/ Å	La/Sr-O(1)/ Å x 4	La/Sr-O(2)/ Å	La/Sr-O(2) / Å x 4	χ^2	Rp/ %	Rwp/ %
298	3.8080(1)	12.4883(4)	1.904(1)	2.076(8)	2.578(1)	2.429(1)	2.714(1)	5.17	2.89	1.99
323	3.8086(1)	12.4963(4)	1.904(1)	2.084(8)	2.581(1)	2.422(1)	2.715(1)	5.54	2.97	2.02
348	3.8085(1)	12.5023(4)	1.904(1)	2.080(8)	2.582(1)	2.427(1)	2.714(1)	5.90	2.95	2.01
373	3.8106(1)	12.5166(4)	1.905(1)	2.081(8)	2.583(1)	2.432(1)	2.716(1)	5.60	2.86	1.95
398	3.8123(1)	12.5294(4)	1.906(1)	2.088(8)	2.585(1)	2.431(1)	2.717(1)	5.60	2.82	1.96
423	3.8140(1)	12.5437(4)	1.907(1)	2.085(8)	2.588(1)	2.438(1)	2.718(1)	5.54	2.73	1.93
448	3.8155(1)	12.5581(1)	1.908(1)	2.093(8)	2.590(1)	2.434(1)	2.720(1)	5.58	2.73	1.92
473	3.8173(1)	12.5914(1)	1.909(1)	2.101(8)	2.592(1)	2.433(1)	2.721(1)	5.54	2.68	1.88
498	3.8189(1)	12.5914(3)	1.909(1)	2.106(7)	2.596(1)	2.431(1)	2.723(1)	5.18	2.57	1.81
523	3.8204(1)	12.6089(3)	1.910(1)	2.114(7)	2.597(1)	2.431(1)	2.724(1)	4.86	2.47	1.76
548	3.8219(1)	12.6266(3)	1.911(1)	2.123(7)	2.600(1)	2.427(1)	2.726(1)	4.48	2.36	1.69
573	3.8234(1)	12.6458(3)	1.912(1)	2.120(7)	2.603(1)	2.436(1)	2.726(1)	4.28	2.27	1.65
598	3.8248(1)	12.6647(2)	1.912(1)	2.119(7)	2.606(1)	2.442(1)	2.727(1)	4.01	2.19	1.61
623	3.8263(1)	12.6841(2)	1.913(1)	2.124(7)	2.609(1)	2.444(1)	2.728(1)	3.99	2.17	1.59
648	3.8275(1)	12.7027(3)	1.914(1)	2.124(7)	2.612(1)	2.449(1)	2.728(1)	4.10	2.21	1.63
673	3.8289(1)	12.7218(3)	1.914(1)	2.127(7)	2.616(1)	2.452(1)	2.729(1)	3.98	2.17	1.62
698	3.8301(1)	12.7393(3)	1.915(1)	2.137(7)	2.618(1)	2.447(1)	2.731(1)	4.24	2.22	1.65
723	3.8313(1)	12.7563(3)	1.916(1)	2.136(7)	2.622(1)	2.452(1)	2.731(1)	4.34	2.25	1.68

Temperature/ °C	a parameter/ Å	c parameter/ Å	Co-O(eq)/ Å	Co-O (ax)/ Å	La/Sr-O(1)/ Å x 4	La/Sr-O(2)/ Å	La/Sr-O(2) / Å x 4	χ^2	Rp/ %	Rwp/ %
748	3.8255(1)	12.7727(3)	1.916(1)	2.139(7)	2.624(1)	2.454(1)	2.732(1)	4.51	2.29	1.70
773	3.8339(1)	12.7886(3)	1.917(1)	2.142(7)	2.627(1)	2.456(1)	2.733(1)	4.56	2.29	1.70

Table b Lattice parameters, selected bond distances and final fit factors for $PrSrCoO_4$ (PXD) (*e.s.d's are given in parantheses*).

Temperature/ °C	a parameter/ Å	c parameter/ Å	Co-O(eq)/ Å	Co-O (ax)/ Å	La/Sr-O(1)/ Å x 4	La/Sr-O(2)/ Å	La/Sr-O(2) / Å x 4	χ^2	Rp/ %	Rwp/ %
298	3.7741(1)	12.3177(3)	1.887(1)	2.058(9)	2.554(1)	2.380(9)	2.690(1)	1.66	3.02	2.38
323	3.7752(1)	12.3261(3)	1.888(1)	2.051(8)	2.555(1)	2.690(1)	2.389(8)	1.73	2.91	2.27
348	3.7764(1)	12.3360(3)	1.888(1)	2.046(8)	2.559(1)	2.689(1)	2.396(8)	1.85	2.88	2.26
373	3.7778(1)	12.3474(3)	1.889(1)	2.060(8)	2.561(1)	2.384(8)	2.620(1)	1.92	2.83	2.21
398	3.7793(1)	12.3592(3)	1.890(1)	2.057(7)	2.563(1)	2.391(8)	2.692(1)	1.86	2.73	2.13
423	3.7811(1)	12.3720(3)	1.890(1)	2.057(7)	2.564(1)	2.396(7)	2.693(1)	1.95	2.70	2.12
448	3.7827(1)	12.3857(3)	1.891(1)	2.054(7)	2.566(1)	2.404(7)	2.694(1)	2.01	2.61	2.04
473	3.7842(1)	12.4000(3)	1.892(1)	2.067(7)	2.569(1)	2.395(7)	2.696(1)	2.06	2.61	2.04
498	3.7859(1)	12.4156(3)	1.893(1)	2.080(7)	2.572(1)	2.387(7)	2.572(1)	2.08	2.60	2.02
523	3.7877(1)	12.4317(2)	1.894(1)	2.083(7)	2.573(1)	2.391(7)	2.700(1)	2.05	2.57	2.01
548	3.7893(1)	12.4482(2)	1.895(1)	2.087(7)	2.577(1)	2.391(7)	2.701(1)	2.08	2.56	1,99
573	3.7910(1)	12.4652(2)	1.896(1)	2.092(7)	2.579(1)	2.391(7)	2.702(1)	1.99	2.49	1.94
598	3.7927(1)	12.4834(2)	1.896(1)	2.103(7)	2.581(1)	2.387(7)	2.705(1)	1.95	2.61	2.03

Temperature/ °C	a parameter/ Å	c parameter/ Å	Co-O(eq)/ Å	Co-O (ax)/ Å	La/Sr-O(1)/ Å x 4	La/Sr-O(2)/ Å	La/Sr-O(2) / Å x 4	χ^2	Rp/ %	Rwp/ %
623	3.7944(1)	12.5012(2)	1.897(1)	2.107(8)	2.584(1)	2.389(8)	2.706(1)	1.80	2.59	2.04
648	3.7960(1)	12.5188(2)	1.898(1)	2.116(8)	2.585(1)	2.388(8)	2.708(1)	1.84	2.60	2.03
673	3.7975(1)	12.5368(3)	1.899(1)	2.115(8)	2.588(1)	2.395(8)	2.709(1)	1.83	2.50	1.95
698	3.7989(1)	12.5540(2)	1.899(1)	2.128(8)	2.509(1)	2.388(8)	2.712(11)	1.91	2.51	1.95
723	3.8003(1)	12.5705(2)	1.900(1)	2.118(8)	2.593(1)	2.403(8)	2.710(1)	1.97	2.54	1.98
748	3.8019(1)	12.5872(2)	1.901(1)	2.119(8)	2.596(1)	2.408(8)	2.711(1)	1.96	2.53	1.96
773	3.8034(1)	12.6029(2)	1.902(1)	2.128(8)	2.597(1)	2.406(8)	2.713(1)	1.85	2.52	1.96
798	3.8047(1)	12.6188(2)	1.902(1)	2.132(8)	2.599(1)	2.406(8)	2.714(1)	1.98	2.51	2.55
823	3.8061(1)	12.6340(2)	1.903(1)	2.132(8)	2.603(1)	2.409(8)	2.715(1)	1.97	2.48	1.93
848	3.8074(1)	12.6485(2)	1.904(1)	2.138(8)	2.605(1)	2.408(8)	2.716(1)	2.02	2.50	1.94
873	3.8087(1)	12.6622(2)	1.904(1)	2.138(8)	2.607(1)	2.413(8)	2.717(1)	1.96	2.45	1.91

Table c Lattice parameters, selected bond distances and final fit factors for $NdSrCoO_4$ (PXD) (*e.s.d's are given in parantheses*).

Temperature/ °C	a parameter/ Å	c parameter/ Å	Co-O(eq)/ Å	Co-O (ax)/ Å	La/Sr-O(1)/ Å x 4	La/Sr-O(2)/ Å	La/Sr-O(2) / Å x 4	χ^2	Rp/ %	Rwp/ %
298	3.7772(1)	12.3115(3)	1.889(1)	2.051(7)	2.554(1)	2.385(7)	2.691(1)	2.13	2.06	1.60
323	3.7782(1)	12.3192(3)	1.889(1)	2.047(7)	2.556(1)	2.391(7)	2.691(1)	2.35	2.07	1.58
348	3.7795(1)	12.3288(3)	1.890(1)	2.052(7)	2.558(1)	2.388(7)	2.693(1)	2.37	2.03	1.56
373	3.7807(1)	12.3393(2)	1.890(1)	2.057(7)	2.561(1)	2.385(7)	2.694(1)	2.38	1.97	1.51
398	3.7823(1)	12.3512(2)	1.891(1)	2.062(7)	2.562(1)	2.385(7)	2.695(1)	2.44	1.93	1.47
423	3.7841(1)	12.3643(3)	1.892(1)	2.061(7)	2.564(1)	2.391(7)	2.696(1)	2.70	2.00	1.52
448	3.7857(1)	12.3778(2)	1.893(1)	2.060(7)	2.565(1)	2.398(7)	2.697(1)	2.54	1.90	1.44
473	3.7874(1)	12.3916(2)	1.894(1)	2.064(7)	2.568(1)	2.397(7)	2.698(1)	2.56	1.87	1.42
498	3.7893(1)	12.4075(2)	1.895(1)	2.066(6)	2.570(1)	2.401(7)	2.699(1)	2.54	1.83	1.40
523	3.7911(1)	12.4228(3)	1.896(1)	2.067(7)	2.573(1)	2.404(7)	2.701(1)	2.75	1.86	1.40
548	3.7911(1)	12.4228(3)	1.896(1)	2.075(6)	2.575(1)	2.401(6)	2.702(1)	2.59	1.78	1.35
573	3.7945(1)	12.4381(2)	1.896(1)	2.075(6)	2.577(1)	2.394(6)	2.705(1)	2.58	1.76	1.35
598	3.7961(1)	12.4710(2)	1.898(1)	2.086(6)	2.580(1)	2.401(6)	2.705(1)	2.61	1.77	1.34
623	3.7976(1)	12.4870(2)	1.899(1)	2.089(6)	2.583(1)	2.404(6)	2.707(1)	2.66	1.75	1.33
648	3.7994(1)	12.5041(2)	1.890(1)	2.094(6)	2.586(1)	2.404(6)	2.708(1)	2.68	1.74	1.32
673	3.8010(1)	12.5207(2)	1.900(1)	2.100(6)	2.588(1)	2.403(6)	2.709(1)	2.75	1.75	1.34
698	3.8024(1)	12.5367(2)	1.901(1)	2.106(6)	2.591(1)	2.404(6)	2.711(1)	2.73	1.74	1.30

Table d Lattice parameters, selected bond distances and final fit factors for $SmSrCoO_4$ (PXD) (*e.s..d's are given in parentheses*).

Temperature/ °C	a parameter/ Å	c parameter/ Å	Co-O(eq)/ Å	Co-O (ax)/ Å	La/Sr-O(1)/ Å x 4	La/Sr-O(2)/ Å	La/Sr-O(2) / Å x 4	χ^2	Rp/ %	Rwp/ %
298	3.7520(1)	12.1970(3)	1.876(1)	2.052(9)	2.534(1)	2.343(9)	2.676(1)	2.14	1.93	1.46
323	3.7528(1)	12.2047(3)	1.876(1)	2.053(9)	2.536(1)	2.343(9)	2.676(1)	2.40	1.95	1.46
348	3.7540(1)	12.2136(3)	1.877(1)	2.057(9)	2.537(1)	2.342(9)	2.677(1)	2.56	1.96	1.48
373	3.7555(1)	12.2249(3)	1.878(1)	2.069(9)	2.540(1)	2.333(9)	2.680(1)	2.63	1.93	1.44
398	3.7569(1)	12.2357(3)	1.878(1)	2.070(9)	2.541(1)	2.336(9)	2.681(1)	2.64	1.91	1.42
423	3.7587(1)	12.2493(3)	1.879(1)	2.058(9)	2.543(1)	2.353(9)	2.680(1)	2.64	1.89	1.42
448	3.7602(1)	12.2622(3)	1.880(1)	2.071(9)	2.546(1)	2.344(9)	2.682(1)	2.68	1.88	1.40
473	3.7618(1)	12.2762(3)	1.881(1)	2.069(9)	2.548(1)	2.350(9)	2.683(1)	2.72	1.86	1.38
498	3.7635(1)	12.2907(3)	1.882(1)	2.071(9)	2.550(1)	2.353(9)	2.684(1)	2.58	1.81	1.35
523	3.7653(1)	12.3059(3)	1.883(1)	2.058(8)	2.553(1)	2.371(9)	2.683(1)	2.56	1.79	1.34
548	3.7670(1)	12.3213(2)	1.883(1)	2.069(8)	2.556(1)	2.364(8)	2.686(1)	2.57	1.74	1.31
573	3.7687(1)	12.3373(3)	1.884(1)	2.083(8)	2.558(1)	2.357(8)	2.688(1)	2.60	1.72	1.29
598	3.7705(1)	12.3545(3)	1.885(1)	2.079(8)	2.562(1)	2.364(8)	2.688(1)	2.68	1.72	1.28
623	3.7724(1)	12.3708(3)	1.886(1)	2.091(8)	2.564(1)	2.358(8)	2.691(1)	2.63	1.69	1.28
648	3.7741(1)	12.3876(2)	1.887(1)	2.090(8)	2.568(1)	2.362(8)	2.691(1)	2.47	1.63	1.24
673	3.7758(1)	12.4046(2)	1.888(1)	2.096(8)	2.571(1)	2.361(8)	2.693(1)	2.53	1.63	1.23
698	3.7776(1)	12.4214(2)	1.889(1)	2.096(8)	2.573(1)	2.367(8)	2.693(1)	2.44	1.58	1.20
723	3.7793(1)	12.4379(2)	1.890(1)	2.108(8)	2.576(1)	2.360(8)	2.696(1)	2.45	1.58	1.19
748	3.7809(1)	12.4537(2)	1.890(1)	2.114(8)	2.578(1)	2.361(8)	2.698(1)	2.50	1.58	1.21
773	3.7825(1)	12.4697(2)	1.891(1)	2.114(8)	2.581(1)	2.365(8)	2.698(1)	2.46	1.55	1.18

Table e Lattice parameters, selected bond distances and final fit factors for $EuSrCoO_4$ (PXD) (e.s.d's are given in parantheses).

Temperature/ °C	a parameter/ Å	c parameter/ Å	Co-O(eq)/ Å	Co-O (ax)/ Å	La/Sr-O(1)/ Å x 4	La/Sr-O(2)/ Å	La/Sr-O(2) / Å x 4	χ^2	Rp/ %	Rwp/ %
298	3.7575(1)	12.2000(5)	1.879(1)	2.030(10)	2.535(1)	2.367(11)	2.677(1)	1.22	2.12	1.68
323	3.7586(1)	12.2077(5)	1.879(1)	2.021(10)	2.535(1)	2.382(10)	2.677(1)	1.20	2.04	1.62
348	3.7596(1)	12.2173(5)	1.880(1)	2.030(10)	2.539(1)	2.372(10)	2.678(1)	1.22	1.98	1.59
373	3.7613(1)	12.2282(5)	1.881(1)	2.037(11)	2.538(1)	2.372(10)	2.680(1)	1.26	1.98	1.58
398	3.7625(1)	12.2399(5)	1.881(1)	2.052(10)	2.543(1)	2.357(11)	2.682(1)	1.25	1.94	1.56
423	3.7641(1)	12.2522(5)	1.882(1)	2.027(10)	2.544(1)	2.386(11)	2.680(1)	1.28	1.94	1.55
448	3.7655(1)	12.2639(5)	1.883(1)	2.058(10)	2.545(1)	2.361(11)	2.685(1)	1.27	1.95	1.56
473	3.7673(1)	12.2787(4)	1.884(1)	2.053(12)	2.548(1)	2.371(11)	2.685(1)	1.20	1.89	1.51
498	3.7693(1)	12.2952(5)	1.885(1)	2.053(12)	2.551(1)	2.375(13)	2.686(1)	1.25	2.03	1.62
523	3.7710(1)	12.3102(5)	1.885(1)	2.061(11)	2.533(1)	2.372(11)	2.688(1)	1.22	2.00	1.58
548	3.7726(1)	12.3257(5)	1.886(1)	2.067(11)	2.556(1)	2.371(11)	2.690(1)	1.18	2.00	1.59
573	3.7745(1)	12.3417(4)	1.887(1)	2.080(11)	2.560(1)	2.361(11)	2.692(1)	1.16	1.91	1.53
598	3.7760(1)	12.3571(5)	1.888(1)	2.064(11)	2.561(1)	2.383(12)	2.691(1)	1.30	1.98	1.58
623	3.7778(1)	12.3736(5)	1.889(1)	2.097(11)	2.565(1)	2.355(11)	2.696(1)	1.23	1.90	1.52
648	3.7795(1)	12.3894(5)	1.890(1)	2.087(11)	2.567(1)	2.370(12)	2.695(1)	1.26	1.93	1.55
673	3.7811(1)	12.4053(5)	1.890(1)	2.089(11)	2.568(1)	2.376(11)	2.697(1)	1.23	1.86	1.49
698	3.7829(1)	12.4218(5)	1.892(1)	2.098(12)	2.573(1)	2.377(11)	2.697(1)	1.26	1.90	1.52
723	3.7865(1)	12.4548(5)	1.893(1)	2.104(12)	2.572(1)	2.378(12)	2.699(2)	1.24	1.96	1.55
748	3.7865(1)	12.4548(5)	1.893(1)	2.104(12)	2.578(1)	2.374(12)	2.701(2)	1.24	1.91	1.51
773	3.7881(1)	12.4694(5)	1.894(1)	2.114(12)	2.579(1)	2.370(12)	2.703(2)	1.25	1.86	1.48
798	3.7896(1)	12.4850(5)	1.895(1)	2.124(12)	2.583(1)	2.363(12)	2.705(2)	1.29	1.89	1.56

Temperature/ °C	a parameter/ Å	c parameter/ Å	Co-O(eq)/ Å	Co-O (ax)/ Å	La/Sr-O(1)/ Å x 4	La/Sr-O(2)/ Å	La/Sr-O(2) / Å x 4	χ^2	Rp/ %	Rwp/ %
823	3.7914(1)	12.5013(5)	1.896(1)	2.128(12)	2.585(1)	2.365(12)	2.706(2)	1.27	1.87	1.49
848	3.7931(1)	12.5155(5)	1.896(1)	2.129(12)	2.587(1)	2.370(12)	2.707(2)	1.22	1.84	1.46
873	3.7945(1)	12.5291(5)	1.898(5)	2.126(12)	2.589(1)	2.377(12)	2.708(2)	1.28	1.88	1.50

Table f Lattice parameters, selected bond distances and final fit factors for $GdSrCoO_4$ (PXD) (*e.s.d's are given in parantheses*).

Temperature/ °C	a parameter/ Å	c parameter/ Å	Co-O(eq)/ Å	Co-O (ax)/ Å	La/Sr-O(1)/ Å x 4	La/Sr-O(2)/ Å	La/Sr-O(2) / Å x 4	χ^2	Rp/ %	Rwp/ %
298	3.7555(2)	12.1555(6)	1.878(1)	2.023(13)	2.531(1)	2.357(13)	2.675(1)	1.18	1.99	1.60
323	3.7566(1)	12.1629(6)	1.879(1)	2.029(12)	2.532(1)	2.354(13)	2.677(1)	1.22	1.99	1.59
348	3.7574(1)	12.1713(6)	1.879(1)	2.017(12)	2.532(1)	2.370(13)	2.676(1)	1.17	1.94	1.55
373	3.7586(1)	12.1805(6)	1.879(1)	2.040(12)	2.535(1)	2.348(12)	2.679(1)	1.23	1.95	1.55
398	3.7596(1)	12.1918(6)	1.880(1)	2.041(12)	2.538(1)	2.350(12)	2.679(1)	1.27	1.98	1.58
423	3.7613(1)	12.2036(6)	1.881(1)	2.044(12)	2.540(1)	2.351(12)	2.681(1)	1.20	1.93	1.53
448	3.7630(1)	12.2165(6)	1.881(1)	2.046(12)	2.540(1)	2.356(12)	2.682(1)	1.20	1.94	1.54
473	3.7645(1)	12.2292(6)	1.882(1)	2.053(12)	2.544(1)	2.350(12)	2.684(1)	1.18	1.92	1.53
498	3.7663(1)	12.2435(6)	1.883(1)	2.067(12)	2.548(1)	2.339(12)	2.686(1)	1.21	1.94	1.55
523	3.7677(1)	12.2582(6)	1.884(1)	2.076(12)	2.548(1)	2.337(12)	2.688(2)	1.23	1.95	1.55
548	3.7694(1)	12.2726(7)	1.885(1)	2.051(12)	2.552(1)	2.365(13)	2.686(1)	1.18	1.91	1.52
573	3.7710(1)	12.2887(6)	1.885(1)	2.067(13)	2.556(1)	2.352(13)	2.688(2)	1.20	1.94	1.55
598	3.7729(1)	12.3033(6)	1.886(1)	2.101(12)	2.557(1)	2.324(13)	2.694(2)	1.20	1.94	1.55
623	3.7743(1)	12.3193(6)	1.887(1)	2.102(13)	2.559(1)	2.330(13)	2.695(2)	1.20	1.94	1.54

Temperature/ °C	a parameter/ Å	c parameter/ Å	Co-O(eq)/ Å	Co-O (ax)/ Å	La/Sr-O(1)/ Å x 4	La/Sr-O(2)/ Å	La/Sr-O(2) / Å x 4	χ^2	Rp/ %	Rwp/ %
648	3.7760(1)	12.3366(7)	1.888(1)	2.085(14)	2.563(1)	2.350(14)	2.693(2)	1.25	1.97	1.57
673	3.7778(2)	12.3517(9)	1.889(1)	2.101(17)	2.562(2)	2.345(18)	2.697(2)	1.25	1.96	1.56
698	3.7791(1)	12.3677(7)	1.890(1)	2.085(14)	2.563(1)	2.367(14)	2.696(2)	1.23	1.96	1.57
723	3.7813(1)	12.3843(7)	1.891(1)	2.136(14)	2.567(1)	2.320(14)	2.703(2)	1.18	1.96	1.56
748	3.7826(1)	12.3998(6)	1.891(1)	2.130(14)	2.570(1)	2.329(14)	2.703(2)	1.18	1.97	1.57
773	3.7845(2)	12.4162(7)	1.892(1)	2.118(14)	2.574(2)	2.344(14)	2.702(2)	1.17	1.94	1.54
798	3.7860(2)	12.4314(7)	1.893(1)	2.137(16)	2.577(2)	2.330(17)	2.705(2)	1.26	2.01	1.60
823	3.7875(1)	12.4477(6)	1.894(1)	2.143(14)	2.581(2)	2.327(14)	2.706(2)	1.20	1.98	1.58
848	3.7892(1)	12.4627(6)	1.895(1)	2.140(15)	2.580(2)	2.340(15)	2.707(2)	1.16	1.96	1.56
873	3.7905(1)	12.4776(6)	1.895(1)	2.139(16)	2.586(2)	2.340(16)	2.707(2)	1.21	1.97	1.57

Table g Lattice parameters, selected bond distances and final fit factors for $LaSrCoO_4$ (PND) (*e.s.d's are given in parantheses*).

Temperature/ °C	a parameter/ Å	c parameter/ Å	Co-O(eq)/ Å	Co-O (ax)/ Å	χ^2	Rp/ %	Rwp/ %
50	3.8041(1)	12.4368(2)	1.902(1)	2.038(1)	0.48	1.63	2.70
100	3.8048(1)	12.4425(2)	1.902(1)	2.040(1)	0.53	1.71	2.77
150	3.8062(1)	12.4526(3)	1.903(1)	2.042(1)	0.56	1.77	2.96
200	3.8095(1)	12.4755(2)	1.905(1)	2.049(1)	2.74	3.78	6.58
250	3.8096(1)	12.4766(2)	1.905(1)	2.049(1)	2.59	3.69	6.27
300	3.8109(1)	12.4877(2)	1.905(1)	2.052(1)	2.69	3.76	6.49
350	3.8134(1)	12.4877(2)	1.907(1)	2.058(1)	2.74	3.78	6.43
400	3.8154(1)	12.5069(2)	1.908(1)	2.063(1)	2.75	3.78	6.60
450	3.8175(1)	12.5238(2)	1.909(1)	2.070(1)	2.77	3.80	6.56
500	3.8195(1)	12.5405(2)	1.910(1)	2.075(1)	2.69	3.72	5.58
550	3.8214(1)	12.5581(2)	1.911(1)	2.079(1)	2.71	3.73	6.39
600	3.8231(1)	12.5761(2)	1.912(1)	2.085(1)	2.56	3.64	6.26
650	3.8249(1)	12.6157(2)	1.913(1)	2.091(1)	2.54	3.63	6.28

Table h Lattice parameters, selected bond distances and final fit factors for $NdSrCoO_4$ (PND) (*e.s.d's are given in parantheses*).

Temperature/ °C	a parameter/ Å	c parameter/ Å	Co-O(eq)/ Å	Co-O (ax)/ Å	χ^2	Rp/ %	Rwp/ %
50	3.7665(1)	12.2531(2)	1.883(1)	2.007(1)	0.64	1.95	3.26
100	3.76723(1)	12.2584(2)	1.884(1)	2.010(1)	0.60	1.88	3.29
150	3.7685(1)	12.2675(2)	1.884(1)	2.013(1)	0.61	1.89	3.19
200	3.7703(1)	12.2852(2)	1.885(1)	2.019(1)	1.36	3.87	5.88
250	3.7701(1)	12.2839(2)	1.885(1)	2.018(1)	1.39	3.42	6.15
300	3.7730(1)	12.3046(2)	1.886(2)	2.025(1)	1.18	3.14	5.45
350	3.7753(1)	12.3228(2)	1.888(2)	2.030(1)	1.27	3.24	5.50
400	3.7775(1)	12.3401(2)	1.889(1)	2.034(1)	1.13	3.05	5.13
450	3.7798(1)	12.3583(2)	1.890(2)	2.040(1)	1.04	2.92	5.02
500	3.7822(1)	12.3769(2)	1.891(2)	2.045(1)	1.11	3.00	5.07
550	3.7844(1)	12.3956(2)	1.892(1)	2.052(1)	1.09	2.96	4.85
600	3.787(1)	12.4192(1)	1.894(1)	2.058(1)	1.04	2.89	4.81

Table i Lattice parameters, selected bond distances and final fit factors for $^{154}SmSrCoO_4$ (PND) (*e.s.d's are given in parantheses*).

Temperature/ °C	a parameter/ Å	c parameter/ Å	Co-O(eq)/ Å	Co-O (ax)/ Å	χ^2	Rp/ %	Rwp/ %
10	3.7540(1)	12.1699(4)	1.877(1)	2.009(1)	0.41	1.55	2.56
50	3.7545(1)	12.7240(3)	1.877(1)	2.006(1)	0.39	1.53	2.60
100	3.7552(1)	12.1774(1)	1.878(1)	2.009(2)	0.47	1.67	3.05
150	3.7564(1)	12.1848(3)	1.879(1)	2.011(1)	0.37	1.48	2.53
200	3.7567(1)	12.1887(3)	1.878(1)	2.011(1)	0.37	1.49	2.50
250	3.7577(1)	12.1957(3)	1.879(1)	2.015(1)	0.36	1.47	2.49
300	3.7653(1)	12.2328(2)	1.883(2)	2.025(1)	0.46	1.74	3.30
350	3.7679(1)	12.2529(2)	1.884(1)	2.030(1)	0.45	1.71	3.32
400	3.7701(1)	12.2706(2)	1.885(1)	2.035(1)	0.48	1.77	3.44
450	3.7724(1)	12.2895(3)	1.886(1)	2.039(1)	0.45	1.71	3.27
500	3.7749(1)	12.3110(3)	1.887(1)	2.047(2)	0.49	1.79	3.37
550	3.7774(1)	12.3332(3)	1.8887(1)	2.055(2)	0.46	1.74	3.40
600	3.7799(1)	12.3577(3)	1.8900(1)	2.062(2)	0.48	1.78	3.42
650	3.7826(1)	12.3845(3)	1.8913(1)	2.069(2)	0.44	1.68	3.27
700	3.7854(1)	12.4122(3)	1.8927(1)	2.081(2)	0.55	1.89	3.34
750	3.7882(1)	12.4402(2)	1.8941(1)	2.089(2)	0.43	1.66	3.24
800	3.7914(1)	12.4717(2)	1.896(1)	2.103(2)	0.51	1.81	3.33
850	3.7939(1)	12.4996(2)	1.897(1)	2.113(2)	0.49	1.78	3.21
900	3.7968(1)	12.5299(3)	1.898(1)	2.113(2)	0.55	1.90	3.27